Microplasma Technology for Influencing Cell-Surface Interactions

Thesis submitted in accordance with the requirements of the University of Liverpool for the degree of
Doctor in Philosophy

By

Kyle George Doherty

May 2014

Acknowledgments

This work was financially supported by EPSRC, grant reference: EP/G048444/1.

Foremost, I would like to thank my supervisors for all their support. Thank you Rachel for your continued support and guidance, and Carl for you words of encouragement. I would like to thank my colleague Jun-Seok Oh for his assistance with the plasma jet and for helping my cut and clean polystyrene for many hours. I would also like to thank the other members of this project: James Bradley, Peter Weightman, Andrew Bowfield and Paul Unsworth, for your encouragement, expertise and our discussions on the results achieved. I would particularly like to thank Paul for the acquisition of the XPS data. Andrew's guidance on the analysis of the XPS data is also appreciated.

Thank you to Mr. Alan Roby of the University of Liverpool, UK for the construction of equipment essential to the plasma jet system. Thank you to Dr. Victoria Kearns (University of Liverpool, UK) for suppling the aRPE-19 cells, to Prof. John Reddan for the N/N1003A cells (Oakland University, MA., USA) and to Prof. Barbara Pierscoinek for the B3 cells (University of Ulster, UK). I would like to thank Dr.s Tim Joyce and Riaz Akhtar for training and technical assistance with use of the AFM.

I would like to thank all of my colleagues in the Department of Eye and Vision Science for their support, discussions and friendship. I would particularly like to thank Victoria and Celia for listening to my rants when required, but also for their guidance and experience in the field of Biomaterials.

Thank you to Rebecca Lace for her love and support throughout the final years of my PhD, and for the many discussions throughout it. I would also like to thank Gareth Evans for his support during my write up. The support and love from my parents, Dennis and Donna, throughout this PhD and during my studies before it will forever be appreciated. I hope that someday I can reciprocate what they have done for me.

Outputs

Academic Conferences

1. Roy Mapstone Research Prize 2010, Liverpool, UK – Oral Presentation (3rd place)
2. UK Society for Biomaterials 2010 Glasgow, Scotland, UK – Poster presentation
3. UK Society for Biomaterials 2011 Greenwich, London, UK – Oral Presentation
4. Postgraduate Researchers in Science Medicine 2011 Liverpool, UK – Oral Presentation
5. European Society for Biomaterials 2011 – Dublin, Ireland – Quick Fire Presentation
6. Surface Science of Biologically Important Interfaces 2011, Port Sunlight, UK – Poster Presentation
7. Young Scientist Forum BIOFUTURE 2011 – Gent, Belgium – Poster Presentation
8. UK Society for Biomaterials 2012 – Nottingham, UK – Poster Presentation
9. International Society for Eye Research 2012 – Berlin, Germany – Poster Presentation

Publications

1. *"Polystyrene Surface Modification for Localized Cell Culture Using a Capillary Dielectric Barrier Discharge Atmospheric-Pressure"* Doherty, K.G., Oh, J.-S., Unsworth, P., Bowfield, A., Sheridan, C.M., Weightman, P., Bradley, J.W., Williams, R.L., Microplasma Jet. Plasma Processes and Polymers, 2013. 10(11): p. 978-989.

Abstract

Microplasma Technology for Influencing Cell-Surface Interactions by Kyle George Doherty

Cataracts are the most common cause of preventable blindness worldwide. During cataract surgery a polymeric intraocular lens (IOL) is used to replace the cloudy natural lens. The most common post-operative complication is posterior capsule opacification (PCO). PCO is a wound healing response related to scarring, in which cellular changes disrupt the light path to the back of the eye through various processes, requiring a costly surgery to restore vision. The material of the IOL has been shown to affect PCO and it is hypothesised that the surface modification of IOL materials may be able to reduce the incidence of PCO. The use of plasmas established in the field of biomaterials modification and atmospheric pressure processes have significant benefits over the previous low pressure systems. In this work investigates the use of an atmospheric pressure plasma jet to modify the surface properties of polymeric materials, with the aim of developing a surface treatment method for use on IOLs.

Materials and Methods

The centre of polystyrene (PS) and poly(methyl methacrylate)(PMMA) surfaces were treated with an atmospheric pressure microplasma jet. The modification of surfaces was characterised by spatially resolved water contact angle, x-ray photoelectron spectroscopy (XPS) and atomic force microscopy (AFM). LECs were seeded onto surfaces and grown for 1-7 days. Cell attachment, growth and morphology were examined microscopically. The concentrations of some cytokines implicated in PCO (transforming growth factor-β2, basic fibroblast growth factor, interleukin-1, interleukin-6, and tumour necrosis factor-α) in culture medium were examined at specific time points. Tissue culture polystyrene and untreated materials served as controls. Atmospheric pressure plasma polymerisation of amine containing monomers using a plasma jet was also investigated.

Results and Discussions

The size of surface treatment could be tailored by altering flow rate and sample-nozzle distance. Surface treatment was due to an increase in surface oxygen content and plasma treatment did not cause a significant change in surface roughness. Plasma treatment increased the LEC adhesion to substrates. LECs were densely populated in the centre of

treated materials and cells lacked the cobblestone morphology typical of epithelial cells. The secretion of inflammatory cytokines by LECs grown on plasma treated surfaces did not appear to be up-regulated in comparison to tissue culture polystyrene, however these results are preliminary. This work demonstrated that atmospheric pressure plasma polymerisation can be achieved using the plasma jet system to incorporate nitrogen functionalisation onto PS surfaces; however oxygen was also incorporated onto surfaces.

Conclusions

This work demonstrates that an atmospheric pressure microplasma jet can be used to modify surfaces in a spatially defined manner, without damaging the polymer surfaces. The increase in surface oxygen promotes cell adhesion which can be confined to an area <3mm. This treatment size is too large to be used to create different spatially defined treatments on IOL optics as the typical optic diameter is only 6mm. The large treatment size is possibly due to gas convection spreading reactive species across the surface of samples when the plasma jet reaches the surface. Plasma polymerisation could possibly be used to incorporate functional groups which promote LEC growth which maintains an epithelial morphology.

Contents

List of Figures

List of Tables

Glossary

αSMA - Alpha Smooth Muscle Actin

AC - Anterior Chamber

AFM - Atomic Force Micrscopy

APTMS - Aminopropyltrimethoxysilane

B3 - Human Lens Epithelial Cell Line

BrdU - Bromodeoxyuridine

BSA - Bovine Serum Albumin

CAM - Cell Adhesion Molecule

CCC - Continuous Curvilinear Capsulorhexis

CCD - Charge-Coupled Device

CK - Cytokeratin

DAPI - 4',6-Diamidino-2-phenylindole Dihydrochloride

DMSO - Dimethyl Sulphoxide

ECM - Extracellular Matrix

EDTA - Ethylenediaminetetraacetic Acid

EGF - Epidermal Growth

FCS - Fetal Calf Serum

FGF - Fibroblast Growth Factor

FHL124 - Human Lens Epithelial Cell Line

HMDSO - Hexamethyldisiloxane

IL-1α - Interleukin-1 Alpha

IL-6 - Interleukin 6

IOL - Intraocular Lens

L-Glut - L-Glutamine

LEC - Lens Epithelial Cells

MEME - Minimum Essential Medium Eagles

MMP - Matrix Metalloproteinase

MPC - Methacryloyloxyethyl Phosphorylcholine

N/N1003A - Rabbit Lens Epithelial Cell Line

NBF - Neutral Buffered Formaldehyde

Nd:YAG - Neodymium-Doped Yttrium Aluminium Garnet

PBS - Phosphate Buffered Saline

PC - Posterior Chamber

PCO - Posterior Capsule Opacification

PCR - Polymerase Chain Reaction

PDMS - Poly Dimethyl Siloxane

PEA - Phenylethyl Acrylate

PEG - Polyethylene Gylcol

PEMA - Phenylethyl Methacrylate

Pen Strep - Penicillin Streptomycin

pHEMA - -Poly 2-Hydroxyethyl Methacrylate

PI - Propidium Iodide

PMMA - Poly Methyl Methacrylate

PS – Polystyrene

RNA – Ribonucleic Acid

RNase – Ribonuclease

RPM – Revolutions Per Minute

RS – Rabbit Serum

SD - Standard Deviation

SEM - Scanning Electron Microscope

TCPS - Tissue Culture Polystyrene

TGFβ ι Transforming Growth Factor Beta

TNF-α - Tumour Necrosis Factor Alpha

UV - Ultraviolet

VUV - Vacuum Ultraviolet

WHO - World Health Organisation

XPS - X-ray Photoelectron Spectroscopy

1 Introduction

Plasma technology has been used extensively to alter the surface chemistry of materials to achieve a desired cellular response. With the emergence of atmospheric pressure low temperature microplasmas spatially defined surfaces chemistries can be tailored efficiently and cost effectively on materials with low melting points. The fibrotic change to ocular tissue known as posterior capsule opacification (PCO) following an implantation of an intraocular lens (IOL) is a major concern in ophthalmology. It has been hypothesised that the promotion of a lens epithelial cell (LEC) monolayer which retains its phenotype or inhibition of LEC migration may reduce or eradicate PCO. This study evaluated the use of a microplasma system to influence cell-surface interactions on polymer materials.

1.1 Biomaterials

A biomaterial can be defined as, “Any substance, other than a drug, or combination of substances, synthetic or natural in origin, which can be used for any period of time, as a whole or as a part of a system which treats, augments, or replaces any tissue, organ or function of the body.” [1]

Biomaterials are used throughout the body in implants for various functions such as: joint replacement, vascular prostheses, dental implants, neural guidance conduits, ophthalmic implants and many others. Many different biomaterials are used within, and on, the eye to improve vision, repair structures and alleviate the effects of injury and disease [2]. Biomaterials and their properties must be chosen to suit their application, for example strong materials for load bearing joint replacements and optically clear materials for those used in the visual pathway. One property which applies to all biomaterials is biocompatibility. Biocompatible material refers to, ”the ability to locally trigger and guide non-fibrotic wound healing, reconstruction and tissue integration.” [3] Biocompatibility must be demonstrated for a material prior to its clinical use and this is outlined in the various parts of ISO standard 10993.

There will inevitably be a biological response to an implanted biomaterial yet a material with good biocompatibility should not elicit an adverse biological reaction; however a positive reaction may be induced. For example foreign body reaction is required for the integration of an implant, or perhaps a strong immune response is required to quickly degrade a biomaterial, if its function requires it. Only the material's surface interacts with the body and the cells within, therefore an understanding of the interface between cells and surfaces are essential to the field of biomaterials.

1.2 Cell-Surface Interactions

Cells only interact with biomaterial surfaces via an adsorbed protein layer. This protein adsorption occurs almost immediately [4], however competition between different proteins for adsorption sites on surfaces can take longer [4-7]. Vroman outlined that smaller proteins initially adsorb onto the surface which are later replaced by larger proteins. This has become known as the Vroman effect [6]. Proteins are long chains of amino acids which a changeable 3D structure, referred to as the protein conformation. Each of the amino acids in the protein have individual physiochemical properties in their side chains, such as: charged, non-charged polar and hydrophobic (or non-polar). The 3D structure of proteins within a given environment is governed by thermodynamic processes, by which the proteins change their shape to achieve the lowest possible interfacial energy with their immediate surrounding medium [7, 8]. The adsorption of proteins onto surfaces and their subsequent conformation are dependent on the composition of a surface – its physiochemical properties – and the structure of the proteins, particularly their polar/non-polar characteristics [9]. Polar (or nondispersive) interactions are a major factor in protein adsorption [10], they can affect specific protein adsorption, the amount of adsorption and the conformation of the adsorbed protein. In an aqueous polar solution, such as water, a protein will form a globular structure with the hydrophilic (water attracting) components on the outside and the hydrophobic (water repelling) components shielded from the water on the inside of the structure. When they encounter a material surface they aim to minimise interfacial energy and attempt to reach thermodynamic equilibrium. This is sometimes achieved by altering their conformation such that a specific site within their amino acid chain may bind with the surface [7, 11, 12]. If the surface is relatively hydrophobic, or non-polar, then hydrophobic components of the protein will attempt to bind to the surface, whereas the hydrophilic components will interact with the water, shielding the hydrophobic surface and amino acids beneath.

Proteins are folded to a specific conformation within the body so that they may bind to certain molecules, such as other proteins or receptors on cell surfaces. Some of these receptors on cell surfaces are integrins, cell adhesion molecules (CAMs), cadherins and selectins [13-16]. These receptors are proteins which span across the cell membrane (trans-membrane) and are responsible not only for cell adhesion but also cell signalling by transmission of information across the cell membrane [15]. They bind to specific sequences of amino acids within a protein [11, 17](Figure 1.1). One such sequence of amino acids is the arginine-glycine-aspartic acid (RGD) sequence, which is present on various extracellular matrix (ECM) proteins such as: fibronectin, collagens, vitronectin, fibrinogen and laminin [14]. For cells to bind to biomaterial surfaces, the biomaterial must have surface properties which will cause the necessary proteins to adsorb in a confirmation which presents peptides such as RGD to the cells. Once cells adhere to a surface (via the proteins) they can secrete and deposit their own ECM molecules to spread, attach more strongly or to engage in processes such as migration and mitosis; however the initial adsorption of proteins, governed by the biomaterial’s surface properties, is crucial. It has often been shown that cells tend to adhere more strongly to proteins adsorbed to more hydrophilic surfaces than more hydrophobic surfaces [5, 10, 11, 18]. The greater amount of polar groups in more hydrophilic surfaces increases the adsorption of proteins responsible for cell adhesion. Cells tend to have greater spreading across high surface energy hydrophilic surfaces than across lower energy hydrophobic surfaces, however it is of note that very hydrophilic surfaces do not promote cell adhesion. Therefore surface modification to increase hydrophilicity to a degree, by incorporation of polar groups, should increase cell adhesion. Atmospheric pressure plasmas operated in air are a proven method of achieving this as they tend to increase polar oxygen groups on the surfaces and have been shown to promote cell adhesion [5, 18, 19]. Cells are also be influenced by a surface directly, not just the adsorbed protein layer, but this occurs following initial adhesion to the protein layer [4]. Factors which influence protein adsorption and cell interactions include chemistry (including charge), topography, and stiffness [7, 20-24].

The processes of protein adsorption and cell attachment are complex. These will be discussed with relevance to plasma-based surface modification and replacement lenses throughout this chapter.

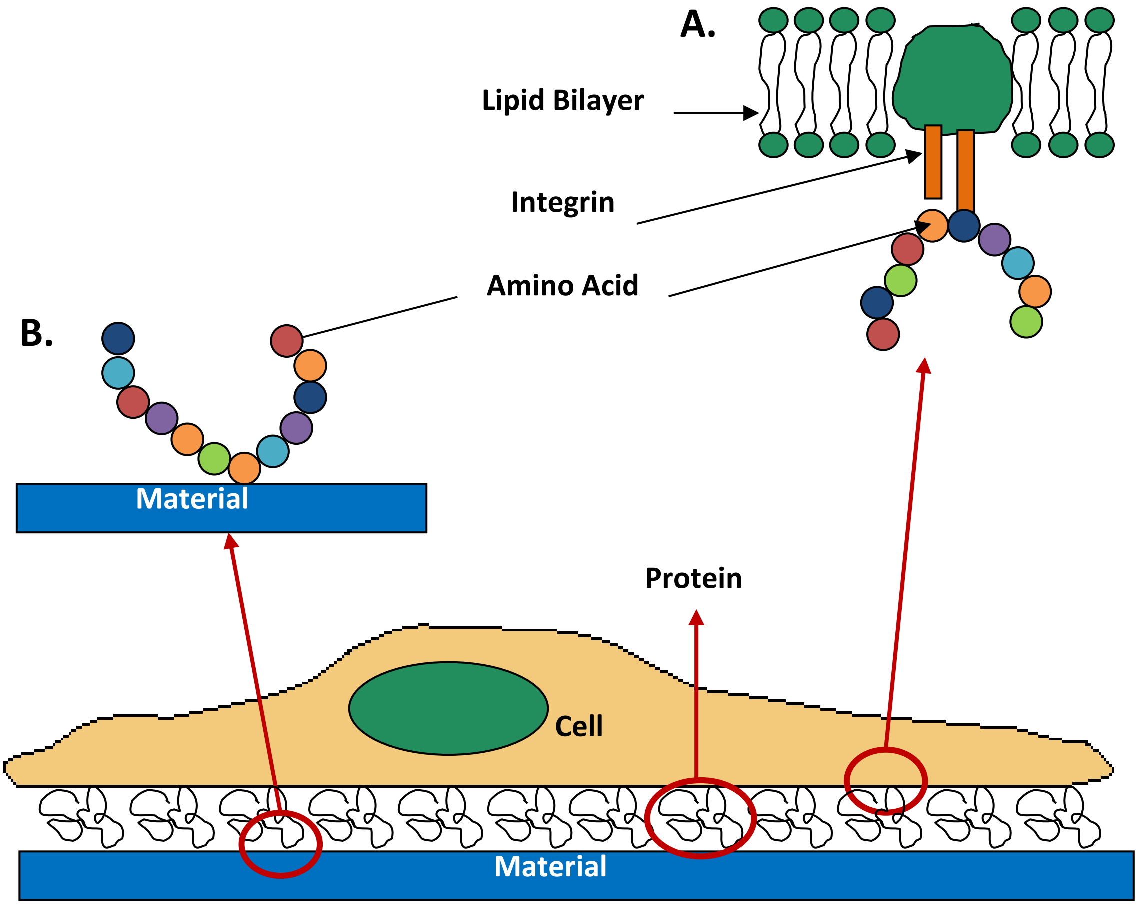

Figure 1.1 Illustration of cell adhesion to a material surface via the binding of a integrin, a trans-membrane protein, to specific amino acids (A) of an adsorbed protein layer (B) [25].

1.3 Anatomy of the Eye

The purpose of the eye is to focus light on the retina where it can be converted to electrical impulses which are sent to the brain. The structures involved in this process will be discussed in this section and are shown on Figure 1.2.

A small portion of the eyes surface, approximately 7% [26], is covered by the transparent cornea. The cornea permits light to enter the eye, protects the internal structures and provides the majority of the focal strength of the eye.

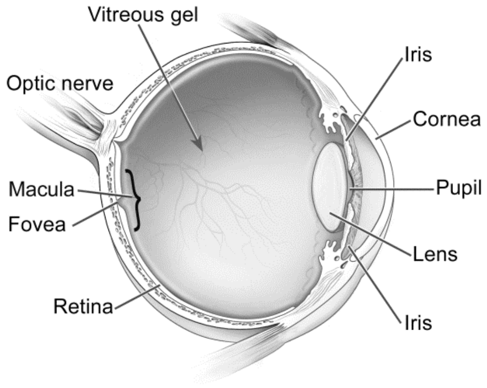

Figure 1.2 Schematic diagram representing the gross anatomy of the eye [27].

Between the cornea and the iris is the aqueous humour. It is a transparent fluid secreted by the vascularised ciliary processes, which are located behind the opaque iris. This fluid passes through the pupil into the anterior chamber where it is then drained via the trabecular meshwork and Schlemm's canal [28]. Its functions included supplying the avascular cornea and lens with nutrients and also maintaining intraocular pressure, the latter is a balance of fluid secretion and drainage which must be maintained in a healthy eye. The iris controls the amount of light which enters the eye. This mechanism is controlled by the pupillae muscles [26]. The crystalline lens provides a fine focus function in the eye in an action known as accommodation. The structure and focus of the lens will be discussed in more detail in the following section. The lens separates the anterior and posterior chambers of the eye, the former has been outlined above and the structures in the latter are discussed below.

The vitreous is a gel-like substance that is posterior to the lens and is the largest part of the eye. The posterior of the vitreous is attached to the retina and its anterior by the ciliary body and lens capsule. It is 99% water but its viscosity has been attributed to the relatively large amount of hyaluronan throughout it [26, 28]. The retina lines most of the posterior surface of the eye and it is here that the eye aims to focus the light which enters it. It contains photoreceptors which detect light and send the information via the optic nerve to the brain. The photoreceptors also perform a pre-computation function before sending impulses on. They can detect variations in light and dark as well as movement [2]. Within the retina are the macula, an area with many ganglion cells (eye neural cells) and the fovea, an area in the central macula with a high density of photoreceptors responsible for sharp central vision.

1.3.1 Anatomy of the Lens

The crystalline lens is a biconvex structure and the radius of curvature is larger on the posterior side than the anterior. It is contained within the lens capsule. The lens capsule is a continuous basement membrane which separates the lens from the surrounding orbital structures. It is a strong structure yet allows the exchange of nutrients and waste between the aqueous humour and the lens cells [29]. The lens capsule is primarily composed of interacting laminin and collagen IV networks; nidogen and proteoglycans stabilise the independent networks [29]. Lens epithelial cells (LECs) reside on the anterior capsule. The cells which reside in the equatorial region proliferate and differentiate into lens fibre cells. During this process they elongate along the anterior epithelium and posterior basement membrane toward the respective poles with the nuclei remaining near the equator. As more lens epithelial cells differentiate they are extended along the epithelium beneath older cells, pushing them deeper into the lens and away from the epithelium. These cells begin to lose their ability for protein synthesis and their organelles (Figure 1.3).

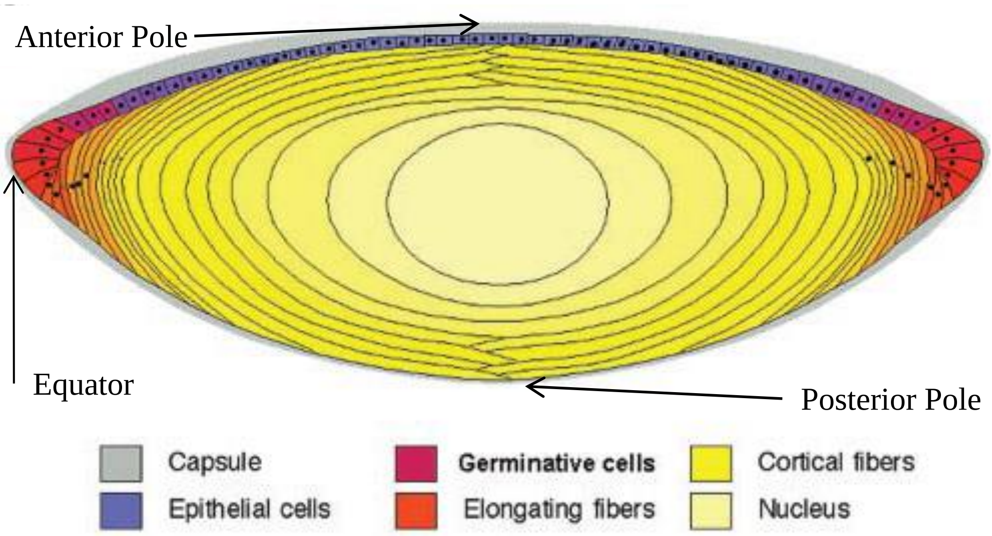

Figure 1.3 Diagram of meridional section of a lens showing the lens capsule and the various layers of cells [30].

After this the cells lose their nuclei and, having separated from the epithelium, the cells become almost like hexagonal pipes. They bind together tightly by tongue and groove-like joints when the flat surfaces meet, and by ball and socket connections at the apices of their hexagonal morphology [26, 28, 31] (Figure 1.4). The cell fibre membranes fuse at their ends in a very ordered fashion displaying distinct fissures or “sutures” in the overall lens [32]. These very tight connections leave very little intercellular space which is a main function of transparency, along with the loss of organelles and de-nucleation.

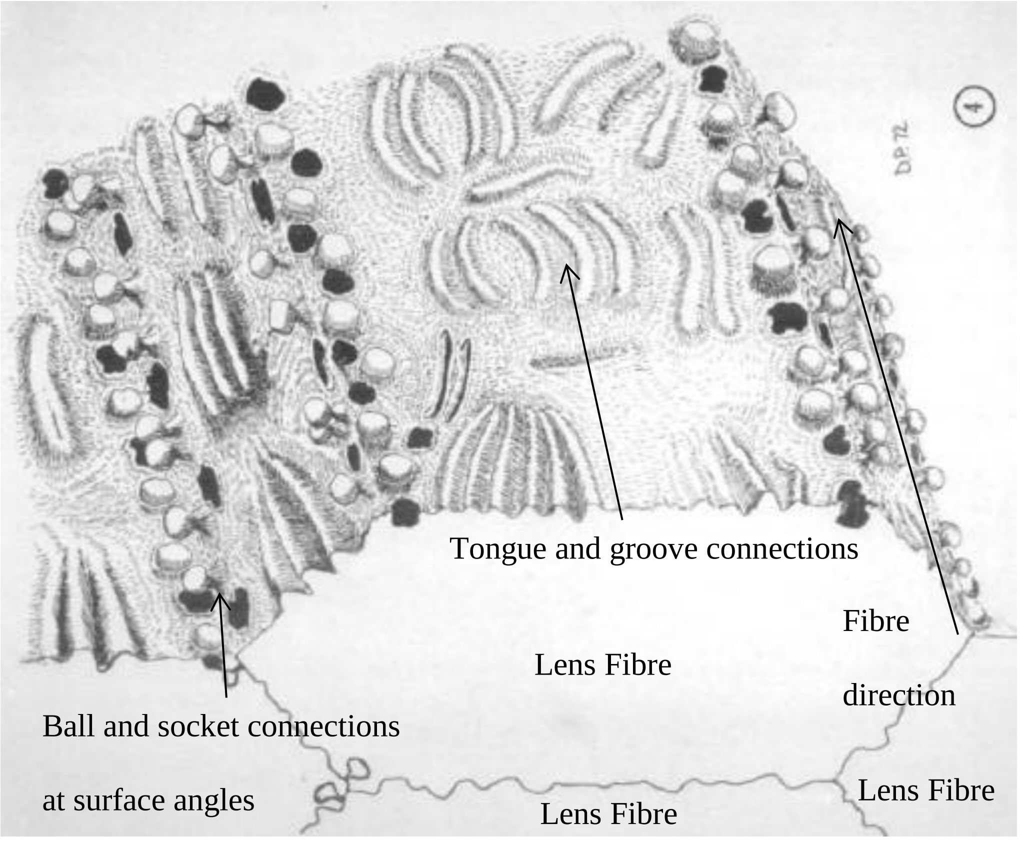

Figure 1.4 Diagram of 3D projection of an equatorial section of the lens showing a traverse hexagonal structure of a lens fibre with intercellular connections [31].

The lens fibres can be divided into regions; the cortical region and the nucleus. The cortical region contains the newer fibre cells and the nucleus consists of the smaller and more densely packed fibres formed in the embryonic and foetal stages, which can be subdivisions of the nucleus. This process happens continuously throughout life causing the lens to become thicker with age. The equatorial diameter changes from 6.5mm to up to 9.5mm after 90 years and the axial length can increase by 1.5mm from 3.5mm from birth to the age of 95 [26]. The increasing thickness and decreasing pliability results in reduced accommodative power with age.

The lens fibres have a very high protein concentration, which gives the lens a high refractive index [32]. The predominant proteins in the lens are known as the crystallins. These proteins tend not to form into aggregates which would cause the scattering of light and are therefore another key function of transparency.

1.3.2 Development of the Lens

In humans the lens placode is formed from the surface ectoderm at the 4mm embryo stage. The surface ectoderm is in contact with the neural ectoderm, which forms the optical vesicle from a monolayer of cuboidal cells. Invagination of the lens placode to form the lens pit begins at the 5mm stage. The optical vesicle invaginates to form the optical cup, which surrounds the lens placode. The lens placode separates from the surface ectoderm by the 9mm embryonic stage after which the lens appears as a hollow sphere with a diameter of ~0.2mm. A monolayer of columnar cells lines the outer wall, this will become the lens epithelium. A basal wall envelops the vesicle and a thin basal lamina is synthesised that thickens to form the lens capsule.

The lens becomes more oval shaped between the 10mm and 13mm embryonic stages. The columnar cells on the posterior capsular differentiate into early lens fibre cells. Over time these fibres are forced towards the centre of the lens and form the nucleus, as stated previously. LEC differentiation continues in the equatorial region and newer fibres encapsulate the nucleus and are referred as the cortex [33-39].

1.3.3 Fine Focusing using the Lens

By changing the curvature of the lens, objects at different distances can be focused onto the retina to provide a clear image. This process is conducted by the ciliary muscle, which alters the angle curvature of the lens and thus changing its focal length. By increasing the lens curvature the focal length is shortened bringing near objects into focus, this is known as accommodation. By decreasing the curvature the focal distance increase thus bringing distant objects into focus, this is known as disaccommodation. The ciliary body is connected to the sclera spur at its anterior and to the choroid at its posterior. The zonule fibres, or zonules, connect the lens capsule to the ciliary body [40-43].

1.3.3.1 Accommodation

Accommodation is an active process in which the ciliary muscle contracts. As it contracts it thickens in the area near the ciliary process, to which the zonules fibres are attached. As it thickens here the zonules fibres relax and are not under tension. This allows the lens to thicken in the anterior-posterior axis and decreases the equatorial diameter, which increases the angle of curvature on the anterior and posterior surfaces. The anterior surface moves towards the cornea as the posterior surface is confined by the vitreous, thus decreasing the size of the anterior chamber. These processes alter the refractive index of the eye (Figure 1.5)[40-43].

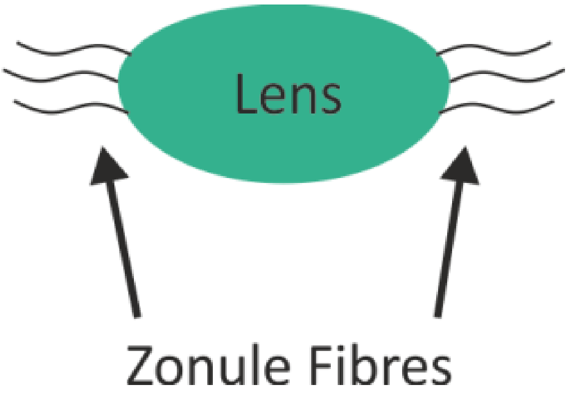

Figure 1.5 Cartoon of accommodation. The ciliary muscle is contracted which causes the zonules fibres to relax. This allows the lens to become more circular. Its anterior-posterior axis thickness increases whilst the equatorial diameter decreases.

1.3.3.2 Disaccommodation

Disaccommodation is obviously the reverse of accommodation. The ciliary muscle relaxes which causes it to be pulled along the surface of the choroid by its posterior anchor. This thins the ciliary body and creates tension in the zonules fibres. The zonules fibres pull on the capsular bag, stretching the lens. This decreases the anterior-posterior lens thickness and increases the equatorial diameter, as this occurs the anterior of the lens moves further away from the cornea. These processes decrease the refractive index of the eye to focus on distant objects (Figure 1.6)[40-43].

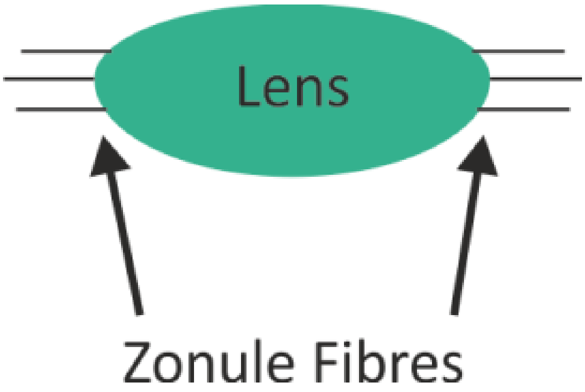

Figure 1.6 Cartoon of disaccommodation. The ciliary muscle is relaxed which causes the zonules fibres to be under tension. This stretches the lens to a more oblong shape. Its anterior-posterior axis thickness decreases whilst the equatorial diameter increases.

1.3.3.3 Changes with Age

The ability of the eye to focus on near objects diminishes with age, this is known as presbyopia, which from the Greek origins means “old eye”. The process is not fully understood but several reasons have been suggested, such as a decrease in the elasticity of Bruch’s membrane. This membrane is behind the retina and it has been suggested that an increase in its stiffness inhibits the ciliary body from moving forward fully when it contracts. Another hypothesis is that an increase in the size of the lens causes a decrease in the anterior chamber size (Figure 1.7). A decrease in the viscosity of the vitreous may mean that the lens could move posteriorly during accommodation. The lens nucleus also hardens with age. These factors may all contribute to presbyopia [34-36, 43].

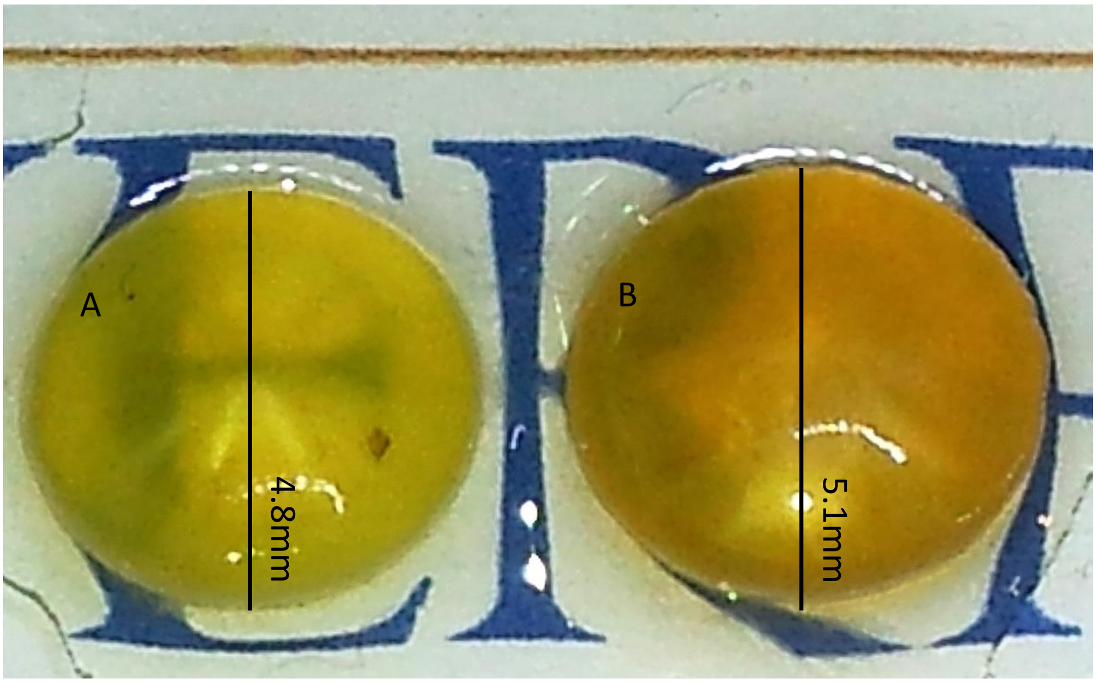

Figure 1.7 Photograph demonstrating the difference in lenses with age. Measurements are cross-sections of the lenses and the lenses may have swollen during fixation, thus do not accurately represent the lens in vivo. The lens from the younger donor (A) is clearer and smaller than the lens from the older donor (B) [44].

1.3.4 Cataracts

Cataracts are a clouding or opacification of the natural crystalline lens (Figure 1.9). They have been attributed to approximately 50% of global blindness (Figure 1.8)[45, 46]. The World Health Organisation believes there are over 124 million people in the world suffering from blindness due to cataracts [47].

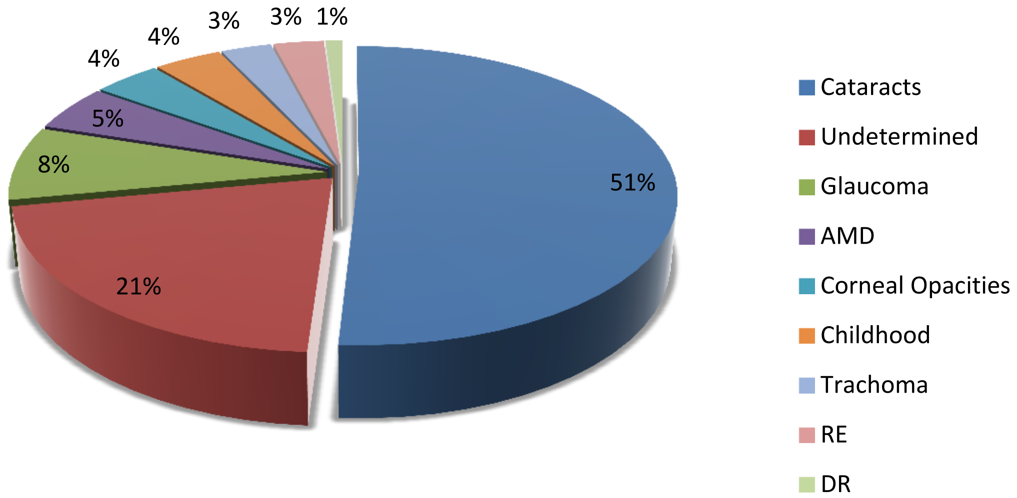

Figure 1.8 Pie chart demonstrating the global causes of blindness as a percentage of total blindness. Data are from World Health Organisation - "Global estimates of visual impairment: 2010" report [48]. AMD, age-related macular degeneration; RE, uncorrected refractive errors; DR, diabetic retinopathy.

There are 3 main types of cataracts:

1. Nuclear – the most common form, which begin in the centre of the lens.
2. Cortical – which originate in the periphery of the lens and appear like spokes.
3. Subcapsular – these occur near the lens capsule. They can be posterior or anterior, the former is more common.

The most common form of cataract is the senile cataract which develops with age [49]. Cataracts can also be caused by trauma, steroid use or they may be congenital. There are many factors that have been attributed to the development of cataracts such as: near-UV radiation [50], smoking [51], alcohol consumption [52], socio-economic factors [51], diet and diabetes [46](Figure 1.9). It has been suggested that avoidance of smoking and from exposure to near-UV radiation are the only avoidable factors [45]. Alcohol consumption is excluded from this as it has been shown that there is a greater prevalence of cataracts in heavy drinkers and abstainers than in moderate drinkers [46, 52].

Costello et al. [53] have shown that there is degradation in the plasma membranes of nuclear fibres with ageing and it is more pronounced in opaque lenses. Using transmission electron microscopy they have shown that the plasma membrane forms undulating curves, some areas suffer degradation, extracellular spaces widen and that protein deposits form in the extracellular spaces. They have shown that increased extracellular space reduces the transparency of the lens nucleus due to frequent changes in refractive index. They also believe that the protein aggregates may cause light scattering. It has been shown previously that the molecular weight of protein aggregates in the lens nucleus increases with age and is greater in cataractous lenses [54]. The unfolded protein response is a cellular response due to aggregation of unfolded proteins in the endoplasmic reticulum. This response can create reactive oxygen species, with or without apoptosis, and is also strongly linked to oxidative stress [55]. The creation of oxidation species could exacerbate several of the previously mentioned cataract causes, which are also related to oxidative stress [45, 50, 51]. This protein degradation and aggregation may be responsible for cataract formation but there are many contributing factors and the mechanisms are not fully understood [34, 40, 53, 56-60].

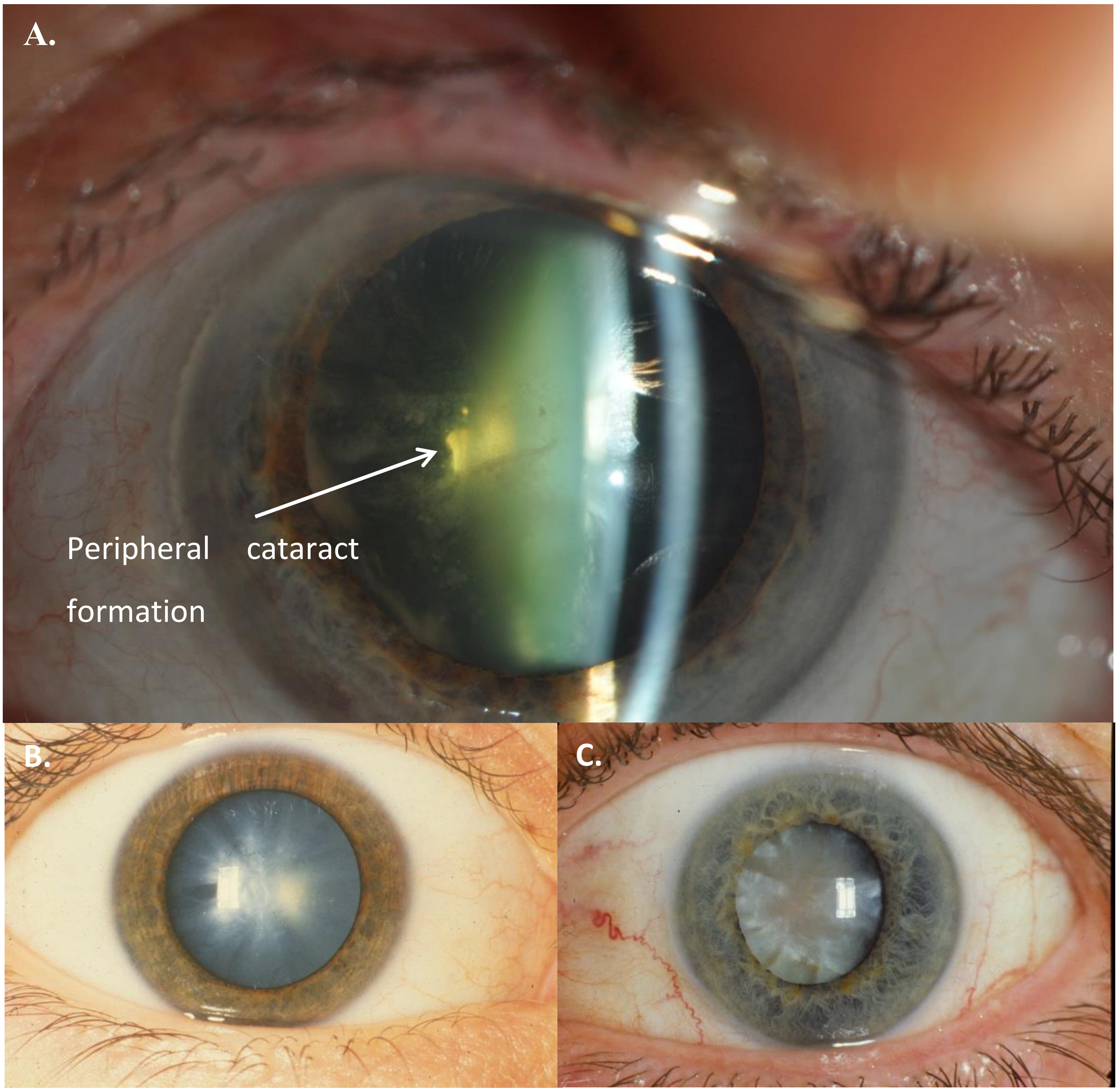

Figure 1.9 Photographs of cataractous lenses. Image A. is a slit lamp photograph of a peripheral cataract taken from a patient in the Royal Liverpool University Hospital prior to surgery [44]. Image B shows a mature cortical cataract, which begins at the lens periphery and is characterised by its spoke like appearance [61]. This is a sudden onset in a patient with Type 1 (juvenile) diabetes. Image C shows a very mature age-related cortico-nuclear cataract [62]. Images B. and C. are extreme cases and would most likely treated before this stage in developed countries.

1.3.4.1 Cataract Surgery

Cataract surgery is the most common ophthalmic procedure [63-66]. Typically the surgery is performed on an outpatient basis and over 70% of UK cataract surgeries are performed under local anaesthesia [67]. The opacified natural lens is removed and a synthetic polymeric lens, called an intraocular lens (IOL) is implanted (Figure 1.10). A brief overview of the surgery will be outlined in the following paragraph. The importance and development of surgical technique on post-operative complications will be address in more detail in Section 1.4.1.1.

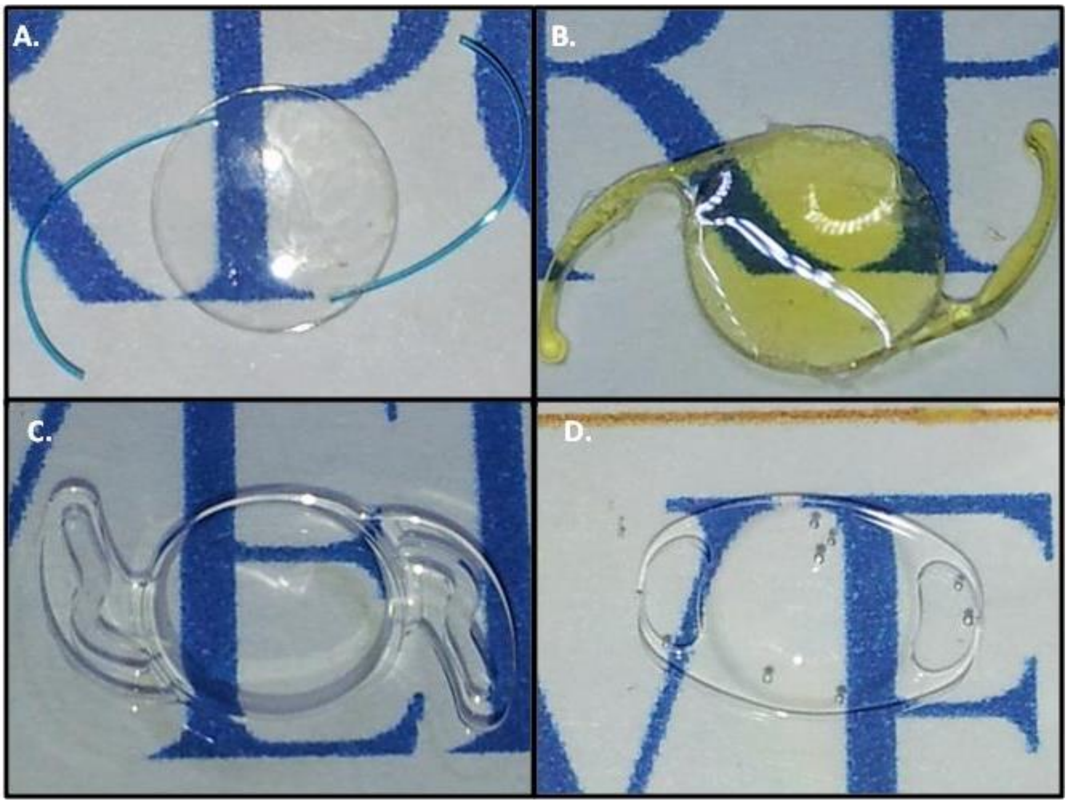

Figure 1.10 Photographs of various intraocular lenses. A. Alcon Acrysof®, B. Alcon Acrysof® with UV filter, C. Rayner C-Flex® and D. Artisan anterior chamber IOL [44].

The surgeon firstly makes an incision in the limbal region of the eye, where the clear cornea meets the white sclera (Figure 1.11A). With modern foldable IOLs which can be rolled allow incisions smaller than 3mm. This small size allows self-healing without the use of sutures. These smaller incisions can reduce the wound healing response and post-operative complications due to this [67]. After this the surgeon must create an opening in the lens capsule to access the cataractous lens fibres. A procedure called a continuous curvilinear capsulorhexis (CCC) is typically used. This method can also reduce post-operative complications compared to previous techniques but this will be addressed in Section 1.4.1.1. Essentially the procedure involves making an incision and then tearing the capsule using shear forces in the direction of the desired tear [67]. Now with access to the lens fibres a phacoemulsification probe is inserted into the lens capsule. This is an ultrasonic probe which is used to break down and aspirate the cataractous lens, leaving the lens capsule intact (Figure 1.11B). The surgeon will attempt to remove all of the LECs from the anterior section of the lens capsule however this is rarely, if ever, achievable [68]. Following this an intraocular lens is placed in the remaining capsular bag (Figure 1.11C&D). Careful surgery with minimal corneal incisions can decrease or prevent the breakdown of the blood-aqueous barrier (BAB). Breakdown of the BAB introduces cytokine signalling molecules to the lens environment; these have been implicated in a post-operative complication associated with wound healing and scarring, known as posterior capsule opacification.

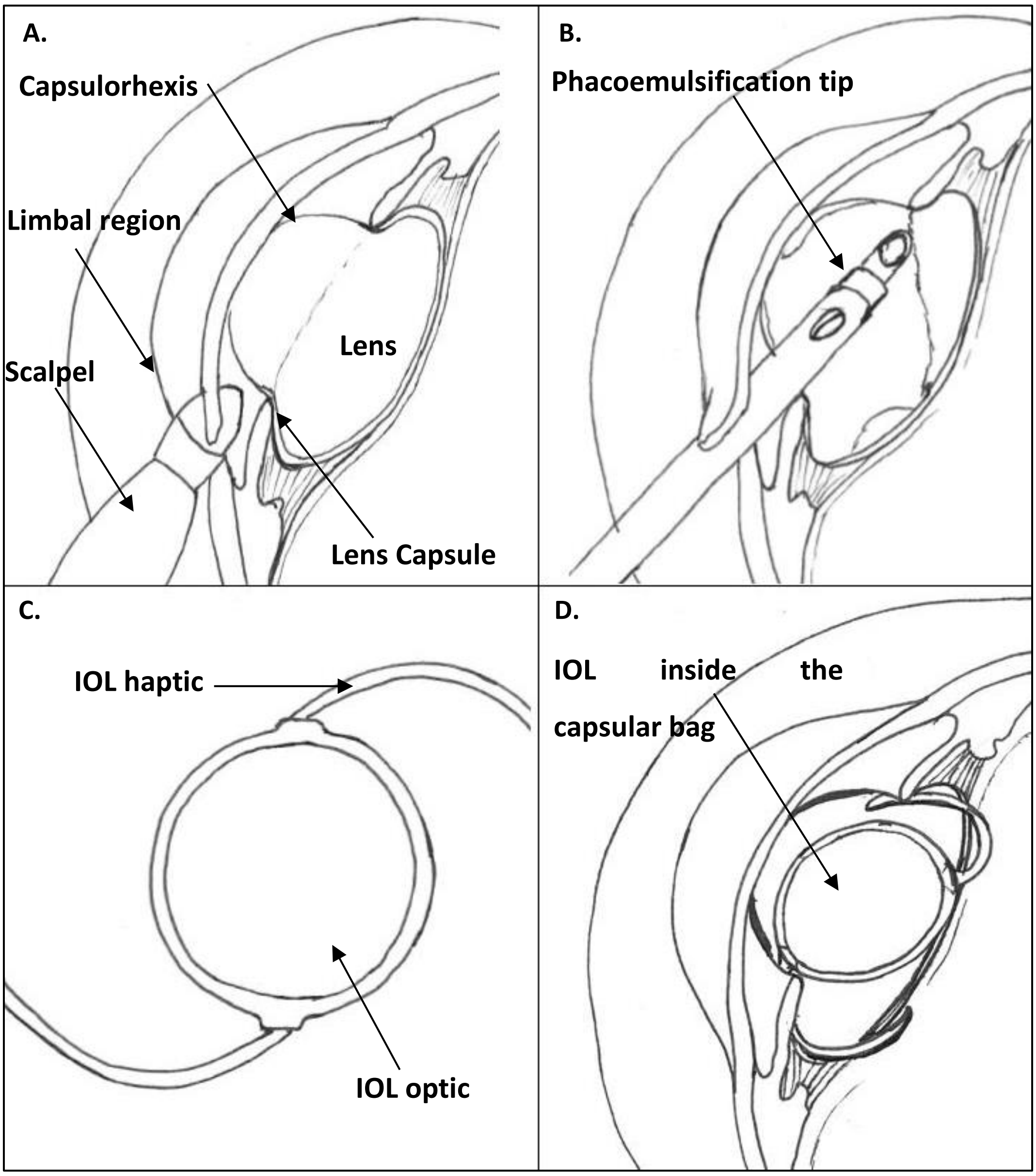

Figure 1.11 Cartoon of cataract surgery. A. The clear corneal incision is made in the limbal region. B. The cataractous lens is removed from the capsular bag by phacoemulsification. C. An intraocular lens (IOL) replaces the focusing function of the natural lens and is composed of haptics which keep it in situ and an optic portion. D. The IOL is placed within the capsular bag and held in situ by the haptics. Courtesy of R. Lace [44](adapted from Healthwise Inc. [69]).

1.4 Posterior Capsule Opacification

Posterior capsule opacification (PCO) is the main post-operative complication following IOL implantation. It stems from a wound healing response to the damage caused by cataract surgery and implantation of an IOL. As stated previously it is highly unlikely that the surgeon will be able to remove all of the LECs from the anterior of the lens capsule during cataract surgery. These residual LECs are stimulated by the injury caused during surgery to proliferate and migrate. These cells migrate to the posterior capsule where they often dedifferentiate into fibroblast-like cells. This dedifferentiation causes a morphological change in the cells, which results in a wrinkling of the posterior capsule to which they are attached (Figure 1.12). The cells are also known to form into islets which later migrate to the optical axis, as well as undergo lenticular fibre differentiation. The former are known as Elsching’s pearls [70, 71] and the latter as Sommerring’s ring [71, 72]. The above mechanisms disrupt the path of light to the retina and cause scattering, thus impairing vision. As the name suggests the posterior capsule becomes opacified. This is also known as a secondary cataract.

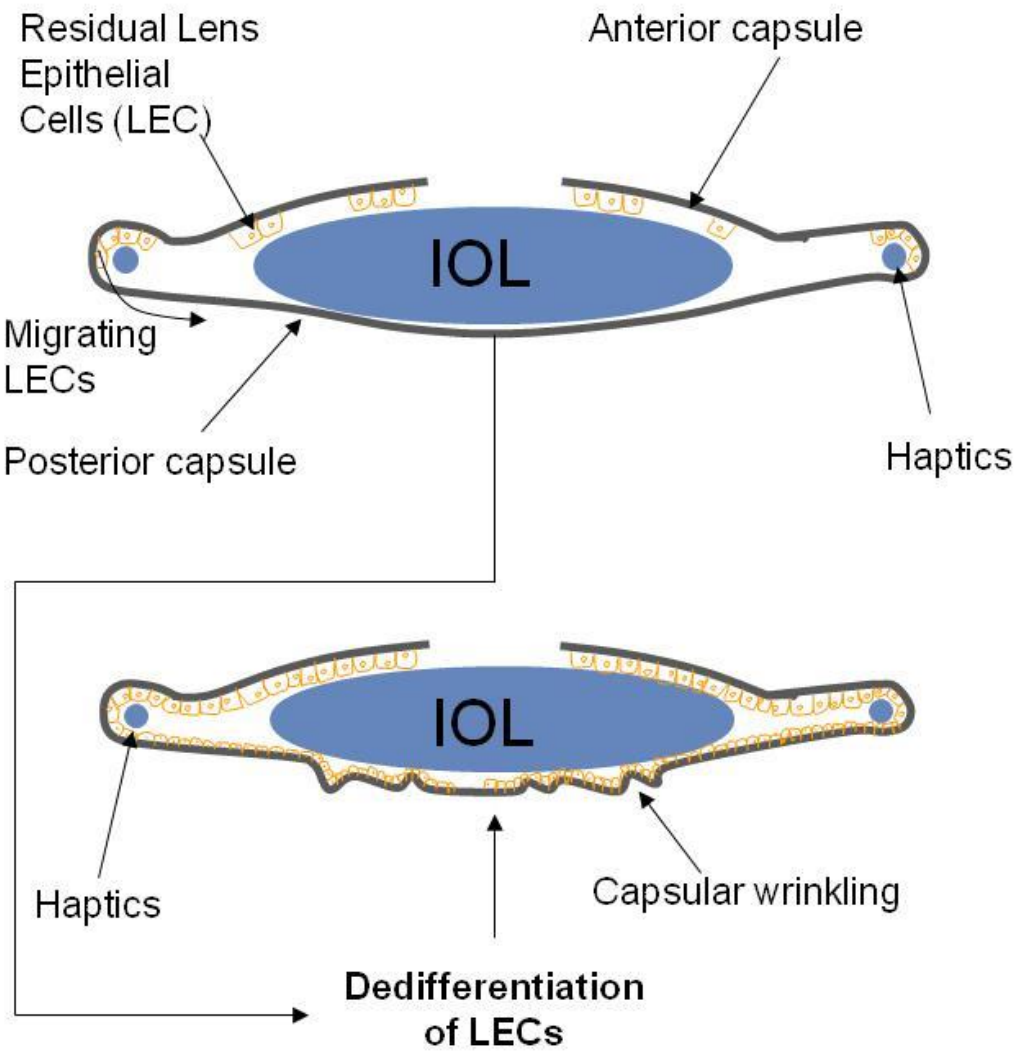

Figure 1.12 Cartoon depicting the basic mechanism of posterior capsule opacification (PCO). Residual lens epithelial cells (LECs) which remain following cataract surgery proliferate and migrate to the previously cell free anterior capsule. Here these LECs dedifferentiate into fibroblast-like cells. During this dedifferentiation the LECs undergo morphological changes which cause them to pull on the posterior capsule to which they are attached and cause it to wrinkle. This wrinkling scatters light as it travels to the retina, impairing sight [25].

Through various methods of study including in vivo observation, post-mortem examination [73], in vivo animal studies, capsular bag models [74] and cell culture studies, researchers have been attempting to elucidate and understand the mechanisms of PCO [37, 75-77]. Through these various methods it has been shown that PCO results from paracrine and autocrine signalling systems. Paracrine signalling comes from other ocular tissues, particularly the aqueous humour. During surgery the blood-aqueous barrier is disrupted, this barrier normally prevents some molecules from entering the aqueous, which allows increased protein levels in the aqueous. These molecules include transforming growth factor-βs (TGF-β), (TGF-β2 is the isoform of particular interest), basic fibroblast growth factor (FGF) and epidermal growth factor (EGF) [70, 76]. Although TGF-β2 is present in the aqueous normally it is mostly in its latent form. Following surgery increased levels are found in an active state [78, 79]. TGF-β2 is believed to be one of the main proteins responsible for epithelial cell dedifferentiation into fibroblast-like cells which are one of the causes of posterior capsule wrinkling [70, 75, 76]. This change is often known as epithelial-mesenchymal transition (EMT) [36, 71, 80-84]. This was shown by increased dose-dependent expression of mesenchymal or fibroblast marker α-smooth muscle actin (αSMA), and the deposition of fibronectin with the addition of TGF-β2 in LECs using the capsular bag model [85]. TGF-β2 has also, paradoxically, been attributed to apoptosis of LECs however, basic FGF has been shown to mediate this effect [86]. Similarly, FGF has been shown to increase proliferation and migration rates of LECs in in vitro and ex vivo capsular bags [87-89]. EGF has been shown to increase proliferation and it is believed to be able to cause differentiation into lens fibre cells, thus a possible cause of Sommerring's rings [76]. It is of note that not only are these growth factors available in the aqueous but that the lens capsule acts as a storage mechanism for them [29]. It has been suggested that other cytokines, typically involved in inflammation, may play a role in the development in PCO [88, 90-95]. Interleukins 1 & 6 (IL-1 and IL-6) have also been detected in the aqueous humour during and after cataract surgery [94, 96-99]. IL-1 and IL-6 have been implicated in the proliferation of LECs, the increased deposition of collagen and the inflammatory response [88, 90, 91, 96].

Autocrine signalling, which is the expression of growth factors, cytokines and proteins by the LECs themselves, also plays a role in the development of PCO. IL-1 and IL-6 have been secreted by explanted anterior capsules [90, 91, 93, 96]. Shigamitsu et al. observed positive antibody staining for IL-6, IL-1 receptor II, FGF, FGF receptor, EGF, TGF-β, TGF-β receptor II, TNF-α and others in the fibrous tissue on lens capsules after cataract surgery [100]. Prada et al. detected IL-1α and tumour necrosis factor-alpha (TNFα) mRNA in LECs [93]. TNF-α has also been detected in the aqueous humour [93] and it has also been detected in Elsching's pearls [100]. Wormstone et al. demonstrated the de novo production of basic FGF and the presence of FGF receptor I in lens capsule explants grown in serum free media [87]. The lens has also been shown to secrete TGF-β2 [78]. TGF-β2 and TGF-β receptor II have been found in LECs by Saika et al. using immunohistochemistry [101].

These signalling systems are not necessarily independent and there are many other factors which contribute. For example it has been hypothesised that matrix metalloproteinases (MMPs)(particularly MMP2 and MMP9) play a role in the remodelling of the ECM on IOLs and in capsular bags, and these changes in ECM may signal different cellular responses such as dedifferentiation [70, 75, 76]. It has been suggested that fibronectin induces MMP-9 expression, which causes expression of MMPs-2 and -14 [102]. As stated earlier TGF-β2 induces fibronectin deposition [85], it has also been reported that MMP-2 is involved in TGF-β2-induced matrix remodelling [103], once activated by MMP-14 [102], and that basic FGF may be required to inhibit the apoptotic effect of TGF-β2 [86]. PCO is therefore not fully understood and research is still underway to understand the mechanisms of this post-surgical response. This research may also find targets for therapeutic agents to inhibit PCO.

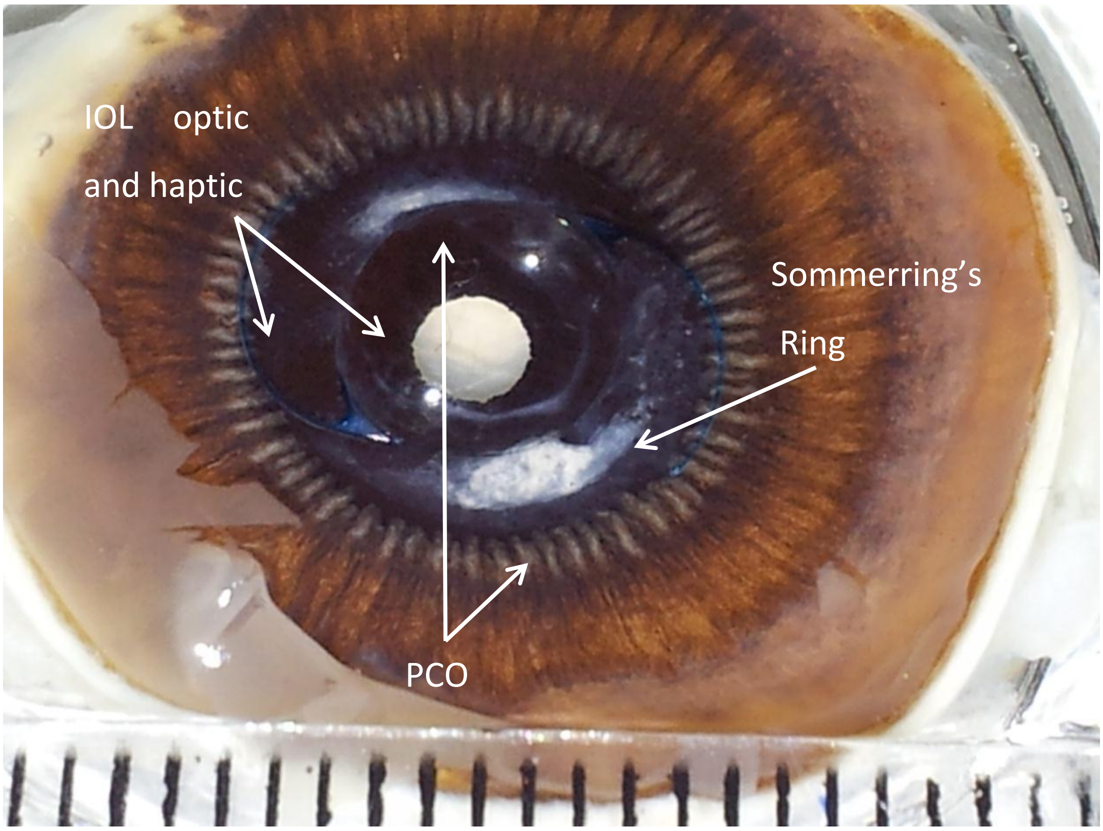

Figure 1.13 Photograph of a donor eye with an implanted intraocular lens (IOL) with posterior capsule opacification (PCO) and Sommerring's ring [44].

The incidence of PCO between studies varies [104]. This may be in part due to the lack of a universal metric for the onset or degree of PCO. The incidence of PCO is often grouped by IOL material in studies, and Schaumberg et al. reported a meta-analysis of PCO reports published between 1979-1996. The authors reported the Nd:YAG capsulotomy rates at 1, 3 and 5-years post-cataract surgery. They were "11.8% (range, 9.3%-14.3%) at 1 year (n = 13,183; 31 articles), 20.7% (range, 16.6%-24.9%) at 3 years (n = 66,496; 19 articles), and 28.4% (range, 18.4%-38.4%) at 5 years (n = 1866; 5 articles)" [105]. A study conducted in 10 centres across France by Boureau et al. reported the rates of PCO for 3 square edge design IOLs: Zeiss-IOLtech's XL-Stabi (n=263), Advanced Medical Optic's AR40E (n=254) and the gold standard, Alcon's Acrysof SA620 (n=250). By 3 years post-surgery PCO had occurred in eyes with 45.4% of XL-Stabi IOLs, 23.3% of AR40E IOLs and only 13.1% of Acrysof IOLs. Using 2005 figures for the number of cataract interventions and the market share of each of the 3 lenses, the authors calculated the total cost of post-capsulotomy complications for the 3 types of lenses to be ~€51.9-54.3 million, i.e. the cost of complications from 2005 until 2031 due to the implantation of the 3 types of lenses in 2005 [106].

1.4.1 Current Treatment Options

There is currently only one treatment option for PCO, that is Nd:YAG (neodymium doped yttrium aluminium garnet) laser capsulotomy. This treatment ablates the opacified posterior capsule, however this procedure is expensive and not without risk. In 5% of patients complications will arise [107]. These include IOL damage, cystoid macular oedema, increased intraocular pressure, retinal detachment or dislocation of the IOL. Due to the expense and technology required this treatment is not available to most of the developing world.

There are various research strategies to prevent or reduce the incidence and onset of PCO which include:

1. Surgical treatment - the improvement of cataract surgery to reduce the wound healing response and clean up residual LECs.
2. Drug delivery - the delivery of various drugs to inhibit the mechanisms of PCO.
3. IOL material and design - the modification of IOL shapes, materials and surfaces.

These research areas are not mutually exclusive and are interconnected; for example drugs can be applied during cataract surgery or IOLs could be used as drug delivery vehicles. These will be discussed in the following sections with a greater focus on IOL material and design.

1.4.1.1 Surgical Treatment

An early area of research into the surgical treatment of cataracts and subsequent PCO was the positioning and fixation of the IOLs. Lenses were placed in the anterior capsule in work mostly conducted in the 1950’s, however these lenses caused inflammation due to abrasion of the cornea. Suturing of IOLs to the iris was also investigated however these suffered from iris erosion and IOL dislocation. Following this IOLs were placed posteriorly, i.e. behind the iris and were fixed using the “j”-shaped haptics. These were originally placed in the sulcus; between the iris and the lens capsule. This positioning resulted in abrasion of the iris and IOL dislocation [43, 75]. This led to the development of “c”-shaped haptics (Figure

1.10A&B), capsulorhexis in “in-the-bag” fixation is still used today (Figure 1.11). This method prevents abrasion with other tissues, and is disputed to create a barrier to cell migration onto the posterior capsule by adhesion of the IOL and posterior capsule [37, 43, 75]. The latter will be discussed further in section 1.4.1.3 below.

One of the benefits of the development of CCC include the improved clean-up of LECs from the equator and anterior capsule. The reduced number of LECs following cataract surgery not only decreases the LECs which can proliferate but also decreases the number which can secrete inflammatory cytokines [37]. This was further aided by “hydrodissection”, the injection/aspiration of a solution into the capsular bag [37, 108]. This has been reported to decrease surgical time [108, 109]. The decrease in size of CCC is also said to be beneficial as it decreases the interaction with the aqueous humour [109, 110]. The development of foldable intraocular lenses, fixed in-the-bag, as well techniques such as hydrodissection, phacoemulsification and CCC have reduced the invasiveness of the surgery and the inflammatory response; however PCO is still prevalent. Research into the use of drugs to target specific cytokines implicit in PCO, e.g. TGF-β2; or more general cellular responses involved, e.g. proliferation, is still underway.

1.4.1.2 Drug Delivery

Anti-proliferative drugs, cell adhesion blockers [111, 112] and apoptosis inducing drugs have been proposed to combat PCO, however the efficacy of these options has not been shown in patients [68, 75, 113, 114]. There is also the danger that these drugs could affect other ocular tissues. Some of the drugs used include thapsigargin [115, 116], 5-fluorouracil (5-FU) [116, 117], mitomycin-C [112], and deoxorubicin [113, 114]. Thapsigargin has been used to inhibit intracellular calcium signalling, a key regulator of lens cell function. It has been demonstrated that it causes increased cell death and reduced proliferation [75, 115]. MG132, a proteosome inhibitor, has been shown to decrease lens cell proliferation and migration even in the presence of various growth factors [75, 118]. Work by Wormstone’s laboratory has investigated the use of TGF-β2 antibody, CAT-152, to reduce EMT in lens cells, and the expression of α-smooth muscle actin [77, 85, 119, 120]. The results show that application of CAT-152 at early time points alleviates the effects of TGF-β2 on LECs, however no work on this has been published since 2006 [120].

The delivery and sustained release is one of the barriers to the use of pharmacological agents. Duncan et al. bound thapsigargin to PMMA IOLs via hydrophobic bonding by immersing the IOLs in thapsigargin dissolved in dimethyl sulfoxide (DMSO). In an in-vitro capsular bag model [121] they demonstrated reduced growth of LECs on the posterior capsule at low concentrations and complete cell death at high concentrations [115]. This work does not discuss the effects thapsigargin may have in surrounding tissue nor any possible release kinetics [115]. Pandey et al. used an intracapsular ring to prevent contraction of the capsular bag and to deliver 5-FU. Results indicated that the migration of LECs on the centre of the posterior capsular bag was reduced, however the authors suggest it may be due to a mechanical effect of the intracapsular ring rather than the presence of 5-FU [117]. A biodegradable implant, Surodex, was developed to slowly release pharmacological agents. It was implanted during cataract surgery and released dexamethasone with the aim of reducing post-operative inflammation [68, 114]. Tan et al. compared the implantation of the Surodex device to conventional 0.1% dexamethasone eye drops in two studies. The first stated that Surodex decreased anterior flare compared to the conventional eye drops up to 30 days post-operatively [122]. The second study, which implanted 2 Surodex devices per eye states that flare was only significantly reduced up to 15 days post-operatively, however the authors mention that the Surodex treatment reduced discomfort, photophobia and lacrimation [122, 123]. Further study of the Surodex implant by Wadood et al. demonstrated that there was no significant difference in flare or subjective inflammation when comparing the Surodex device to normal dexamethasone eye drops [124]. Although various pharmacological agents, and their delivery, have been investigated none have yet shown to been clinically conclusive in the fight against PCO [68, 75, 114, 123].

1.4.1.3 Intraocular Lenses

The idea of intraocular lenses was first proposed by Harold Ridley in 1949 [125]. In essence an IOL is a polymeric disc, which provides the optical function of the lens, held in-situ by the capsular bag. Typically, IOLs are held in place in the capsular bag by polymeric haptics which press against the equatorial region of the capsular bag.

1.4.1.3.1 Intraocular Lens Materials

IOLs were originally made from poly(methyl methacrylate) (PMMA). During World War II doctors noticed that shards of PMMA left in pilots eyes after attack elicited very little foreign body reaction, giving Harold Ridley the idea for their use as an ocular implant. There have been many developments in the materials used for the manufacture of IOLs. Mainly in the use of hydrophobic or hydrophilic acrylics (and their co-polymers) and silicone i.e. poly(dimethyl siloxane) (PDMS). The acrylics typically used for hydrophobic lenses are phenylethyl methacrylate (PEMA) or phenylethyl acrylate (PEA), whereas hydrophilic lens have a poly(hydroxyethylmethacrylate) (PHEMA) base [2, 125]. The chemical structure of the different lens materials can be seen below in Figure 1.14.

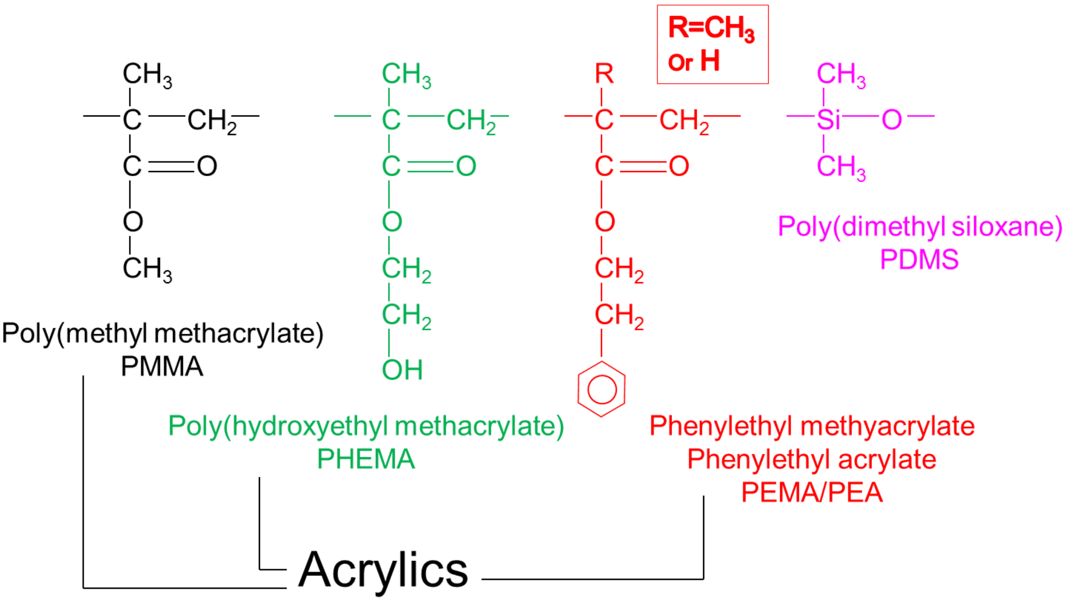

Figure 1.14 Chemical Structures of Common IOL Materials.

PMMA is not often used as a lens material in the developed world, however due to its low cost is still commonly used in developing countries. It is a homopolymer that is a rigid and glassy material at room temperature. Clinicians now tend to prefer the acrylic copolymers, or silicone, over PMMA as they are flexible and can be inserted through smaller corneal wounds.

Hydrophilic hydrogel lenses are generally made from PHEMA and copolymers with water content ranging from about 18% to 38% [75]. It is the hydroxyl group (OH) within the monomer which gives them their hydrophilic nature (Figure 1.14). This polar functional group allows the monomer to orientate itself so that it can more readily form hydrogen bonds when in contact with polar liquids such as water, increasing its hydrophilicity [126]. As the monomers are present throughout the polymer, water is absorbed into the material.

Hydrophobic acrylic IOL's are made from combinations of PMMA, PEMA, PEA and (poly)trifluorethylmethacrylate (PTFEMA) [127]. The phenyl ring within PEMA and PEA monomers is a stable, low energy structure that does not readily share electrons. It is this that causes the materials hydrophobicity. Alcon's Acrysof® hydrophobic IOL is considered the gold standard in the UK and favoured by many surgeons.

Silicone is a highly hydrophobic foldable material [75]. It is also a highly elastic and an oxygen permeable material [2, 125]. The low refractive index of silicone is said to reduce glare, compared to acrylic materials [125], but the acrylics' high refractive index allows for thinner lenses and thus smaller incisions [107].

Material used in IOL design has a varying effect on the incidence of PCO. There is markedly less cell and matrix deposition on silicone than PMMA yet there tends to be a greater amount of fibrotic tissue on silicone IOLs. Saika (2004) proposes that silicone induces a greater cellular response than PMMA [75]. A study by Hollick et al. (2000) has shown that implanted silicone lenses have a mean percentage area of opacified capsule of 17%, in comparison to 46% for PMMA and 63% for hydrogel lenses after a 2 year period. It also states that of the patients with silicone IOL implants none required Nd:YAG capsulotomy at 2 years post implantation [128].

Hydrophilic acrylic IOLs tend to have an increased degree of PCO compared to PMMA, silicone or hydrophobic acrylics (determined by "objective image analysis software") [75, 128] and a high rate of Nd:YAG laser posterior capsulotomy (28%) at 2 years post implantation [128]. Hydrogel lenses were introduced as the efficacy as a biomaterial had been demonstrated previously. Authors often refer to the good "biocompatibility" of hydrogel lenses without defining what they mean by biocompatible, which is a term that is dependent upon the application. Most likely authors are referring to minimal immune response to the material, however the high rates of PCO would suggest that it is not as biocompatible for the use as an IOL as other materials. The terms “hydrogel IOL” and “hydrophilic IOL” are generally used to refer to lenses based on PHEMA. The properties of the lenses can be tuned by the addition of different monomers and crosslinking agents [107]. A paper by Tognetto et al. demonstrated that adhesion of various cell types and the extent of anterior capsule opacification differed for 3 commercially available “hydrophilic” lenses [129].

1.4.1.3.2 Intraocular Lens Shape

There have been changes in IOL design, most notably the progression from rigid IOLs to foldable IOLs allowing for smaller incisions in cataract surgery. The employment of the square-edge design made Alcon Acrysof® the leading IOL. The basis of the design effectiveness is that the square edge forms a physical barrier with the lens capsule, inhibiting the migration of the LECs [130-133]. A barrier is formed when the optic portion of the IOL binds to the collagenous capsule (Figure 1.15). This is typically done via a layer of fibronectin. This IOL-fibronectin-cell monolayer-fibronectin-capsule binding has been termed the “sandwich theory” but Linnola et al., who conducted various immunohistochemical and laboratory studies on this principle [73, 134-138]. Linnola et al. histologically examined autopsy eyes from donors who had had cataract surgery and implantation of PMMA, silicone, Alcon Acrysof® and Alcon hydrogel lenses for fibronectin, laminin, vitronectin and collagen IV. They demonstrated that this sandwich structure was typically observed with Acrysof® lenses, and that the other ECM proteins were typically not present in this sandwich structure. The authors discuss that as the main binding sites in fibronectin are for cells and collagen then fibronectin functions as a mediator to bind the IOL to the capsule [73]. In a previous study Linnola et al. demonstrated by radiolabelling proteins that more fibronectin binds Acrysof® hydrophobic acrylic lenses compared to lenses of other materials. The difference in fibronectin adsorption was significant when Acrysof® were compared to hydrophilic acrylic and silicone lenses, but not PMMA. As PMMA is a relatively hydrophobic acrylic this is not unexpected [138]. Johnston et al. also reported similar concentrations of fibronectin adsorbed to Acrysof® and PMMA lenses at early time points yet greater concentrations on Acrysof® following 7 days of incubation [139]. The efficacy of the square edge design is widely accepted. In Linnola and co-authors’ sandwich theory the “sandwich” prevents the migration of LECs onto the posterior capsule. The authors state that the sandwich typically contains LECs and is strongly related to fibronectin, however the authors do not discuss how LECs within this sandwich are inhibited from migrating to the posterior capsule [73, 134]. The deposition of fibronectin has also been implicated in EMT [83], and its deposition by LECs is also induced in the presence of TGF-β2 [85].

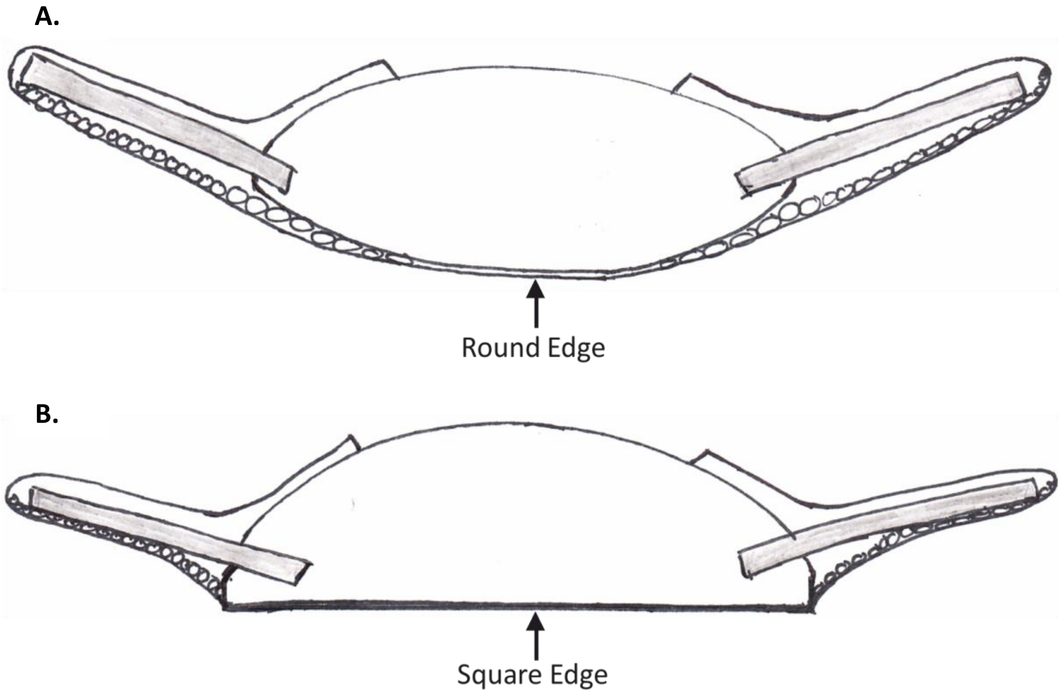

Figure 1.15 Cartoon of the square edge principle. The square edge forms a barrier between the IOL optic and the posterior capsule which inhibits the migration of residual LECs onto the posterior capsule [44].

Since the inception of the design, other square-edge IOLs have been made from different materials such as silicone and hydrophilic acrylics [132]. They have shown reduced incidence of PCO yet the Acrysof® still shows marked improvement over its competitors. In the study reported by Boureau et al. mentioned previously, the Nd:YAG capsulotomy rates of 3 square edge lenses were compared. The rates of Nd:YAG capsulotomy were much higher for hydrophilic acrylic lenses (45.4%, Zeiss-IOLtech’s XL-Stabi lenses) compared to hydrophobic acrylic lenses (13.1%, Alcon’s Acrysof® and 23.3% AMO’s AR40E lenses) [106].

Although some studies do report that square edge silicone lenses have reduced PCO compared to hydrophobic acrylic lenses [132, 140, 141], Alcon's Acrysof® lenses are often stated as the gold standard [2, 75]. This may be in part due to the fact that silicone IOLs may have a higher rate of anterior capsule opacification, or contraction of the CCC [71, 132, 142], and also that silicone IOLs tend to stick to silicone oils used as a tamponade agent in vitreoretinal surgery and are therefore not suitable in these cases [71, 143]. Another possible reason is that silicone lenses unfold in the capsular bag quicker than hydrophobic acrylic lenses, which may result in increased trauma or a greater chance of decentration [107].

1.4.1.3.3 Intraocular Lens Surface Modification

Although the development of foldable intraocular lenses, which allowed smaller incisions, and the square edge IOL optic design helped to reduce the incidence of PCO, it is still a major burden on the worlds' health care systems and the quality of life of those afflicted. PCO is also particularly prevalent in children and young adults who undergo cataract surgery. These patients typically have the posterior capsule ablated prior to the onset of PCO as it is often considered inevitable with young patients [144]. Differences regarding PCO and other complications have been associated with the lens material [70, 75, 142, 144]. As stated previously the body only interacts with a biomaterial's surface, therefore the surface modification of intraocular lens materials could be a strategy to reduce the incidence and clinical burden of PCO. There are 2 hypotheses for the implementation of this strategy: create a surface which allows LEC growth but stimulates LECs to form a monolayer and maintain their epithelial phenotype, or create a surface which inhibits the attachment and migration of LECs completely. In the following section some of the research in this field will be outlined briefly.

Early research into the modification of IOL materials involved the immobilisation of heparin onto surfaces in the late 1980's [145, 146]. A recent 12-year follow-up study in which Rønbeck et al. studied the PCO rates in patients who either had heparin-surface-modified (HSM) PMMA (Pharmacia & Upjohn, 809C), silicone (Allergan, SI-40NB) or acrylate (Alcon, Acrysof®). Of the patients with HSM PMMA lenses 57% underwent Nd:YAG capsulotomy prior to the follow-up period compared to 29% for the silicone lenses and 32% for the acrylate lenses [147]. In a related study the authors report that the incidence of “glistenings”, which are microbubbles or microcavities in the lenses, was lowest on the HSM PMMA lenses [148].

More recent methods of surface modification of IOL materials, or materials potentially used as IOLs, include the binding of phospholipids to silicone [149-151] and the binding of selenium to PHEMA [152]. Research conducted in Zhejiang University, People’s Republic of China demonstrated that MPC-modified-silicone decreased macrophage, platelet and LEC adhesion [149]; decreased adhesion and colonisation of bacteria [150], and decreased the adhesion of silicone oil [151]. The studies were conducted in vitro and unmodified silicone was used as a control. No clinical studies have yet been published. Pot et al. demonstrated using an ex vivo canine lens capsular bag model that the binding of selenium decreased the degree of PCO [152].

Much of the other current research into the modification of the surface of IOLs utilises physical processes such as UV or plasma-modification. Various different functional groups can be added to surfaces using different plasma gases [5, 18, 64, 127, 153], plasma pre-treated surfaces can be used to bind other molecules [154, 155] or thin films can be created on surfaces by plasma polymerisation [156, 157]. In the following section the basic structure and formation of plasmas, plasma surface modification and plasma polymerisation will be discussed.

1.5 Plasma Technology

1.5.1 Plasma - The Fourth State of Matter

Plasmas are often referred to as the fourth state of matter. They consist of electrons and energised atoms and molecules, such as radicals and metastables, as well as photons in the visible and UV spectrum, contained in a background gas (i.e. the gas that was ionised). Atoms and molecules are often collectively referred to as "species". Plasmas are generally electrically neutral. Plasma makes up a large part of the matter in the known universe. Examples are the stars, Earth's ionosphere, some interstellar medium and the auroras [156, 158]. Naturally occurring examples on Earth include lightning and flames.

Research into plasmas began with the ionisation of gases in the late 19th century but the term plasma was not used until Irvine Langmuir coined it in 1929 [156, 159]. The application of plasma technology accelerated in the 1950's with the development of integrated circuits. Plasma technology is still used today for the manufacture of electrical systems. Plasmas are formed in the lab by the ionisation of gas, often by applying a voltage across the gas [160].

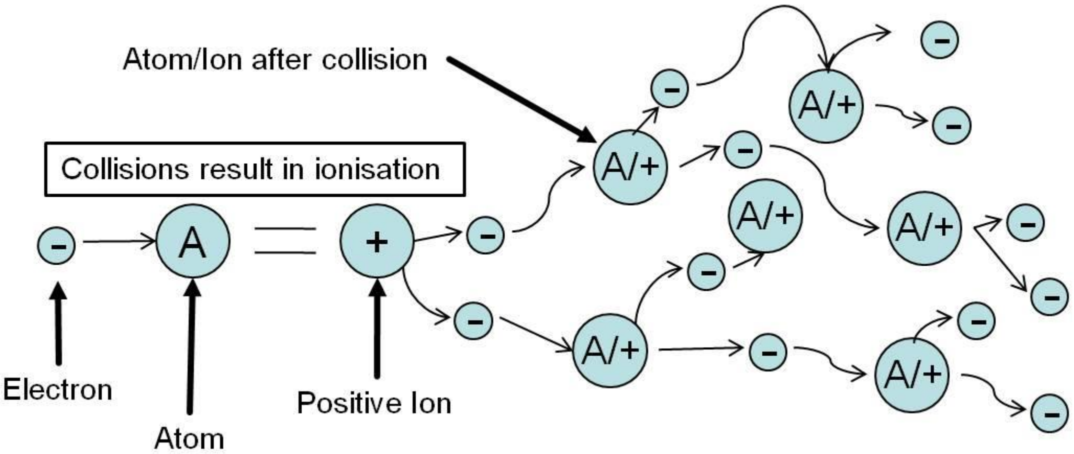

Figure 1.16 Simplified diagram of ionisation cascade by electron-atom collision. (-) is an electron, (A) is an atom, (+) is a positive ion and (A/+) is an atom which becomes an ion following collision.

In the laboratory the gases which will be ionised (sometimes called breakdown gas or operating gas) are often confined in a space between electrodes. The electrodes can be positive and negative, powered and grounded or a singular, powered electrode. The application of a high voltage to these electrodes creates an alternating electric field which can transfer energy to the gas. This causes the atoms or molecules within the gas to increase their vibration and movement. The species collide with each other, transferring energy between one another and increasing the momentum of some particles. When a collision occurs with enough energy it can cause the release of an electron from the outer shell of the atom, which also creates a positive ion (ionisation). These free electrons and ions are influenced further by the electric field, causing more collisions with greater momentum and greater energy. This can cause other reactions in the gas, such as molecular dissociation (e.g. the dissociation of molecular O_2 into atomic O), the creation negative ions or the removal of protons to create free radicals. The reactions which occur are dependent upon the chemistry of the breakdown gas and the energy supplied. This process cascades and causes the breakdown of the gas (Figure 1.16). During this thermodynamically favourable reactions are also occurring, such as recombination of positive and negative ions, or electrons in excited species which may drop to their low-energy ground states by emission of excess energy as a photon. The wavelength of the emitted photons are dependent on the gas chemistry and are observed in the characteristic glow of plasmas, e.g. aurora borealis or neon lights. Photons can be in the visible or more energetic, i.e. in the UV range. These emitted photons can strike other species and provide them with energy causing more reactions to occur [160, 161]. Due to all the varied processes occurring in plasmas, and the varied chemical and physical states they create, has lead authors to describe plasmas as a “soup” of energetic species and photons.

There are a huge number of design variations in plasma systems; this large degree of variability can make comparisons difficult. The electrode material, design and positions can all be changed. The power source can be altered, whether AC, DC, microwave or radio frequencies. The voltage applied to the electrodes and its direction can be changed, as well as the frequency. The operating gas also affects the plasma properties, especially the reactive species contained created. The gas can be inert (such as helium, argon and neon), molecular (such as oxygen, nitrogen and air) or mixtures of these [158, 162]. The multitude of designs affords plasma technology many applications. Some examples are polymer deposition, sputtering (the coating of a surface by the release of atoms from an electrode), sterilisation, altering of surface chemistry, spectroscopy, arc welding, ignition source in combustible engines, thermonuclear experiments, gas clean-up, luminescent lamps and more [163].

1.5.2 Atmospheric Pressure Low Temperature Plasmas

For many years plasmas for materials surface modification were typically operated at low pressures. The low pressures meant that there were fewer gas atoms present, which allowed the excited species more room to travel and gain momentum, i.e. the species had longer mean free paths. These low pressure systems required expensive equipment such as vacuum chambers and pumps to decrease the pressure, but the plasmas were more stable in the evacuated environments [162]. In recent years plasmas operating in higher pressure, including atmospheric pressure, have been investigated extensively [158, 164, 165]. From an applications perspective atmospheric pressure is more beneficial. The lack of vacuum equipment means that plasma systems are less expensive to construct and maintain, they are more portable, and they can be more easily incorporated into in-line manufacturing processes.

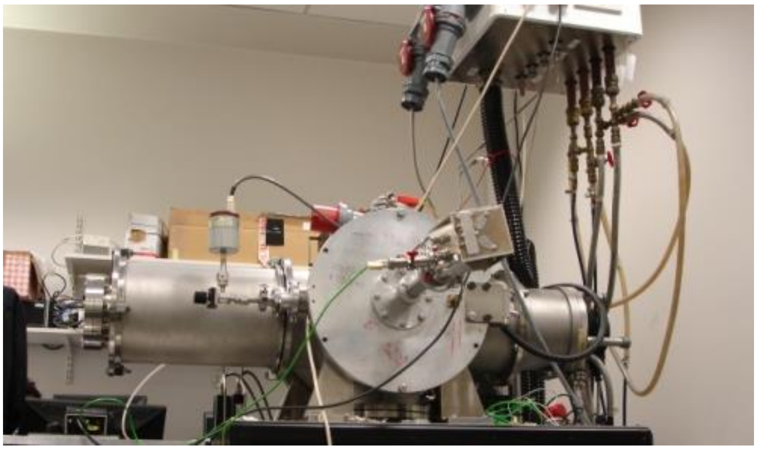

Figure 1.17 High vacuum plasma sputtering system.

Another area of increasing interest is what is often referred to as cold or low-temperature plasmas. Cold or low-temperature is a broad undefined term, but often the cold nature of these plasmas are attributed to their non-equilibrium state. The non-equilibrium state refers to the difference in temperature between the larger ions and the smaller electrons. In non-equilibrium plasmas the electrons typically have a much higher temperature than the heavier ions and the neutral species, which can be approximately, or close to, room temperature (~300K) [166, 167]. This is in part due to the fact that electrons have around 10^4 – 10^5 times less mass than ions yet are effected by electrical charge equally (in opposite polarity), this causes the electrons to be accelerated 10^4 – 10^5 more than the ions [156]. Cold atmospheric pressure plasmas can be used to modify the surfaces of materials with low melting points, such as various polymers [168-170], or even treated cells and tissue and sterilise surfaces by non-thermal methods[19, 171-174]. These latter applications have recently been dubbed “Plasma Medicine” [164, 175, 176].

1.5.3 Microplasmas

When operating in atmospheric pressure the distance between the electrodes, or geometry of ring electrodes, on a plasma system can be key to obtaining a plasma discharge. This is due Pachen’s law which states that the breakdown voltage required to create a discharge in a gas between two electrodes is a function of pressure and the distance between the electrodes: application of this principle is sometimes referred to as “pd scaling” [158, 160, 162, 177, 178]. For this reason atmospheric pressure plasma systems tend to have electrode separations or geometries in the mm range or in the µm range. Plasma systems with discharge regions in the order of ~1mm or less are often referred to “microplasmas”. Scientific interest in atmospheric pressure plasmas and microplasmas has increased greatly over the past decade. Typical of plasma systems there are a multitude of microplasma system designs. One such design is the plasma jet.

1.5.4 Plasma Jets

Atmospheric pressure plasma jets have been used recently to create discharges at the mm scale [179, 180] and to create microdischarges [170, 181, 182]. They typically have an open ended capillary through which a gas is passed. Using various designs the gas is ionised as it leaves or before it exits the capillary. Often systems operate using a dielectric barrier discharge (DBD) configuration. DBD is a system in which the electrodes (or electrode and gas medium) are separated by a dielectric material. A dielectric is an insulating material that undergoes polarisation when influenced by an electric field. As a voltage is generated by the plasma system's electrodes, the charges (positive and negative) separate in the dielectric material. Dielectric barriers can be used in atmospheric pressure plasmas to limit current arcing between electrodes and the creation of “streamers” (filamentary arcs)[177]. Arcing can be destructive to materials.

A plasma jet can be operated using the dielectric barrier glow discharge principle. In the diagram below, the electrode is around the outside of a quartz capillary. Quartz is a dielectric material. Two interfaces are of interest in this system: the electrode-capillary interface on the outside of the capillary, and the capillary-gas interface on the inside of the capillary. When a positive charge is created in the electrode it will polarise the charges in the quartz capillary; the negative charges in the quartz capillary will be attracted to the electrode-capillary interface (see notation A in Figure 1.18). This results in a positive charge being created at the capillary-gas interface (see notation B in Figure 1.18). This creates an electric field across the gas which increases the momentum of the gaseous species, e.g. helium atoms. If the electrode voltage is high enough it will ionise the gas passing through the capillary creating a plasma. The charged species within the gas, e.g. positive ions and negative electrons, are affected by the electrode via the dielectric material. When the electrode is positive the ions will be repelled to the centre of the gas and the electrons will be attracted to the capillary-gas interface (see notation C in Figure 1.18). When the power source alternates polarity i.e. becomes negative, all the charged particles switch places. The plasma electrons that were held at the inner wall of the capillary are repelled and collide with other particles within the plasma. It is this mechanism of attraction and repulsion with an alternation in electrode polarity that aids DBD systems in maintaining a plasma discharge. A mechanism of repulsion and release can occur with a pulsed DC voltage. In this example only interactions at a single electrode are presented for the sake of clarity, however a grounded electrode may also be present [168, 179, 183-189]

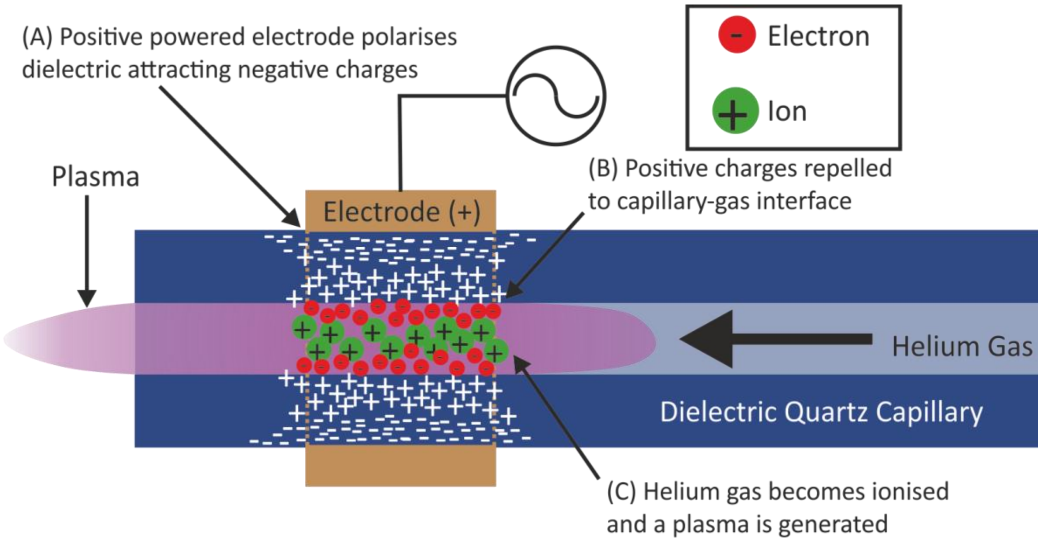

Figure 1.18 Cartoon of dielectric barrier discharge mechanism. Quartz capillary is polarised by the positive electrode causing a negative charge to build at the electrode-capillary interface (A), which causes positive charges to accumulate at the capillary-gas interface (B). As the current to the electrode alternates the energy is supplied to the gas which becomes ionised (C), thus forming a plasma.

The flow of gas can carry the reactive, excited species created in this discharge region out of the capillary (Figure 1.18), for example towards a surface to be treated. This area is often referred to as the afterglow. It has been shown that plasma jets such as this do not create a continuous stream of reactive species but in fact, the reactive species are created in groups and carried from the discharge region. These have been termed plasma bullets and are created at particular times of the wave form of the supplied voltage (Figure 1.19) [186, 188, 190, 191].

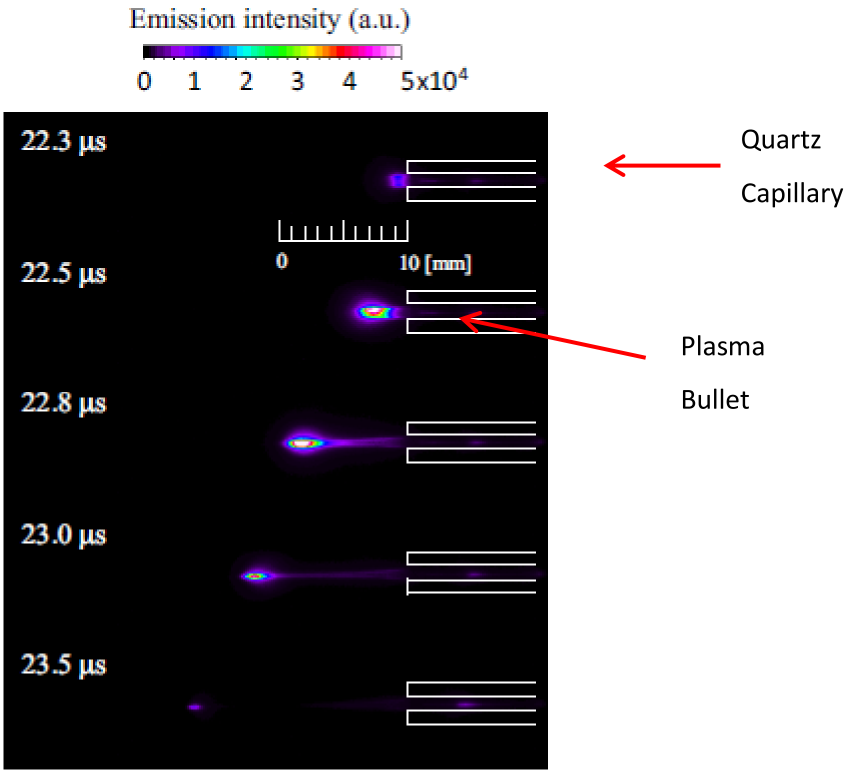

Figure 1.19 A time series of photographs of a plasma bullet exiting a quartz capillary taken with an intensified charged coupled device (ICCD) camera. Image adapted from [188].

1.5.5 Pin Plasmas

Pin plasmas (sometimes referred to as plasma needles) are another type of plasma system which are based on coronal discharge, rather than the glow discharge of a DBD plasma jet outlined above. In these systems a high voltage is applied to a pin or “needle”. The geometry of this type of electrode presents a sharp tip at which charge can accumulate. When the voltage is large enough charges at the pin tip ionise the surround gas and can create a coronal plasma discharge. The pins at which the plasma is formed often have diameters of a couple of hundred microns [167, 192-194]. These systems have recently been used as sources of surface ionisation for spectrometry [192, 195] but have also been used to treat tissues and cells, which can result in membrane permeabilisation and apoptosis [167, 194]

1.6 Plasma Modification of Polymers

Plasmas have been used for a long time to modify the surface properties of materials in a wide range of applications. Due to the nature and energy of the species created within plasmas they only penetrate the first few atomic layers of material surfaces; this makes them excellent tools for surface modification, leaving the properties of the bulk material intact. This section will investigate the surface modification of polymeric materials with (typically atmospheric pressure) plasmas. Many physicochemical processes play a role in surface modification and these processes are not necessarily independent of each other [160, 196]. The surface modification by plasmas will be grouped into 2 fields in this section:

- Surface Treatment - the treatment of a surface by species created by the ionisation of a gas.
- Plasma Polymerisation - the creation or deposition of thin films onto surfaces by the polymerisation of a gaseous suspension of monomers in a plasma.

1.6.1 Surface Treatment

Many of the varied species within a plasma (ions, electrons, radicals and photons) can alter the surface of a polymer (Figure 1.20). The extent at which these species affect the polymer surface depends on many things. These include the energy, density and chemistry of the species, the wavelength of the photons, the distance they need to travel and the chemistry of the polymer surface. When the species reach a polymer surface they can change the structure provided they have enough energy. Ions are known to cause etching of a surface (typically from molecular gases e.g. O_2, $N_{2\ldots}$), UV photons can break surface bonds or cause cross-linking, radicals and ions can be incorporated into the surface [162, 169, 197, 198].

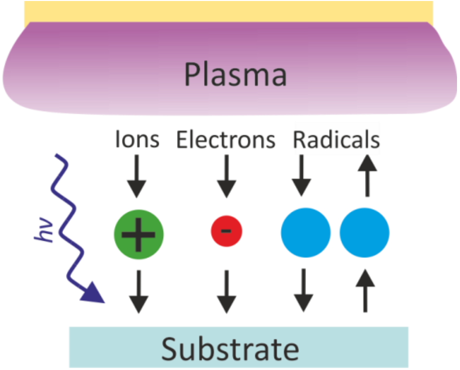

Figure 1.20 Cartoon of the species involved in plasma treatment including UV photons (*hv*), ions, electrons and radicals.

When a surface is treated with a plasma created from “inert” gases such as helium, argon and neon it often results in the addition of oxygen, even if the surface is treated in vacuum. This phenomenon is due to radical implantation on the sample surface. These surface radicals act as intermediates in the changing surface chemistry. Their free electrons quickly combine with other atoms or molecules in thermodynamically favourable reactions. Most often the surface radicals react with oxygen in the air to create hydroxyl, carboxyl and other oxygen containing functional groups. Radicals created on the surface of materials by inert gas plasmas in vacuum can combine with oxygen species (such as molecular oxygen or water vapour) when they are removed from the vacuum into air (Figure 1.21). This post-processing reaction has often been observed, even when gases such as nitrogen have been used, or following plasma polymerisation [169, 197-200]. When plasmas are generated in air or with the addition of oxygen, it is difficult to distinguish whether the oxygen present on the surface following treatment was incorporated directly during treatment, or was due to radicals created on the surface, however it is likely to be a combination of these effects. The incorporation of polar oxygen functional groups onto polymer surfaces is typically characterised by a reduction in contact angle and the observation of these species by x-ray photoelectron spectroscopy (XPS).

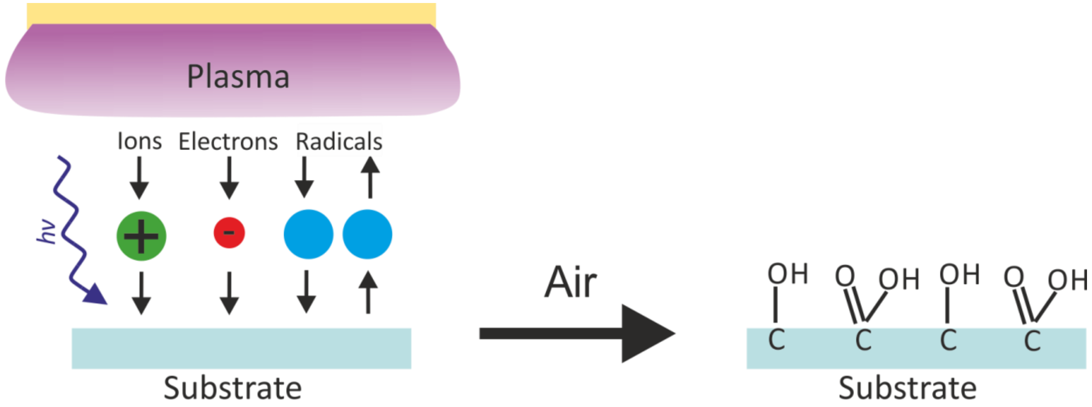

Figure 1.21 Cartoon of post-treatment functionalisation by air creating hydroxl and carboxyl functional groups.

A study by Yuen et al. (2006) investigated the plasma treatment (low pressure) of common IOL materials: PMMA, silicone and hydrophobic acrylic (Alcon's Acrysof® lenses). PMMA was treated with a nitrogen plasma, whereas silicone and Acrysof® were treated with air plasmas. All samples were placed in water following treatment to initiate oxygen functionalisation via interaction with water and surface radicals as outlined in previous work [201]. Plasma treatment decreased the contact angle of all materials and also significantly increased the number of primary bovine LECs observed on treated materials at 16 and 24 days post-seeding. Yuen and co-authors also comment that the morphology of LECs on treated PMMA and silicone were more epithelial than those on untreated materials [64].

Matsushima et al. (2006) treated acrylic IOLs (Hoya's VA-60 BB lenses) with either a UV/ozone system or an argon plasma (pressure not stated). The authors demonstrated the presence of hydroxyl (-OH) and carboxyl (COOH) groups, not present on untreated surfaces, following either treatment. The treatment of lenses increased the adhesion of fibronectin and primary rabbit LECs. Untreated and treated lenses were also implanted in rabbits following phacoemulsification. After 2 weeks the animals were sacrificed and the thickness of the LEC growth between the posterior capsule and lenses was examined. There was a significantly thinner layer of LECs on the central portion of the capsule/lens when treated lenses were implanted compared to untreated lenses [202].

D’Sa et al. (2010) demonstrated that atmospheric pressure DBD plasma treatment in air of polystyrene (PS) and PMMA increased the surface oxygen of these polymers. This corresponded to the adsorption of albumin in a different conformation on treated surfaces compared to untreated surfaces. In a competitive protein adsorption study the authors noted that serum proteins replaced some of the albumin which had adhered on the surface, but only on treated surfaces [5]. The authors also demonstrated that the difference in the protein adsorption on treated and pristine PS and PMMA resulted in a greater number of adhered B3 LECs on the treated surfaces. The LECs on treated surfaces also had a more spread morphology compared to LECs on untreated surfaces [5, 18]. In other work D’Sa and co-authors demonstrate that the hydroxyl groups bound to the surface following plasma treatment can be used in wet chemical reactions, to bind both poly(ethylene glycol) methyl ether methacrylate [203] and hyaluronic acid [155]. In this latter experiment the authors demonstrated that plasma treatment enabled the chemisorption of 3-aminopropyltrimethoxysilane (APTMS) which created an amine surface functionality. Hyaluronic acid could then be immobilised to the amine functionality. Whereas APTMS encouraged LEC adhesion (as amine functionalised surfaces are known to increase cell adhesion) the immobilised hyaluronic acid inhibited LEC adhesion to the PS [155]. If the amine or plasma treated surfaces could be used to encourage an epithelial monolayer which retained it phenotype, then any of these surfaces (plasma treated, amine and hyaluronic acid) could be used to combat PCO.

Similarly, Zhang et al. (2009) bonded poly ethylene glycol (PEG) and/or heparin to PMMA IOL surfaces following low pressure argon plasma treatment. The authors suggest the plasma treatment with argon created surface radicals which formed oxygen functionalities when the samples were removed from vacuum to air. Following this samples were soaked in PEG or heparin solutions then treated with the plasma again. This is known as plasma-induced polymerisation. The resultant PEG and/or heparin surfaces were demonstrated to reduce the adhesion of platelets [154]. The attachment of LECs was not investigated.

An atmospheric pressure argon plasma was used by Wang et al. (2009) to modify the surface of hydrophobic acrylic lenses (66 Vision Tech Co.’s FV-60A lenses). Again, the authors believe exposure to air following treatment introduced the increased concentration of oxygen and nitrogen (nitrogen increased by only 0.3%), and subsequent reduction in contact angle from 92° to 70-77° (depending on storage time). The authors demonstrate that the plasma treatment of acrylic IOLs significantly decreased the number of platelets and macrophages, when examined 24hrs after the cells were seeded. When B3 LECs were seeded onto untreated and treated lenses there were significantly fewer LECs on the lenses treated for the longest times (180 and 360s treatment times) compared to untreated at 24hrs; however there was no difference between the number of LECs on untreated lenses and those plasma treated for shorter durations (10 and 60s treatment times). At 72hrs post-seeding there was no significant difference between the numbers of LECs on treated or untreated surfaces. The LEC morphologies were also similar between materials [153].

1.6.1.1 Spatial Resolution

The use of atmospheric pressure microplasma jets for functionalising surfaces is a research topic of growing interest. Yet there are not many current publications which investigate the spatial confinement of the treat areas. Even fewer papers have reported the spatially resolved cellular attachment onto surfaces treated with microplasma jets.

It has been demonstrated that microplasma jets can be used to encourage spatially defined cell growth on polymeric materials [19, 170]. In both studies plasma jets, with nozzles diameters of 100-150µm, were scanned in a line across a polymer surfaces. The authors demonstrated that cells (human aortic endothelial and HeLa cells) adhered to tracks with widths of a few hundred micrometers. Yet these reports have vague methodology and possibly lack of repetition. The spatial modification of the surface also lacks detailed characterisation [19, 170].

In 2007 Soba et al. reported surface functionalisation by a helium/ammonia with an area of ~500µm by XPS imaging. In this study however the pressure was “near atmosphere” (720-730Torr; 760Torr = 1atm), and a reaction chamber with various pumps were used. Although operating in the same pressure range this system still required a plasma reactor chamber and pumping mechanisms [204]. The smallest spatial modifications induced by atmospheric pressure plasma jets reported, to the best of the authors knowledge, has taken place in Shizuoka University, Hamamatsu, Japan. Kakei et al. (2010) reported etching of acrylic resin resist films in tracks of 500-700nm, using a jet with a 500nm nozzle. The track widths were measured by AFM. The change in the surface chemistry was not studied and could possibly be wider than these etched tracks [181]. Motrescu et al. (2012) et al. used a 2-step process to create amine functionalised dots as small as 20µm in diameter. Polymer surfaces (polyethylene and polyurethane) are first pre-treated with a helium plasma for 0.01-0.1s and subsequent treated with helium + 3% ammonia plasmas for 3s. The size of the resultant amine functionalisation was determined using a fluorescent microscope and a fluorescently tagged sulfodicholorphenol ester which binds to amines. The authors were able to achieve dots of 20µm with a 1µm ID nozzle [205]. The size of the oxygen functionalisation was not investigated and would be of interest from a biomaterial perspective. These results may be promising for biomaterial applications yet no work in this field has yet been published.

1.6.2 Plasma Polymerisation

Plasma polymerisation is the deposition of thin films onto surfaces from monomers suspended in the gas phase. Some examples of monomer precursors used include heptylamine ($C_7H_{17}N$) [189, 200], octafluorocyclobutane (C_4F_8) [206], acrylic acid ($CH_2{=}CHCO_2H$) [207, 208] and hexamethyldisiloxane (HMDSO, $O[Si(CH_3)_3]_2$) [209]. Many other forms of monomer can and have been used. The polymerised film does not have the same chemistry as a typical polymer synthesised from the monomer, which can be due to fragmentation [160]. Reactions with ions and monomer units in the gas phase can lead to polymerisation of the monomers [210]. The variables in plasma systems outlined previously persist in plasma polymerisation systems yet there is the added variables of the monomer chemistry, structure, flow rate etc. Monomers to be polymerised are often incorporated into an inert gas (helium, argon etc.) to which the discharge voltage is applied [189, 206, 209, 211, 212], although monomers can be placed on a surface prior to treatment with a plasma [154]. The monomers can form into oligomer units in the gas phase before bonding to a surface [189].

Although atmospheric pressure plasma polymerisation is a field of growing scientific interest, little has been published on the plasma polymerisation of surfaces using plasma jet systems. Benedikt et al (2006, 2007) have demonstrated the deposition of carbon [212] and siloxane [209] surfaces using atmospheric pressure microplasma jets. The authors did not report the size of modification and oxygen was also incorporated into the carbon films. The deposition of fluorocarbon films in areas with diameters of ~7-10mm has been demonstrated by Vogelsang et al (2012). The main drawback of this study was the use of a pump to purge the air species from the reaction chamber, which was subsequently filled with nitrogen [206].

In recent work by Carton et al. (2012) acrylic acid was deposited onto glass surfaces using an atmospheric pressure jet system operated in air. The authors seeded human ovarian carcinoma cells onto surfaces. The numbers of cells on the treated surfaces were similar to glass and tissue culture polystyrene controls at 24hrs, however there were fewer cells on treated surfaces compared to controls at 48 and 72hrs. The authors state that this may in part be due to instability of the coatings in culture medium but that similar results are reported in the literature for comparisons of acrylic acid films and glass controls [208].

1.7 Hypothesis and Aims of this Thesis

It has been demonstrated that atmospheric pressure microplasma jets can be used to modify the topography and chemistry of polymer surfaces and may be used to encourage the attachment of cells when operated in air. Plasma polymerisation using plasma jets has also been demonstrated. Microplasma jet systems may prove to be a useful tool for cost effective surface modification of polymeric biomaterials, however little research has yet been published on the use of systems for modification in a spatially defined manner.

The overall aim of the project was to determine if an atmospheric pressure microplasma jet could be used to create a spatially defined treatment on polymeric surfaces to control cell-surface interactions, which can be applied to IOLs to inhibit the advancement of PCO. This can be divided into 2 smaller aims, which are:

1. A surface treatment which can inhibit LEC attachment to the lens material, and thus prevent LECs from migrating onto the posterior capsule and developing into PCO.
2. A surface treatment which will encourage LEC growth and the formation of a monolayer of cells which maintain their characteristic epithelial phenotype and thus morphology. This would prevent the cells from wrinkling the posterior capsule or forming multi-layered sheets, thus allowing light to pass uninterrupted to the retina.

The main objectives of this project were:

- To develop and optimise an atmospheric pressure microplasma jet to create spatially defined treatments, without the use of a mask.
- To investigate the use of the microplasma jet to modify acrylic materials, for possible applications in IOLs.
- To investigate and develop the use of a plasma jet system for plasma polymerisation of monomers onto surfaces at atmospheric pressure.
- To demonstrate that the surface modification influenced cell attachment to the polymer surface.
- To demonstrate that the surface modification influenced the LEC response to the polymer surface.

- To demonstrate that a pin plasma device could be used to modify polymer surfaces in a non-destructive manner.

2 Materials and Methods

This chapter will explain the methods and materials used through-out this thesis. Firstly, the various techniques used will be summarised, followed by explanations of specific experiments and the details of the techniques used within them.

2.1 Materials

For preliminary experiments 240µm thick polystyrene, pre-cut into 20x20mm squares were used (Goodfellow Cambridge Ltd., UK). Subsequently, polystyrene was obtained as a 1.2mm thick sheet (Goodfellow Cambridge Ltd., UK) and was cut into 10x10mm or 20x20mm squares. PMMA was purchased as 1mm thick 10x10mm squares (Advent Plastics, UK). An "R" symbol was etched into the top left corner of the rear side of the samples. The reverse side of the sample was not used for any analysis. This "R" symbol appeared reversed in the top left side of the sample when viewed from the front (Figure 2.1). All axes and coordinates used to describe positions on a sample throughout this thesis will be assumed to be from the front perspective.

Sample surfaces were cleaned by rinsing in 100% isopropanol (Fisher Scientific, UK), followed by ultrasonication in isopropanol for 3 minutes at 42kHz and 70W. Samples were given a final rinse in isopropanol then dried under compressed N_2 (BOC, UK) flow. Samples were allowed to relax for a minimum of 24hrs before use, or used directly after preparation.

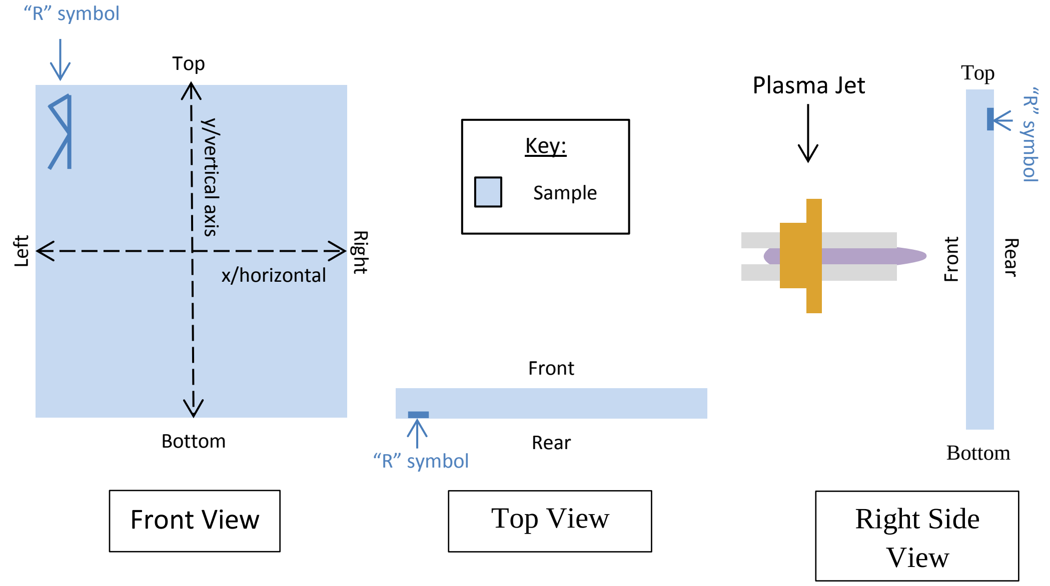

Figure 2.1 3-Plan view diagram displaying the axes and position terms of the sample that will be used throughout the thesis in relation to the "R" symbol. The "R" symbol etched into the rear of the sample, and hence is reversed in the front view, allowed repeatable orientation during treatment and analysis.

2.2 Plasma Systems and Experimental Design

2.2.1 Surface Modification by Atmospheric Pressure Plasma Jet

Various plasma system setups were used throughout this study, outlined in the following sections. In brief, the plasma setups consisted of a quartz glass tube (Robson Scientific, UK) through which helium gas (purity: 99.996%, BOC, UK) flowed. Flow rate was controlled by either rotameter(s) (Influx Measurements Ltd., UK), or by digital mass flow meter and controller (MKS, UK). The energy required to dissociate the helium gas was supplied via a powered copper ring electrode (8mm length) around the quartz tube, with or without a grounded electrode. The electrode was powered by high AC voltages (peak-peak) of either 6kV or 8kV, at a frequency of 10kHz. The frequency was generated by a function generator (TG2000, AIM-TTI Instruments, UK), which drove a commercial audio amplifier (HQ power, Belgium) used to alter the voltage. Throughout this thesis voltage is expressed as the peak-to-peak voltage - the absolute amplitude of the signal. Following the audio amplifier, a voltage step-up transformer (Express Transformers, UK) generated the high voltages required to ignite the plasma. Once plasma discharge was achieved, systems were allowed to run for at least 15 minutes prior to treatment, this allowed possible contaminants and air remnants to be flushed from the tubing. Samples were placed at a set distance(s) from the opening, or nozzle, of the quartz capillary from which the jet exited. Defined as the distance from the nozzle to the front surface of the sample, and referred to as the sample-nozzle distance.

2.2.1.1 Preliminary Epithelial Cell Culture on Plasma Jet Treated Samples

A preliminary study using ARPE-19 cell line as an epithelial model was conducted. ARPE-19 cells were grown on TCPS, untreated PS, treated PS and half-treated PS. PS samples were 20x20mm and 240µm thick. To create the half-treated PS the top half of a PS sample was masked by another larger piece of PS, which was removed following plasma treatment (Figure 2.2).

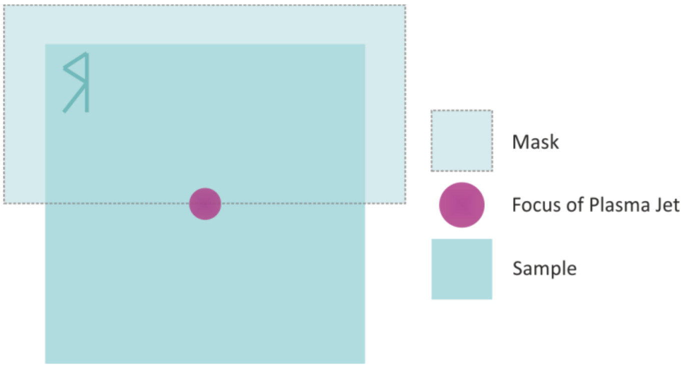

Figure 2.2 Illustration of half-treated sample masking. A larger piece of PS was used to mask the top half of samples during treatment. This mask was removed following treatment.

2.2.1.1.1 Plasma Jet

In this study the plasma jet was ignited within a quartz tube with a 1mm internal diameter (ID) and a 3mm outer diameter (OD). A forward powered electrode was positioned 10mm from the tube nozzle; a grounded electrode was positioned 20mm back away from the forward powered electrode. Flow rate was controlled by a rotameter (Figure 2.3). The following plasma parameters were used:

- 6kV$_{\text{peak-peak}}$
- 482sccm flow rate
- 60 second treatment time
- 5mm sample-nozzle distance

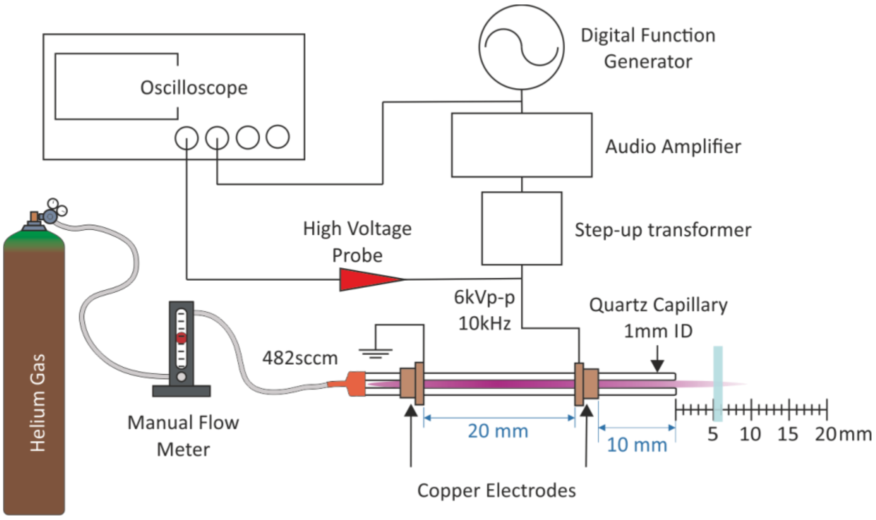

Figure 2.3 Schematic of plasma system setup for ARPE-19 preliminary study. Plasma jet parameters were: 6kVp-p, 10kHz, 482sccm, 60s treatment, 5mm sample-nozzle distance.

2.2.1.1.2 Cell Culture

ARPE-19 cells were seeded at a density of 1x10^{4}cells/cm^2 onto 3 samples per experimental condition. Samples were placed in a 6-well plate and grown for a total of 5 days. Cells were fixed with NBF and stained with PI and phalloidin (sections 2.4.2.2 and 2.4.2.4). Images were taken in the centre of the samples, with x10 and x5 objectives, on the Zeiss Axiovert 200 to illustrate the effect of plasma jet treatment on LEC attachment and growth.

2.2.1.2 “Shadowing” Experiments

In an attempt to elucidate possible mechanisms by which the plasma jet modifies the surface barriers, or “shadows”, were placed between the jet and samples. This was to interrupt the gas flow from the jet, which carries reactive species, and also to halt UV photons which only travel in a straight line. Both UV photons and reactive species could possibly break surface chemical bonds and allow surface modification. Various shadow materials, shapes, sizes and positions were investigated at multiple sample-nozzle distances. All “shadows” were positioned vertically in the centre of the gas flow (example in Figure 2.4). All treated samples were 20x20mm, 1.2mm thick PS. Experiments will be grouped by shadow material. Samples were analysed by contact angle.

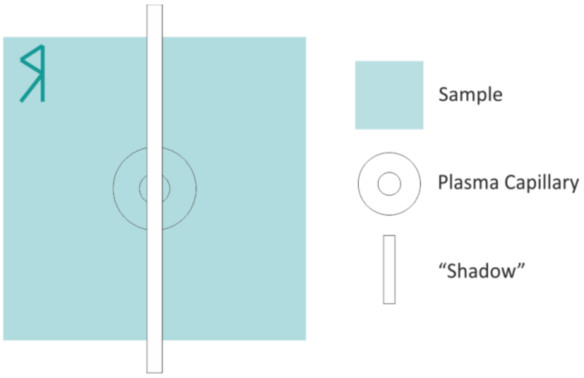

Figure 2.4 Schematic of the orientation and position of a “shadow” relative to a sample and the plasma capillary.

2.2.1.2.1 Plasma Jet

The following plasma jet configuration was used for all subsequent “shadowing experiments”. The plasma jet was ignited within a quartz tube with a 1mm internal diameter (ID) and a 3mm outer diameter (OD). In this study the forward electrode was grounded and positioned 10mm from the tube nozzle; a powered electrode was separated from the ground electrode by 20mm. Flow rate was controlled by a rotameter and maintain at 138sccm throughout the subsequent experiments. (Figure 2.5). The following plasma parameters were used:

- $6kV_{peak\text{-}peak}$
- 138sccm flow rate
- 20s treatment time

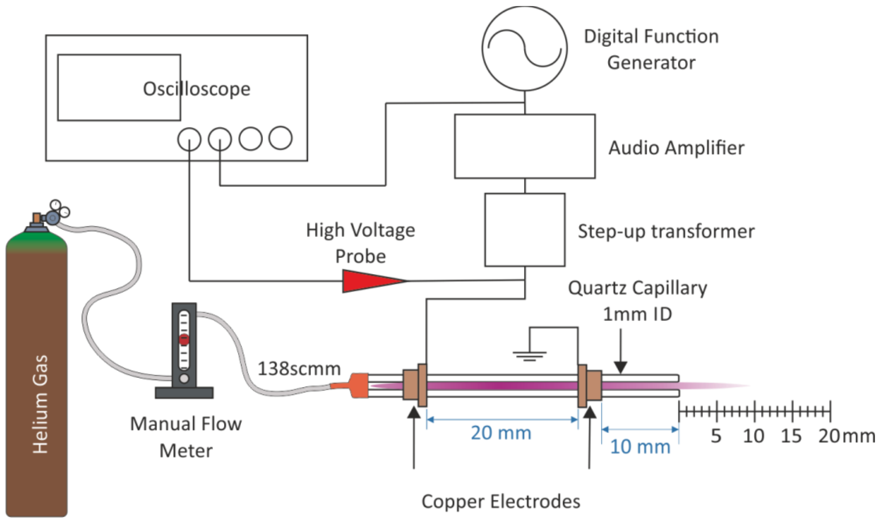

Figure 2.5 Schematic of plasma system setup used throughout "shadowing" experiments. Plasma discharge was created in 1mm ID tube, with an 8kVp-p voltage input and 138scmm flow rate.

2.2.1.2.2 Paper Shadows

Initial preliminary tests used paper strips, cut to different widths, which were held in the jet flow path. Paper "shadows" were positioned 7mm from the nozzle, whilst PS samples were positioned 10mm from the samples.

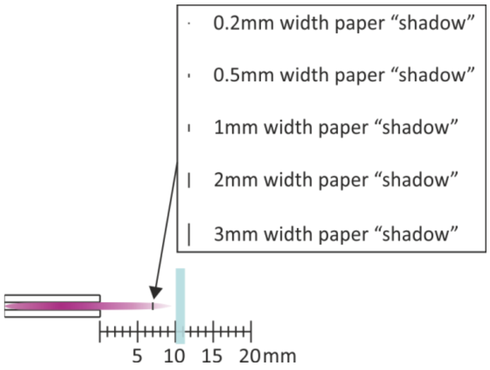

Figure 2.6 Schematic illustration sample and "shadow" positions for paper "shadowing" experiment.

2.2.1.2.3 Plastic Shadowing

In this experiment the distances of the sample and shadow relative to the nozzle were investigated, as well as the shadow thickness. Shadows of width 1.2mm, 2mm and 3mm were cut from 1.2mm thick PS. With this shadow, 2 sample-nozzle positions (10mm and 25mm) were investigated with various shadow-nozzle positions. The shadow-nozzle distance was defined as the distance from the nozzle to the surface of the shadow facing the nozzle. When the sample was placed 10mm from the nozzle, the various shadow sizes were placed 8mm from the nozzle (Figure 2.7.A). The 2mm width shadow as also positioned at 4 and 6mm from the nozzle (Figure 2.7.B). When the sample was positioned 25mm from the nozzle, the 2mm width shadow as placed at 5, 10, 15 and 20mm from the nozzle (Figure 2.7.C).

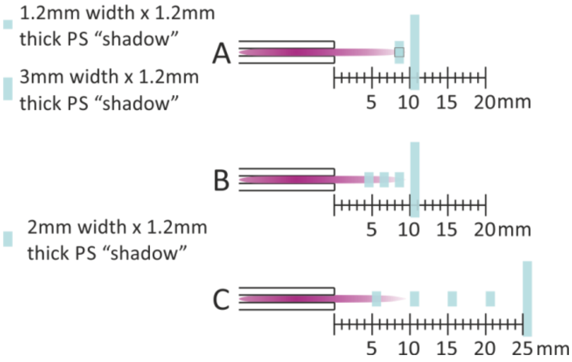

Figure 2.7 Schematic representing the 2 sample positions and the various sample-shadow widths and distances used in this experiment. (A) When the sample was 10mm from the nozzle the shadows of 1.2mm and 3mm width were placed 8mm from the nozzle. (B) A 2mm width shadow was also positioned at nozzle-shadow distances of 4, 6 and 8mm. (C) When the sample was at a distance of 25mm the 2mm width shadow was placed 5, 10, 15 and 20mm from the nozzle.

2.2.1.2.4 Quartz Capillary Shadows

Both the paper and plastic shadows displayed a flat-edged barrier to the plasma gas flow. The following experiment used a quartz capillary, placed at a fixed distance (centre of the capillary was 2mm from the nozzle), which presents a smooth, rounded barrier to the gas flow. The quartz capillary was the same as used in the plasma jet system and thus had a 3mm OD and a 1mm bore. As the quartz capillary was transparent it was possible that photons could pass through it, therefore paper was placed in the bore as an opaque photon blocker. Various sample-nozzle distances were investigated; these were 10, 12, 14, 16, 18 and 20mm.

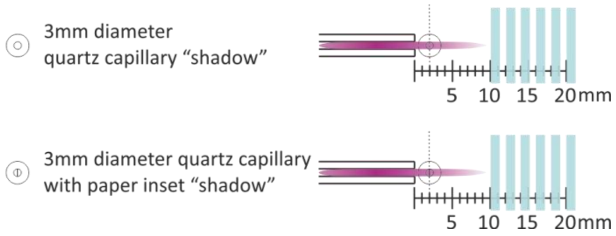

Figure 2.8 Schematic of the 3mm OD quartz capillary shadow and shadow with paper insert. The shadows were fixed at 2mm from the nozzle and samples were placed at 10, 12, 14, 16, 18 and 20mm from the nozzle.

2.2.1.2.4.1 Cell Culture

N/N1003a LECs were seeded onto samples to observe the effect of the shadowing on the cell growth area. Samples were placed 10mm from the nozzle and a capillary shadow with paper inset was fixed at 2mm from the nozzle. Samples were also treated without a shadow and untreated PS and TCPS served as controls. Cells were seeded at 1x10^{4}cells/cm^2 and cultured for 7 days. Representative phase contrast micrographs were taken at days 1, 4 and 7. Cells were also fixed with methanol and stained with methylene blue (section 2.4.2.1) at these time points.

2.2.1.2.5 Blackened Glass Rod Shadows

To ensure the blocking of photons blackened glass rods of varying diameters were obtained and used as shadows. Blackened glass rods of 3 diameters were used: 1mm, 2mm and 3mm. These were used as shadows when samples were placed at 2 different distances from the nozzle: 10mm and 20mm. When describing the distance of blackened rods it is intended that the distance is from the nozzle to the centre of the rods. When the 10mm sample-nozzle distance was used blackened rods were placed at 2mm, 4mm, 6mm, and 8mm from the nozzle (Figure 2.9.A-C). When samples were placed 20mm from the nozzle shadows were positioned at 2mm, 6mm, 10mm, 14mm and 18mm from the nozzle.

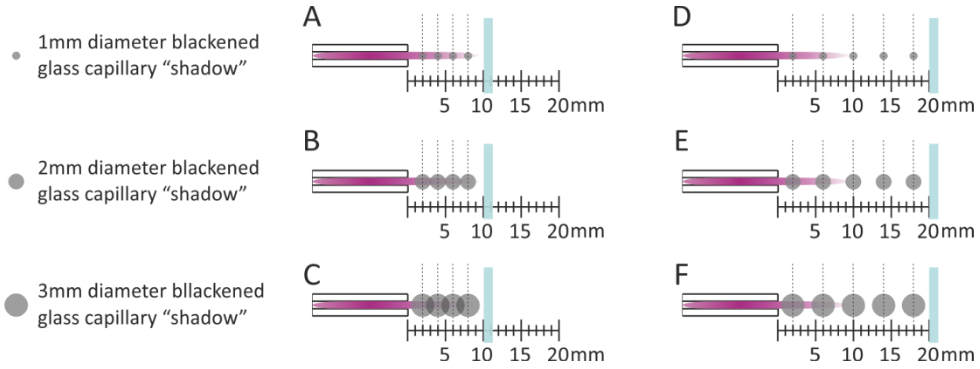

Figure 2.9 Schematic illustration the various experimental conditions used for the blackened glass rod shadowing experiment. Rods of various thicknesses, 1-3mm, were placed at a variety of positions (2-8mm) at a sample distance of 10mm relative the jet nozzle, and 2-18mm when the samples were 20mm from the nozzle.

2.2.1.3 100µm ID Microplasma Jet

Using a plasma jet with a capillary opening of ≈100µm the effect of flow rate and sample-nozzle distance was investigated. The effect of sample ageing post treatment was also investigated. All samples were cut to a size of 10x10mm^2 from 1.2mm thick PS.

2.2.1.3.1 Ageing

To examine the stability of the plasma treatment samples were treated then aged in air and water for various time lengths ranging from 0 days to up to 1 year. The effect of ageing time and condition was investigated by contact angle analysis and cell culture. The ageing conditions used for contact angle analysis and cell culture around outlined below in sections 2.2.1.3.1.3 and 2.2.1.3.1.4 respectively.

2.2.1.3.1.1 Vessel Cleaning for Storage in Water

Prior to ageing glass vessels (Agar Scientific, UK), used to store treated and untreated samples in water, were cleaned. Vessels were rinsed 3 times with 10% nitric acid (Sigma-Aldrich, UK) then left submerged in 10% nitric acid overnight. Vessels were removed from nitric acid and rinsed thoroughly in deionised water. Vessels were then half filled with deionised water for sample storage.

2.2.1.3.1.2 Plasma Jet

The 100µm capillary opening was created from a 1mm ID, 3mm OD quartz tube. The tube was heated and turned until the lumen closed. The closed lumen was the filed until it opened. An image of the lumen opening was taken using a CCD camera and the size calculated using a reference of a known size. The forward grounded electrode was positioned ≈10mm from the tip. A powered electrode followed, with an electrode gap separation of ≈20mm. Flow rates were set by the manual rotameter. To ignite the plasma jet the voltage supplied to the powered electrode was increased to 8kV peak-to-peak. A schematic of the plasma setup is detailed in Figure 2.10. The following plasma conditions were used:

- 8kV$_{\text{peak-peak}}$
- ≈130sccm flow rate
- 20s treatment time

- 10mm sample-nozzle distance

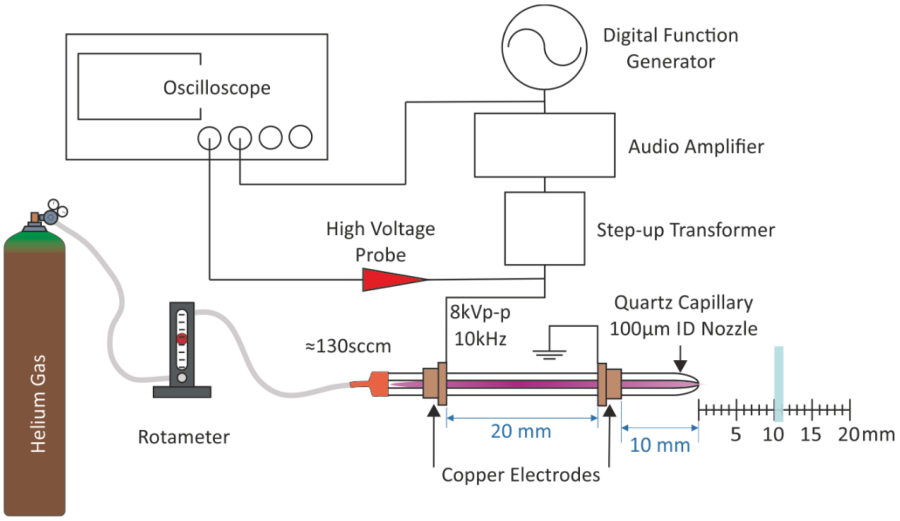

Figure 2.10 Schematic of plasma setup for 100µm ID jet preliminary study. The plasma parameters were: 8kVpeak-peak, 10kHz, flow rates of ≈130sccm and sample-nozzle distance 10mm.

Following treatment samples were either placed in Petri dishes and sealed with parafilm (Fisher Scientific, UK), or samples were placed in individual glass vessels containing water. Untreated samples were stored under the same conditions.

2.2.1.3.1.3 Water Contact Angle

Contact angle profiles were analysed from treated and untreated polystyrene, stored both in air and water for various time periods. Prior to analysis samples stored in water were dried under pressurised N_2 flow. Samples were analysed on the day of treatment, one set of samples was briefly dipped in water and dried at this time point. Contact angle profiles were also measured at the following time points: 0 days, 1 day, 4 days, 7 days, 2 weeks, 4 weeks, 8 weeks and 1 year. The DSA100m "micro-drop" contact angle system (section 2.3.1.3) was used. The spatial resolution between each drop was 500µm. Each condition was measured in triplicate.

2.2.1.3.1.4 Cell Culture

The effect of sample storage in air and water for various periods of time was investigated by cell culture. N/N1003A rabbit LECs were seeded onto samples at $1x10^4$cells/cm^2.

Samples were fixed with NBF at 1hr, 4hrs and 24hrs post-seeding and stained with PI (section 2.4.2.2) and phalloidin (section 2.4.2.4) to examine the effect of storage on cell attachment. Samples were mounted inverted on glass slides and marked coverslips were mounted on top of adhered cells inside TCPS wells. Micrographs were taken with the Zeiss Axiovert 200. Triplicate samples were used for each experimental condition. The sample storage times and media are detailed in Table 2.1 below.

Table 2.1 details the storage times and media of aged samples investigated by cell culture. It also includes designations which will be used later in this thesis. TCPS served as a control.

Treatment	Storage Media	Storage Time	Designation
Tissue Culture Treatment	NA	NA	TCPS
Treated	Air	0 days	Treated-Air-0d
Treated	Air	4 days	Treated-Air-4d
Treated	Air	1 week	Treated-Air-1w
Treated	Air	1 month	Treated-Air-1m
Treated	Deionised Water	4 days	Treated-H_2O-4d
Treated	Deionised Water	1 week	Treated-H_2O-1w
Treated	Deionised Water	1 month	Treated-H_2O-1m
Untreated	Air	0 days	Untreated-Air-0d
Untreated	Air	4 days	Untreated-Air-4d
Untreated	Air	1 week	Untreated-Air-1w
Untreated	Air	1 month	Untreated-Air-1m
Untreated	Deionised Water	4 days	Untreated-H_2O-4d
Untreated	Deionised Water	1 week	Untreated-H_2O-1w
Untreated	Deionised Water	1 month	Untreated-H_2O-1m

2.2.1.3.2 Preliminary Study of Flow Rate and Sample-Nozzle Distance

A preliminary study to examine the effect of flow rate and sample-nozzle distance was investigated to determine which parameters would be best suited for further examination.

2.2.1.3.2.1 Plasma jet

The 100µm capillary and electrode positions (section 2.2.1.3.1.2) were used. Flow rates were set by the manual rotameter. A schematic of the plasma setup can be n in Figure 2.11. The following plasma conditions were used:

- $8kV_{peak\text{-}peak}$
- 22sccm (low), 150sccm (medium) and 300sccm (high) flow rates
- 20s treatment time
- 1mm, 5mm and 10mm sample-nozzle distance

The various experimental conditions are

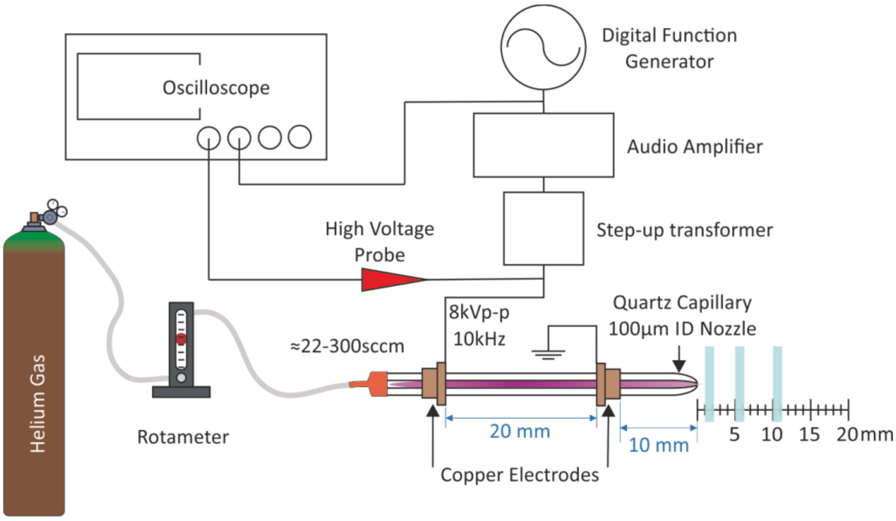

Figure 2.11 Schematic of plasma setup for 100µm ID jet preliminary study. The plasma parameters were: $8kV_{peak\text{-}peak}$, 10kHz, flow rates of ≈22-300sccm and sample-nozzle distances of 1, 5 and 10mm.

Table 2.2 outlines various experiment parameters, parameter designations and methods of analysis for the preliminary 100µm ID jet study.

Parameter	**Flow Rate**	**Sample-Nozzle Distance**	**Analysis**	**Designation**
Untreated Polystyrene	NA	NA	Contact Angle	UT
Low flow – 1mm	≈22scmm	1mm	Contact Angle	L1
Low flow – 5mm	≈22scmm	5mm	Contact Angle	L5
Low flow – 10mm	≈22scmm	10mm	Contact Angle	L10
Medium flow – 1mm	≈150scmm	1mm	Contact Angle	M1
Medium flow – 5mm	≈150scmm	5mm	Contact Angle	M5
Medium flow – 10mm	≈150scmm	10mm	Contact Angle	M10
High – 1mm	≈300scmm	1mm	Contact Angle	H1
High – 5mm	≈300scmm	5mm	Contact Angle	H5
High – 10mm	≈300scmm	10mm	Contact Angle	H10

2.2.1.3.3 Investigation of the Effect of Flow Rate and Sample-Nozzle Distance

Following the preliminary examination (section 2.2.1.3.1) further investigation was conducted. Digital mass flow meter and controller allowed for accurate control of lower flow rates required for the 100µm ID nozzle.

2.2.1.3.3.1 Plasma Jet

The 100µm capillary and electrode positions (section 2.2.1.3.2.1) were used. In these experiments flow rates were set by the digital mass flow meter and controller and are therefore accurate. Schematic of the plasma setup can be n in Figure 2.12. The plasma system has previously been described by Doherty et al. (2013)[168]. The following plasma conditions were used:

- 8kV$_{peak\text{-}peak}$
- 30sccm (low) and 150sccm (high) flow rates
- 20s treatment time
- 1mm and 10mm sample-nozzle distance

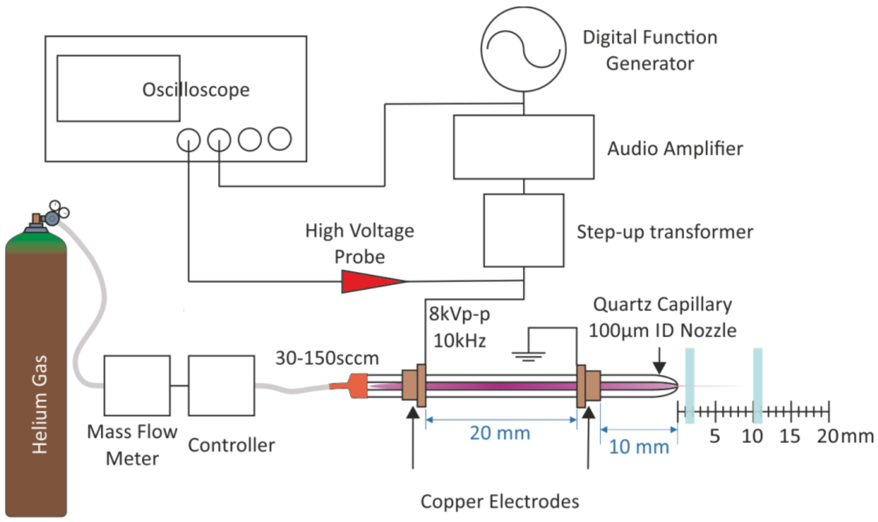

Figure 2.12 Schematic of plasma system setup for flow rate-distance study. Plasma jet parameters were: 8kV$_{peak\text{-}peak}$, 10kHz, 30-150sccm, 20s treatment, 1-10mm sample-nozzle distance.

Table 2.3 lists the various parameters, parameter designations and which methods of analysis were used within the study to determine the effects of flow rate and distance on treatment size.

Parameter	Flow Rate	Sample-Nozzle Distance	Analysis	Designation
Tissue Culture Polystyrene	NA	NA	Contact Angle, Cell Culture, ELISA, Multiplex	TCPS
Untreated	NA	NA	Contact Angle, AFM, XPS, Cell Culture, ELISA, Multiplex	UT
Low flow – 1mm	Low	1mm	Contact Angle, AFM, XPS, Cell Culture, ELISA, Multiplex	L1
Low flow – 10mm	Low	10mm	Contact Angle, AFM, Cell Culture, ELISA, Multiplex	L10
High flow – 1mm	High	1mm	Contact Angle, AFM, Cell Culture, ELISA, Multiplex	H1
High flow – 10mm	High	10mm	Contact Angle, AFM, Cell Culture, ELISA, Multiplex	H10

2.2.1.4 Microplasma Jet Treatment of Poly(Methyl Methacrylate)

To investigate the possible use of a microplasma jet for modification of IOLs PMMA was used as a model acrylic material. 10x10mm PMMA (1mm thick) and PS samples (1.2mm thick) were treated with a plasma jet at 1mm with a low flow rate from a 100µm ID nozzle. Previous testing confirmed that these conditions created the smallest treatment area.

2.2.1.4.1 Plasma Jet

The 100µm ID quartz tube outlined in section 2.2.1.3.2.1 was used. The forward grounded electrode was positioned ≈10mm from the tip. A powered electrode followed; the electrode gap separation was ≈20mm. Flow rate was controlled by the digital flow meter and controller. All treated samples were positioned 1mm from the nozzle. A schematic of the plasma setup can be n in Figure 2.13. The plasma parameters were as follows:

- 8kV$_{\text{peak-peak}}$
- 30sccm
- 20s treatment time
- 1mm sample-nozzle distance

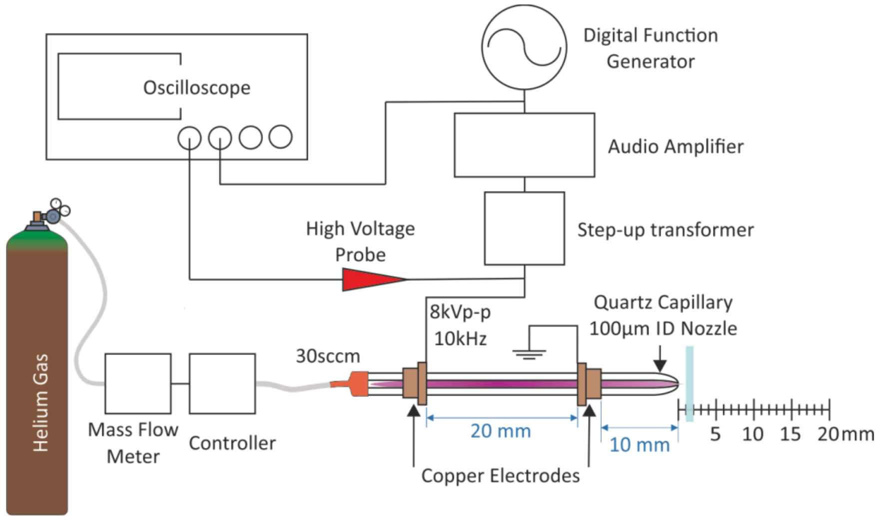

Figure 2.13 Schematic of plasma system setup used to treat PMMA and PS samples. Plasma jet parameters were: 8kVpeak-peak, 10kHz, 30scmm flow rate, 20s treatment time and 1mm sample-nozzle distance.

Table 2.4 lists the various substrates, including designations assigned to them, and analysis techniques used throughout the PMMA study.

Parameter	Analysis	Designation
Tissue Culture Polystyrene	Cell Culture, ELISA, Multiplex	TCPS
Untreated Poly(methyl methacrylate)	Contact Angle, AFM, XPS, Cell Culture, ELISA, Multiplex	UT-PMMA
Untreated Polystyrene	Contact Angle, AFM, XPS, Cell Culture, ELISA, Multiplex	UT-PS
Treated Poly(methyl methacrylate)	Contact Angle, AFM, XPS, Cell Culture, ELISA, Multiplex	T-PMMA
Treated Polystyrene	Contact Angle, AFM, XPS, Cell Culture, ELISA, Multiplex	T-PS

2.2.1.5 Plasma Polymerisation - Pre-Discharge Mixing

Various plasma jet set-ups were used during plasma polymerisation. Plasma polymerisation is the formation of a polymer thin film on a surface from monomers, using a plasma source to polymerise these monomers. In this work monomers were stored in a round-bottom flask; helium was passed through the round-bottom flask to carry a suspension of monomers to the plasma discharge recharge region between the electrodes. The flow of monomers mixes with a main helium flow, which typically has a flow rate an order of magnitude higher than the monomer containing flow. In the initial preliminary work the flow of monomers mixed with the main helium flow rate prior to reaching the plasma discharge region, this has been termed “pre-discharge mixing”.

2.2.1.5.1 Plasma System

The plasma was generated in a quartz capillary of 1mm ID and 3mm OD with the grounded electrode downstream. Electrodes were separated by ~12mm. Approximately 10ml of monomer solution, allylamine (Allyl, Sigma-Aldrich, UK) or heptylamine (Heptyl, Sigma-Aldrich, UK), was placed in a round-bottom flask. Helium gas, at a flow rate of ≈20sccm, was passed through this flask following which it mixed with a main helium gas stream with a flow rate of ≈500sccm. Manual rotameters were used in this work. Rotameters and electrode power supply were as previously described (section 2.2.1). The mixed helium flows then passed into the quartz capillary and the plasma discharge region. Some samples were pre-treated for 3mins with just a ≈500sccm main helium flow rate to produce a functionalised surface, and subsequently treated for 5s with helium:monomer mixture. A schematic of the plasma setup is detailed in Figure 2.14. The following plasma conditions were used:

- $6kV_{peak\text{-}peak}$
- ≈500sccm main helium flow rate; ≈20sccm helium:monomer mixture flow rate
- 3mins Helium treatment time; 5s helium:monomer treatment time
- 5mm sample-nozzle distance

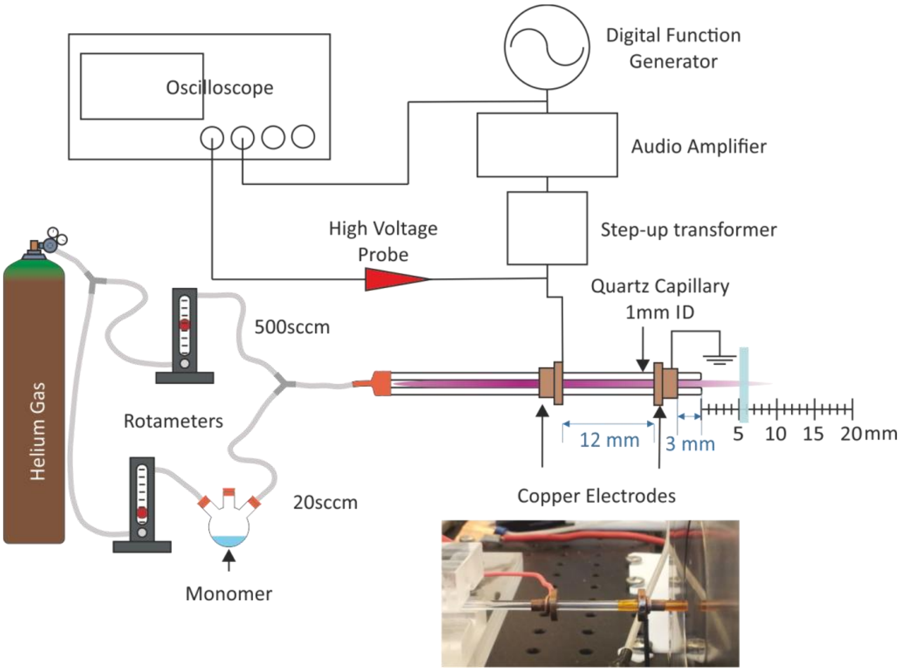

Figure 2.14 Schematic of plasma system setup used for preliminary plasma polymerisation experiment. Allylamine and heptylamine monomers were used for polymerisation. Main helium flow and helium:monomer flows were mixed prior to reaching the plasma discharge region. Plasma jet parameters were: 6kVpeak-peak, 10kHz, 500sccm main helium flow rate; 20sccm helium:monomer flow rate, 3min helium only pre-treatment time, 5s helium:monomer treatment time and 5mm sample-nozzle distance.

Table 2.5 lists the various conditions, including designations assigned to them, and analysis techniques used throughout the preliminary plasma polymerisation (pre-discharge mixing) study.

Condition	**Analysis**	**Designation**
Untreated Polystyrene	Contact angle, XPS	UT-PS
Helium Treated Polystyrene	Contact Angle, XPS	He Treated PS
Allylamine on Untreated Polystyrene	Contact Angle, XPS	Allyl on UT-PS
Allylamine on Helium Pre-Treated Polystyrene	Contact Angle, XPS	Allyl on He Treated PS
Heptylamine on Untreated Polystyrene	Contact Angle, XPS	Heptyl on UT-PS
Heptylamine on Helium Pre-Treated Polystyrene	Contact Angle, XPS	Heptyl on He Treated PS

2.2.1.6 Plasma Polymerisation - Pre-Discharge Mixing (Chamber)

Following the previous study polymerisation was attempted in a helium atmosphere to exclude oxygen. A small chamber which contained a gas inlet and outlet was constructed. The helium was flowed into the chamber and the pressure was maintained around 1 atmosphere. Helium was allowed to flow into the chamber for 10mins prior to treatment to evacuate the oxygen. The chamber was constructed by Mr Alan Roby of the Department of Electrical Engineering and Electronics in the University of Liverpool.

2.2.1.6.1 Plasma System

The plasma system design was similar to the previous work (section 2.2.1.5.1) however there were some differences. Only a forward powered electrode was used and samples were treated in a chamber filled with helium. Samples were inset in a sample holder which could be removed from the side of the chamber. A barrier was positioned between the sample and the jet whilst the chamber was allowed to fill with helium for 10mins prior to treatment. At the time of treatment the barrier was slid out of the path of the plasma jet.

Samples were treated for 20s. Samples were placed ~10mm from the nozzle. Samples were also treated without the ignition of the plasma jet to investigate if monomers were deposited on the surface from the gas flow alone. The monomer flow was mixed with the main helium flow pre-discharge similar to the previous work. A schematic of the plasma setup is detailed in Figure 2.15. The following plasma conditions were used:

- 6kV$_{\text{peak-peak}}$
- ≈500sccm main helium flow rate; ≈20sccm helium:monomer mixture flow rate
- 20s helium:monomer treatment time
- 5mm sample-nozzle distance

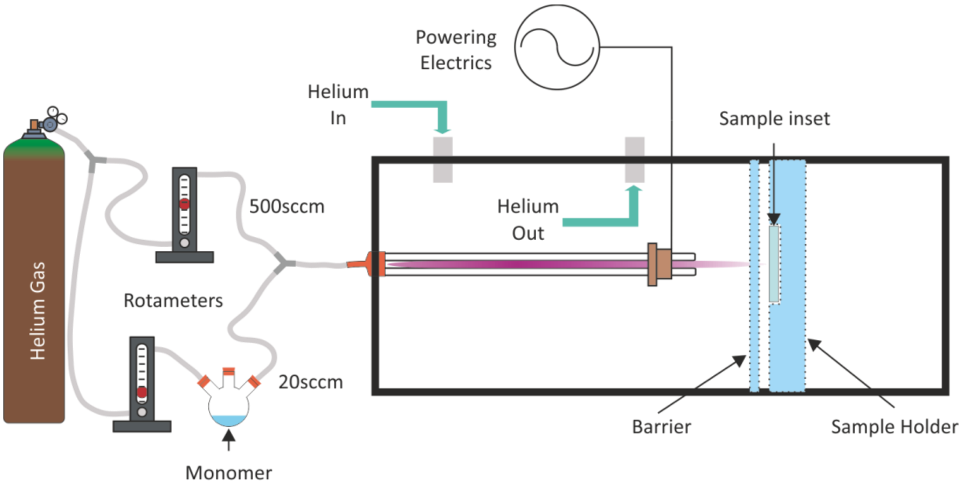

Figure 2.15 Schematic of plasma system setup used for preliminary plasma polymerisation experiment. Allylamine and heptylamine monomers were used for polymerisation. Main helium flow and helium:monomer flows were mixed prior to reaching the plasma discharge region. Samples were treated in a chamber containing a helium atmosphere. Plasma jet parameters were: 6kVpeak-peak, 10kHz, 500sccm main helium flow rate; 20sccm helium:monomer flow rate, 20s treatment time and 10mm sample-nozzle distance.

Table 2.6 lists the various conditions, including designations assigned to them, and analysis techniques used throughout the preliminary plasma polymerisation (pre-discharge mixing - chamber) study.

Condition	**Analysis**	**Designation**
Tissue Culture Polystyrene	Cell Culture	TCPS
Untreated Polystyrene	Contact angle, XPS, Cell Culture	UT-PS
Allylamine with Plasma Ignition	Contact Angle, XPS, Cell Culture	Allyl with plasma
Allylamine without Plasma Ignition	Contact Angle, Cell Culture	Allyl without plasma
Heptylamine with Plasma Ignition	Contact Angle, XPS, Cell Culture	Heptyl with plasma
Heptylamine without Plasma Ignition	Contact Angle, Cell Culture	Heptyl without plasma

2.2.1.7 Plasma Polymerisation - Post-Discharge Mixing

Following previous work a new approach was taken to polymerisation. The addition of heptylamine directly to an active plasma discharge was investigated. This has been termed "post-discharge mixing".

2.2.1.7.1 Plasma System

A new Y-shaped quartz capillary was made by melting one 2.4mm ID, 4mm OD capillary onto another an angle of ≈30°, approximately 25mm back from the nozzle the plasma was to exit. A single powered electrode was approximately 40mm back from the capillary nozzle. Helium was flowed, at a rate of 500sccm, into the primary capillary and was dissociated into plasma near the electrode. This flow carried the excited species along the capillary towards the nozzle. Downstream from the electrode a mixture of helium:heptylamine was added to the plasma at a velocity of 20sccm. Rotameters and electrode power supply were as previously described (section 0). The plasma set-up has also been described by Oh and Bradley (2013)[189]. PS squares of 10x10mm, 1.2mm thick were placed 5mm from the nozzle and treated for 10 minutes with helium alone or helium:heptylamine mixture (Figure 2.16). Untreated polystyrene served as a control. A list of plasma parameters are as follows:

- 8kVp-p
- 500sccm He and 20sccm He:heptylamine mixture
- 10min treatment time
- 5mm sample-nozzle distance

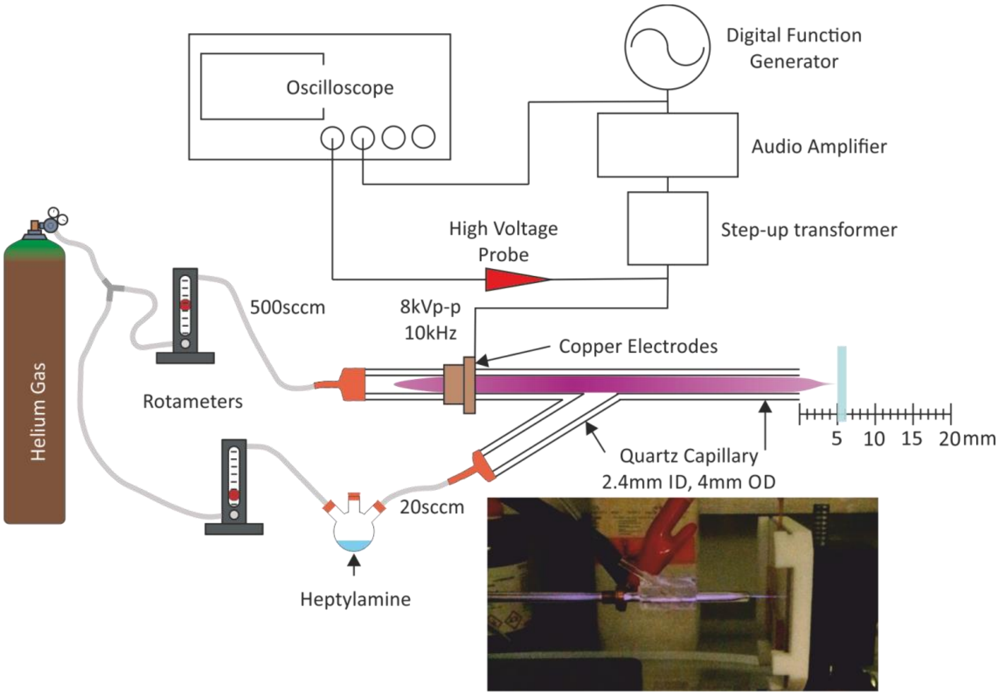

Figure 2.16 Schematic of plasma system setup, with photograph inset, used to add heptylamine to an active plasma. The Y-configuration capillary allowed addition of a He:heptylamine mixture downstream from the powered electrode. Plasma jet parameters were: 8kVpeak-peak, 10kHz, 500scmm primary He flow and 20sccm He:heptylamine mixture, 10min treatment time and 5mm sample-nozzle distance.

Table 2.7 outlines the treatment parameters, analysis techniques used and parameter designations.

Parameter	**Analysis**	**Designation**
Tissue Culture Polystyrene	Cell Culture, ELISA, Multiplex	TCPS
Untreated Polystyrene	Contact Angle, XPS, AFM, Cell Culture, ELISA, Multiplex	UT
He Treated Polystyrene	Contact Angle, XPS, AFM, Cell Culture, ELISA, Multiplex	He
He:Heptylamine Mixture Treated Polystyrene	Contact Angle, XPS, AFM, Cell Culture, ELISA, Multiplex	He:Heptyl

2.2.1.8 Treatment of Polystyrene with a Pin Plasma System

An alternative microplasma source, a “pin plasma”, was also investigated. This plasma system generated a coronal plasma discharge at the point of a 200µm diameter tungsten wire. This small plasma source was used to modify 10x10mm, 1.2mm thick, PS surfaces which were investigated by contact angle analysis, AFM and cell culture. An initial contact angle experiment was conducted to investigate the effect of different treatment parameters on polystyrene. Following this fewer conditions were chosen for further investigation by cell culture and AFM analysis.

2.2.1.8.1 Pin Plasma

A 200µm diameter tungsten wire was passed through a 300µm bore in a ceramic tube with an OD of 4mm. The tungsten wire protruded approximately 5mm from the base of the ceramic tube. The tungsten wire was powered by a purpose built high voltage generator, which was driven by a signal generator (TG2000, AIM-TTI Instruments, UK) set to the + square wave function. A grounded copper ring electrode was positioned at the base of the ceramic tube approximately 3mm above the tip of the tungsten wire (Figure 2.17). Samples were position ≈1.3mm from the tip of the tungsten wire and treated at 15-20kHz and 13-17kV$_{peak\text{-}peak}$; these values represent the lowest levels at which a stable discharge could be maintained and the upper limit of the equipment. The plasma was ignited in air at atmospheric pressure and unlike the plasma jets there is no gas flow. The pin plasma system was constructed by Mr. Alan Roby and operated by Dr. Andrew Bowfield of Department of Electrical Engineering and Electronics, University of Liverpool [192]. The following plasma conditions were used:

- 15-20kHz
- 13-17kV$_{peak\text{-}peak}$
- ≈1.3mm sample-tip distance
- 20-40s treatment times

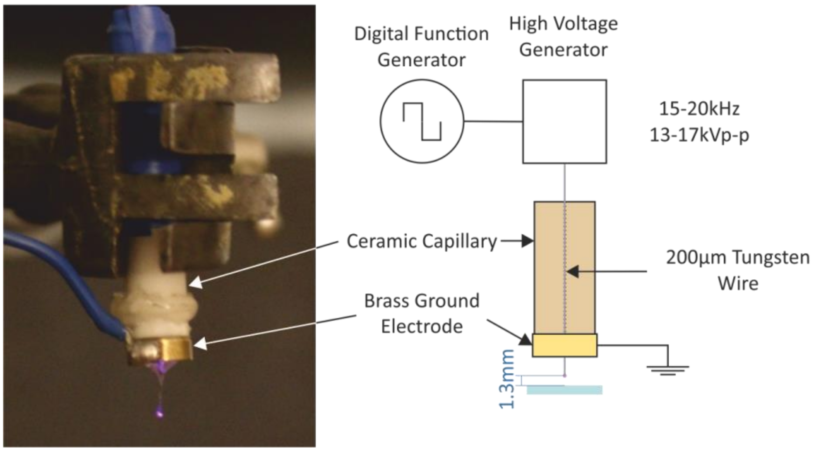

Figure 2.17 Annotated photograph of the pin plasma system with a schematic representation. A corona discharge was created at the end of a tungsten wire which passed through ceramic dielectric barrier tube. The wire was powered by digital function generator in + square wave mode which drove a high voltage generator.

2.2.1.8.2 Initial Water Contact Angle Study

Using the DSA100m "micro-drop" contact angle system (section 2.3.1.3) water contact angle profiles were analysed on various combinations of treatment parameters outlined in Table 2.8 below. The spatial resolution between each drop was 500µm, 3 samples for each experimental condition were used.

Table 2.8 details the various parameters used in the initial pin plasma contact angle study including treatment conditions and designations.

Parameter	Frequency	Voltage	Treatment Time	Designation
Tissue Culture Polystyrene	NA	NA	NA	TCPS
Untreated Polystyrene	NA	NA	NA	UT
15kHz – 13kVp-p -20s Treated Polystyrene	15kHz	13kVp-p	20s	15kHz–13kVp-p-20s
15kHz – 13kVp-p – 40s Treated Polystyrene	15kHz	13kVp-p	40s	15kHz–13kVp-p-40s
15kHz – 17kVp-p – 20s Treated Polystyrene	15kHz	13kVp-p	20s	15kHz–17kVp-p-20s
15kHz – 17kVp-p – 40s Treated Polystyrene	15kHz	13kVp-p	40s	15kHz–17kVp-p-40s
20kHz – 13kVp-p – 20s Treated Polystyrene	20kHz	17kVp-p	20s	20kHz–13kVp-p-20s
20kHz – 13kVp-p – 40s Treated Polystyrene	20kHz	17kVp-p	40s	20kHz–13kVp-p-40s
20kHz – 17kVp-p – 20s Treated Polystyrene	20kHz	17kVp-p	20s	20kHz–17kVp-p-20s
20kHz – 17kVp-p – 40s Treated Polystyrene	20kHz	17kVp-p	40s	20kHz–17kVp-p-40s

2.2.1.8.3 Further Investigation

Following initial contact angle analysis it was determined that 20 seconds treatment time was sufficient therefore samples in the following work were treated for 20 seconds.

Table 2.9 details the various parameters used in the follow-up pin plasma experiments, treatment conditions, analysis methods and designations.

Parameter	**Frequency**	**Voltage**	**Analysis**	**Designation**
Tissue Culture Polystyrene	NA	NA	Cell Culture	TCPS
Untreated Polystyrene	NA	NA	Contact Angle, AFM, Cell Culture	UT
15kHz – 13kVp-p Treated Polystyrene	15kHz	13kVp-p	Contact Angle, AFM, Cell Culture	15kHz – 13kVp-p
15kHz – 17kVp-p Treated Polystyrene	15kHz	13kVp-p	Contact Angle, Cell Culture	15kHz – 17kVp-p
20kHz – 13kVp-p Treated Polystyrene	20kHz	17kVp-p	Contact Angle, Cell Culture	20kHz – 13kVp-p
20kHz – 17kVp-p Treated Polystyrene	20kHz	17kVp-p	Contact Angle, AFM, Cell Culture	20kHz – 17kVp-p

2.3 Physical and Chemical Analysis

2.3.1 Contact Angle

Contact angle measurements were taken with two different systems throughout the course of this research. These systems and the methods will be detailed in the following sections.

2.3.1.1 CAM100 Instrument

The CAM100 contact angle meter (KSV Instruments Ltd., Finland) was used as a quick method to determine if a sample had been treated. This system was operated manually and a short video was taken using a CCD camera controlled by CAM100 software (KSV Instruments Ltd., Finland), 10 frames at 1 frame per second (fps) were captured. The centre of a sample was positioned approximately beneath the needle. A ≈0.3µl drop of deionised water was forced from the needle tip. The sample stage was then raised until the drop contacted the sample. When the stage was lowered the drop remained on the sample surface. After a baseline was manually set the contact angle was automatically calculated by the CAM100 software using a tangent method. The mean contact angle for each set of 10 frames was calculated.

2.3.1.2 DSA100 Instrument

Initial spatially resolved contact angle was performed using the DSA100 drop shape analysis system (Krüss GmBH, Germany). In this system 0.2µl drops of deionised water were dispensed from a needle and syringe via DSA3 software (Krüss GmBH, Germany). Water drops were placed across the horizontal axis of a treated sample at a resolution of 2.5mm using a micro-step x-y stage controlled by the DSA3 software. 10 frames at 1fps were captured using a CCD camera controlled by the DSA3 software. The baseline was set manually and images were analysed by the DSA3 software using the circle method. The mean contact angle for each set of 10 frames was calculated.

2.3.1.3 DSA100m Instrument Modification

DSA100m “micro-drop” modification to the Krüss DSA100 was also conducted. This modification included additional lenses on the camera to improve magnification, an LED illuminator which provided an illumination source closer to the sample and piezoelectric dosing unit capable of dispensing drops in the picolitre range [220]. The volume of deionised water dispensed was controlled by altering the signal voltage and pulse time sent to the piezoelectric dosing unit; 80V and 200µs were used for these experiments. Drops were placed upon samples with a spatial resolution of 250µm or 500µm depending on experiment. A video was recorded at 25fps and began recording as soon as the drop was dispensed. The first frame containing a steady drop on the sample surface was measured using the circle method. Subsequent frames of each video were not measured as water drops very quickly evaporated, altering the contact angle.

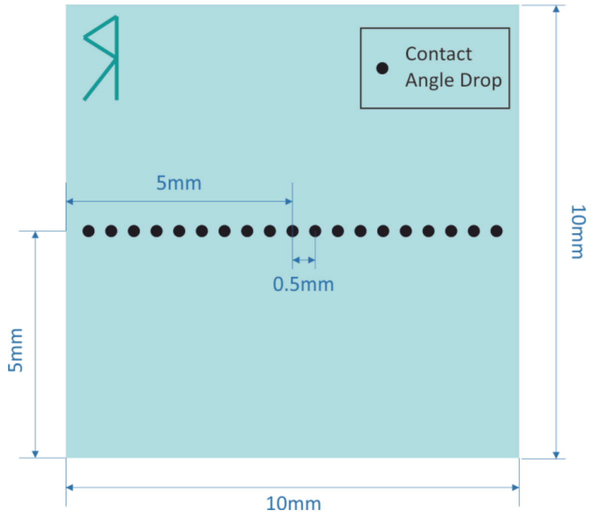

Figure 2.18 Illustration depicting an example of drop positions for a contact angle profile with a 0.5mm resolution on a 10x10mm sample.

Contact angle profiles were taken across the horizontal axis of samples through the centre of the treatment (example in Figure 2.18). As the 1.2mm thick PS was cut by hand samples were not always exactly 10x10mm. Therefore, the focus of the plasma jet was aligned to be centred 5mm from the bottom of the sample, and 5mm in from the left edge of the sample. The mean contact angle corresponding to each position along the profile was calculated. 2-D contact angle maps were taken by placing drops in a grid pattern with spatial resolution of 250µm or 500µm between points (example in Figure 2.19).

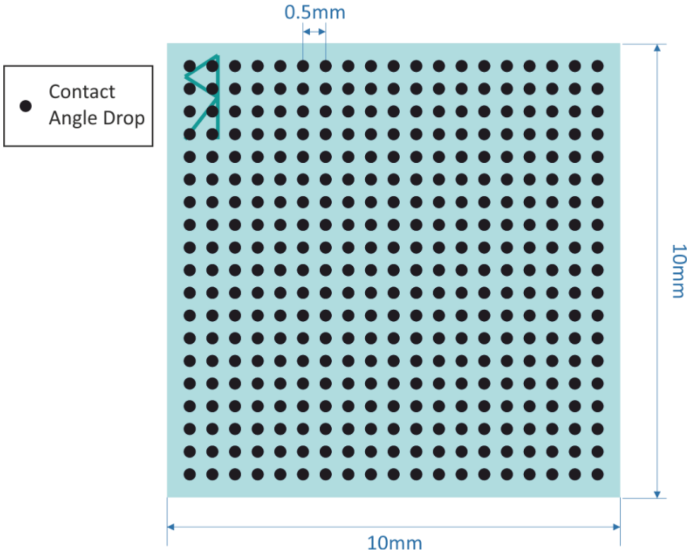

Figure 2.19 Illustration of the drop positions for a 2-D contact angle map. Spatial resolution of drops was 500µm.

2.3.2 X-Ray Photoelectron Spectroscopy (XPS)

The spectrometer used in this study was designed in Liverpool and constructed in Manchester by KSV, UK. The instrument used for these studies has been described previously[221]. The x-ray source was a "multicrystal Al Kα monochromator on a 0.7m Rowland circle which subtends a solid angle of ~0.1 sterradian at the specimen thus providing high sensitivity and high resolution (< 0.5eV) XPS capability at 1486.6eV" [221]. The sample holder accommodated relatively large sample sizes (12×12 mm^2) and was mounted on an *x-y-z* stage which also had the capability of being rotated through 360°. The x-ray 'spot' focused on a sample surface was ≈1.5×7mm^2 in size.

Single broad scan or high resolution spectra were taken in the centre of the sample. For spatially resolved XPS samples were translated through the x-ray 'spot' along the horizontal axes of samples, and broad scans were taken every mm. The edge of the sample was determined by the presence of spectra from the sample holder. Broad scan and high resolution spectra were acquired at pass energies of 100eV and 50eV respectively. The C1s of all spectra were calibrated to a binding energy of 285eV. All peak components were fitted with a 70% Guassian: 30% Lorentzian function and the position restricted by ±0.5eV. Full width at half maximum (FWHM) was limited between 0.5-2eV.

2.3.3 Atomic Force Microscopy (AFM)

A Multimode 8 AFM with NanoScope V controller was used in normal tapping mode with a silicon cantilever of spring constant 40N/m. A 500 x500nm^2 region was scanned at a rate of 1Hz with 512 samples/line with the NanoScope software (ver. 8.10). Using the NanoScope analysis software (ver. 1.4). scans were subjected to 0th order plane fit, to remove centre data and 0th and 1st order flattening, to centre data and remove tilt. The mean roughness (R_a) and root mean square roughness (R_q) for each parameter were averaged from 4 scans in the centre of the samples. All equipment, probes and software were supplied by Bruker, UK.

2.4 In Vitro Studies

2.4.1 Cell Culture

All cell culture was conducted within a class II microbiology laminar flow cabinet. Prior to use the cabinet was opened and switched on to allow the air to be circulated, surfaces were cleaned with 1% virkon (DuPont, UK) and 70% ethanol (University of Liverpool, Chemistry Department, UK) at the beginning and end of each work session. All items were sprayed with 70% ethanol immediately before being placed in the cabinet. All cell culture flasks and well plates were made from polystyrene (PS) and treated with proprietary CELLSTAR® treatment (Griener Bio-One, UK) for adherent cells.

2.4.1.1 Cell Lines and Medium

Three cell lines were used throughout this study (table 1). Cell lines were used in this study as the provide a greater reproducibility compared to primary cells, are readily available and do not require donors and can allow larger samples sets compared in ex vivo models. Retinal pigmented epithelial cell line (ARPE-19) [213](American Type Culture Collection (ATCC), USA), obtained from Dr. Victoria Kearns, University of Liverpool, UK; was used as a preliminary cell model prior to the obtainment of lens epithelial cells. ARPE-19 cells were maintained with 1:1 (vol/vol) mixture Dulbeccco's Modified Eagles's Medium (DMEM, Sigma-Aldrich, UK) and Nutrient Mixture F-12 Ham (F-12, Sigma-Aldrich, UK) supplemented with 2mM L-glutamine (L-Glut), 100U/ml penicillin G, 100µg/ml streptomycin, 2.5µg/ml amphotericin B (all from Sigma-Aldrich, UK) and 10% foetal calf serum (FCS, Biosera, UK). A rabbit lens epithelial cell (LEC) line, N/N1003A[214], was kindly donated by Prof. John R.

Reddan of Oakland University, USA. N/N1003A rabbit LEC line was maintained using minimum essential medium eagle (MEM, Sigma-Aldrich, UK) supplemented with 2mM L-glut, 8% rabbit serum (RS, Sigma-Aldrich, UK). A human LEC line, B3[215], was used as a model for human LECs once obtained. The B3 LEC line (ATCC, USA) was kindly donated by Prof. Barbara Pierscionek of University of Ulster, Northern Ireland. Human B3 LECs were maintained with MEM supplemented with 2mM L-glut and 10% FCS.

Table 2.10 details cell lines used during this study, the people who provided the cells and culture medium in which they were grown.

Cell Type	Code	Origin	Culture Medium
Retinal Pigmented Epithelium	ARPE-19	Provided by Dr. Victoria Kearns, University of Liverpool, UK - originally from ATCC, USA	DMEM:F-12 (1:1) + 10% FCS, 2mM L-Glut, 100U/ml penicillin G, 100µg/ml streptomycin, 2.5µg/ml amphotericin
Rabbit LEC	N/N1003A	Provided by Prof. John Reddan, Oakland University, USA	MEM + 8% RS + 2mM L-Glut
Human LEC	B3	Provided by Prof. Barbara Pierscionek, University of Ulster, UK - originally from ATCC, USA	MEM + 10% FCS + 2mM L-Glut

All cells were incubated at 37°C and 5% CO_2 and fed every 3-4 days. During feeding approximately ⅔ of the medium was removed from the vessel and replaced with fresh medium. Cells were passaged, frozen or plated for experiments following the protocols outlined below.

2.4.1.2 Passaging Cells

Cells were passaged at approximately ~70% confluency; to do this the medium was removed and discarded. Cells were washed with calcium and magnesium free phosphate buffered saline (PBS, Dulbecco A, Oxoid, UK) to remove non-adherent and dead cells. A solution of 0.5mg/ml porcine trypsin and 0.2mg/ml EDTA (trypsin/EDTA 10X, Sigma-Aldrich, UK) in PBS was applied to the remaining adherent cells. These were incubated at 37°C with 5% CO_2 for 2-4 minutes until most cells had detached from the surface of the vessel. An equal volume of serum containing medium was added to the cell suspension to inactivate the trypsin. This solution was centrifuged (SIGMA 3K15, Phillip Harris Scientific) at ~180xg for 5 minutes then the supernatant was discarded. Following these steps cells were passaged, frozen (section 2.4.1.3) or plated for experiments (section 2.4.1.4). To passage cells were resuspended in fresh medium and split into new vessels at 1:5 ratio, this required cells to be split every 6-7 days. No cell line was used after 45 passages.

2.4.1.3 Freezing and Thawing of Cells

A stock of cryopreserved cells was created to maintain lower passages and a reserve of cells for use at later dates. Cells were detached from culture vessels using trypsin/EDTA solution as outlined above (section 2.4.1.2). Following centrifugation the supernatant was discarded and cells were resuspended in 900µl of medium containing 20% serum. Specific medium and serum used depended upon the cell line (section 2.4.1.1). The 900µl cell suspension was transferred to a labelled cyrovial and 100µl dimethyl sulphoxide was added as a cyroprotectant. Cyrovials were placed in a “Mr. Frosty” freezing container (Fisher Scientific, UK) and subsequently placed in a -80°C freezer for 4hrs to allow a controlled decrease in temperature. Cyrovials were moved to liquid nitrogen Dewars (-196°) for long term storage.

To thaw cells a cyrovial was removed from liquid nitrogen and defrosted in a water bath at 37°C for 1-2 minutes. The defrosted cell suspension was quickly transferred to a centrifuge tube containing 10ml warmed medium specific to the cell line, and centrifuged at 180g for 5 minutes. The supernatant was discarded and cells were resuspended in fresh medium. The cell suspension was transferred to a new culture vessel and placed in the incubator at 37°C with 5% CO_2.

2.4.1.4 Seeding Cells

During experiments cells were seeded at a known density expressed as cells per cm^2. To achieve a known cell density cells were counted on a haemocytometer. A glass coverslip was fixed over the gridded counting area of the haemocytometer. Following trypsinisation and resuspension in culture medium, 10μL of cell suspension was pipetted onto the haemocytometer. Cells were counted in each quadrant of the grid, the mean of which represented the number of cells $x10^4$/ml of cell suspension. A dilution factor was calculated by dividing the number of cells/ml by the desired cells/cm^2. Using the area of the substrate, the required the volume of cell suspension was calculated. The remaining required volume of medium was added to the cell suspension and mixed well prior to ding, this volume depended upon sample size and/or working volume of well. 90μl/cm^2 of cell suspension was pipetted across the surface of 10x10mm coverslips which were incubated for 2 hours to allow cells to settle and adhere (Figure 2.20). After 2 hours more media was added to achieve the working volume of the well (typically 1ml for a 24 well plate). To tissue culture polystyrene (TCPS) wells, cells suspended in the working volume of the well were pipetted directly into the wells, and then placed in the incubator. Prior to cell seeding all samples were sterilised by UV treatment using CL-1000 crosslinker (UVP) for 5 minutes at 1500mJ/cm^2. Cells were seeded at $1x10^4$cells/cm^2, unless otherwise stated.

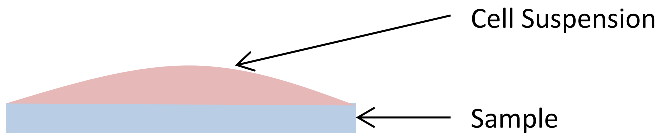

Figure 2.20 Schematic of cell suspension pipetted onto the surface of polymer samples. Following 2hrs incubation the culture well was filled with the working volume of medium.

2.4.2 Immunocytochemistry

Various immunocytochemical stains were used throughout this thesis. The protocols for these are outlined in the sections below (2.4.2.1 - 2.4.2.5). After staining PS or PMMA coverslip samples were either mounted inverted onto glass slides using VECTASHIELD® HardSet™ fluorescent mounting medium containing 4',6-diamidino-2-phenylindole (DAPI) dihydrochloride (Vector Laboratories, UK), mounted with a mounting medium not containing DAPI, or wells were filled with PBS. For TCPS well samples one of the aforementioned mounting media was placed in the wells, followed by a coverslip (Agar Scientific, UK) which was marked at specific positions with a diamond tip pen to create a counting grid (section 2.4.3).

2.4.2.1 Methylene Blue

Cells were stained with 0.05% (w/v) methylene blue (Sigma-Aldrich, UK) to allow visualisation of cell growth without a microscope using the following protocol:

1. Culture medium was removed.
2. Cells were washed 3 times with PBS.
3. Cells were fixed with absolute methanol (Chemistry Department, University of Liverpool, UK) for 5 minutes.
4. Cells were washed 3 times with PBS.
5. Cells were incubated with methylene blue for ~5 minutes.
6. Cells were washed with water until the water ran clear.

2.4.2.2 Propidium Iodide

Propidium Iodine (PI) (Sigma-Aldrich, UK) intercalates between the helices of DNA and causes cell nuclei to fluoresce red (excitation 491-496nm: emission 636-642nm). A PI working solution of 10% ribonuclease (RNase, Sigma-Aldrich, UK), 89.5% PBS and 0.5% PI was used. The final PI concentration was 500µg/ml. The following protocol was used to stain nuclei with PI:

1. Culture medium was removed.
2. Cells were washed 3 times with PBS.
3. Cells were fixed with 10% neutral buffered formaldehyde (NBF, BIOS Europe Ltd., UK) at room temperature for 10 minutes.

4. NBF was discarded.
5. Cells were washed 3 times with PBS.
6. Cells were incubated at room temperature, not in direct light, for 5 minutes with PI solution.
7. Cells were washed 3 times with 0.1% tween 20/PBS.

2.4.2.3 DAPI

DAPI dihydrochloride (Life Technologies, UK) is a blue fluorescent dye (excitation 358nm: emission 461nm) which binds to adenosine-thiamine clusters of DNA. DAPI was diluted at a ratio of 1:3000 into PBS to create a working stock which was stored in that dark at 4°C for up to 1 month. Stain solution was made by diluting the working stock 1:10 with PBS. The final concentration of DAPI was ~167ng/ml. Staining procedure was similar to PI protocol (Section 2.4.2.2) and is as follows:

1. Culture medium was removed.
2. Cells were washed 3 times with PBS.
3. Cells were fixed with 10% NBF at room temperature for 10 minutes.
4. Cells were washed 3 times with PBS.
5. Cells were incubated at room temperature, not in direct light, for 5mins with DAPI staining solution.
6. Cells were washed 3 times with 0.1% tween 20/PBS.

2.4.2.4 Phalloidin

Phalloidin is a phallotoxin which binds to the F-actin filaments of a cell cytoskeleton. Throughout this study Alexa Fluor® 488 (excitation 495: emission 518) conjugated phalloidin (Life Technologies, UK) was used. Phalloidin was dissolved in 1.5ml methanol and stored at 4°C. Prior to use phalloidin was diluted 1:40 in PBS:tween 20 (Sigma, UK) to a final concentration of 5U/ml. The following staining protocol was used:

1. Culture medium was removed.
2. Cells were washed 3 times with PBS.
3. Cells were fixed with 10% NBF at room temperature for 10 minutes.
4. Cells were washed 3 times with PBS.

5. Cells were permeabilised with 1%(v/v) triton X-100 (Sigma-Aldrich, UK) in PBS for 5 minutes.
6. Triton X-100 solution was removed and cells were washed three times with 0.1% tween 20/PBS.
7. Cells were incubated with phalloidin at room temperature for 30 minutes away of direct light.
8. Cells were washed 3 times with 0.1% tween 20/PBS.

2.4.2.5 Primary and Secondary Antibody Staining

N/N1003A and B3 lens epithelial cell lines were stained for the presence of αB-crystallin and various cytokeratin proteins as markers for lens epithelial cells [214, 216-218]. A mouse monoclonal anti-αB crystallin primary antibody (Abcam, UK) was used. Various cytokeratin antibody clones, each of which binds to specific cytokeratins, were used and are outlined below in Table 2.11.

Table 2.11 outlines the clone and manufacturer of cytokeratin antibodies and the specific cytokeratins they bind to.

Clone, Manufacturer, Country	**Cytokeratins**	**Concentrations Used**
NCL-5D3 anti-mouse, Santa Cruz, USA	8 and 18	2µg/ml
C11 anti-mouse, Santa Cruz, USA	4, 5, 6, 8, 10, 13 and 18	2µg/ml
AE1/AE3 anti-mouse, Dako, UK	1, 2, 3, 4, 5, 6, 7, 10, 13, 14, 15, 16 and 19	975ng/ml
MNF116 anti-mouse, Dako, UK	5, 6, 8, 17 and probably 19	1.7µg/ml
RCK108 anti-mouse, Dako, UK	19	200ng/ml

The primary antibodies were fluorescently tagged with an Alexa Fluor® 488 goat anti-mouse IgG secondary antibody (Life Technologies, UK). As a negative control mouse IgG (Dako, UK) was substituted in place of the primary antibody. As a blocking agent 10%(v/v) goat serum (Sigma-Aldrich, UK) solution was made in 1%(w/v) BSA:PBS. The staining procedure was as follows:

1. Culture medium was removed.
2. Cells were washed three times with PBS.
3. Cells were fixed with methanol for 5 minutes or 10% NBF for 10 minutes.
4. Cells were washed three times with PBS.
5. Cells were permeabilised with 1% triton X-100 (Sigma-Aldrich, UK) in PBS for 5 minutes at 4°C.
6. Cells were washed three times with 0.1% tween 20/PBS.
7. Cells were incubated with 10% goat serum at 37°C for 30 minutes.
8. Goat serum was not washed and samples were incubated with primary antibody or IgG negative control, at a concentration of 1:100 (2µm/ml) in 1% BSA/PBS, at 4°C overnight.
9. Cells were washed three times with 0.1% tween 20/PBS.
10. Secondary antibody was added at a concentration of 1:100 or 1:250 in 1%BSA:PBS and incubated at 37°C for 30 minutes.
11. Cells were washed three times with 0.1% tween 20/PBS.

2.4.3 Cell Growth Study and Cell Growth Area Montages

Representative images were taken of live cells throughout the growth period in cell culture using an inverted phase contrast microscope (Diaphot, Nikon, UK) with a Nikon D1 digital SLR camera, at various time points. To quantify cell growth across the various experimental conditions micrographs were taken at defined points across the sample. Micrographs of fluorescently stained cell nuclei were taken with x10 objective lens in the centre of the sample, 1.5mm, 3mm and 4mm away from the centre of the sample. Images were taken in both the x and y axes, in both positive and negative sides of the centre point. Therefore 4 images for 1.5mm, 3mm and 4mm were taken on each sample (Figure 2.21).

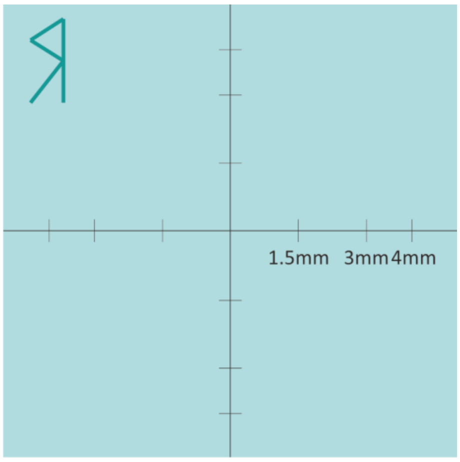

Figure 2.21 Diagram depicting micrograph positions on a sample for cell growth analysis.

To perform cell growth analysis on TCPS control samples, coverslips used to mount samples were marked with a diamond tip pen at the various positions, to create positions for counting cells (Figure 2.22).

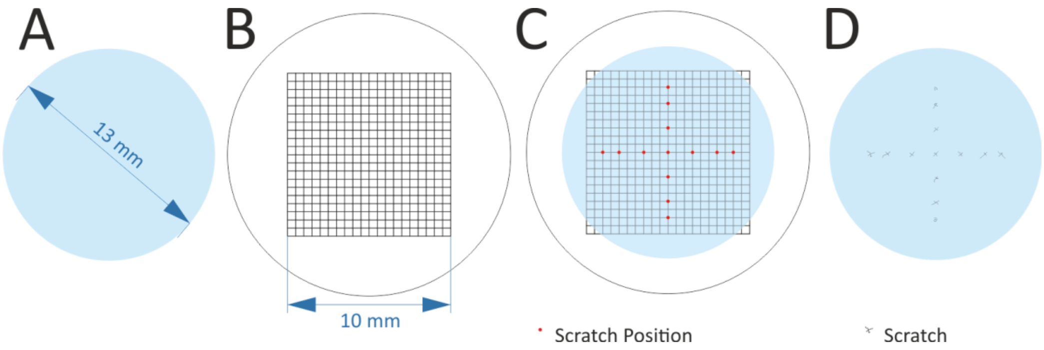

Figure 2.22 Diagram depicting the process of marking coverslips to be mounted in TCPS control wells for cell growth analysis. A. A 13mm glass coverslip to fit a 24-well plate, was placed on a (B.) 10x10mm graticule with a 0.5mm resolution. Scratches were made on the coverslip at (C.) various positions using the graticule for reference. The coverslip was mounted in the TCPS well and the scratch positions could be n using transmitted light

To determine the diameter of the cell growth area, micrographs of stained cell nuclei or cytoskeleton were taken across each axis with an x5 objective. Each micrograph overlapped the adjacent micrograph, allowing for image stitching and a montage across each axis to be produced (Figure 2.23). Each axis was stitched individually due to software/hardware constraints. The diameter of cell growth area was then measured.

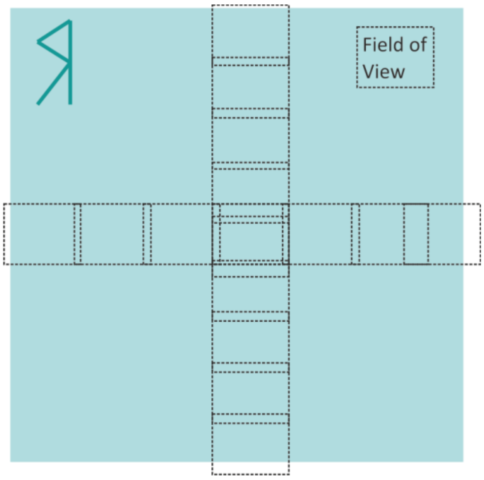

Figure 2.23 Diagram displaying overlapped fields of view used in creating montage image to measure the diameter of the cell growth area.

2.4.4 Image Analysis

All micrographs, excluding those for the pin plasma experiment, for cell growth and montage analysis were taken with an Axiovert 200 inverted microscope (Zeiss, UK), and captured using Axiovision software (Zeiss, UK). Micrographs for the pin plasma experiments were captured using an Observer Z1 inverted microscope (Zeiss, UK), and captured using Zen software (Zeiss, UK). All cell nuclei were counted using ImageJ software package version 1.43m (National Institutes of Health, USA). Within the ImageJ package cells were either counted manually using the “cell counter” plug-in, or a macro was written which converted the image to binary and utilised the “analyse particles” function. Cells were assumed to be mononuclear.

To create montage images from which the diameter of cell growth could be calculated 2 software packages were used. Images taken using the Axiovision software were stitched using the MosiacJ[219] plugin for ImageJ. Images taken during the pin plasma experiment were stitched within the Zen software at the time of capture. The diameter of the cell growth area was measured from the composite montage images using the “measure” function in either Axiovision software, or Zen software for the pin plasma experiment. The “measure” functions in each software were calibrated to the optics of the corresponding microscope. High magnification fluorescent images were taken with a x40 objective lens on both the Zeiss Axiovert 200 and Observer Z1 microscopes.

2.4.5 TGF-β2 ELISA

To determine the level of TGF-β2 secreted by the LECs in culture an enzyme-linked immune sorbent assay (ELISA, R&D Systems, UK) was performed on the cell culture supernatants. At various cell growth time points culture medium was removed from cells, during routine feeding. The medium for each different substrate condition was pooled. Samples were centrifuged at 1000xg for 15mins at 4°C and stored at -20°C. A summation of the manufacturer’s protocol is outlined below. Volumes are per well on a 96 well plate.

1. To activate TGF-β2 within supernatant.
    1.1. 25µL of 1N HCl was added to 125µL of sample and incubated for 10mins at room temperature.
    1.2. 25µL of 1.2N NaOH/0.5M HEPES was added.
    1.3. 800µL of Calibrator Diluent was added and samples were assayed within 2hrs.
2. TGF-β2 standard series was prepared.
    2.1. TGF-β2 stand was reconstituted with 2ml Calibrator Diluent and placed on a rocker for 15 minutes.
    2.2. A 6-point 1:2 series dilution was made using the reconstituted standard and Calibrator Diluent. Reconstituted standard served as the high standard and the Calibrator Diluent served as the zero standard, making a total of 8 points for the standard curve.
3. Assay procedure was followed.
4. Wash buffer was diluted following manufacturer’s instructions.
    4.1. 100µL of Assay Diluent was added to each well.
    4.2. 100µL of standard, controls or activated samples were added to wells.
    4.3. Plate was covered with adhesive strip and allowed to incubate for 2hrs at room temperature.

4.4. Wells were emptied and washed with wash buffer three times.

4.5. 200µL TGF-β2 Conjugate was added.

4.6. Plate was covered with an adhesive strip and incubated for 2hrs at room temperature.

4.7. Substrate solution was prepared by mixing colour reagents "A" and "B" in equal volumes. Solution was protected from light and used within 15mins.

4.8. Wells were washed 3 times.

4.9. 200µL of substrate solution was added.

4.10. Plate was protected from light and incubated for 20mins at room temperature.

4.11. 50µL of the stop solution was added to each well and thoroughly mixed.

4.12. The absorbance of each well was measured at 450nm and 570nm using a µQuant™ microplate spectrophotometer (BioTek Instruments Inc., USA) .

Readings for each standard, control and sample were taken in duplicate. The duplicate readings were averaged. The readings taken at 570nm were subtracted from the 450nm mean, to correct for optical imperfections in the plate. The zero standard optical density was subtracted from all measurements. The response values from the spectrophotometer and the independent standard series concentration values were input to ReaderFit (Hitachi Solutions, USA). This calculated a 4-parameter logistical curve-fit for the standard curve and calculated the TGF-β2 concentration for the samples and controls. The calculated TGF-β2 concentrations for controls and samples were multiplied by 7.8 to compensate for dilution during the activation stage (step 1).

2.4.6 Cytokine Multiplex Assay

A magnetic bead-based multiplex assay was used to determine the concentration of inflammatory cytokines: interleukin-1α (IL-1α), interleukin-6 (IL-6), basic fibroblastic growth factor (basic-FGF) and tumour necrosis factor-α (TNF-α) in cell culture supernatants. The multiplex assay kit and each of the cytokines were purchased from Bio-Rad, USA. IL-1α was from the human cytokine group II and the remaining cytokines were from human cytokine group I; this required the mixing of standards and detection antibodies which are detailed in the protocol below. During feeding, culture medium was removed from cells and reserved at various time points. Samples were centrifuged at 1000xg for 15 minutes at 4°C and stored at -20°C. The manufacturer's protocol was followed and is summarised below.

During incubation sealing tape was placed of the wells. In the washing steps a magnetic plate holder was used to retain the beads in the wells.

1. Standards were prepared
    1.1. Standards for human cytokine groups I and II were reconstituted in 250µL each.
    1.2. Standards were gently vortex and incubated on ice for 30 minutes.
    1.3. Nine polypropylene tubes were labelled “S1” –“S8” and “blank”.
    1.4. 72µl of standard diluent was pipetted into tube “S1” and 150µL into the remaining tubes.
    1.5. 64µl from each standard was pipetted into tube “S1”.
    1.6. 50µL from tube “S1” was pipetted into tube “S2”; a 1:4 serial dilution was continued until tube “S8”.
2. Beads coupled with capture antibodies for each cytokine were prepared. Each vial of coupled beads was specific to a cytokine.
    2.1. Beads were vortexed for 30 seconds each.
    2.2. 3.45mL assay buffer was pipetted into a polypropylene tube.
    2.3. 575µL of each set of coupled beads was added to the assay buffer. This allowed 50µL of bead suspension per well, plus 20% excess.
3. 50µL of coupled beads were added to each well.
4. Wells were washed twice with wash buffer.
5. 50µL of standards, controls and samples were added to wells.
6. The plate was incubated on a shaker for 30 minutes at room temperature.
7. Detection antibodies were prepared during incubation. Each vial of detection antibody was specific to a single cytokine.
    7.1. 1.8mL of detection antibody diluent was pipetted to a polypropylene tube.
    7.2. 300µL of each detection antibody was added to the detection antibody diluent. This allowed 25µL of diluted detection antibody per well with 20% excess.
8. Sealing tape was removed and wells were washed three times.
9. 25µL of diluted detection antibodies were added to each well.
10. The plate was sealed and incubated on a shaker at room temperate for 20 minutes.
11. During incubation streptavidin-phycoerythrin(PE) was prepared.
    11.1. Streptavidin-PE tube was vortexed for 30 seconds.

    11.2. 60µL of streptavidin-PE was mixed with 2.97mL assay buffer and protected from light until ready to use.
12. After detection antibody incubation sealing tape was removed and plate was washed three times.
13. 50µL of streptavidin-PE was added to each well.
14. The plate was incubated on a shaker at room temperate for 10 minutes.
15. Following incubation the plate was washed 3 times.
16. 125µL of assay buffer was added to each well.
17. The plate was sealed then shaken at 1,100rpm for 30 seconds.
18. Sealing tape was removed and plate was placed in the Bio-plex 200 system (Rio-Rad, USA) for analysis.

Bio-Plex Manager 5.0 software (Bio-Rad, USA) was used to read and analyse the data. A protocol was set within the software, such that the software could extrapolate data from the information provided and the readings from the plate. Information provided included positions of standards, controls and samples on the plate; which cytokines and corresponding bead fluorescent regions were used; which standards, base concentrations for each cytokine and dilution factors were used. Readings for each standard, control and sample were measured in duplicate; duplicate readings were averaged. The readings from the blank standard for each cytokine were subtracted from all other readings for that specific cytokine. The Bio-Plex Manager 5.0 software used a 5-parameter logistic regression method to determine a standard curve for each cytokine, from these standard curves the software calculated observed cytokine concentrations.

2.5 Statistical Analysis

Statistical analysis was performed using IBM SPSS v. 20 statistics software (IBM, USA,) and results are reported as means ± standard deviation. Statistical significance was measured by one-way ANOVA unless otherwise stated. One-way ANOVA's were followed by Tukey's test or Dunnett's T3 test if homogeneity of variances was upheld or violated, respectively. Statistical significance was assumed when $p<0.05$.

3 Results

3.1 Antibody Characterisation

To characterise lens epithelial cells (LECs) they were stained with αB-crystallin, a common lens cell marker[214, 217], and various cytokeratin clones. Cytokeratin antibody clones and the specific cytokeratins each clone binds to are outlined in Table 3.1 below. Rabbit N/N1003a[214] and human B3[217] LEC lines were stained. Mouse IgG was used as a negative control and retinal pigmented epithelial cell line (aRPE-19) was used as a positive control. All cell lines were negative for mouse IgG staining (Figure 3.1). αB-crystallin staining was observed in all cell lines. The aRPE-19 cell line[213] was positive for cytokeratin however both LEC lines were negative for all cytokeratin clones. Very few individual B3 cells appeared to express cytokeratin. Only the NCL-5D3 clone is displayed in Figure 3.1 to avoid repetition.

Table 3.1 outlines the clone and manufacturer of cytokeratin antibodies and the specific cytokeratins they bind to.

Clone, Manufacturer	**Cytokeratins**
NCL-5D3 anti-mouse, Santa Cruz	8 and 18
C11 anti-mouse, Abcam	4, 5, 6, 8, 10, 13 and 18
AE1/AE3 anti-mouse, Dako	1, 2, 3, 4, 5, 6, 7, 10, 13, 14, 15, 16 and 19
MNF116 anti-mouse, Dako	5, 6, 8, 17 and probably 19
RCK108 anti-mouse, Dako	19

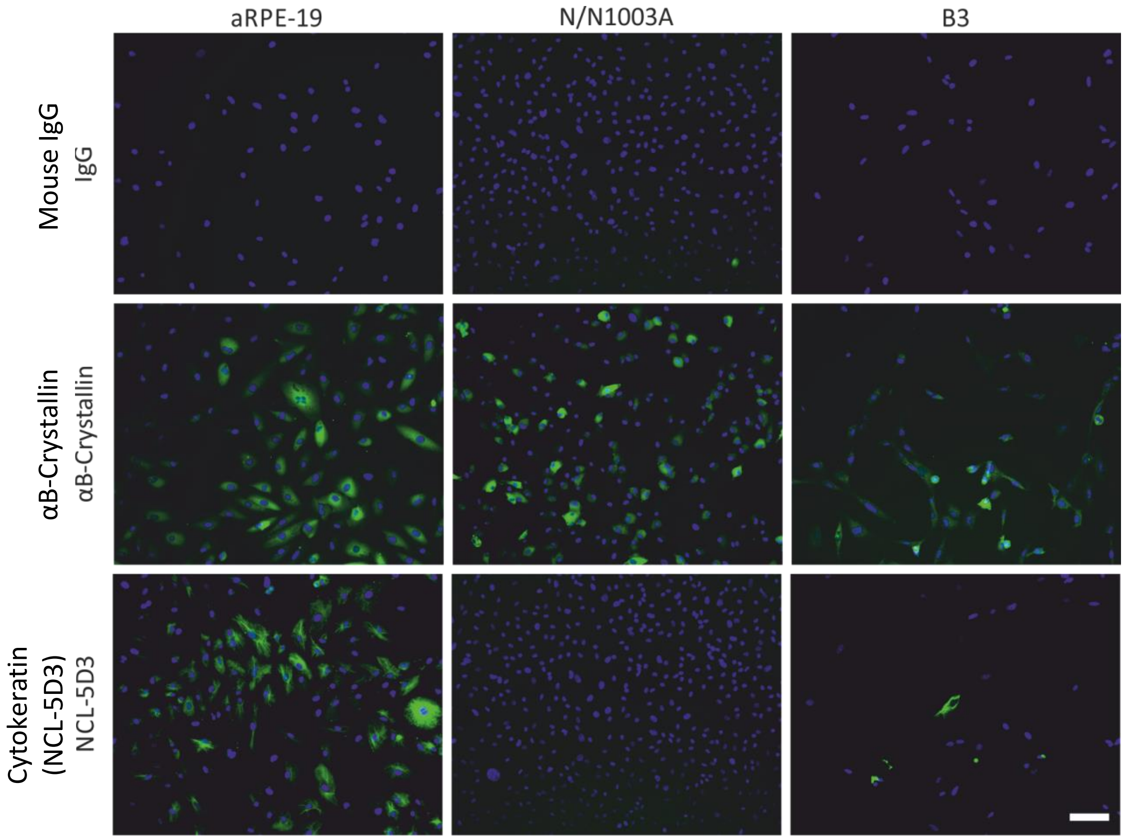

Figure 3.1 Representative micrographs of antibody staining (green) and DAPI nuclear staining (blue) of retinal pigmented epithelial cells (aRPE-19), rabbit lens epithelial cells (N/N1003A) and human lens epithelial cells (B3) on tissue culture polystyrene (TCPS). aRPE-19 cells served as a positive control for both αB-crystallin and NCL-5D3 anti-bodies. Scale bar = 100µm.

3.2 Preliminary Epithelial Cell Culture on Plasma Jet Treated Samples

aRPE-19 were seeded onto TCPS wells had wide-spread morphology after 5 days of growth, whereas only a few cells were attached to untreated polystyrene (UT-PS). Treated polystyrene (PS) demonstrated cell growth similar to TCPS. Samples that were half-treated using a mask displayed a distinct boundary of cell growth at the interface of masked and unmasked regions. Cells on TCPS, treated and half-treated PS had not yet formed an epithelial monolayer but areas of higher cell density on treated samples displayed typical epithelial cobblestone morphology. This preliminary study exhibited that treatment with a He plasma jet enables epithelial cell attachment and proliferation (see Figure 3.2).

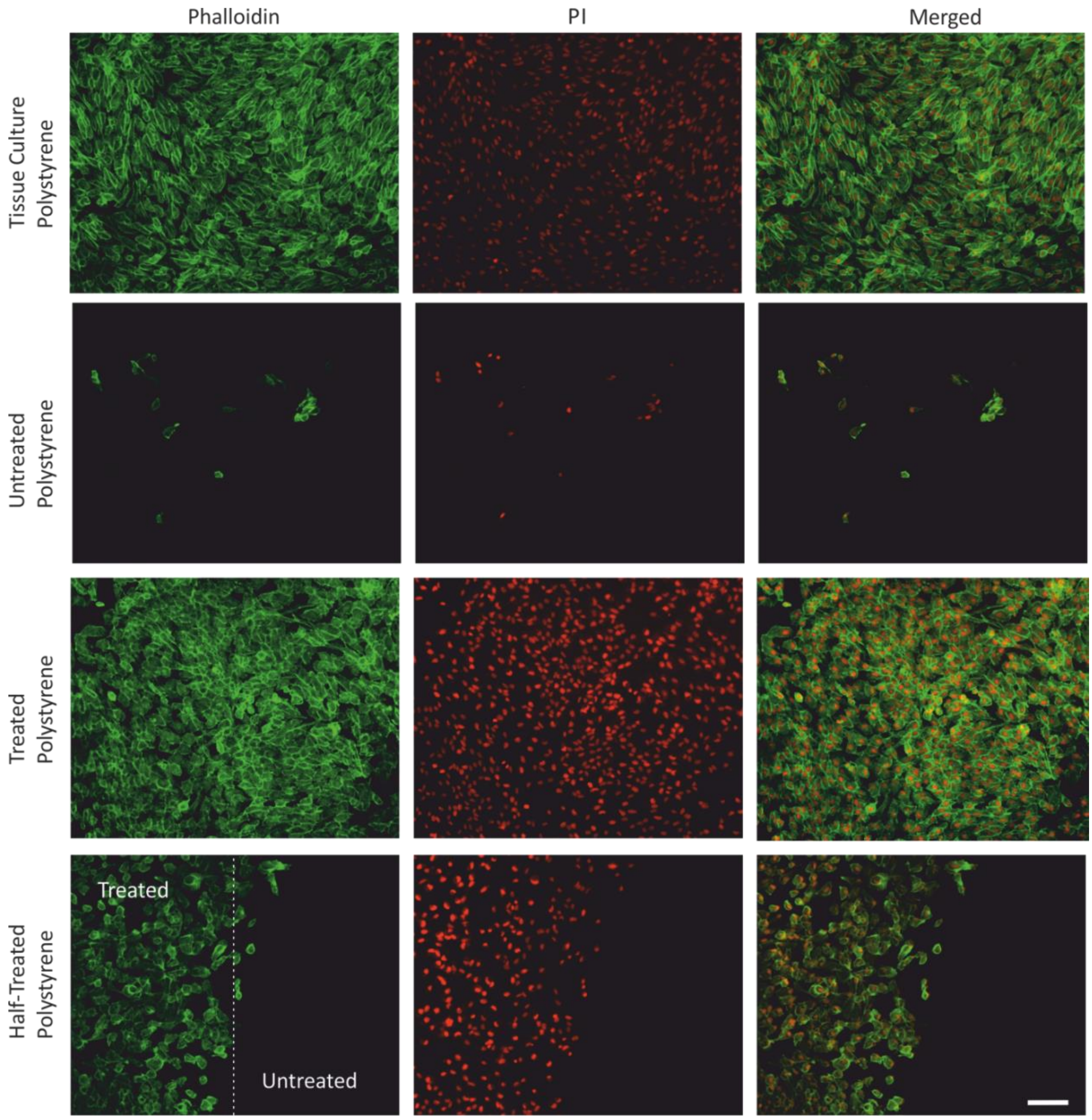

Figure 3.2 Representative fluorescent micrographs of aRPE-19 cells seeded onto tissue culture polystyrene (PS), untreated PS, treated PS and half-treated PS. Cell cytoskeletons were stained with phalloidin (green) and nuclei were stained with propidium iodide (red). Dotted line represents the boundary of the treated region. Scale bar = 100µm.

3.3 Shadowing Experiments

To elucidate possible mechanisms of plasma jet surface modification, barriers of different geometries were placed between the sample and nozzle in the flow of helium gas. This blocked the path of bond-breaking photons and disrupted the gas flow carrying species (electrons, ions, atoms and molecules) which could alter the surface chemistry. These barriers created a “shadow” effect on treated surfaces, i.e a reduction in treatment on the sample in an area behind the barrier. In these experiments the jet parameters were fixed (10kHz, $6kV_{peak\text{-}peak}$) but the barrier widths, geometries and materials were changed; as were the distances of both samples and shadows from the jet nozzle. This section mostly deals with contact angle profiles taken across the surface of treated PS; for this section and the subsequent contact angle sections some nomenclature and assumptions are outlined below:

- positions were discrete points on the surface of a sample and will be referred to with respect to the centre of the profile/sample; the centre of the profile/sample is 0mm on all contact angle line graphs
- *"…across the sample"* refers to the contact angle profile across the entire surface of a single parameter
- Reference to the *"edge"* of samples/profiles are the left and right side of the contact angle line graphs, typically the 3-4mm positions (for 10x10mm samples)
- *"section"* or *"region"* refers to multiple positions of a single profile
- *"untreated region"* refers to the section in which contact angle was approximately the same as untreated polystyrene (~80°)(or approximately 59° in the case of untreated PMMA, see section 3.5.1), this was typically at the edge (3-4mm from the centre) of a treated sample
- *"more untreated"* means that the contact angle was tending toward 80° (for PS)
- *"more treated"* means that the contact angle was tending toward 0°
- *"treated region"* refers to the section of a contact angle profile in which contact angle was less than ~75-80°
- *"maximum/minimum (maxima/minima)"* refers to the highest and lowest contact angle(s) of a profile respectively
- *"maximum treatment"* refers to the lowest contact angle
- a *"level"* contact angle profile refers to a profile which varies by <5° between positions (e.g. 4mm = 80.1°, 3.5mm = 79.3°, 3mm = 76.7°, 2.5mm = 82° etc.)
- It was assumed plasma jet treatment created a circular treated area
- the *"width"* of a treated area (or *"diameter"*, as treated areas were assumed to be circular) will be defined as the distance along a contact angle profile at which contact angle was ~x°, where x was dependent on treatment condition and will be defined in each section

- treatment with a plasma jet will decrease the contact angle in the centre of a sample, i.e. the contact angle will be lower in the positions closer to the centre compared to the contact angle at the edges; creating a “treated region”

3.3.1.1 Paper Shadowing

In initial tests barriers of various widths were cut from paper. The paper barriers and samples were placed 7mm and 10mm from the nozzle respectively. When barriers were placed within the gas stream they created a shadow effect within the treated region; a shadow effect was a section within the treated region of a sample which was more untreated than the areas surrounding it. For example the peak in contact angle observed in the centre of the 0.2mm wide barrier parameter was considered an effect of the barrier (Figure 3.3).

No discernible shadow effect was observed on PS with the presence of 0.5mm and 1mm wide paper barriers, however clear shadow effects were observed when the barrier width was 1.2mm or 1.5mm; these created a wider shadow effect compared to the 0.2mm parameter (Figure 3.3). The contact angle across the entire surface of samples with the 2mm and 3mm parameters was ~80° indicated that these barriers blocked all treatment. When barriers with widths larger than the internal diameter (ID) of the jet nozzle (1mm) were used broad shadow effects were observed.

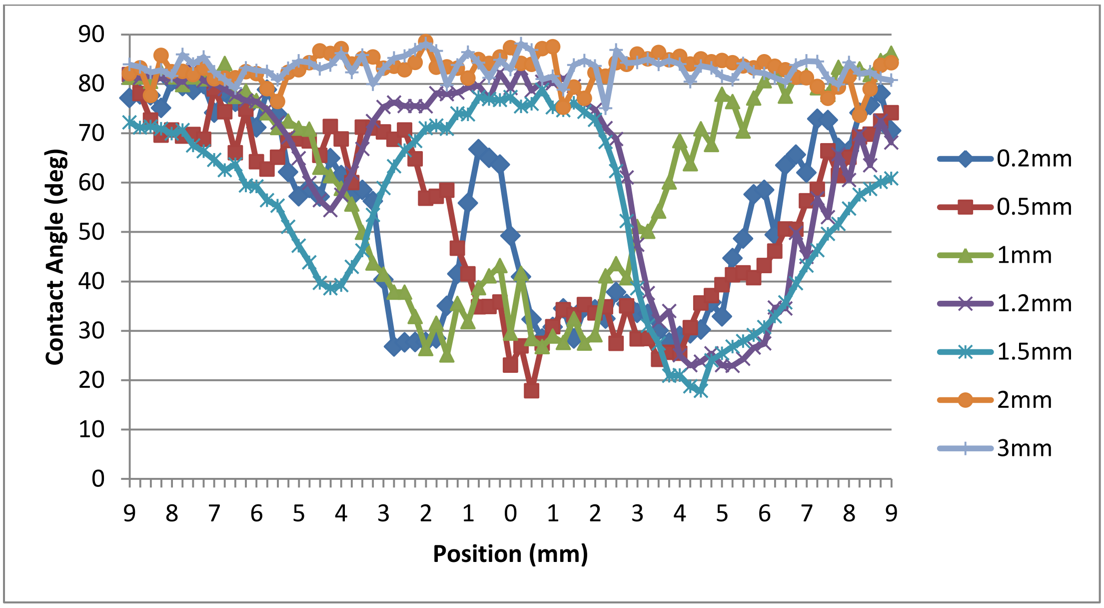

Figure 3.3 Line graph of contact angle profiles taken across polystyrene (PS) samples treated with a plasma jet. Samples were placed 10mm from the plasma jet nozzle and paper barriers of various width (0.2-3mm) were placed 7mm from the nozzle. Contact angle measurements were taken across central axes of samples at a resolution of 0.25mm. Profiles were from single samples.

3.3.1.2 Plastic Shadowing

Paper was considered too weak to present a stable flat barrier therefore plastic barriers were investigated. Samples were treated (at a 10mm sample-nozzle distance) with the presence of a plastic barrier in the focus of the jet, which provided a sturdy flat edged barrier to the helium flow. Treatment without a shadow resulted in a decrease in contact angle from approximately 50° at the sample edge, to ≈30° in the centre of the sample, thus creating a broad trough in the contact angle profile (Figure 3.4). When a 1.2mm wide barrier was placed in the path of the jet no discernible effect was observed; the contact angle profile was similar to samples treated without a barrier. When a 3mm wide barrier was placed in the path of the plasma jet a very broad shadow effect could be observed in the contact angle profile. This broad shadow was slightly left of the centre position resulting in the asymmetry observed in the troughs.

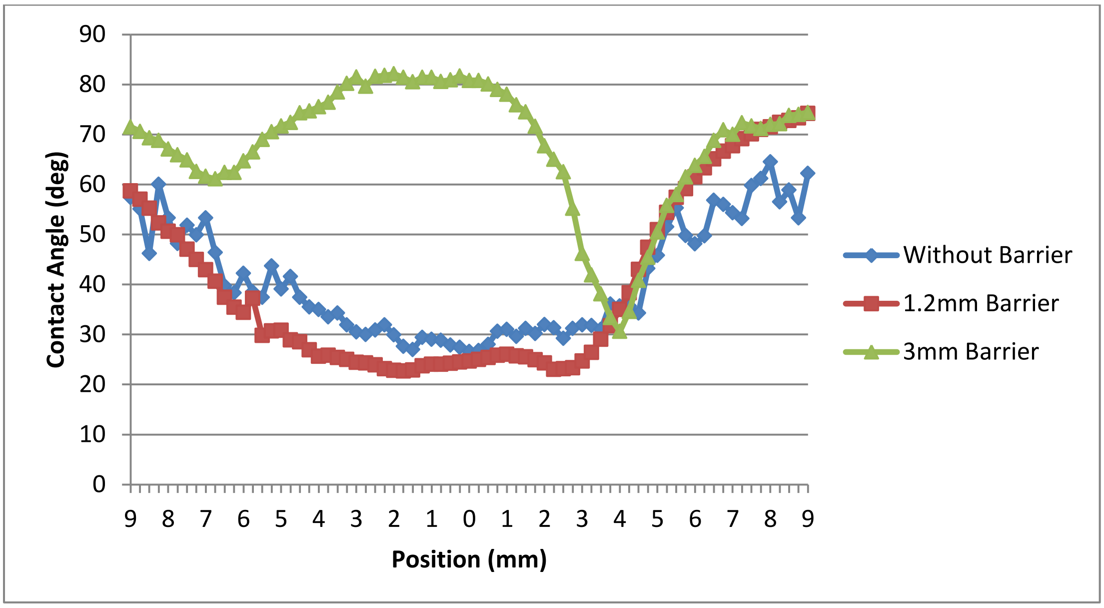

Figure 3.4 Line graph of contact angle profiles taken across polystyrene (PS) samples treated with a plasma jet. Samples were placed 10mm from the plasma jet nozzle and plastic barriers of various width (1.2mm and 3mm) were placed 8mm from the nozzle. Contact angle measurements were taken across central axes of samples at a resolution of 0.25mm. Profiles were from single samples.

In an additional test a plastic shadow of 2mm width was placed 4mm, 6mm and 8mm from the nozzle; the samples were fixed at 10mm from the nozzle. When PS was treated without a barrier the contact angle profile was >65° at the edges and decreased to ~25° ± 10° in the centre region (Figure 3.5). When the barrier was placed 4mm from the nozzle no clear shadow effect was observed; however the narrowness of the central trough, and the rise and fall of contact angle observed at the right 3-9mm section of the profile suggested that the barrier may have been misaligned. A small peak in contact angle was observed within the treated area when the barrier was placed 6mm from the nozzle. This appeared symmetrical and was most likely a shadow effect. When the barrier was placed at 8mm from the nozzle a peak, of similar width to that observed for the 4mm parameter, was present. These results indicate that the position of the barrier affected the extent of the shadowing, with a greater blockage of treatment when the barrier was closer to the sample.

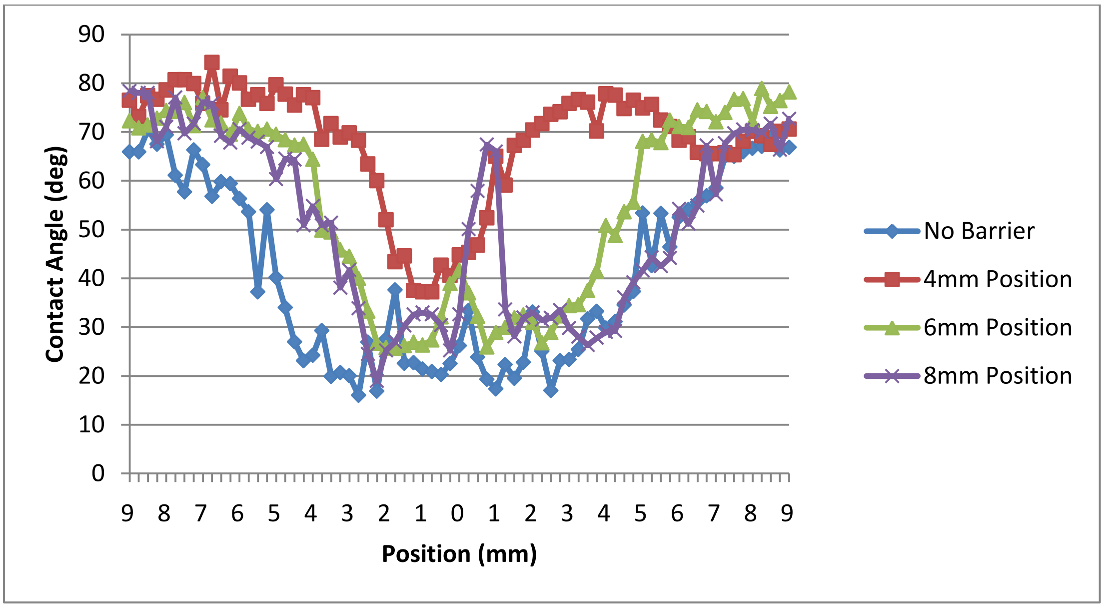

Figure 3.5 Line graph of contact angle profiles taken across polystyrene (PS) samples treated with a plasma jet. Samples were placed 10mm from the plasma jet nozzle and a 2mm wide plastic barriers was placed 4mm, 6mm and 8mm from the nozzle. Contact angle measurements were taken across central axes of samples at a resolution of 0.25mm. Profiles were from single samples.

Similar to the previous experiment PS samples was fixed at a set distance, 25mm from the nozzle, and a 2mm width barrier was positioned at various distances relative to the nozzle (5mm, 10mm, 15mm and 20mm). When PS was treated without a barrier the contact angle was reduced from approximately 80° at the edges to ~20° in the centre (Figure 3.6). When a barrier was placed 5mm from the nozzle no treatment was observed on PS samples (contact angle at all positions was >80°). When the barrier was positioned at 10mm and 15mm from the nozzle the contact angle decreased to <70° to the left of the centre indicating that they may have been slight treatment but the shadow was misaligned. A shadowing effect was observed to the left of the centre position on PS when the barrier was placed 20mm from the nozzle. The right side of sample was clearly more treated, adding further evidence that the barrier may have been misaligned or asymmetric (Figure 3.6).

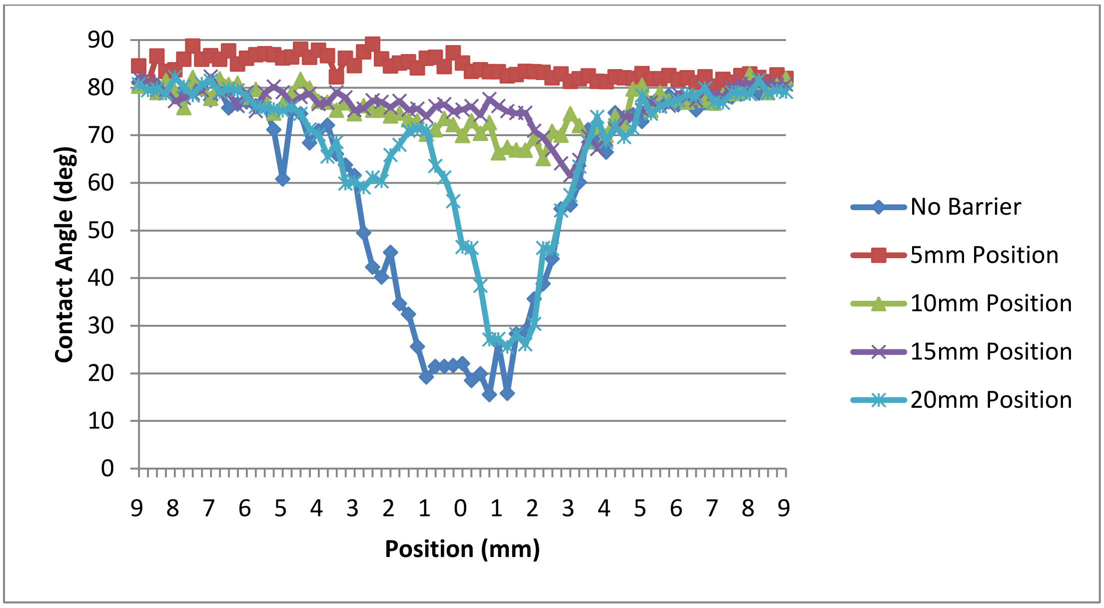

Figure 3.6 Line graph of contact angle profiles taken across polystyrene (PS) samples treated with a plasma jet. Samples were placed 25mm from the plasma jet nozzle and a 2mm wide plastic barriers was placed 5mm, 10mm, 15 and 20mm from the nozzle. Contact angle measurements were taken across central axes of samples at a resolution of 0.25mm. Profiles were from single samples.

3.3.1.3 Glass Capillary Shadowing

Glass capillaries were used as barriers to the plasma gas flow which presented a circular geometry as opposed to a flat-faced barrier in the previous experiments. Cells were also seeded on samples treated with and without capillary shadows and grown for 7 days.

3.3.1.3.1 Contact Angle

A 3mm diameter quartz capillary barrier was placed 2mm from the jet nozzle. Samples were treated at 10, 12, 14, 16, 18 and 20mm from the nozzle with the barrier in-situ. When a sample was positioned 10mm from the nozzle the contact angle gradually decreased from ~80° at the edge of the sample to a minimum of 24.7° in the central treated region. The central treated region displayed an asymmetry that was not present in the other parameters, which presented a smooth decrease in contact angle toward the centre of the profile (Figure 3.7). As the samples were positioned further from the nozzle and shadow the extent of treatment decreased, i.e. the trough in the contact angle profile became more narrow and shallow with distance from the nozzle. No distinct shadow effect, as defined as a peak in contact angle within a treated region, was observed.

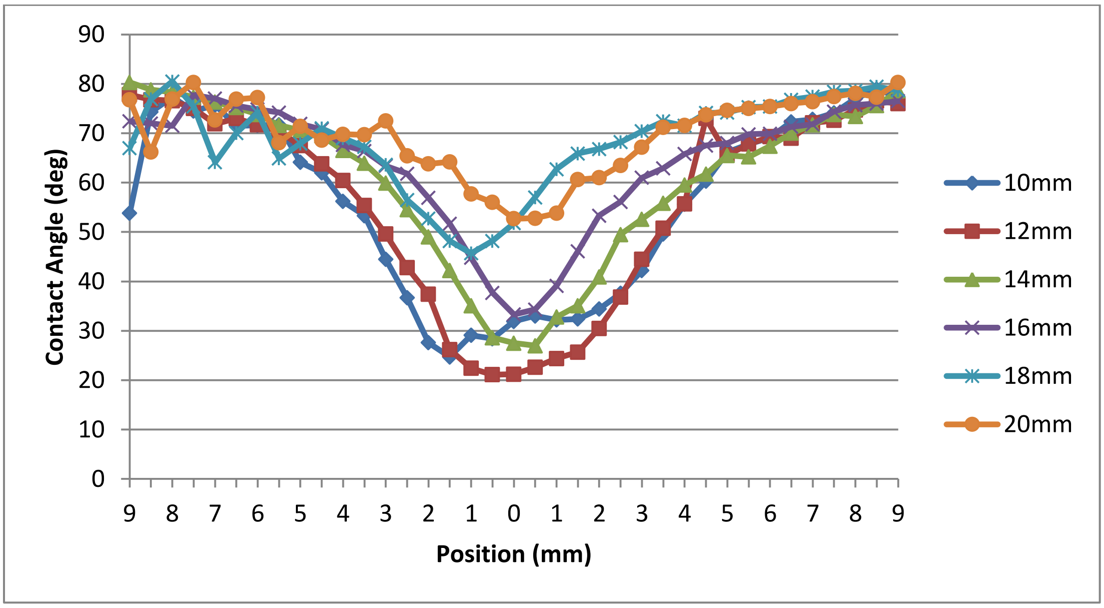

Figure 3.7 Line graph of contact angle profiles taken across polystyrene (PS) samples treated with a plasma jet. Samples were placed 25mm from the plasma jet nozzle and a 3mm outer diameter glass capillary barrier was placed 10mm, 12mm, 14mm, 16mm, 18mm and 20mm from the nozzle. Contact angle measurements were taken across central axes of samples at a resolution of 0.25mm. Profiles were from single samples.

3.3.1.3.2 Cell Culture

N/N1003A LECs seeded onto TCPS had attached after 1 day of culture and had a spread morphology. By day 4 confluent patches of LECS became apparent on TCPS wells and cells in confluent areas beginning to develop an epithelial cobblestone morphology. By day 7 a confluent epithelial monolayer had formed within TCPS wells. On UT-PS few cells were attached by day 1 and attached cells typically displayed a rounded morphology, with some cells having slightly more spread or spindle morphology. By day 4 cells on UT-PS had formed poorly attached clumps of rounded cells, with some cells having a spindle morphology. Some small patches of spread cells had grown on untreated PS by day 7 yet many cells still displayed a rounded morphology. Cells on samples treated without and with a barrier appeared similar to each other. In the centre of the samples there were more attached cells with a well spread morphology compared to TCPS. By day 4 most of the central area of treated samples had confluent growth of LECs, and by day 7 the central areas had confluent monolayers with cobblestone morphologies.

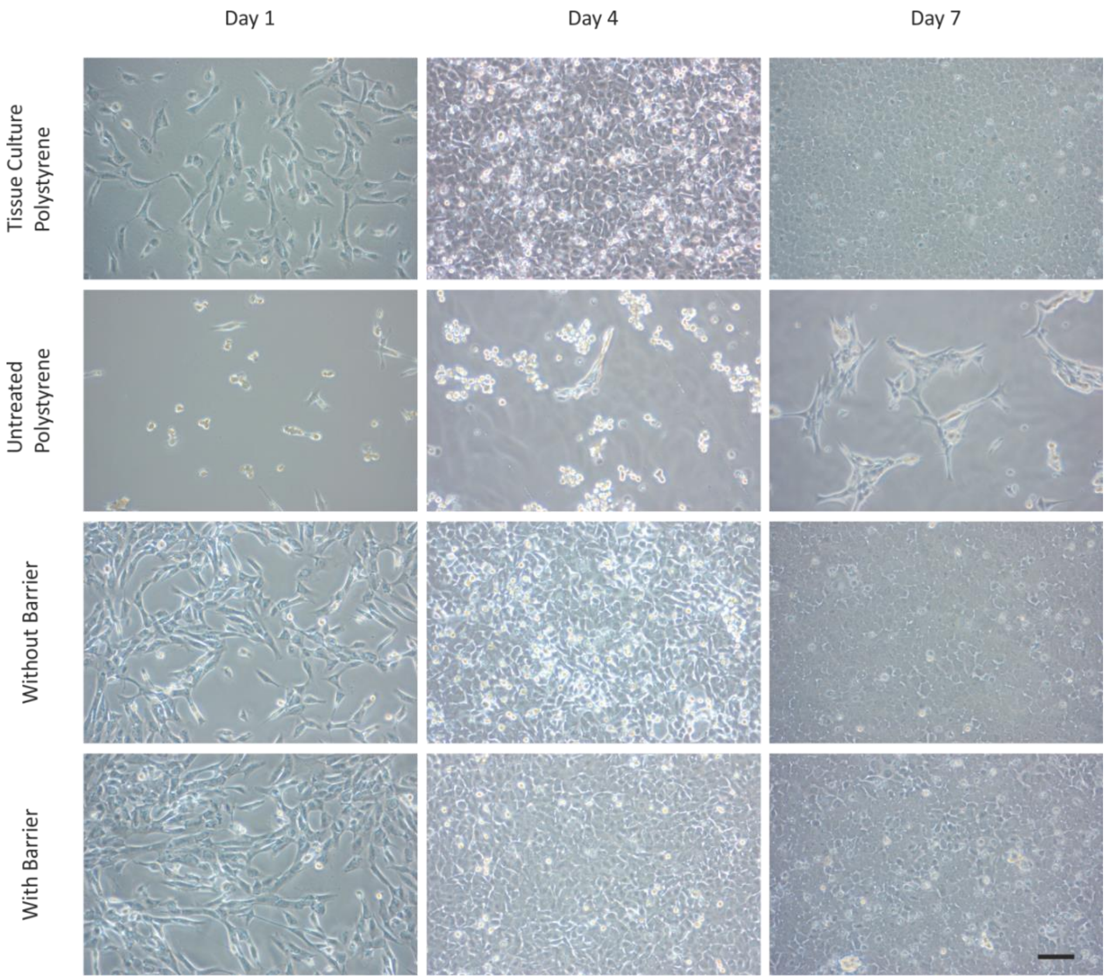

Figure 3.8 Phase contrast micrographs of N/N1003A rabbit LECs grown on tissue culture polystyrene (TCPS), untreated polystyrene (UT-PS) and polystyrene (PS) treated with or without a glass capillary barrier. Micrographs were taken in the centre of samples at days 1, 4 and 7. Scale bar = 100µm.

Due to the low cell density on TCPS at day 1 most cells were not visible when photographs of cells stained with methylene blue taken with a handheld camera. At day 4 it was observed that cells covered most of the area of the TCPS wells. Methylene blue staining of TCPS wells at day 7 appeared similar to the day 4 staining, however it was difficult to match the lighting conditions. At day 7 LECs covered the whole of the tissue culture wells. No cells could be seen on UT-PS when stained with methylene blue. On samples treated both with and without a glass capillary barrier a small concentration of cells could be seen in approximately the centre of the samples on day 1. At day 4 there was a dense staining in a circular pattern, with a distinct boundary, in the centre of samples treated without a barrier. There was some spotted staining around this dense area. Samples treated with a barrier were similar at this time point however the dense circular staining in the sample centre had smaller diameter and a less define boundary. Spotted staining around the dense area covered a larger area compared to samples treated without a barrier. At day 7 a monolayer of cells covered most of the samples treated without a barrier, which was demonstrated by a uniform blue staining across the centre of the samples. The staining of samples treated with a barrier did not cover as large an area, compared to samples treated without a barrier.

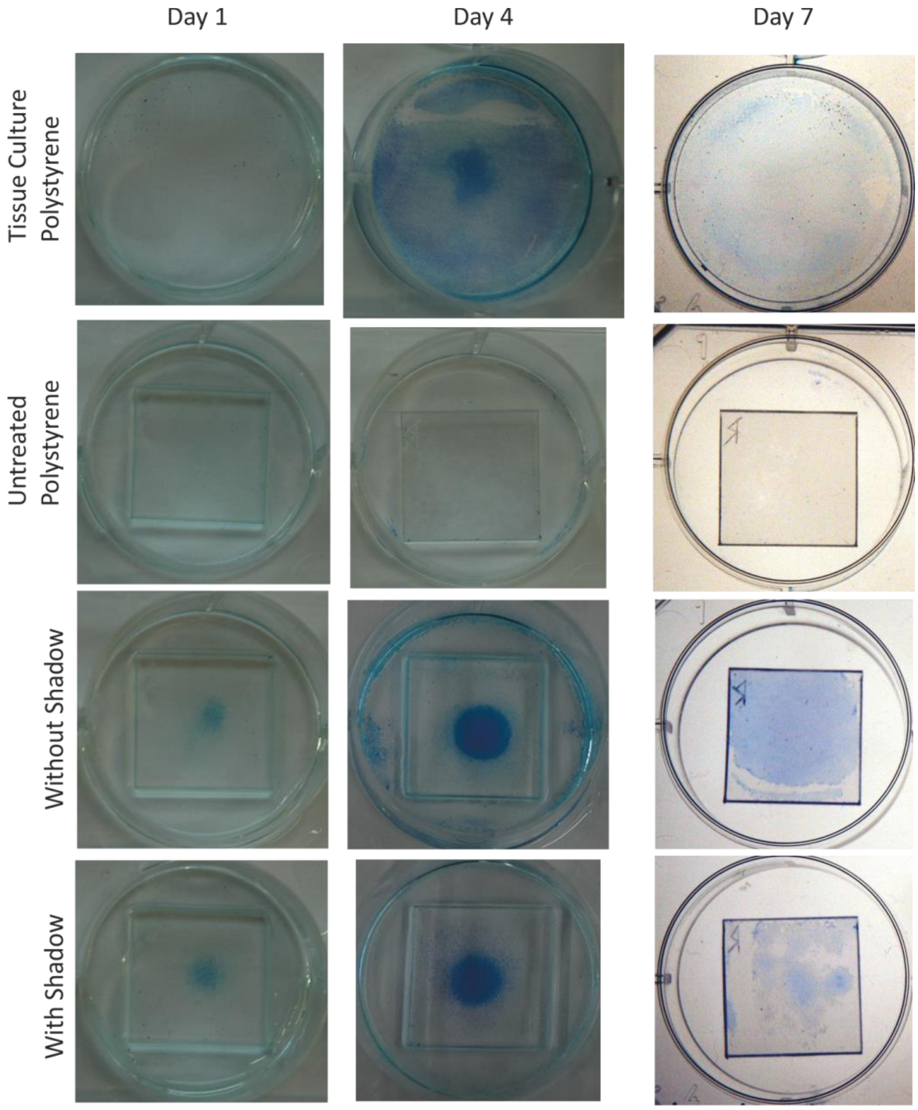

Figure 3.9 Photographs of methylene blue staining of tissue culture polystyrene (TCPS), untreated polystyrene (UT-PS), polystyrene (PS) treated without a barrier and PS treated with a barrier. Samples were fixed and stained at days 1, 4 and 7 and photographs were taken with a Nikon D5 camera, however the lighting conditions on the day 7 plate could not be matched to the earlier time points. Samples were approximately 20x20mm.

3.3.2 Blackened Glass Rod Shadows

Blackened glass rods were obtained to prevent the transmission of photons, which could possibly modify the surface, through the barriers. These rods presented a barrier with a circular geometry to the plasma gas flow. Rods of 1mm, 2mm and 3mm diameter were obtained and placed at various positions from the nozzle. In this experiment, two sample positions were used: 10mm and 20mm. For clarity, results will be grouped into 6 figures each with a single rod diameter and sample-nozzle-distance, e.g. 1mm diameter-10mm sample distance, 2mm diameter-10mm sample distance, 3mm diameter-20mm sample distance. Within each figure variation in treatment will be the position of the rod relative to the nozzle.

When samples were placed 10mm from the nozzle and no barrier was placed in the jet stream contact angle decreased from >40° at the left side of the sample to 20°, which continued across the sample (Figure 3.10). When the 1mm width barrier was placed at various distances from the sample the only appreciable change in the contact angle was at the right of the profile. The contact angle in this region was higher when the barrier was closer to the nozzle. This indicates that as the barrier was closer to the nozzle it caused a reduction of the treatment effect on the surface and the effect of the barrier on treatment decreased as the barrier was moved further from the nozzle, i.e. the profiles became more similar to the “No Barrier” condition (Figure 3.10). As more treatment was observed on the right side of the profiles it is possible that the samples/sample holder was misaligned with respect to the plasma jet.

This reduction of treatment was observed for larger diameter barriers also (Figure 3.11 and Figure 3.12). The reduction of treatment effect created by the larger diameter barriers can be characterised as a narrowing of the trough in the contact angle profiles (i.e. reduction of the width of treatment), and an increase in the minimum contact angle of a profile (i.e. a decrease of the maximum treatment). The reduction in treatment also increases with the diameter of the barrier (Figure 3.10, Figure 3.11 and Figure 3.12).

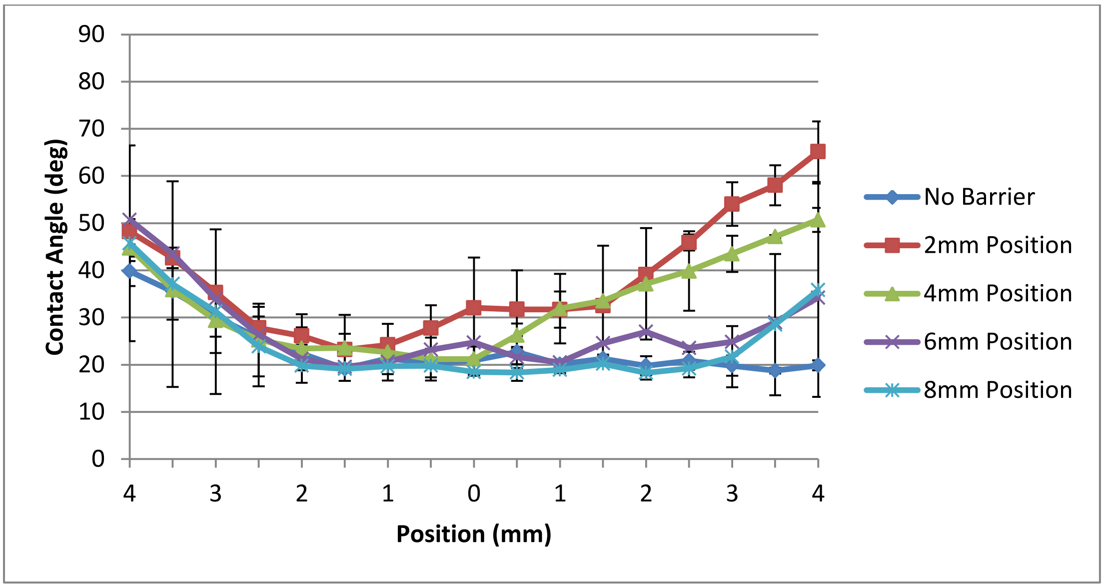

Figure 3.10 Line graph of contact angle profiles taken across polystyrene (PS) samples treated with a plasma jet. Samples were placed 10mm from the plasma jet nozzle and a 1mm diameter blackened glass rod barrier was placed 2mm, 4mm, 6mm and 8mm from the nozzle. Contact angle measurements were taken across the central axes of samples at a spatial resolution of 0.5mm. Profiles are the mean of 3 samples. Error bars are ± 1 standard deviation.

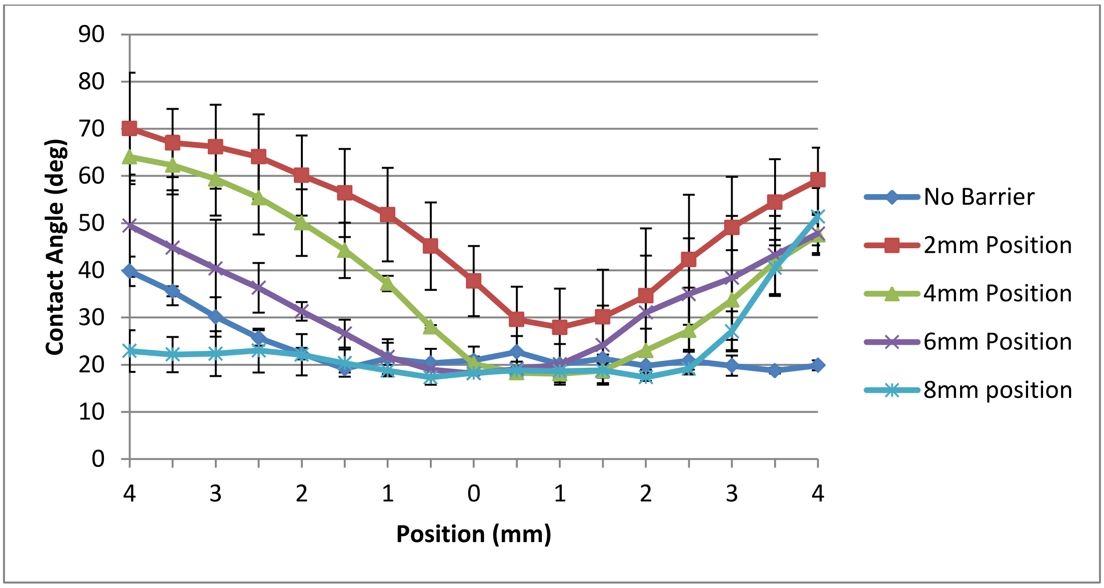

Figure 3.11 Line graph of contact angle profiles taken across polystyrene (PS) samples treated with a plasma jet. Samples were placed 10mm from the plasma jet nozzle and a 2mm diameter blackened glass rod barrier was placed 2mm, 4mm, 6mm and 8mm from the nozzle. Contact angle measurements were taken across central axes of samples at a resolution of 0.5mm. Profiles are the mean of 3 samples. Error bars are ± 1 standard deviation.

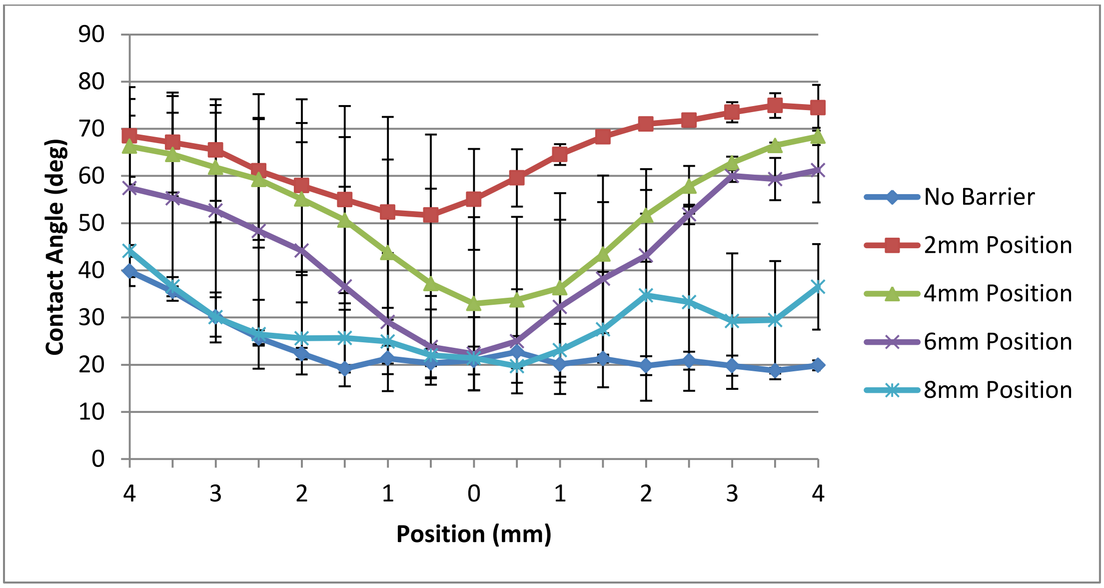

Figure 3.12 Line graph of contact angle profiles taken across polystyrene (PS) samples treated with a plasma jet. Samples were placed 10mm from the plasma jet nozzle and a 3mm diameter blackened glass rod barrier was placed 2mm, 4mm, 6mm and 8mm from the nozzle. Contact angle measurements were taken across central axes of samples at a resolution of 0.5mm. Profiles are the mean of 3 samples. Error bars are ± 1 standard deviation.

When samples were positioned 20mm from the nozzle the contact angle decreased from ≥39° at the edges to ~20° in the centre region. When a 1mm diameter barrier was placed 2mm from the nozzle there was almost no treatment at the sample 20mm from the nozzle (Figure 3.13). When the 1mm diameter barrier was placed 6mm and 10mm there was clearly treatment to the right of the sample centre. When the barrier was placed 14mm from the centre a shadowing effect, or peak within the treated area, was observed. When the barrier was placed close to the sample at 18mm the contact angle profile was similar to the no barrier parameter, however the contact angles in the centre were not as low.

When a wider barrier was used (2mm diameter) severe reduction of treatment was observed at the 2mm, 6mm and 10mm positions. The contact angle in the centre of the 14mm and 18mm parameters did decrease to ~20° similar to the no barrier parameter, however the contact angles at the edges where higher indicating a reduction in the effect of treatment.

The a large reduction in treatment was observed when the barrier was positioned 2mm, 6mm and 10mm with the 2mm diameter barrier was also observed for the 3mm diameter. When the barrier was positioned 14mm from the nozzle the profile was also similar to the 2mm diameter - 14mm distance parameter. However when the barrier was positioned close to the sample at 18mm from the nozzle a shadow effect was observed.

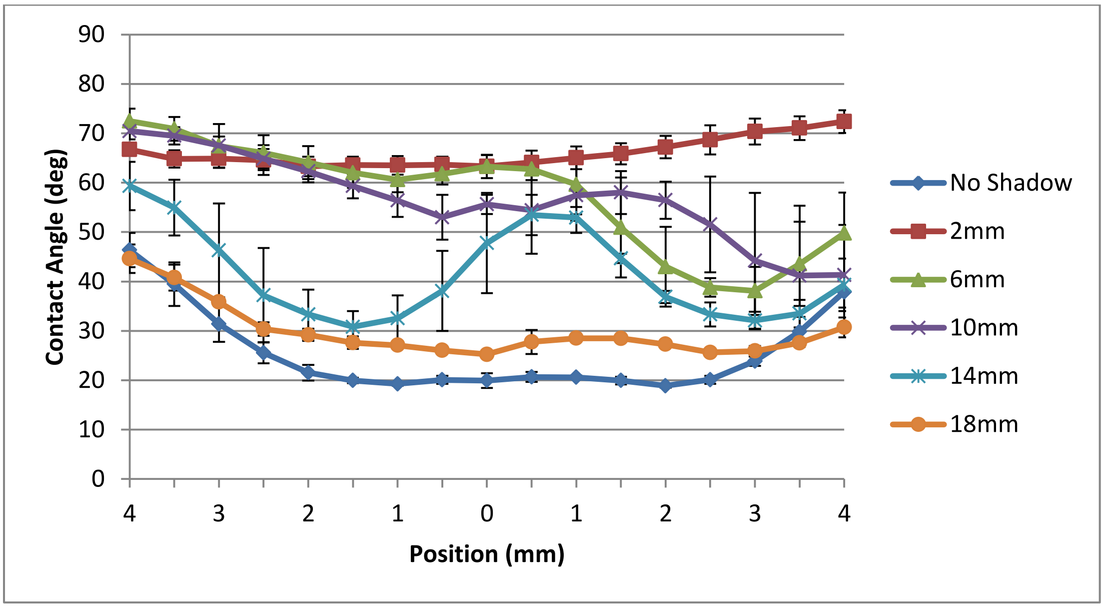

Figure 3.13 Line graph of contact angle profiles taken across polystyrene (PS) samples treated with a plasma jet. Samples were placed 20mm from the plasma jet nozzle and a 1mm diameter glass rod barrier was place 2mm, 6mm, 10mm, 14mm and 18mm from the nozzle. Contact angle measurements were taken across central axes of samples at a resolution of 0.5mm. Profiles are the mean of 3 samples. Error bars are ± 1 standard deviation.

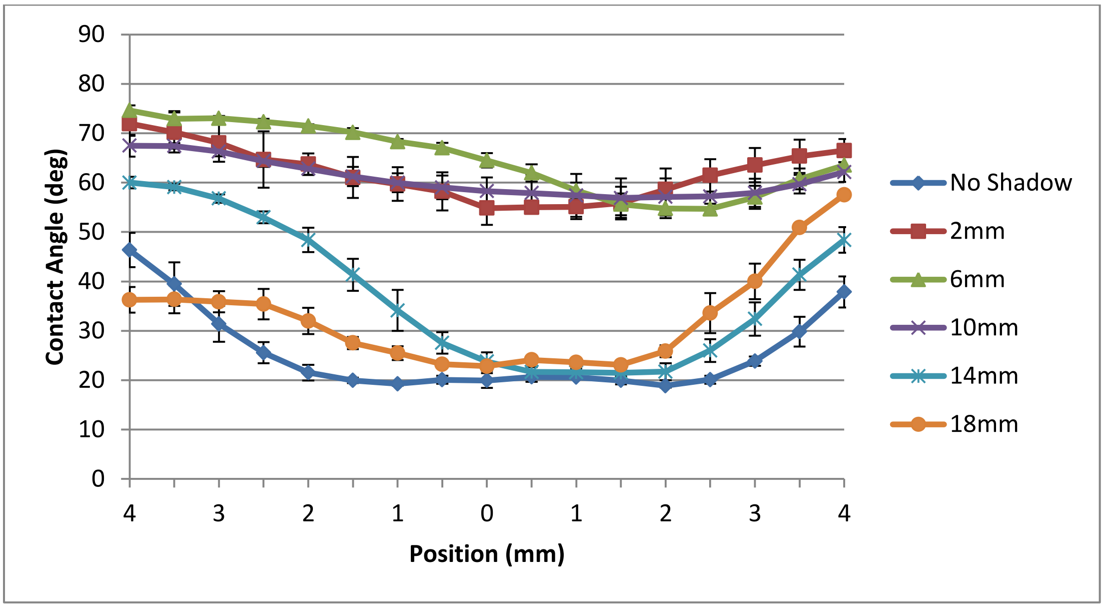

Figure 3.14 Line graph of contact angle profiles taken across polystyrene (PS) samples treated with a plasma jet. Samples were placed 20mm from the plasma jet nozzle and a 2mm diameter blackened glass rod barrier was place 2mm, 6mm, 10mm, 14mm and 18mm from the nozzle. Contact angle measurements were taken across central axes of samples at a resolution of 0.5mm. Profiles are the mean of 3 samples. Error bars are ± 1 standard deviation.

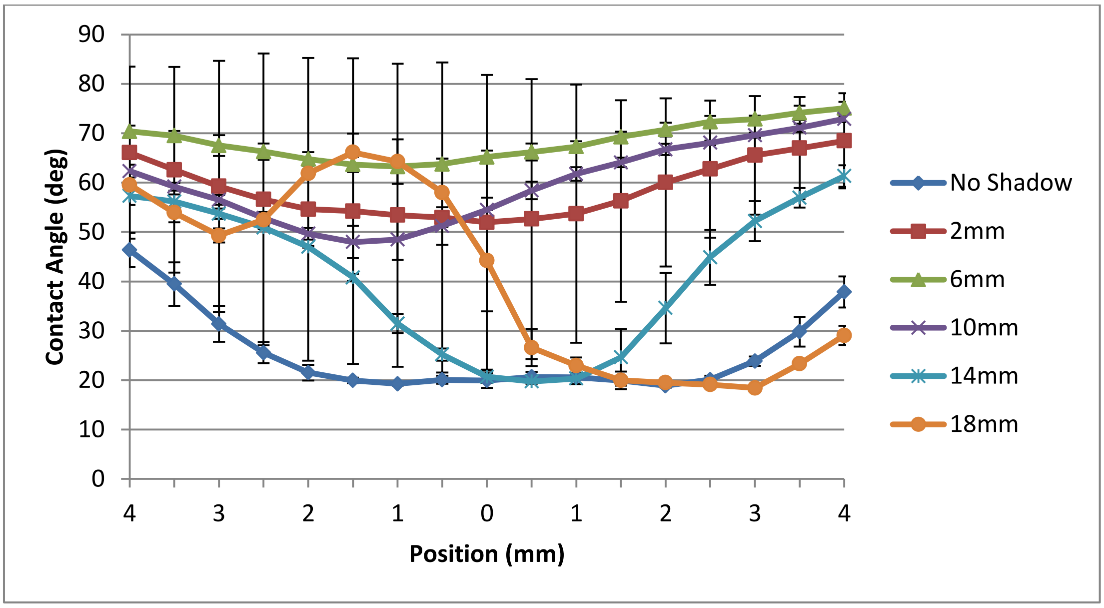

Figure 3.15 Line graph of contact angle profiles taken across polystyrene (PS) samples treated with a plasma jet. Samples were placed 20mm from the plasma jet nozzle and a 3mm diameter blackened glass rod barrier was place 2mm, 6mm, 10mm, 14mm and 18mm from the nozzle. Contact angle measurements were taken across central axes of samples at a resolution of 0.5mm. Profiles are the mean of 3 samples. Error bars are ± 1 standard deviation.

3.4 100µm Microplasma Jet

3.4.1 Ageing

To examine different storage methods samples were either aged in water or air for a maximum of 52 weeks. As this experiment was conducted once, statistical analysis could not be conducted.

3.4.1.1 Contact Angle

When untreated polystyrene (UT-PS) samples were stored in air the contact angle generally remained similar to each other and constant across the sample surface throughout the storage time, however there was a noticeable drop in contact angle of ~10° on the left side of the week 52 profile (Figure 3.16). The average contact angle for all positions at all time points was 83.4° ± 3.4°. At 4 weeks storage in air the contact angle profile had the highest average of 88.2° ± 0.7°, week 52 the lowest average contact angle of 77.8° ± 2.2°.

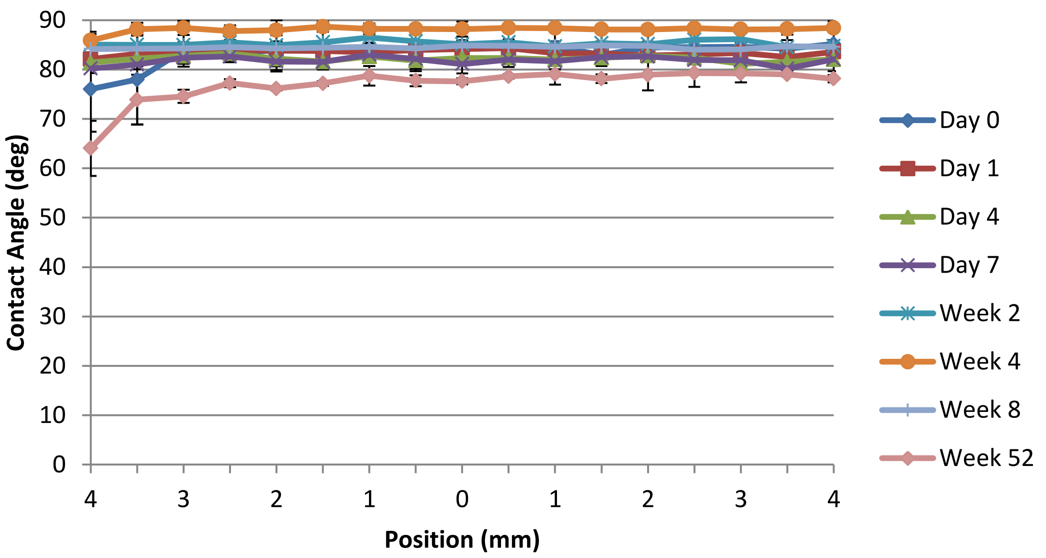

Figure 3.16 Line graph of contact angle profiles of untreated polystyrene (UT-PS) samples stored in air for 0 days, 1 day, 4 days, 7 days, 2 weeks, 4 weeks, 8 weeks and 52 weeks. Contact angle measurements were taken across central axes of samples at a resolution of 0.5mm. Profiles are the mean of 3 samples. Error bars are ± 1 standard deviation.

When UT-PS samples were stored in deionised water the contact angle across the surface of a single parameter remained approximately constant (Figure 3.17). The average contact angle across each parameter decreased with storage duration. Standard deviations were also larger at later time points. The average contact angle for the profiles taken at day 0 and day 1 were very similar at 80° ± 1.7° and 78.2° ± 2.7° respectively. By day 4 the average contact angle dropped to 71.1° ± 5°. The average contact angle for 7 days and 2 weeks storage in water were similar: 65.8° ± 7.4° and 64.8° ± 4.8° respectively. The average contact angle measurements at 4 and 8 weeks were also similar: 49.9° ± 6.3°and 49° ± 10.3° respectively. Following 52 weeks in storage the average contact angle of UT-PS stored in water had dropped to 39.7° ± 3.9°, ~40° lower than the original day 0 contact angle value of 80° ± 1.7°.

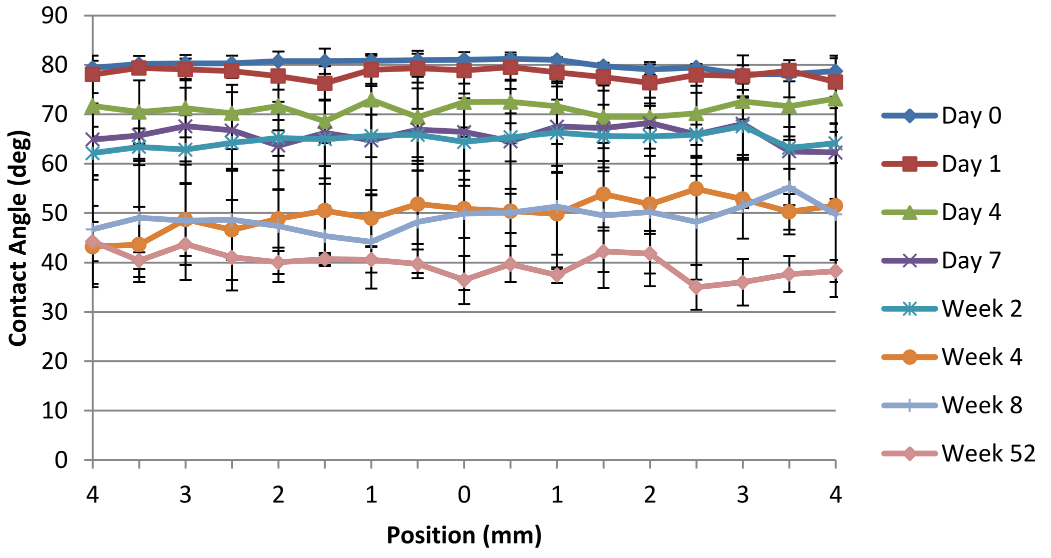

Figure 3.17 Line graph of contact angle profiles of untreated polystyrene (UT-PS) samples stored in deionised water for 0 days, 1 day, 4 days, 7 days, 2 weeks, 4 weeks, 8 weeks and 52 weeks. Contact angle measurements were taken across central axes of samples at a resolution of 0.5mm. Profiles are the mean of 3 samples. Error bars are ± 1 standard deviation.

The contact angle of treated PS (T-PS) samples stored in air showed little difference between day 0 – 8 weeks at both treated (centre) regions (~20 – 37°) and untreated (edge) regions (>80°) (see Figure 3.18). The lowest contact angle was observed at day 0, which reached <20° in the central treated area. Samples stored for 1, 4, 7 days and 8 weeks had contact angles ranging from 20-30° in the central treated regions, however when samples were stored for 2 and 4 weeks the contact angle in the central treated regions was approximately 35-37°, with standard deviations <2°. When samples were stored for 52 weeks in air the contact angle drastically increased in the central treated region, compared to earlier time points. At week 52 the contact angles across the sample had a lesser variance compared to earlier time points. Shown by a reduced contact angle in the untreated region from >80° to less than 70° on the left side, and the central treated region increasing in contact angle to approximately 60°, with a minimum contact angle of 56.3°± 5°.

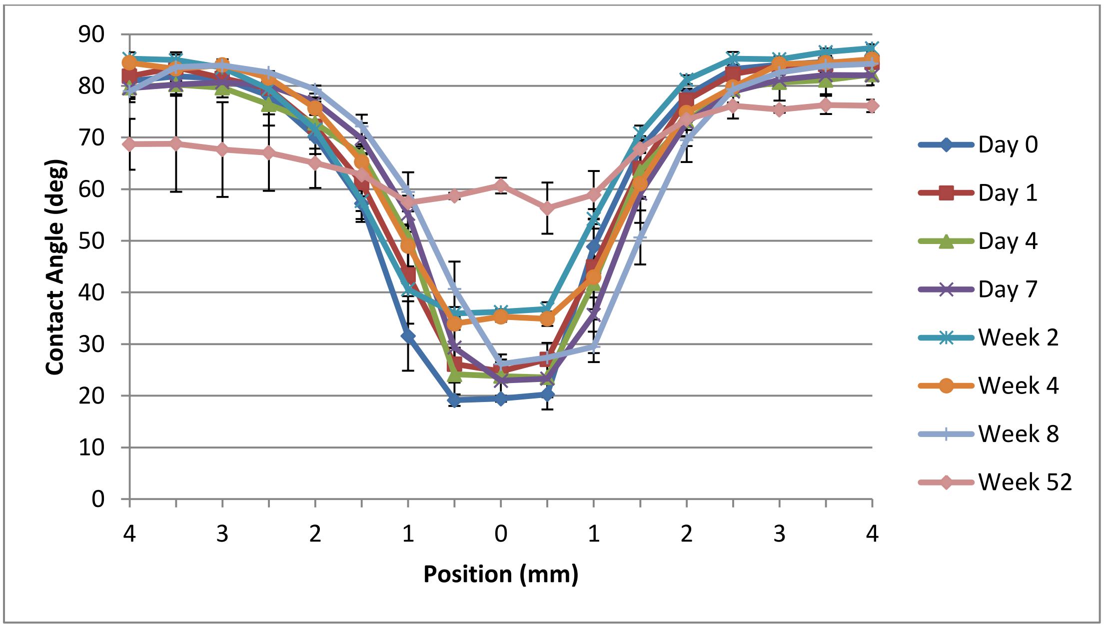

Figure 3.18 Line graph of contact angle profiles of plasma treated polystyrene (T-PS) samples stored in air for 0 days, 1 day, 4 days, 7 days, 2 weeks, 4 weeks, 8 weeks and 52 weeks. Contact angle measurements were taken across central axes of samples at a resolution of 0.5mm. Profiles are the mean of 3 samples. Error bars are ± 1 standard deviation.

When T-PS samples were stored in deionised water the contact angle at the edge untreated regions decreased with age. The standard deviations at the edges of the sample also generally increased with storage duration (Figure 3.19). At day 0 the contact angle at the untreated edge region was between 75° and 80°. After 8 weeks in water storage, the contact angle at the untreated edge regions ranged from 36.9° ± 13.7° (left side) to 41.5° ± 12.4° (right side). The contact angle in the central treated region on days 0, 1, 4, 7 and week

8 remained between 20-26°. The contact angle in the treated centre area at week 2 and 4 were approximately 30° - 35°, similar to the centre treated region of samples stored in air. Following storage in water for 52 weeks the contact angle profile became almost level ranging between ~40° in the centre to ~50° at the edge. Peculiarly the contact angles at the untreated edge were not as low as the contact angle observed at week 8. Treated PS samples stored in deionised water for 4 weeks, 8 weeks and 52 weeks in general had a less varied contact angle profile across the sample compared to other time points, also the distinct central treatment region was not as pronounced.

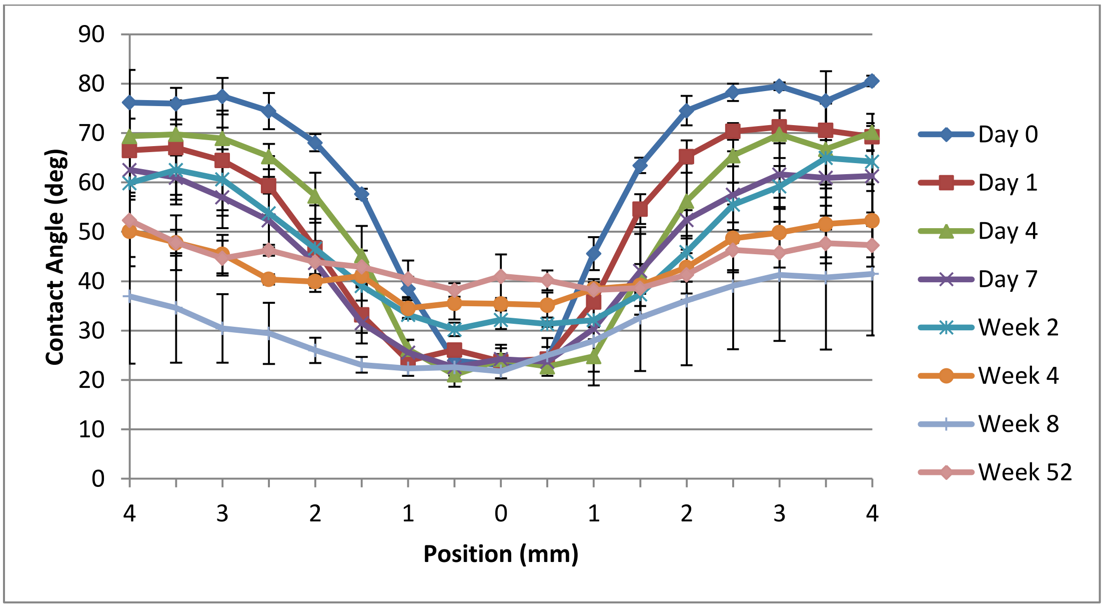

Figure 3.19 Line graph of contact angle profiles of plasma treated polystyrene (T-PS) samples stored in deionised water for 0 days, 1 day, 4 days, 7 days, 2 weeks, 4 weeks, 8 weeks and 52 weeks. Contact angle measurements were taken across central axes of samples at a resolution of 0.5mm. Profiles are the mean of 3 samples. Error bars are ± 1 standard deviation.

3.4.1.2 Cell Culture

N/N1003A rabbit lens epithelial cells were seeded onto both treated and untreated PS samples stored in either air or water for various lengths of time; for a list of parameters and parameter designations see Table 2.1, Section 2.2.1.3.1.3. Samples were fixed at 1 hour, 4hours and 24 hours. The numbers of LECs per field of view were counted in the centre of samples and at 1.5mm, 3mm and 4mm from the centre, which will be referred to as "positions". The following results will be grouped by incubation time points; at each time point untreated and treated parameters will be discussed separately and with separate charts: this was due to the large number of variables. The scale of the y-axis of charts containing untreated and treated conditions within a time point will be the same. TCPS control appears on both untreated and treated charts for ease of comparison. Within each chart the substrate parameters (e.g. Unteated-H2O-1w) will be discussed individually, in terms of the number of cells at each position. Statistical analysis was excluded as the experiment was only conducted once.

3.4.1.2.1 **Ageing Cell Culture - 1 Hour**

The number of LECs on TCPS ranged from 28-41 cells per field of view across all positions after 1 hour. There was a smaller intra-parameter variation across positions compared to any other parameter at the 1 hour incubation time point (Figure 3.20). The number of LECs on untreated PS was typically highest in the central position (Untreated-Air-4d being the only exception) and deceased with distance from the centre. The number of cells in the centre of the Untreated-Air-0d parameter (96 ± 20 cells per field of view) was much higher than all other parameters at this time point, included treated samples: for the remaining untreated parameters the number of LECs in the centre ranged from 30-61 cells per field of view. By 4mm from the centre the number of cells on the all untreated air-stored samples ranged from 6-10 cells per field of view. There was no clear difference between neither storage duration nor storage medium for untreated PS at this time point, particularly with the lack of statistical analysis.

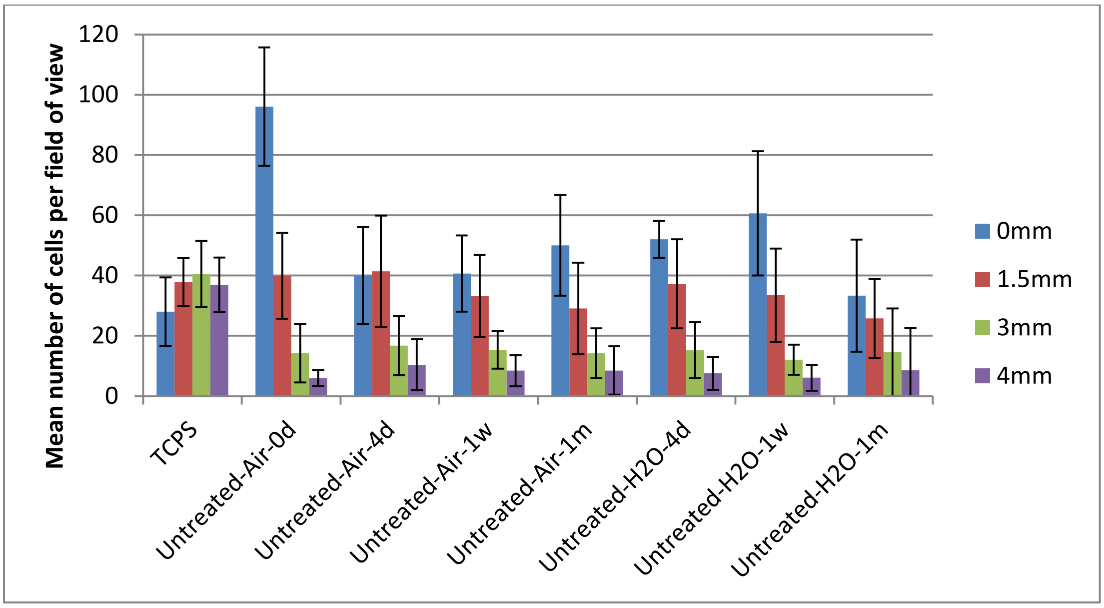

Figure 3.20 Bar chart displaying mean number of N/N1003A rabbit lens epithelial cells (LECs) per field of view at the centre of samples and 1.5mm, 3mm and 4mm from the centre of samples at 1 hour post-seeding. Untreated polystyrene (PS) was stored in air (Air) or water (H_2O) for 0 days (0d), 4 days (4d), 1 week (1w) or 1 month (1m). Tissue culture PS (TCPS) served as a control. Profiles are the mean of 3 samples. Error bars are ± 1 standard deviation.

As mentioned above TCPS had 28-41 cells per field of view across all positions at the 1hr incubation time point. As with untreated PS, the number of cells on treated PS was generally higher in the centre and decreased with distance from the centre (Figure 3.21). There was a larger variation in the number of cells in the centre of treated PS (24-69 cells per field of view) compared to untreated PS, if the anomalous untreated-air-0d was excluded. The number of cells at the 4mm position on treated samples ranged from 4-14 cells per field of view. The numbers and pattern of LECs; i.e. the reduction of cells from the centre to the edge, were similar for both treated and untreated PS, stored in both air and water, at the 1 hour incubation time point, however without repetition and statistical analysis the results are inconclusive.

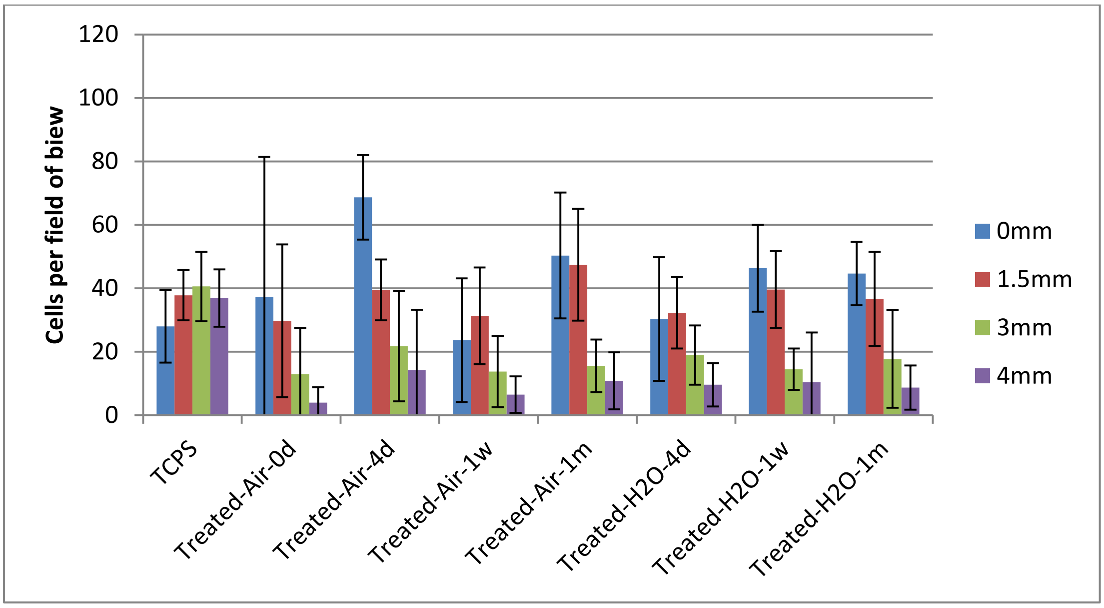

Figure 3.21 Bar chart displaying mean number of N/N1003A rabbit lens epithelial cells (LECs) per field of view at the centre of samples and 1.5mm, 3mm and 4mm from the centre of samples at 1 hour post-seeding. Samples were treated polystyrene (PS) stored in air (Air) or water (H_2O) for 0 days (0d), 4 days (4d), 1 week (1w) or 1 month (1m). Tissue culture PS (TCPS) served as a control. Profiles are the mean of 3 samples. Error bars are ± 1 standard deviation.

3.4.1.2.2 Ageing Cell Culture - 4 Hours

After 4 hours of growth the numbers of LECs on TCPS ranged from 129-157 cells per field of view, more than 3 times the amount observed at the 1 hour incubation time point (Figure 3.22). LEC growth in the centre of untreated PS increased similarly to TCPS. The number of cells more than doubled at each position in comparison to day 1, which resulted in a larger difference in the number of LECs in the centre and the 4mm position; however, this excludes the Untreated-Air-1m parameter, which had low cell numbers (<50 cells per field of view) at all positions. The number of cells in the centre of untreated samples ranged from 98-193 cells per field of view (excluding the Untreated-Air-1m parameter), and the number of cells at the 4m position ranged from 17-24 cells per field of view on all parameters. There was typically greater number of LECs on water stored samples compared the relative positions on air stored samples. Shorter storage times also resulted in higher numbers of LECs in the centre position.

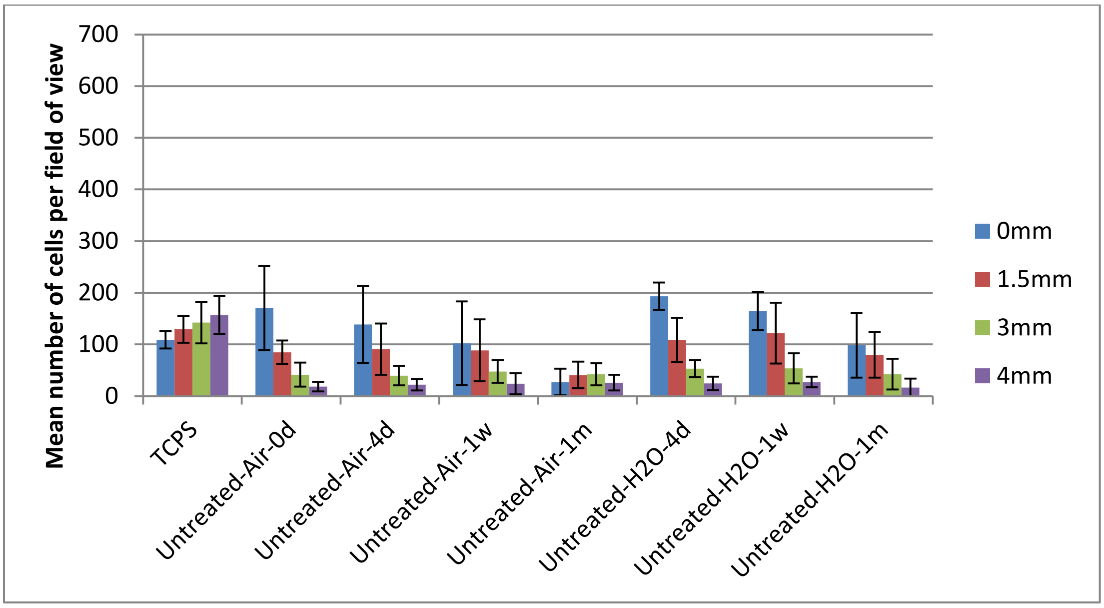

Figure 3.22 Bar chart displaying mean number of N/N1003A rabbit lens epithelial cells (LECs) per field of view at the centre of samples and 1.5mm, 3mm and 4mm from the centre of samples at 4 hours post-seeding. Untreated polystyrene (PS) samples were stored in air (Air) or water (H_2O) for 0 days (0d), 4 days (4d), 1 week (1w) or 1 month (1m). Tissue culture PS (TCPS) served as a control. Profiles are the mean of 3 samples. Error bars are ± 1 standard deviation.

As stated above the numbers of cells on TCPS ranged from 129-157 cells per field of view at the 4 hour incubation time point (Figure 3.23). There were more cells in the centre and 1.5mm positions than the 3mm and 4mm positions on treated PS samples stored in air or water. Strikingly, the increase in number of LECs in the centre of treated samples stored in air (163-455 cells per field of view) was much higher than those stored in water (82-148 cells per field of view), however the standard deviations were large on the air stored parameters. On the Treated-Air-1w and Treated-Air-1m there were much more LECs in the centre position compared to samples stored in air for shorter durations. At the 3mm and 4mm positions there was much less variation in the number of LECs on treated PS compared to the centre and 1.5mm positions. At 4mm from the centre the number of LECs on all treated PS ranged from 10-26 cells per field of view, which was similar to the 4mm position on untreated PS. Storage duration in water seemed to have little effect on cell number, however there were more cells in the centre and 1.5mm positions of the Treated-H2O-1m parameter compared to the other water storage parameters.

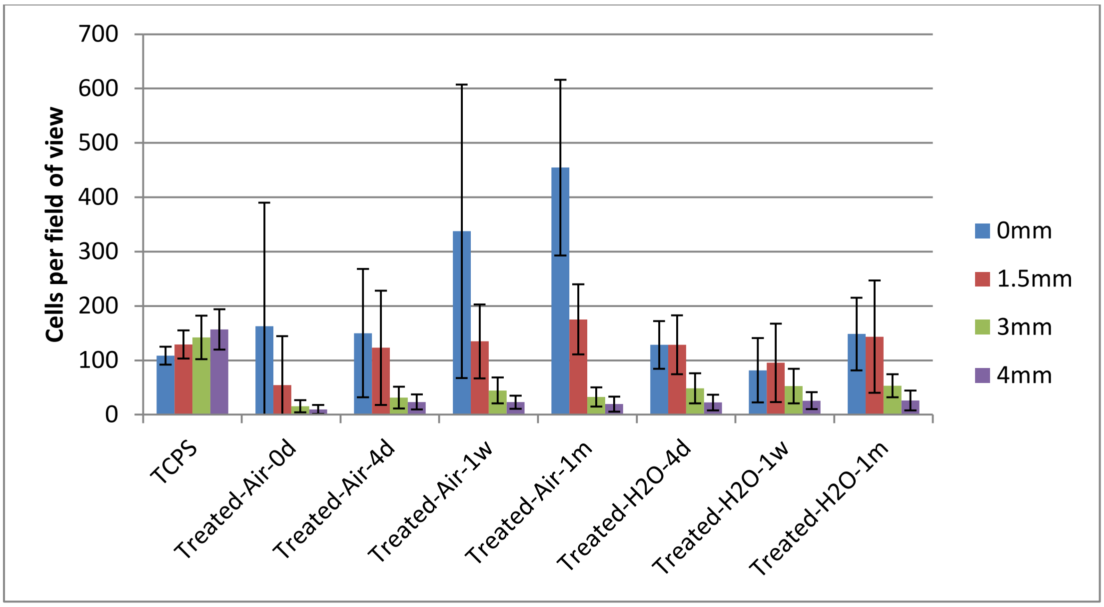

Figure 3.23 Bar chart displaying mean number of N/N1003A rabbit lens epithelial cells (LECs) per field of view at the centre of samples and 1.5mm, 3mm and 4mm at 4 hours post-seeding. Treated polystyrene (PS) samples were stored in air (Air) or water (H2O) for 0 days (0d), 4 days (4d), 1 week (1w) or 1 month (1m). Tissue culture PS (TCPS) served as a control. Profiles are the mean of 3 samples. Error bars are ± 1 standard deviation.

3.4.1.2.3 Ageing Cell Culture - 24 Hours

Following 24 hours of incubation, the numbers of cells across all positions of TCPS (43-58 cells per field of view)(Figure 3.24) was less than half the cell number observed for TCPS at the 4 hour incubation time point, similar to the number of cells observed at the hour 1 incubation time point. The number of cells in the centre of untreated samples ranged from 45-100 cells per field of view; this resulted in a smaller difference in LEC number between the centre and 4mm position (13-32 cells per field of view) on the untreated parameters, compared to the 4 hours incubation time point. Inversely to the 4 hour time point there were fewer cells in the centre and 1.5mm positions of samples stored in water, compared to the equivalent samples stored in air; however, this difference was small. No obvious pattern due to storage time was observed.

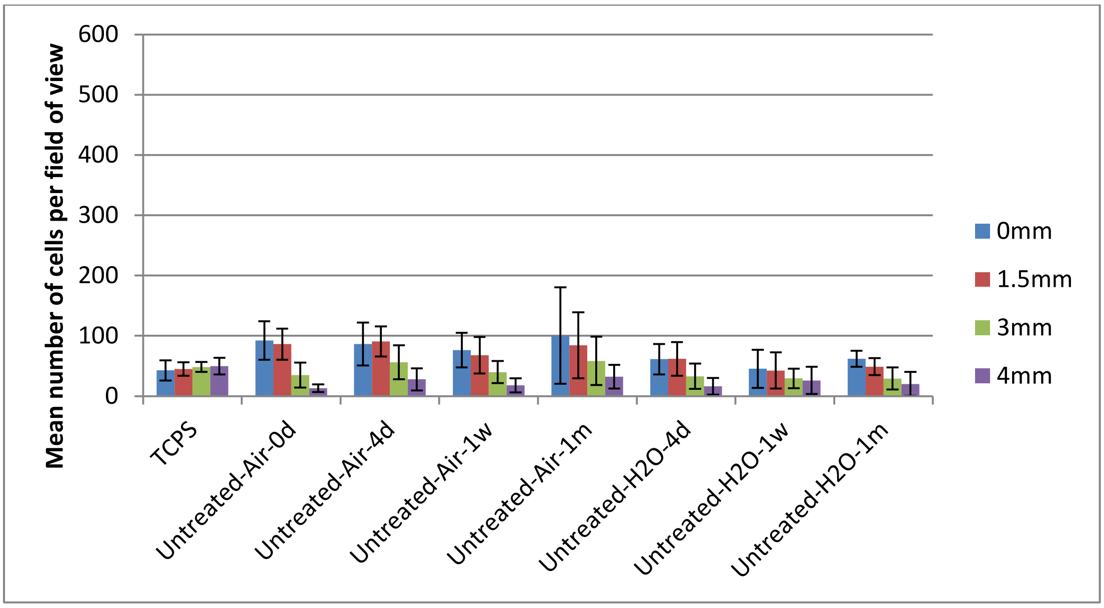

Figure 3.24 Bar chart displaying mean number of N/N1003A rabbit lens epithelial cells (LECs) per field of view at the centre of samples and 1.5mm, 3mm and 4mm from the centre of samples at 24 hours post-seeding. Untreated polystyrene (PS) samples were stored in air (Air) or water (H_2O) for 0 days (0d), 4 days (4d), 1 week (1w) or 1 month (1m). Tissue culture PS (TCPS) served as a control. Profiles are the mean of 3 samples. Error bars are ± 1 standard deviation.

There were a large number of LECs in the central position of treated samples following 24 hours of growth (247-524 cells per field of view)(Figure 3.36), irrespective of storage medium. There were also many LECs in the 1.5mm position of treated PS (155-262 cells per field of view). Little cell attachment and growth remained to be seen at the 4mm position (7-34 cells per field of view), at which the number of LECs were similar to those observed on untreated PS at the 4mm position. There was no clear link between samples stored in air and cell attachment; however the number of LECs in the centre of treated samples stored in water increased with storage time.

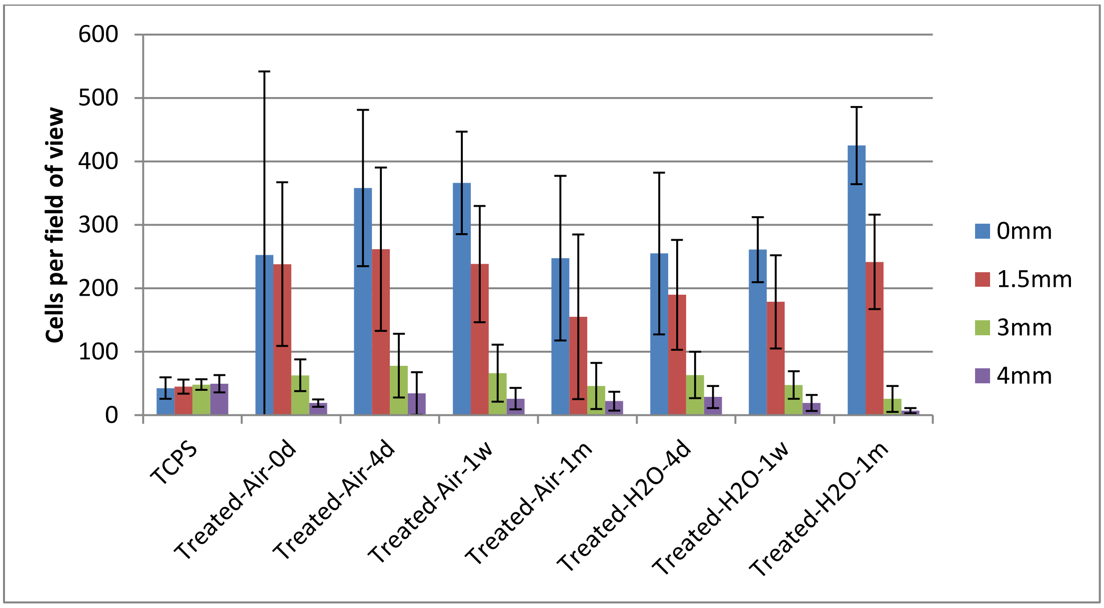

Figure 3.25 Bar chart displaying mean number of N/N1003A rabbit lens epithelial cells (LECs) per field of view at the centre of samples and 1.5mm, 3mm and 4mm from the centre of samples at 24 hours post-seeding. Samples were treated PS stored in air (Air) or water (H_2O) for 0 days (0d), 4 days (4d), 1 week (1w) or 1 month (1m). Tissue culture PS (TCPS) served as a control. Profiles are the mean of 3 samples. Error bars are ± 1 standard deviation.

In summation; there was a notable increase in the number of LECs on TCPS at the 4 hour incubation time point, however this reduced by 24 hours of incubation. Both untreated and treated samples stored either in air or water for any duration typically had the highest number of LECs in the central position, and the number of LECs decreased with distance from the centre. In some conditions in the 1hr and 4hr time points there were more cells in the centre of untreated samples compared to the treated counterparts. Similar to TCPS, there was an increase in the number of cells in the centre of untreated PS between the 1 and 4 hour incubation periods but this decreased again by an extent by 24 hours. The number of LECs in the centre and 1.5mm position of treated PS generally increased with incubation time. There was no clear link between cell attachment and storage methods.

3.4.2 Preliminary Study of the Effects of Flow Rate and Distance

Three different flow rates: low, medium and high, with increasing distance away from the jet nozzle at 1mm, 5mm and 10mm distance were investigate. These various parameters were investigated to determine the size of treatment, with the aim of reducing the number of variables for further examination. Smaller treatment areas were preferable. PS coverslips were used for this study. Results will be grouped together and discussed in terms of the flow rates: low, medium and high.

3.4.2.1 Contact Angle

3.4.2.1.1 Low Flow Rate

When PS samples were placed 1mm from the microplasma jet nozzle, and treated with the low flow rate (~22sccm) a sharp decrease in contact angle was observed in the centre of the samples. The contact angle decreased from ≥80° at the edges, to <20° in the central treated area (Figure 3.26). The length of the contact angle profile with <20° was 1.5mm. When samples were positioned 5mm from the nozzle, the reduction in contact angle from the sample edges toward the centre was more gradual. Only one point on the contact angle profile was <20°. When samples were positioned 10mm from the nozzle, the decrease of contact angle became less pronounced, with the central treated region having a minimum contact angle of 43.5°. Large standard deviations (10mm) were observed within this central treated region.

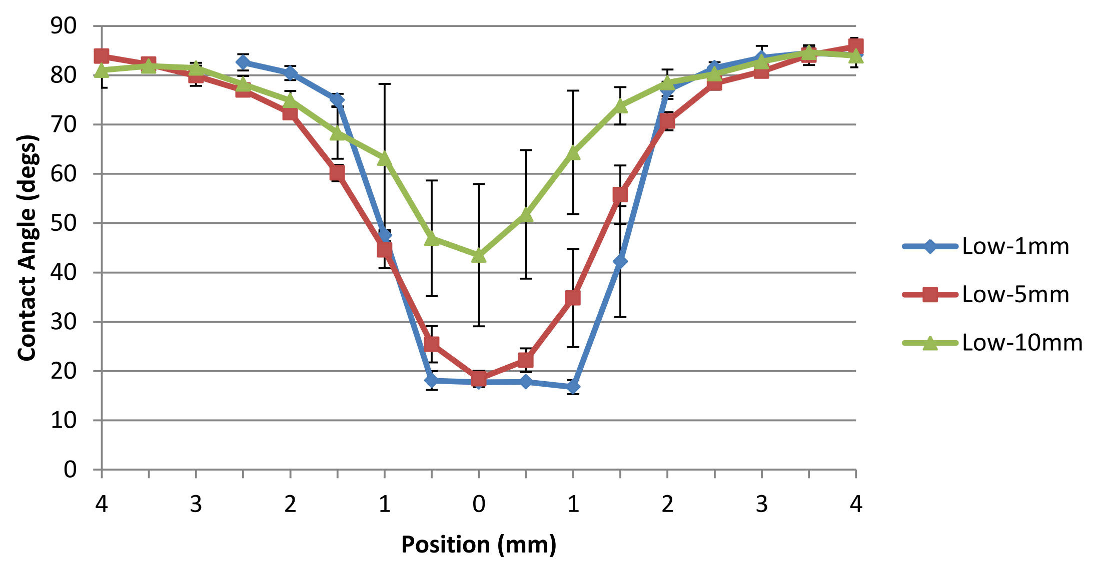

Figure 3.26 Line graph of contact angle profiles taken across plasma treated polystyrene samples at distances of 1mm, 5mm and 10mm from the nozzle. A low flow rate of ~22sccm was used. Contact angle measurements were taken across the central axes of treated polystyrene samples with a spatial resolution of 0.5mm. Profiles are the mean of 3 samples. Error bars are ± 1 standard deviation.

3.4.2.1.2 Medium Flow Rate

When a medium flow rate (~150sccm) was used to treat samples the width of the treatment was larger than that observed for the low flow rate. Typically samples did not have an untreated region at the edge characterised by a contact angle of ~80° or greater, excluding a single point on the 1mm profile which reached 80° ± 4.6° (Figure 3.27). Samples treated at 1mm, 5mm and 10mm all had treatments in the centre resulting in contact angles of ≤20°, however the width of these regions of treatment differed between the parameters. The diameter where the contact angle profile had a contact angle of ≤20° was 3.5mm for the 1mm and 5mm parameters and 1.5mm for the 10mm parameter. The 1mm parameter displayed a sharper decrease in contact angle and higher maximum contact angle on the left side compared to the 5mm and 10mm parameters.

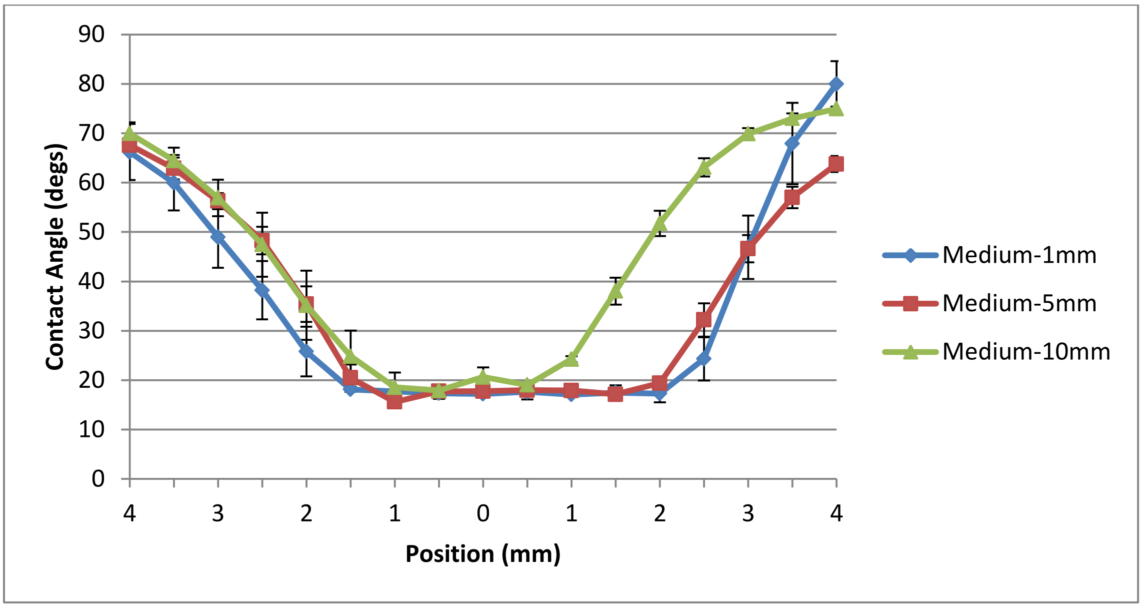

Figure 3.27 Line graph of contact angle profiles taken across samples placed at 1mm, 5mm and 10mm away from the nozzle. A medium flow rate of ~150sccm was used. Contact angle measurements were taken across the central axes of treated polystyrene samples with a spatial resolution of 0.5mm. Profiles are the mean of 3 samples. Error bars are ± 1 standard deviation.

3.4.2.1.3 High Flow Rate

Samples treated with the high flow rate (~300sccm) did not have contact angles which were 80° indicating the entire surface of the samples were treated. The contact angles at the edges of the 1mm parameter were higher than those of the 5mm and 10mm parameters (Figure 3.28). The contact angle in the centre of samples treated with the high flow rate had a greater variance than those of the low and medium flow rates. The maximum treatment in the centre was observed to be ~20-30° for all high flow rate parameters, whereas with low and medium flow rates this was ≤20°. The length of the profile which indicated maximum treatment (<30°) was 3.5mm for the 1mm parameter, 5mm for the 5mm parameter and 4.5mm for the 10mm parameter.

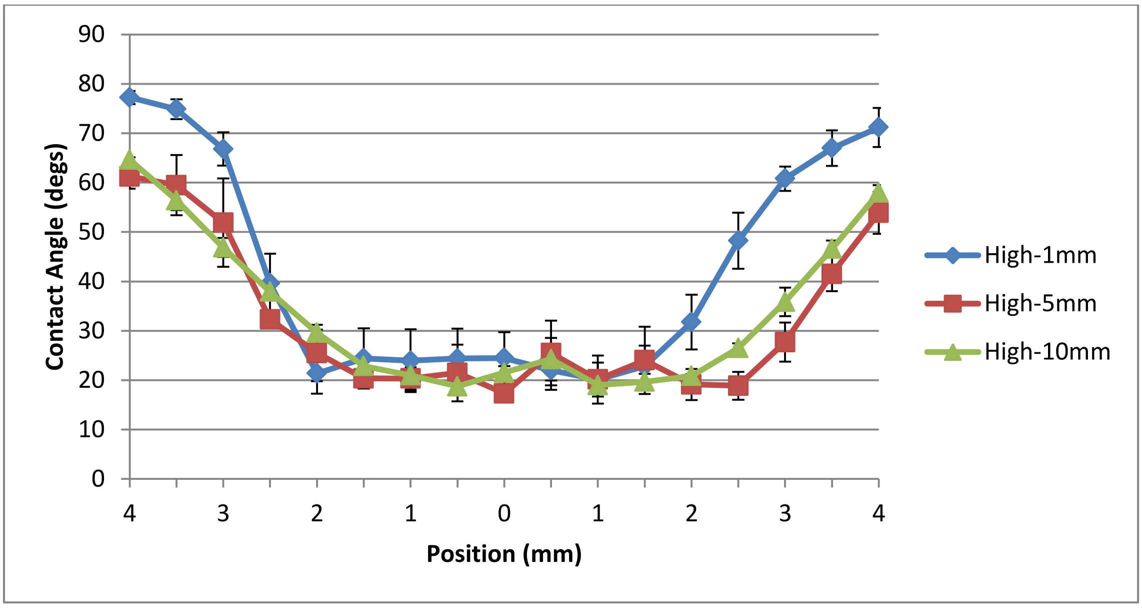

Figure 3.28 Line graph of contact angle profiles taken across samples which were positioned 1mm, 5mm and 10mm distance away from the nozzle. A flow rate of ~300sccm was used. Contact angle measurements were taken across the central axes of treated polystyrene samples with a spatial resolution of 0.5mm. Profiles are the mean of 3 samples. Error bars are ± 1 standard deviation.

In summation; when treated with a low flow rate the width of the treatment was smaller than those observed at the higher flow rates, however the change in contact angle due to treatment with the low flow rate decreased as samples were positioned further from the nozzle. When samples were treated with the medium flow rate the width of the treatment area was smaller on the 10mm parameter compared to the 1mm and 5mm parameters. With a high flow rate the 1mm distance had the smallest width of treatment. In samples treated a low and high flow rate the 1mm distance had the most defined treatment area, however when samples were treated with the medium flow rate the 10mm distance had the most defined treatment area.

3.4.3 Investigation of the Effects of Flow Rate and Distance

Following the previous preliminary flow rate and distant work further in-depth investigation using various cell culture and surface analysis techniques was conducted. It was decided to continue with fewer parameters to make analysis of various techniques manageable. Low and high flow rates at 1mm and 10mm sample-nozzle distances were investigated as the preliminary results indicated distinct treatment areas and they represented the minimum and maximum capabilities of the plasma setup.

3.4.3.1 Contact Angle

The average contact angle of TCPS and UT-PS was 35° ± 2.3° and 77° ± 6° (Figure 3.29), respectively. The contact angle of UT-PS decreased to 63.6° ± 14.5° at the left side of the sample, between the 4mm-3mm position.

There was a distinct decrease in contact angle in the central treated area of low flow rate - 1mm sample-nozzle distance (L1) parameter, from approximately 77° at the untreated edges to <30° in the centre of the sample. This central treated area was 1.5mm wide. The contact angle of L1 parameter was significantly lower ($p<0.05$) than UT-PS between the positions of left-2mm and right-1.5mm (total 3.5mm).

When samples were placed 10mm from the nozzle and treated with a low flow rate (L10) there was a reduction in the effect of the treatment, shown by a higher contact angle in the central area compared to L1 parameter. The contact angle reduced from >70° at the edges to a minimum of 55° ± 15.9° in the central region. Large standard deviations were observed in the centre of the L10 parameter profile. The contact angle of L10 parameter was significantly lower ($p<0.05$) than UT-PS between the positions of left-2mm and right-4mm (total 6mm).

When samples were treated with the high flow rate at either 1mm (H1) or 10 mm (H10) sample-nozzle distance the contact angle never exceeded 70°. The average contact angle in the centre treated region for both of these parameters reduced to ~25°. When samples were positioned 1mm away from the nozzle a very wide treatment region in the centre was observed. The contact angle in this central region which was ~25° spanned 4.5mm across the H1 profile. The width of this centre region decreased to 2.5mm when samples were positioned 10mm away from the nozzle. The contact angle of both the H1 and H10 parameters was significantly lower ($p<0.05$) than UT-PS between the positions of left-3.5mm and right-4mm (total 7.5mm).

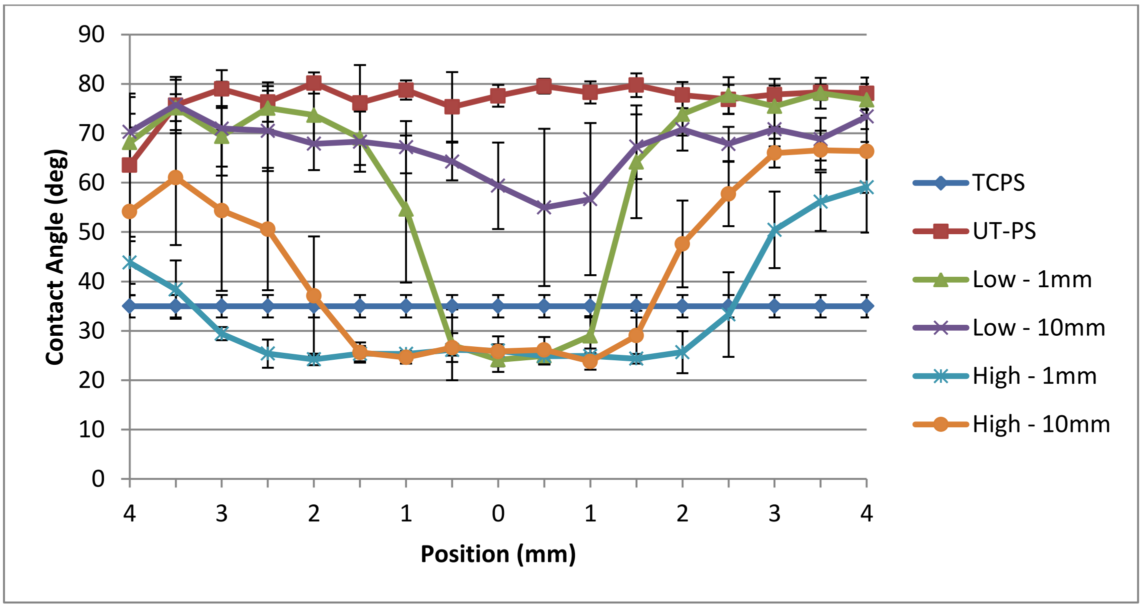

Figure 3.29 Line graph of contact angle profiles taken across polystyrene (PS) samples treated with a plasma jet at 1mm and 10mm distance from the nozzle with low (30sccm) and high (150sccm) flow rates. Tissue culture polystyrene (TCPS) and untreated PS (UT-PS) served as controls. Contact angle measurements were taken across central axes of samples at a resolution of 0.5mm. Error bars are ± 1 standard deviation.

From the 2D contact angle maps it was observed that there was little change in the contact angle across the surface of UT-PS which had an average contact angle of 78.2° ± 4.3° (Figure 3.30). The 2D contact angle maps for L1 parameter demonstrated the treatment area was approximately circular. The treated area of the L10 parameter was much more irregular in shape compared to the other treatment parameters. The minimum contact angle in the central treated area (56.3°) for L10 was also higher than that of the other treated parameters. The contact angle profile of the H1 parameter demonstrated an almost circular pattern, however this was wider than that of the L1 parameter. The H10 parameter contact angle profile was smaller and more circular than the H1 parameter map, yet it was still larger than that of the L1 parameter map.

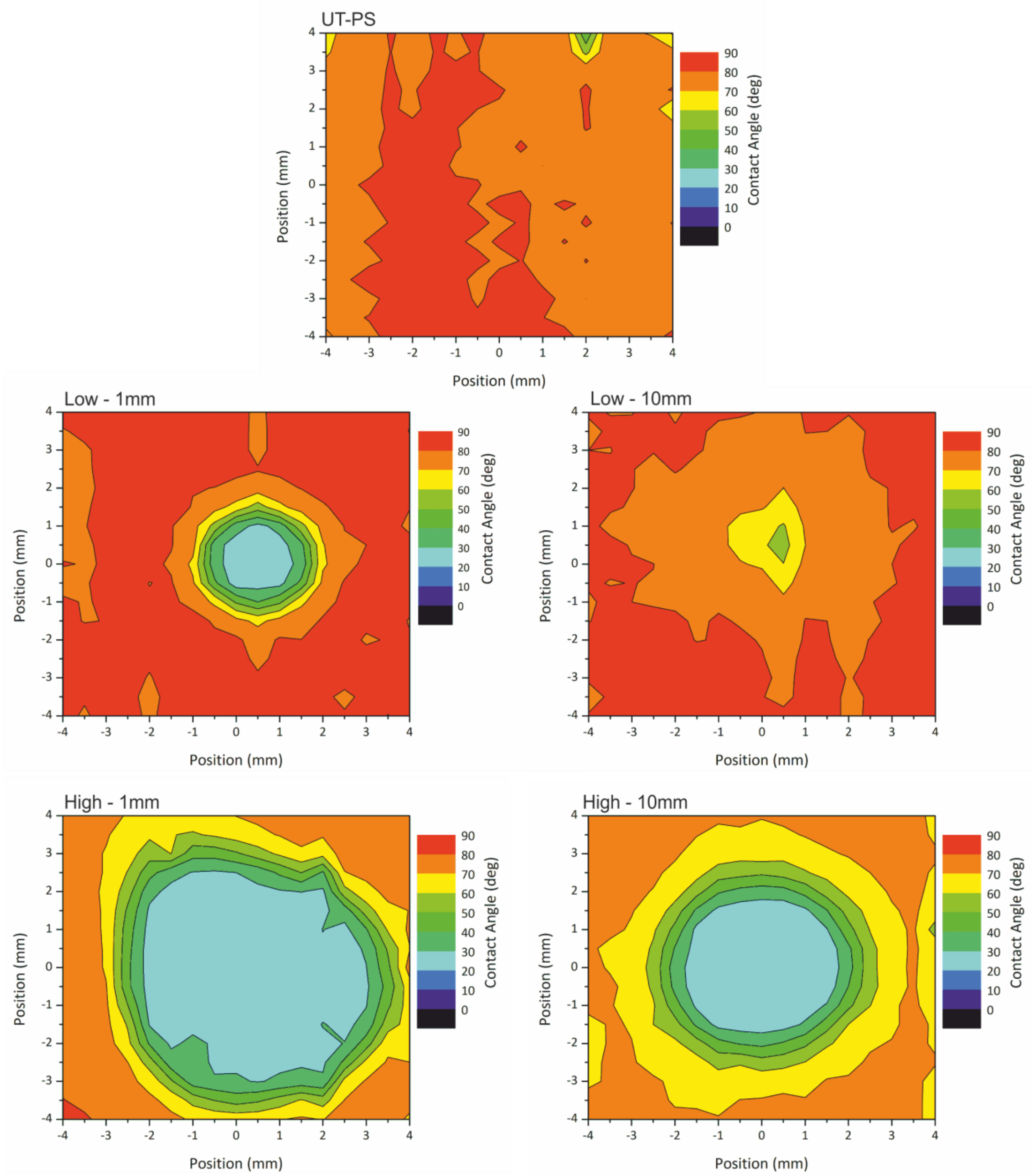

Figure 3.30 2D Contact angle plots of untreated polystyrene (UT-PS) and PS treated with a microplasma jet. Contact angle measurements were made with a spatial resolution of 0.5mm. Maps are from single samples.

3.4.3.2 Atomic Force Microscopy

AFM analysis of UT-PS determined the root mean squared roughness (Rq) to be 0.9 ± 0.6nm and the average roughness (Ra) to be 0.6 ± 0.3nm. The micrographs appeared relatively smooth with a few small features. When surfaces were treated with the microplasma jet the Ra and Rq values increased. For L1 parameter the Rq was 0.9 ± 0.5nm and the Ra was

0.7 ± 0.3nm. These samples typically had a greater density of features compared to UT-PS. The Rq and Ra of samples treated with L10 parameter were 1.1 ± 0.7nm and 0.7 ± 0.4nm respectively. These samples appeared similar to the UT-PS. Samples treated with high flow rate, 1mm and 10mm sample-nozzle distance had the highest roughness values of all parameters and displayed a higher number of features, similar to the L1 distance parameter. For the H1 parameter the Rq was 1.1 ± 0.9nm and the Ra was 0.9 ± 0.7nm. When the samples were placed 10mm (H10) from the nozzle the Rq and Ra values were 1.3 ± 0.5nm and 0.9 ± 0.3nm, respectively.

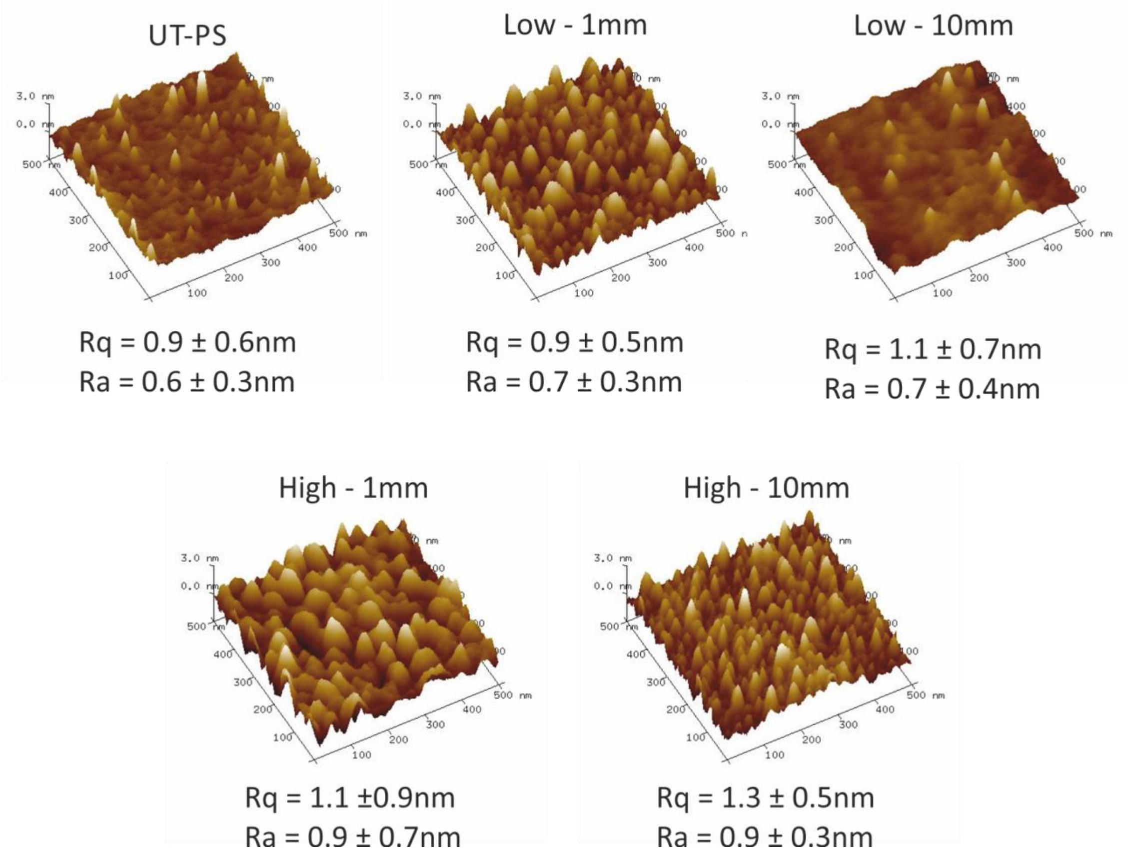

Rq = 0.9 ± 0.6nm
Ra = 0.6 ± 0.3nm

Rq = 0.9 ± 0.5nm
Ra = 0.7 ± 0.3nm

Rq = 1.1 ± 0.7nm
Ra = 0.7 ± 0.4nm

Rq = 1.1 ±0.9nm
Ra = 0.9 ± 0.7nm

Rq = 1.3 ± 0.5nm
Ra = 0.9 ± 0.3nm

Figure 3.31 AFM micrographs with average roughness (Ra) and root mean squared roughness (Rq) values ± standard deviations for untreated polystyrene (UT-PS) and PS treated with a microplasma jet. Mean Ra and Rq were determined from 4 measurements in the centre of 4 samples per parameter. The mean AFM was preformed in tapping mode at a frequency of 1Hz with 512samples/line, using silicone cantilever with a spring constant of 40N/m.

Although there were changes in roughness between the parameters, these were not statistically significant (p>0.05).

3.4.3.3 X-Ray Photoelectron Spectroscopy

Broad scan spectra of UT-PS and T-PS were taken, as were high resolution spectra of the C1s and O1s peaks. C1s high resolution peaks for UT-PS and T-PS were resolved into 5 components: C-C/C-H at 285eV, C-O at 285.7eV, C=O/O-C-O at 287.3, O=C-O at 289.7 and π-π* shake-up satellite peak at 291.7eV. The O1s high resolution scans were resolved into 2 components on treated PS: O=C at 532.1eV and O-C at 533.9eV [5].

The broad scan x-ray photoelectron spectra indicate that the presence of O1s was difficult to detect on UT-PS (Figure 3.32). The high resolution O1s peak could not be resolved into components due to the high level of noise. The large contribution from the C-C/C-H was evident in the high resolution C1s spectra; however there was a large contribution from the C-O component, but this was mostly beneath the envelope of the C-C/C-H component.

The presence of oxygen was clearly demonstrated on the broad scan spectra of T-PS (Figure 3.32). The high resolution spectra for the O1s peaks on T-PS indicated that the single bond O-C component contributed slightly more than the double bond O=C component. The high resolution spectra of C1s for T-PS demonstrated that although C-C/C-H contributed to most of the area under the peak, there was a large C-O component. The other oxygen containing components contributed little and there was a small π-π* shake-up peak. From the high resolution spectra of UT-PS and T-PS it was evident that there was an asymmetry to the peak shape, therefore and asymmetric function was added to the Gaussian:Lorentzian line shape for the contributions in this experiment.

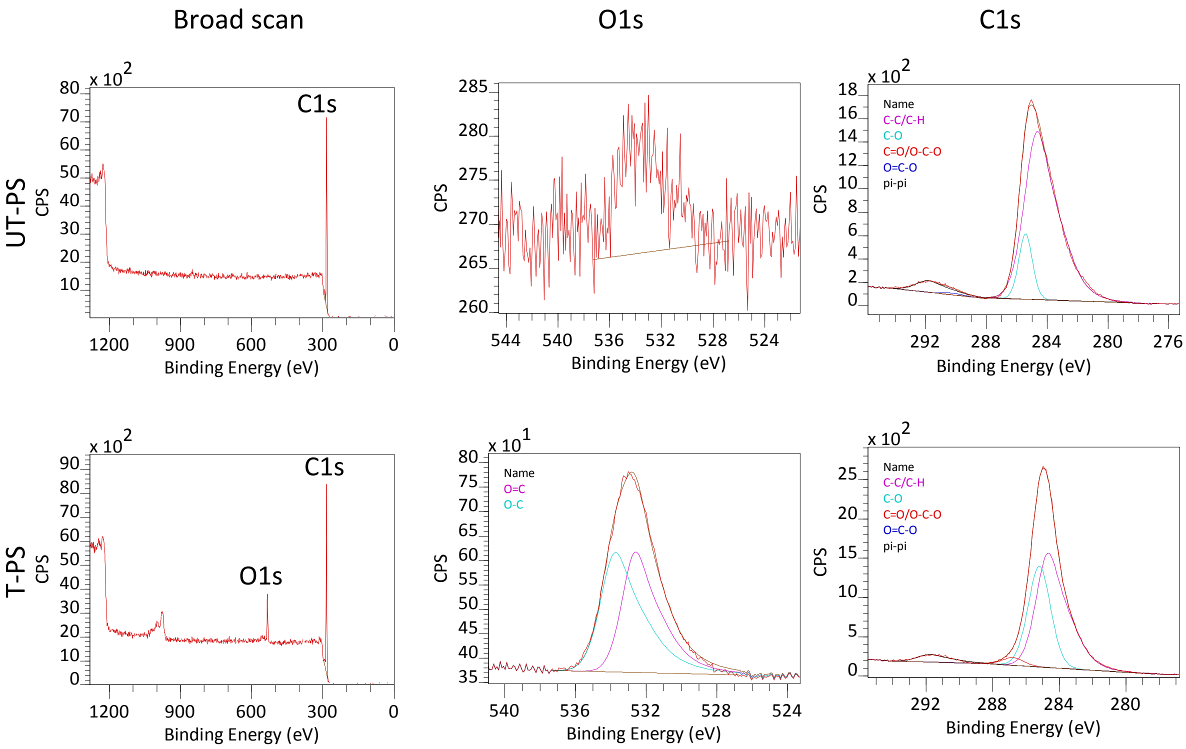

Figure 3.32 X-ray photoelectron spectrographs of untreated polystyrene (UT-PS) and treated polystyrene (T-PS). Broad scans were taken at pass energy of 100eV; C1s and O1s high resolution scans were taken at 50eV. An asymmetry, resulting in a tail on the low binding energy side, was observed on the high resolution scans therefore a asymmetric function was added to the Gaussian:Lorentzian line functions.

The surface atomic concentration UT-PS and T-PS were determine from the areas under the peak on broad scan XPS spectra and presented as % ± standard deviations. High resolution spectra were used to determine the contribution of various peak components to the total area. The broad scan spectra of UT-PS demonstrated that 3.9 ± 1.1% oxygen was present, carbon was the only other element present on the spectra. Despite the presence of oxygen from the broad scans, on UT-PS samples the O1s peaks could not be resolved into components due to high levels of noise. The high resolution C1s spectra for UT-PS were resolved into various components, with the largest contribution from C-C/C-H structure (74.3 ± 2.8%). The C-O component contributed 17.8 ± 1.4%, whilst C=O/O-C-O and O=C-O contributed a total of 1.8 ± 1.2%. The π-π* shake-up component contributed 6.1% to the C1s peak.

Following plasma treatment (T-PS), the broad scan spectra indicated that oxygen contributed 20.5 ± 4.7% of the total surface atomic concentration. The high resolution spectra of the O1s peaks demonstrated that the O-C single bond contributed 53.8 ± 1.1% compared to 46.1 ± 1.1 for the double bond O=C contribution. High resolution C1s spectra demonstrated that the C-C/C-H component provided the main contribution to the C1s peak (52.7 ± 6.1%). The second largest contribution was from C-O component (42.2 ± 5.8%). The C=O/O-C-O comprised 1.2 ± 1.3% of the total C1s peak, whilst the O=C-O did not contribute to the C1s peak. The π-π* shake-up peak was 4% of the total area for the C1s peak. The difference in the O/C ratio demonstrates that there was a 6.5 fold increase in the surface atomic oxygen concentration following plasma treatment.

Table 3.2 Atomic concentrations determined from x-ray photoelectron spectroscopy as percentages ± standard deviation of oxygen and carbon for untreated polystyrene (UT-PS) and treated polystyrene (T-PS). Total concentration was derived from the area of peaks in broad scan spectra (pass energy of 100eV), whereas the peak components were derived from high resolution spectra (pass energy of 50eV). Mean concentrations determined from 3 samples.

		UT-PS	**T-PS**
O1s (at%)	**Total**	3.9 ± 1.1	20.5 ± 4.7
	O=C	0.0	46.1 ± 1.1
	O-C	0.0	53.8 ± 1.1
C1s (at.%)	**Total**	96.1 ± 1.1	79.5 ± 4.7
	C-C/C-H	74.3 ± 2.8	52.7 ± 6.1
	C-O	17.8 ± 1.4	42.21 ± 5.8
	C=O/O-C-O	1.5 ± 1	1.2 ± 1.3
	O=C-O	0.3 ± 0.2	0 ± 0
	π-π*	6.1 ± 0.6	4 ± 0.5
	O/C ratio	0.04	0.26

Broad scan spectra were taken across the surface of treated polystyrene with a spatial resolution of 1mm to determine if the concentration of oxygen altered with distance. The oxygen concentration at the centre of the sample was 23.8% and this decreased with distance to <5% at the edges, which was within the range of oxygen observed on UT-PS.

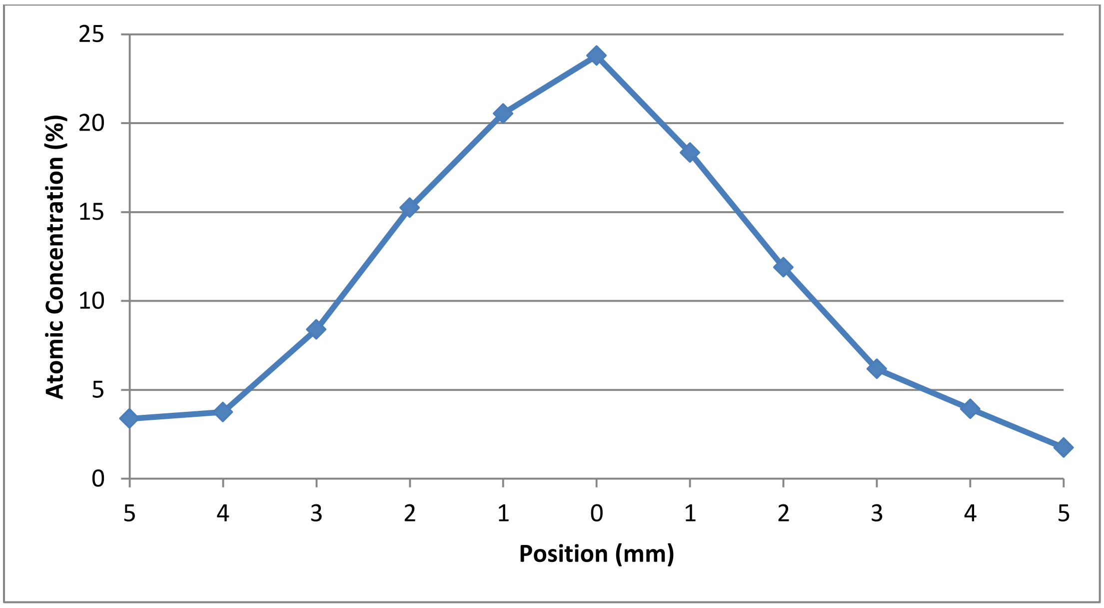

Figure 3.33 Line graph of the atomic oxygen concentration, as determined from x-ray photoelectron spectroscopy broad scan spectra (100eV pass energy), across the surface of a single sample of microplasma jet treated polystyrene (PS). Concentrations determined from a single sample.

3.4.3.4 Cell Culture

The number of N/N1003A rabbit LECs was counted in the centre of the sample and also 1.5mm, 3mm and 4mm away from the centre point.

3.4.3.4.1 Cells Counts - Day 1

At day 1 LEC counts were similar (69-77 cells per field of view) at all positions on TCPS (Figure 3.34) and were not significantly different from each other ($p=0.102$). There was almost no cell attachment on UT-PS regardless of position (2-8 cells per field of view)($p=0.44$). UT-PS had significantly fewer cells than TCPS at all positions ($p \leq 0.001$).

On samples treated with the L1 parameter there was a high number of LEC attachment in the centre position (484 ± 28 cells per field of view) and almost no cells at the 4mm position (2 ± 3 cells per field of view). The decrease in cell number at each subsequent position was significant from the previous ($p<0.005$) until the 3mm position. The samples treated with the L1 parameter had significantly more cells than TCPS at the centre and 1.5mm positions ($p\leq0.001$), and had significantly fewer cells at the 3mm and 4mm positions ($p<0.001$). The samples treated with L1 parameter had significantly more cells than UT-PS at the centre and 1.5mm positions ($p<0.001$), however there was no significant difference at the 3mm and 4mm positions ($p>0.1$) indicating the samples treated with the L1 parameter were untreated at these positions.

The samples treated with the L10 parameter had the highest density of cells in the centre position compared to all other parameters on day 1 (585 ± 136 cells per field of view). The number of LECs decreased with distance from the centre, to 14 ± 24 cells per field of view at the 4mm position. Similar to the L1 parameter, the decrease in cell number at each subsequent position was significant ($p<0.05$) until the 3mm position. The samples treated with the L10 parameter had significantly more cells than TCPS at the centre and 1.5mm positions ($p\leq0.05$), a similar number of cells at the 3mm position ($p=0.8$) and significantly fewer cells at the 4mm positions ($p<0.001$). Compared to UT-PS, samples treated with the L10 parameter had significantly more cells in the centre and 1.5mm positions ($p\leq0.001$), however there was no significant difference in the number of LECs between samples treated with the L10 parameter and UT-PS at the 3mm and 4mm positions ($p>0.1$), therefore samples treated L10 could be said to be untreated at the 3mm and 4mm positions.

There was also a high density of LECs in the centre of samples treated with the H1 parameter (484 ± 128 cells per field of view), which decreased to 57 ± 86 cells per field of view at 4mm from the centre. The centre and 1.5mm positions were not significantly different from each other ($p=0.591$) but both positions had significantly more LECs than the 3mm and 4mm positions ($p<0.05$). The 3mm and 4mm positions were not significantly different from each other ($p=0.157$). The samples treated with the H1 parameter had significantly more cells than TCPS at the centre and 1.5mm positions ($p<0.05$) but were not significantly different to the TCPS at neither the 3mm nor 4mm positions (p>0.1). UT-PS had significantly fewer cells than samples treated with the H1 parameter at the centre, 1.5mm and 3mm from the centre (p<0.05). The samples treated with the H1 parameter were not significantly different to UT-PS at the 4mm position; although, as stated there were not significantly fewer cells at the 4mm position than TCPS; therefore the samples treated with H1 parameter were not untreated at the 4mm position.

The samples treated with the H10 parameter decreased from 565 ± 60 cells per field of view in the centre, to 51 ± 59 cells per field of view at 4mm from the centre. Similar to samples treated with the H1 parameter, the centre and 1.5mm positions had significantly more cells than the 3mm and 4mm positions (p<0.001), but there was no significant difference within these groups (p>0.05). The samples treated with the H10 parameter had significantly more cells than both TCPS and UT-PS at the centre, 1.5mm and 3mm positions (p<0.05), however H10 samples was neither significantly different from TCPS nor UT-PS at the 4mm position and cannot be considered untreated at this position.

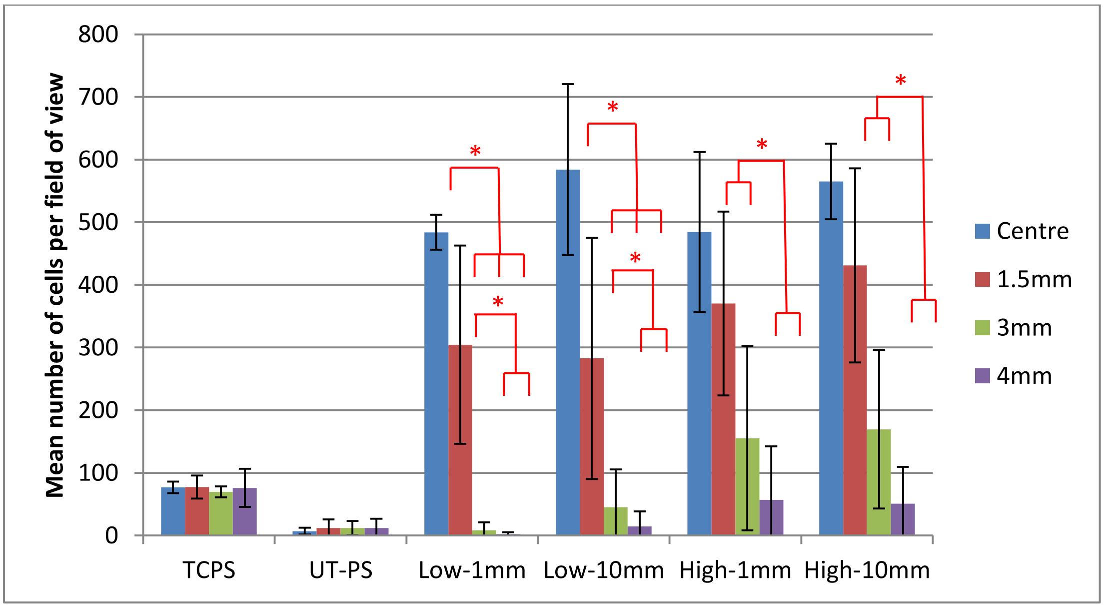

Figure 3.34 Bar chart displaying mean number of DAPI stained N/N1003A rabbit lens epithelial cells (LECs) per field of view at the centre of samples and 1.5mm, 3mm and 4mm from the centre of samples at day 1. Significant differences are only graphically displayed for intra-parameter differences. * indicates significant difference of p<0.05, as determined by one-way ANOVA. Error bars are ± 1 standard deviation.

3.4.3.4.2 Cells Counts - Day 7

By day 7 the cell number had increased to 867-941 cells per field of view across all positions on TCPS, there was no significant difference between the positions ($p=0.35$)(Figure 3.35). There was no significant difference in the number of LECs on any positions on UT-PS (1-8 cells per field of view) ($p=0.158$). There were significantly more cells on TCPS than UT-PS at every position on day 7 ($p<0.001$).

The L1 parameter showed a similar pattern across all positions as day 1. There were 1661 ± 104 cells per field of view in the centre position and only 4 ± 4 cells at the 4mm position. The centre position and 1.5mm position were significantly different to all other positions ($p<0.01$), but the 3mm and 4mm positions were similar ($p=0.864$). The L1 parameter had significantly more cells at the centre position compared to TCPS ($p<0.001$). There were slightly more cells on the L1 positions compared to TCPS at 1.5mm from the centre but there was a large degree of viability and this was not significant ($p=1$). The L1 parameter had significantly fewer cells than TCPS at the 3mm and 4mm positions ($p<0.001$). The L1 parameter had significantly more cells than UT-PS at the centre and 1.5mm positions ($p<0.001$), however L1 parameter was not significantly different to UT-PS at the 3mm and 4mm positions ($p=1$) indicating the L1 parameter was untreated at these positions.

The L10 parameter had a large number of cells in the centre (1784 ± 114 cells per field of view) which decreased with distance from the centre to a minimum at the 4mm position (7 ± 11 cells per field of view). The centre and 1.5mm positions on L10 were similar and not significantly different to each other ($p=0.112$). There was a large and significant decrease in number of LECs from the 1.5mm position to the 3mm and 4mm positions ($p<0.001$). The L10 parameter had significantly more cells than TCPS at the centre and 1.5mm positions ($p<0.001$), and significantly fewer cells than TCPS at the 3mm and 4mm positions ($p<0.001$). The L10 parameter also had significantly more cells than UT-PS at the centre and 1.5mm positions ($p<0.001$), but was not significantly different to UT-PS at the 3mm and 4mm positions ($p>0.5$) and therefore may be considered untreated at the 3mm and 4mm positions.

The H1 had a high number of cells at all positions but the number of LECs did decrease with distance from the centre. There were 1731 ± 64 cells per field of view in the centre, and 993 ± 343 cells per field of view at the 4mm position. The centre and 1.5mm position were not significantly different from each other ($p=0.221$), however the 3mm and 4mm positions were significantly different to all other positions ($p \leq 0.001$). The H1 parameter had significantly more cells than TCPS at the centre, 1.5mm and 3mm positions ($p>0.001$). There was no significant difference between H1 and TCPS at the 4mm position ($p=1$). There were significantly fewer cells on UT-PS than the H1 parameter at all positions on day 7 ($p>0.001$), and therefore no position can be considered untreated.

The H10 parameter was similar to the H1 parameter. There were 1600 ± 69 cells per field of view at the centre, and 705 ±511 cells per field of view at the 4mm position. The centre and 1.5mm positions had a very similar number of LECs ($p=0.989$), whereas the 3mm and 4mm positions were significantly different to all other positions ($p<0.05$). Similarly to H1, the H10 parameter had significantly more cells than TCPS at the centre, 1.5mm and 3mm position ($p>0.05$) and there was no significant difference at the 4mm position ($p=0.677$). The H10 parameter had significantly more cells than UT-PS at all positions ($p<0.001$) and therefore no position was considered untreated.

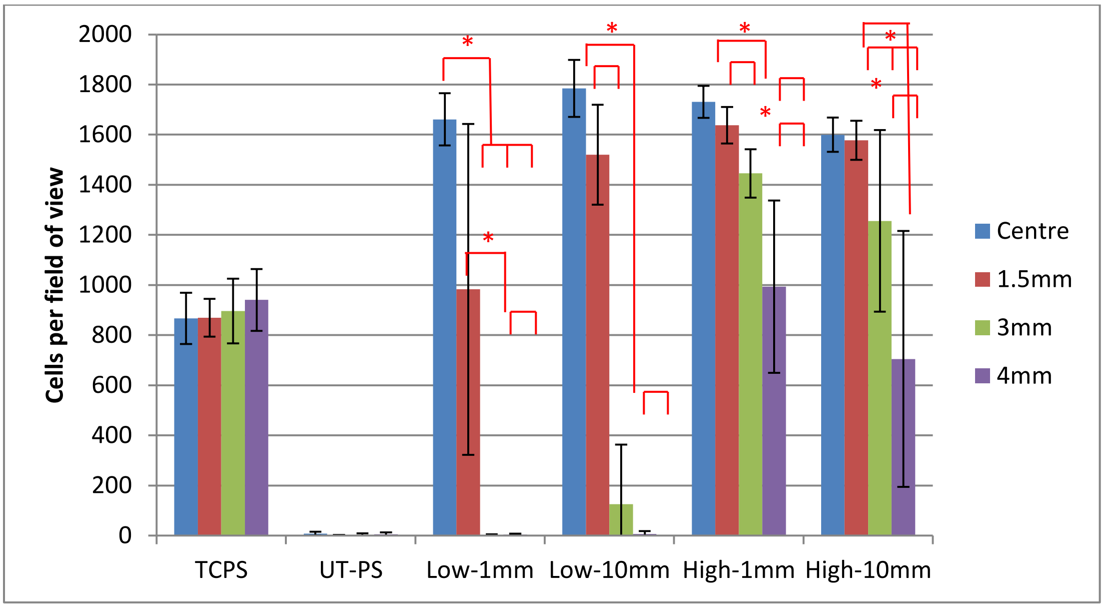

Figure 3.35 Bar chart displaying mean number of DAPI stained N/N1003A rabbit lens epithelial cells (LECs) per field of view at the centre of samples and 1.5mm, 3mm and 4mm from the centre of samples after 7 days of growth. Significant differences were graphically displayed for intra-parameter differences. * indicates significant difference of p<0.05, as determined by one-way ANOVA. Error bars are ± 1 standard deviation.

3.4.3.4.3 Cell Montages

The diameter of cell growth on treated samples was determined from stitched micrographs taken with a 4x objective. As TCPS and UT-PS had homogenous growth across the surfaces they were excluded. LECs typical bound to the central treated region of treated samples, forming an approximately circular area of growth. The diameter of cell growth area was defined as the distance between the boundaries of a confluent or densely populated LEC growth situated in the centre of treated samples. Samples treated with the L1 parameter had the smallest diameters of cell growth, of all parameters, on both day 1 and day 7: on day 1 the diameter was 3.4 ± 0.4mm (Figure 3.36). The treated L10 parameter had the second smallest diameters of cell growth (4 ± 0.5mm) and was not significantly different to the L1 parameter, nor was it different to the treated H1 and H10 parameters ($p>0.05$) at day 1. The diameter of cell growth for H1 and H10 were 5.6 ± 1.6mm and 6.3 ± 1.6mm respectively at day 1, and were significantly larger than the L1 parameter ($p=0.032$ for H1 parameter and $p=0.027$ for the H10 parameter).

At day 7 the diameter of cell growth for the L1 parameter was similar to that of day 1 (3.3 ± 0.2mm) (Figure 3.36 and see example in Figure 3.37a), and had a significantly smaller diameter of cell growth than all other treatment parameters ($p<0.001$). At day 7 the diameter of cell growth on the L10 parameter had increased (4.5 ± 0.4mm)(example in Figure 3.37b), however this was still significantly smaller than the high flow rate parameters ($p<0.001$). By day 7 LECs had spread across virtually the whole sample for high flow rate parameters and were not significantly different from each other ($p>0.05$) The diameter of cell growth was 8.8 ± 0.4mm for the H1 parameter, and 8.1 ± 0.7mm for the H10 parameter (examples in Figure 3.37c and d).

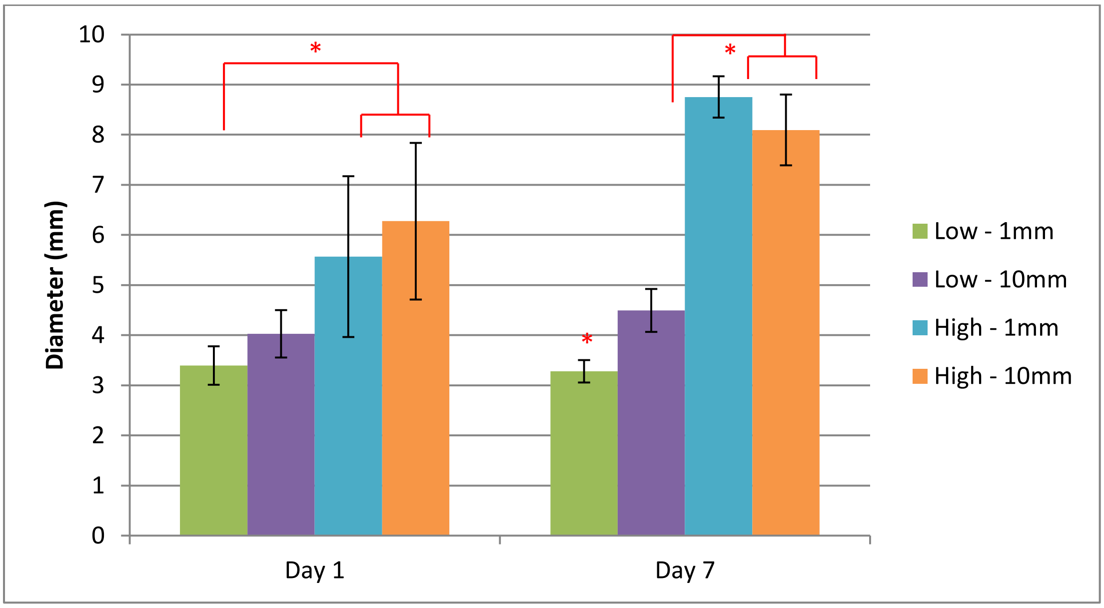

Figure 3.36 Bar chart of diameters of cell growth across samples measured from stitched micrographs of fluorescently stained N/N1003A lens epithelial cells (LECs) at day 1 and day 7 on treated polystyrene (PS) samples. Significant differences were graphically displayed for differences within time points. * indicates significant difference of $p<0.05$, as determined by one-way ANOVA. Error bars are ± 1 standard deviation.

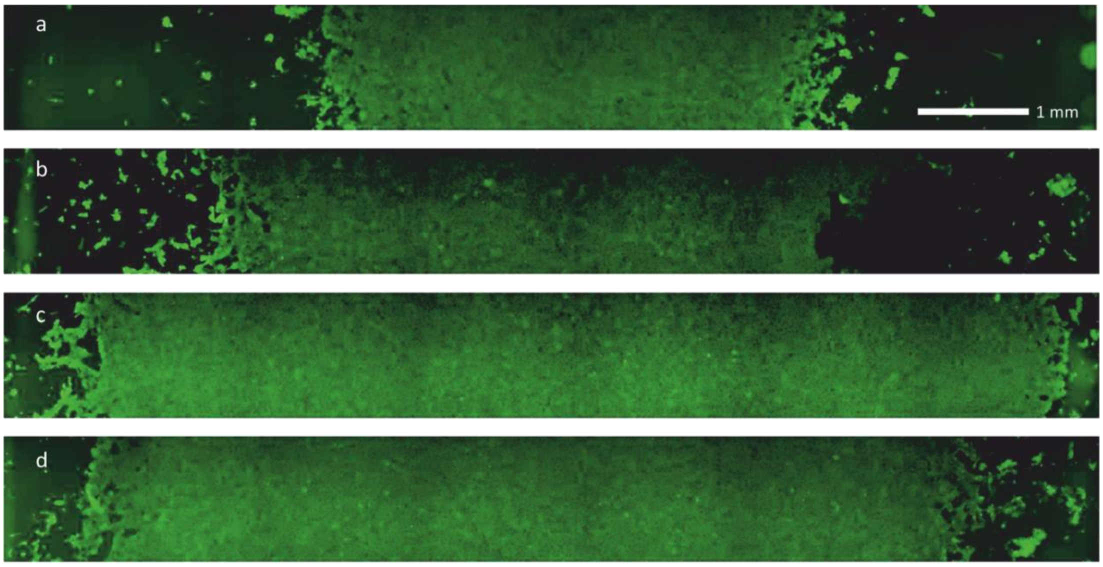

Figure 3.37 Stitched micrographs from individual micrographs taken across the centre of treated samples at day 7. The cytoskeleton of N/N1003A lens epithelial cells were fluorescently stained with phalloidin (green), on samples treated with the low flow rate - 1mm distance (a), low flow rate - 10mm (b), high flow rate - 1mm (c) and high flow rate - 10mm (d) parameters.

3.4.3.4.4 **High Magnification**

High magnification micrographs were taken within the centre of the samples to display the cellular morphology (Figure 3.38). LECs grown on TCPS for 7 days displayed the typical "cobblestone" epithelial morphology with strong actin localisation at the cell boundaries (Figure 3.38a). UT-PS had a low LEC density and those cells present had a rounded morphology suggesting poor adhesion (Figure 3.38b). Micrographs of treated samples showed the presence of LECs, however although the cells appeared well spread they had high actin density and the presence of directional stress fibres (Figure 3.38c-f) and thus do not demonstrate the typical 'cobblestone' morphology.

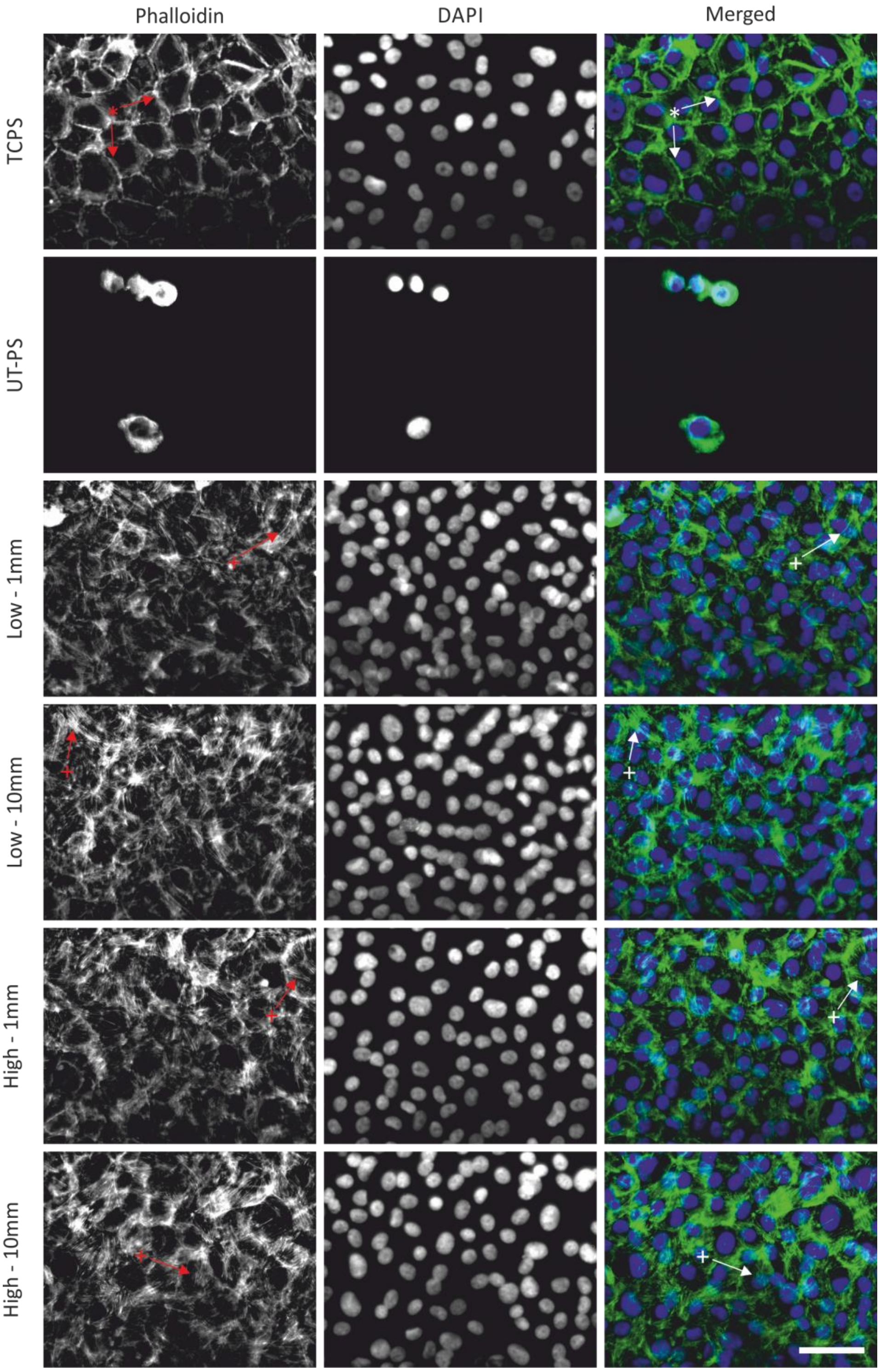

Figure 3.38 High magnification micrographs of phalloidin f-actin staining (green), DAPI nuclear staining (blue) and merged micrographs on tissue culture polystyrene (TCPS), untreated polystyrene (UT-PS) and polystyrene treated with low and high flow rates, at 1mm and 10mm sample-nozzle distances at day 7. * = actin localisation at cell periphery, + = actin stress fibres. Scale bar = 50µm.

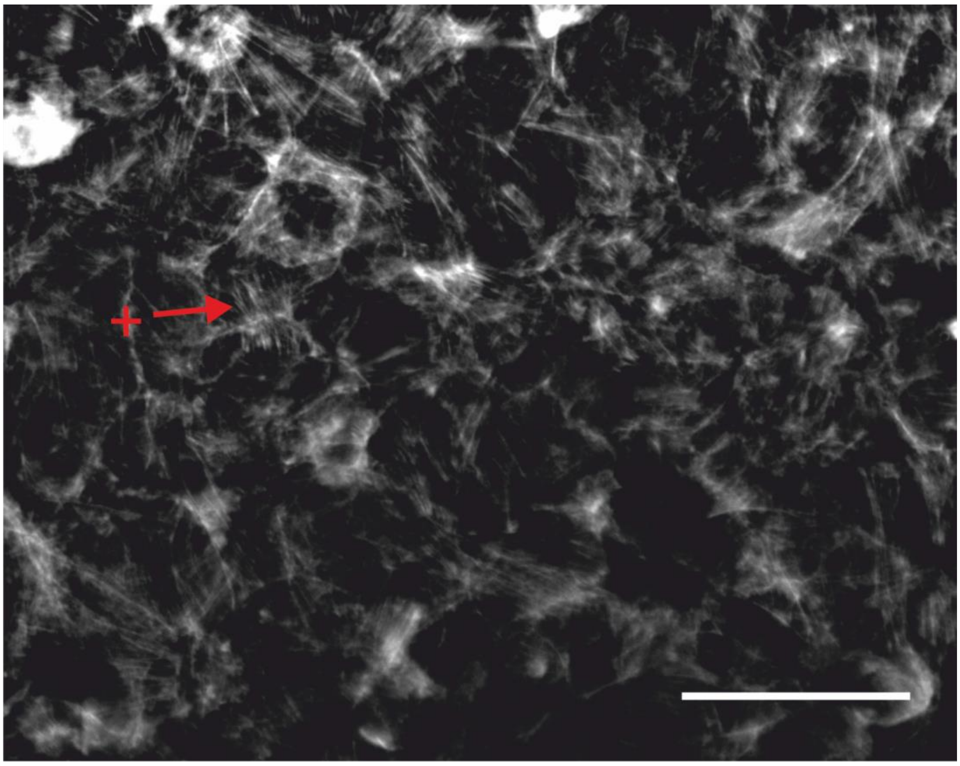

Figure 3.39 High magnification micrograph of phalloidin f-actin staining of lens epithelial cells grown on polystyrene, treated with the low flow rate - 1mm distance parameter on day 7. + = actin stress fibres. Scale bar = 50µm.

3.4.3.5 Preliminary TGF-β2 ELISA

The level of transforming growth factor-beta 2 (TGF-β2) in culture medium removed from wells containing LECs grown on treated PS and UT-PS and TCPS controls was examined using an enzyme-linked immunosorbant assay (ELISA). Due to a small number of samples this work was preliminary and therefore the data lacks standard deviations and statistical analysis as it was conducted once. Medium from 4 wells were pooled for each parameter and each measurement was analysed in duplicate. Only the control samples were within the detection limits of the assay at day 1: the levels of TGF-β2 present in medium taken from TCPS and UT-PS wells was 42pg/ml and 80pg/ml, respectively (Figure 3.40). At day 7 the TGF-β2 concentration in medium removed from TCPS wells had increased to 1372pg/ml. The TGF-β2 concentration in medium removed from UT-PS wells had also increased to 430pg/ml. On day 7 the level of TGF-β2 was detectible in medium taken from wells containing all treated samples, however the concentrations of TGF-β2 were lower than those observed in medium from TCPS and UT-PS wells. By day 7 medium from wells containing samples treated with L1 and L10 parameters had concentrations of TGF-β2 of 184 and 284pg/ml respectively, whereas wells containing samples treated with H1 and H10 parameters had higher concentrations of 544 and 487pg/ml respectively.

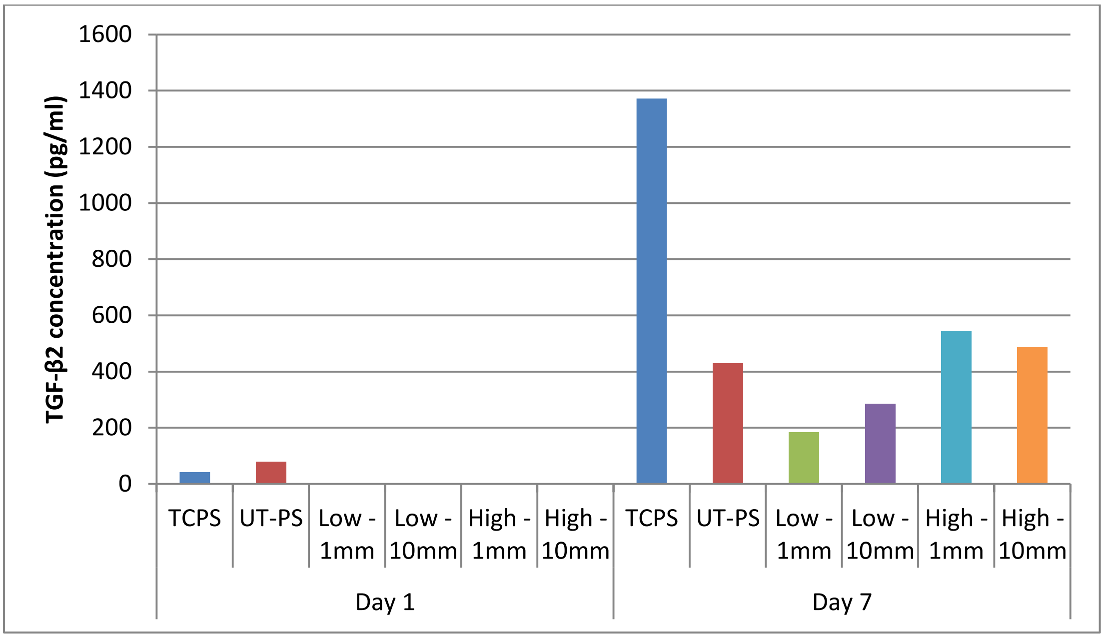

Figure 3.40 Bar chart depicting the concentration of transforming growth factor-β2 (TGF-β2) in culture medium from wells containing N/N1003A rabbit lens epithelial cells grown on tissue culture polystyrene (TCPS), untreated polystyrene (UT-PS) and polystyrene treated with low and high flow rates, at 1mm and 10mm sample-nozzle distances as determined by ELISA. N/N1003a lens epithelial cells were grown for up to 7 days. Medium was removed at day 1 or at day 7. In the case of day 7 cells had been fed at day 4. Medium from 4 wells for each parameter were pooled and values are the mean of 2 measurements.

3.4.3.6 Cytokine Multiplex Assay

The concentration of IL-1α, IL-6, basic FGF and TNF-α in medium taken from wells containing LECs grown on TCPS, UT-PS and treated PS was determined by magnetic bead-based multiplex assay. Due to a small number of samples this work was preliminary and therefore the data lacks standard deviations. Medium from 4 wells were pooled for each parameter and each measurement was analysed in duplicate. Medium was collected at days 1 and 7. The concentrations of IL-1α and IL-6 in medium were below the detection limits of the assay. The concentration of basic FGF in medium from TPCS wells was 0.6pg/ml on day 1, and 2pg/ml on day 7. Medium from wells containing LECs grown on UT-PS had higher levels of basic FGF at 1.2pg/ml and 8.3pg/ml at days 1 and 7 respectively. At day 7 medium from wells in which LECs were grown on PS treated with the L1 parameter had the highest concentration of basic FGF in medium at 11.4pg/ml. The concentrations of basic FGF in medium from wells in which LECs were grown on PS treated with the L10, H1 and H10 parameters ranged between 1.9-3.2pg/ml.

All concentrations of TNF-α were below the standard range. Concentration of TNF-α at day 1 was similar to the basic FGF concentration at day 1, ranging between 0.2-1.1pg/ml. On day 1 medium removed from the H1 parameter had the lowest concentration with 0.2mg/ml and L10 parameter had the highest concentration of 1.1pg/ml. By day 7 the concentrations of TNF-α in medium removed from wells containing TCPS, UT-PS and L1 treatment parameters were ≤0pg/ml following normalisation of data. The concentrations of TNF-α in medium detected for the L10, H1 and H10 parameters were 0.7, 1.4 and 1.2pg/ml respectively at day 7.

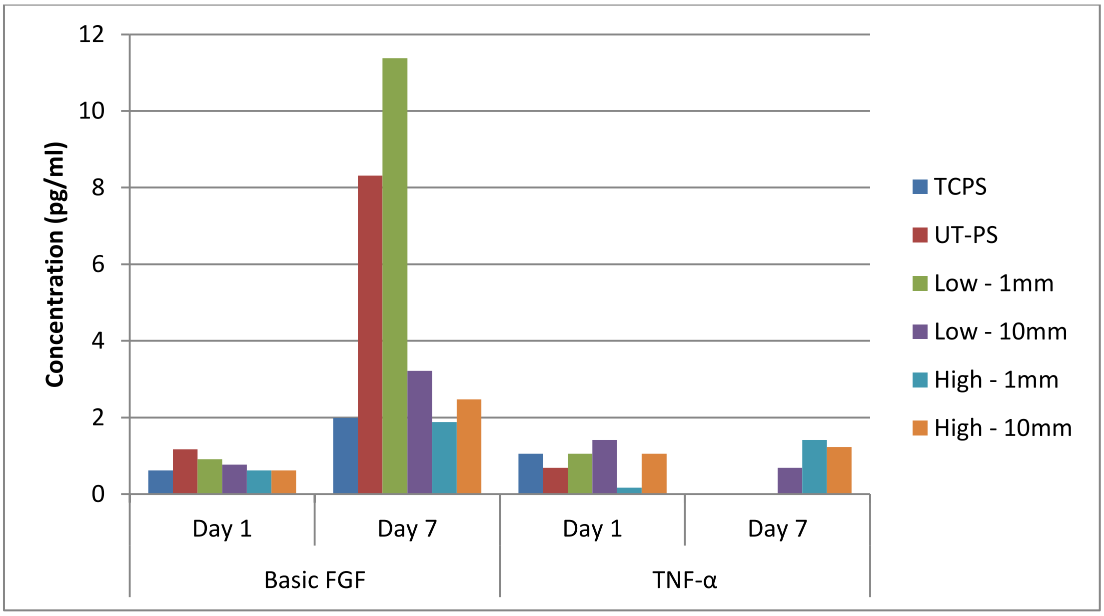

Figure 3.41 Bar Chart demonstrating concentrations of basic fibroblastic growth factor (FGF) and tumour necrosis factor-α (TNF-α) in medium, as determined by magnetic bead-based multiplex assay, at day 1 and day 7. Medium was taken from wells in which N/N1003a lens epithelial cells were grown on tissue culture polystyrene (TCPS), untreated polystyrene (UT-PS) and polystyrene treated with low and high flow rates, at 1mm and 10mm sample-nozzle distances. Medium from 4 wells for each parameter were pooled and values are the mean of 2 measurements.

3.4.3.7 Seeding Density

3.4.3.7.1 Seeding Density Cell Counts

LECs were seeded onto materials at various densities and the number of cells at discrete positions determined from micrographs. The results are grouped by the seeding density and displayed in a single graph (Figure 3.42).

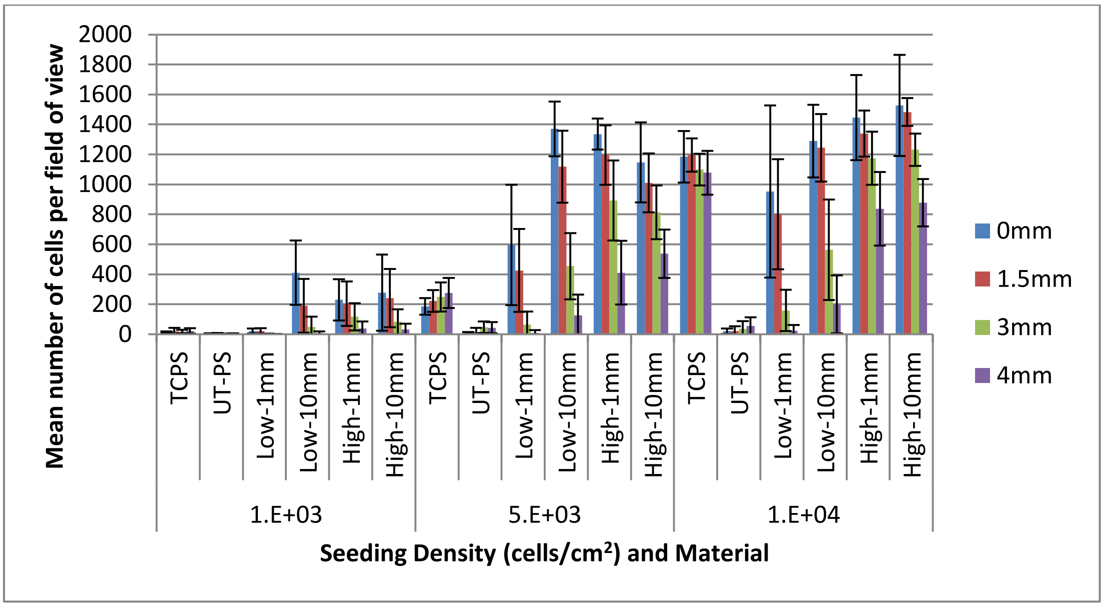

Figure 3.42 Bar chart displaying mean number of N/N1003A rabbit lens epithelial cells (LECs) per field of view at the centre of samples and 1.5mm, 3mm and 4mm from the centre of samples after 7 days of growth. The number of cells was determined from micrographs of nuclei stained with DAPI. Cells were assumed to be mononuclear. LECs were seeded onto tissue culture polystyrene (TCPS), untreated polystyrene (UT-PS) and polystyrene treated with low and high flow rates, at 1mm and 10mm sample-nozzle distances. LECs were seeded onto materials at various seeding densities: 1x10^{3}cells/cm^2

(1.E+03), 5x10^{3}cells/cm^2 (5.E+03) and 1x10^{4}cells/cm^2 (1.E+04). Values are the mean of 3 samples. Error bars are ± 1 standard deviation.

3.4.3.7.1.1 1x10^{3}cells/cm^2 Seeding Density

There were few LECs on materials seeded with a density of 1x10^{3}cells/cm^2 after 7 days of growth. On TCPS wells there were 14-22 cells per field of view at day 7 and on UT-PS the number of LECs ranged from 1-4 cells per field of view.

On the L1 parameter there were very few cells attached at day 7; there were 21 ± 18 cells per field of view in the centre which decreased to 0 ± 1 cells per field of view at the 4mm position. In the centre of the L1 parameter the number of cells was similar to TCPS, whereas at the 4mm position the number of LECs was similar to UT-PS.

On the L10 parameter there were 410 ± 215 cells per field of view in the centre, this was the largest number of cells per field of view observed on materials seeded at density of 1x10^{3}cells/cm^2. The number of cells on L10 decreased with distance to 8 ± 11 cells per field of view at the 4mm position. There were more cells in the centre, 1.5mm and 3mm positions of L10 compared to TCPS and fewer cells at the 4mm position. At the 4mm position there were only slightly more cells on L10 than UT-PS, however without statistical analysis it was not possible to determine if the L10 parameter could be considered untreated at this position.

The high flow rate parameters were similar to each other: there were 230 and 278 cells per field of view in the centre of the H1 and H10 parameters respectively, which had decreased to 39 and 32 cells per field of view at the 4mm position, for H1 and H10 respectively. There were more cells in the central positions of the high flow rate parameters than TCPS and at the 4mm position there were still slightly more cells than TCPS. At all positions on high flow rate parameters there were more cells than on UT-PS.

3.4.3.7.1.2 5x10^{3}cells/cm^2 Seeding Density

When LECS were seeded onto materials at a density of 5x10^{3}cells/cm^2 there were more LECs on TCPS and the central positions of treated materials than the samples seeded at

1×10^3cells/cm^2. On TCPS the number of cells increased slightly with distance from the centre. There were 186 ± 55 cells per field of view in the centre position, which had increased to 276 ± 101 cells per field of view at the 4mm position. There were slightly more LECs on UT-PS when seeded with 5×10^3cells/cm^2 compared to 1×10^3cells/cm^2 following 7 days of growth. When seeded with 5×10^3cells/cm^2 the number of LECs observed on UT-PS ranged from 8-43 cells per field of view, however there were large variances observed on the positions with the higher cells counts.

On the L1 parameter there were 596 ± 402 cells per field of view in the centre position, and the number of cells decreased with distance to 9 ± 19 cells per field of view at the 4mm position. There were more cells at the centre and 1.5mm positions on the L1 parameter compared to TCPS, and fewer cells on 3mm and 4mm positions compared to TCPS. There were more cells on the L1 parameter on the centre, 1.5mm and 3mm positions compared to UT-PS and a similar number of cells at the 4mm position. It is likely that the L1 parameter was untreated at the 4mm position.

Similar to the 1×10^3cells/cm^2 density there were more cells in the centre of L10, H1 and H10 compared to the L1 parameter. There were 1370 ± 182 cells per field of view in the centre of the L10 parameter, which decreased with distance from the centre to 127 ± 139 cells per field of view at the 4mm position. There were more cells on the L10 parameter at the centre, 1.5mm and 4mm positions compared to TCPS and there were fewer cells at the 4mm position on the L10 parameter. There were more LECs on L10 parameter than UT-PS at all positions indicating that no position was untreated.

The number of LECs in the centre of the H1 parameter was similar to the L10 parameter (1336 ± 104 cells per field of view), however there were more cells at the 4mm position of H10 (411 ± 212 cells per field of view) compared to the L10 parameter. On the H10 parameter there were 1147 ± 268 cells per field of view in the centre position. The number of LECs decreased with distance from the centre to 537 ± 161 cells per field of view at the 4mm position. Both the high flow rate parameters had more cells at all positions when compared to TCPS or UT-PS.

3.4.3.7.1.3 1x10^{4}cells/cm^2 Seeding Density

When cells were seeded onto TCPS at a density of 1x10^{4}cells/cm^2 (1078-1185 cells per field of view after 7 days of growth) there were more cells compared to the 5x10^{3}cells/cm^2. On UT-PS there were 21-57 cells per field of view and the number of cells increased with distance from the centre, however the variance also increased with distance from the centre.

On the L1 parameter there were 952 ± 574 cells per field of view in the centre position. The number of cells on the L1 parameter decreased with distance from the centre to 23 ± 32 cells per field of view, which was similar to UT-PS.

On the L10 parameter the number of LECs in the centre was 952 ± 243 cells per field of view and the number of cells decreased with distance from the centre to 200 ± 193 cells per field of view at the 4mm position. L10 parameter had a similar number or slightly more LECs than TCPS at the centre and 1.5mm positions, however there were fewer LECs than TCPS at the 3mm and 4mm position. There were more cells on the L10 parameter compared to UT-PS at all positions indicating that no position on L10 parameter was untreated.

The numbers of LECs on the high flow rate parameters were similar to each other. There were 1446 and 1527 cells per field of view in the centre of the H1 and H10 parameters respectively. The number of LECs decreased with distance from the centre to 837 and 878 cells per field of view at the 4mm position, on the H1 and H10 parameters respectively. There were more cells in the centre of the high flow rate parameters than TCPS and by the 4mm position there were fewer LECs on than TCPS; however there were still more LECs on the high flow rate parameters at all positions compared to UT-PS, indicating the entire sample surfaces were untreated.

3.4.3.7.2 Seeding Density Cell Growth Diameter

The diameter of cell growth following 7 days of culture was calculated for treated PS from stitched images taken across the centre of the samples. Each of the seeding densities were grouped together, and for each seeding density the L1 parameter had the smallest diameter and L10 parameter the second smallest. The diameter of cell growth was difficult to determine on materials which were seeded with the $1x10^3$cells/cm^2 density due to the low number of LECs and the fact that a monolayer had not formed; therefore, the data for this seeding density are more subjective.

When LECs were seeded at $1x10^3$cells/cm^2 the L1 parameter had a diameter of cell growth of 4.1 ± 0.7mm, which was the smallest diameter of cell growth observed for all materials and seeding densities. The L10 parameter had a diameter of cell growth of 5.5 ± 0.9mm after 7 days. The high flow rate parameters had diameters of cell growth of 7.1 ± 0.9 and 6.8 ± 0.9mm for the H1 and H10 parameters respectively.

When LECs were seeded at a density of $5x10^3$cells/cm^2 the diameter of cell growth observed for the L1 parameter increased 1mm (5.1 ± 0.9mm) compared to the $1x10^3$cells/cm^2 density, and the diameter for the L10 parameter had increase 2mm (7.5 ± 0.9). The diameter of cell growth for the H1 parameter was 8.4 ± 0.7mm and the diameter of the H10 parameter was larger yet at 9.4 ± 0.3mm.

When LECs were seeded at $1x10^4$cells/cm^2 the diameter of cell growth on the L1 parameter (5.1 ± 0.7mm) was the same as that when LECs were seeded with $5x10^3$cells/cm^2. The diameter of cell growth observed for the L10 parameter was slightly smaller (7.5 ± 0.9mm) than the diameter observed at the lower seeding density 5x103cells/cm^2. The diameters of cell growth for the high flow rate parameters were similar to each other: 8.8 ± 0.3 and 9 ± 0.4mm for the H1 and H10 parameters, respectively.

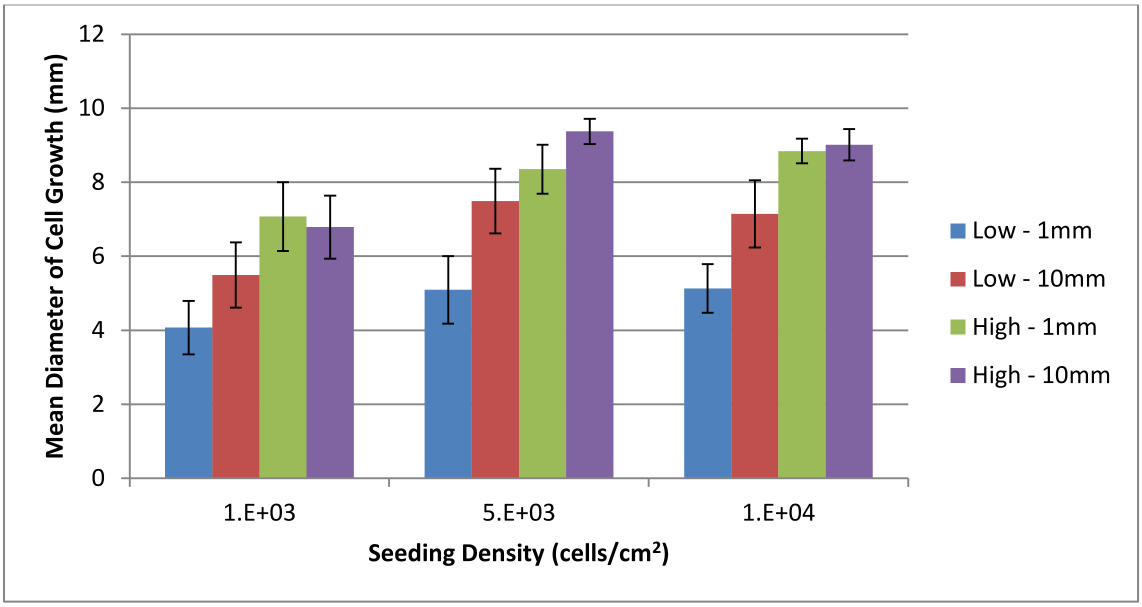

Figure 3.43 Bar chart of diameters of cell growth across samples measured from stitched micrographs of fluorescently stained N/N1003A lens epithelial cells (LECs) at day 1 and day 7 on treated polystyrene (PS) samples with various seeding densities: 1x10^{3}cells/cm^2 (1.E+03), 5x10^{3}cells/cm^2 (5.E+03) and 1x10^{4}cells/cm^2 (1.E+04). Polystyrene was treated with low and high flow rates, at 1mm and 10mm sample-nozzle distances. Values are the mean of 3 samples. Error bars are ± 1 standard deviation.

3.4.3.7.3 Seeding Density High Magnification

There were very few LECs attached to UT-PS at day 7 for any seeding density; cells which had attached typically had a rounded morphology. When seeded at 1x10^{3}cells/cm^2 LECs were not confluent on any material by day 7, however LEC density appeared greater on PS treated with L10, H1 and H10 parameters compared TCPS. When seeded at 5x10^{3}cells/cm^2 cells on TCPS had not reached confluence and actin stress fibres were present. LECs in the centre of plasma treated substrates appeared confluent and some cuboidal LECs were present on these surfaces, particularly L10, H1 and H10; however actin stress fibres were also visible. When seeded at 1x10^{4}cells/cm^2 LECs on TCPS were confluent and appeared epithelial with strong actin localisation present at the cell boundaries, however some stress fibres were still observed. A higher density of LECs was observed on plasma jet treated samples compared to the 5x10^{3}cells/cm^2 seeding density. There was a greater presence of actin stress fibres compared to the lower seeding density and some cells may have been growing on top of others.

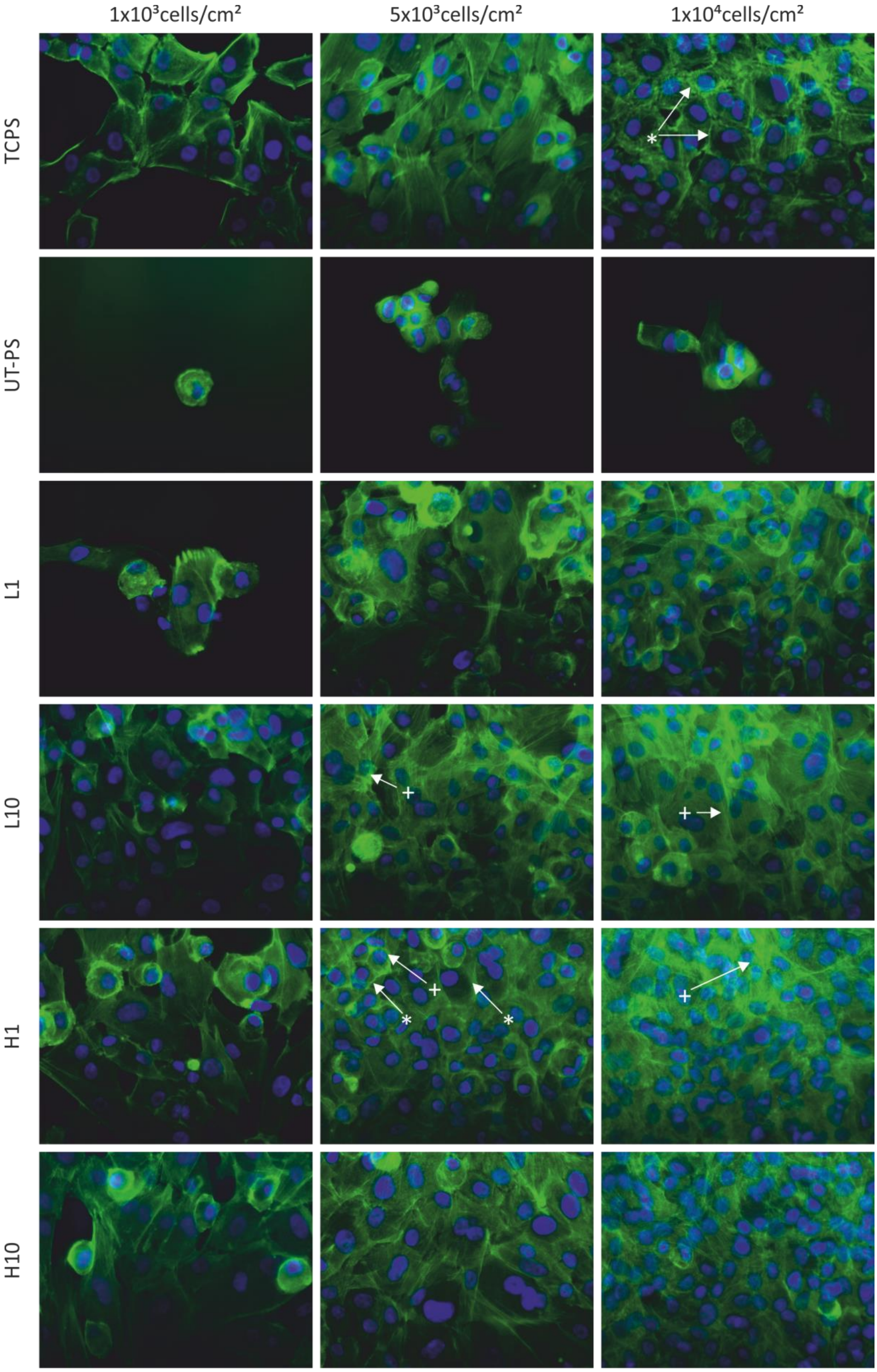

Figure 3.44 Representative high magnification micrographs of phalloidin f-actin staining (green), DAPI nuclear staining (blue) and merged micrographs on tissue culture

polystyrene (TCPS), untreated polystyrene (UT-PS) and polystyrene treated with low and high flow rates, at 1mm and 10mm sample-nozzle distances. LECs were seeded at densities of 1x10^{3}cells/cm^2, 5x10^{3}cells/cm^2 and 1x10^{4}cells/cm^2. Micrographs were taken at day 7. * = actin localisation at cell periphery, + = actin stress fibres. Scale bar = 50µm.

3.5 Microplasma Treatment of Poly(Methyl Methacrylate)

Following optimisation of the flow rate and sample-nozzle distance, to achieve the most defined and smallest treatment area, the effect of microplasma jet treatment on poly(methyl methacrylate)(PMMA) was investigated as a model for acrylic based IOLs.

3.5.1 Contact Angle

To characterise the extent of treatment and the treatment area contact angle measurements were taken across the centre of samples with a resolution of 0.5mm. The average contact angle of TCPS was 35° ± 2.3° (Figure 3.45). The average contact angle measured across the surface of untreated PMMA (UT-PMMA) was 58.9° ± 1.8°. Treated PMMA (T-PMMA) had a similar contact angle to UT-PMMA at the edge of the samples (~59°). Treatment with a microplasma jet reduced the contact angle of PMMA to ~35° (in the centre region). The region in which contact angle was ~35° spanned of 0.5mm. The contact angle of T-PMMA was significantly lower than UT-PMMA between the positions of left-1mm and right-1.5mm (2.5mm total). UT-PS had an average contact angle of 81.1° ± 3.6°. The contact angle at the edge of treated PS (T-PS)(~79°) samples was similar to UT-PS; again treatment with a microplasma jet successfully decreased this contact angle in the centre to ~25° and this contact angle spanned 1.5mm of the central region. The contact angle of T-PS was significantly lower than UT-PS between the positions of left-2mm and right-3mm (total distance of 5mm).

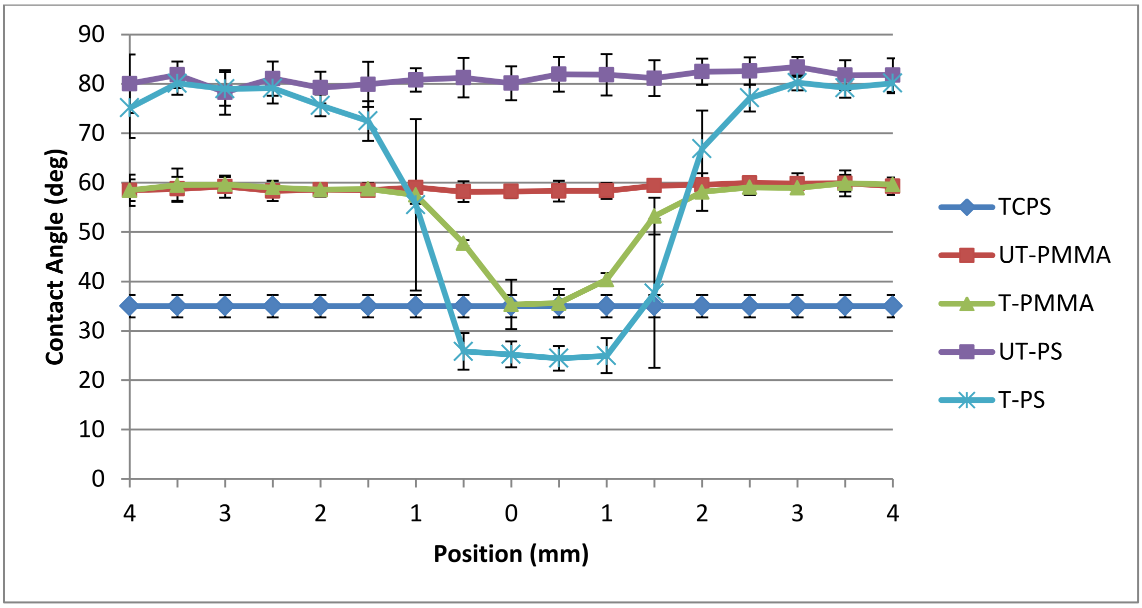

Figure 3.45 Line graph of contact angle profiles of tissue culture polystyrene (TCPS), untreated poly(methyl methacrylate)(UT-PMMA), treated poly(methyl methacrylate)(T-PMMA), untreated polystyrene (UT-PS) and treated polystyrene (T-PS). Contact angle measurements were taken across central axes of samples at a resolution of 0.5mm. Error bars are ± 1 standard deviation.

2D contact angle profiles demonstrated that UT-PMMA had a homogenous surface with an average contact angle of 63.9° ± 1.7° (Figure 3.46). The edge regions of T-PMMA samples had a similar contact angle to UT-PMMA, >60°, which reduced to <50° in the central treated area. This centre treatment area was approximately circular. UT-PS also had a homogenous surface with a contact angle of 78.9° ± 2.7°. The edge regions of the T-PS (~79°) had a similar contact angle to the UT-PS control. The central treated area was approximately circular and had a minimum contact angle of ~28°.

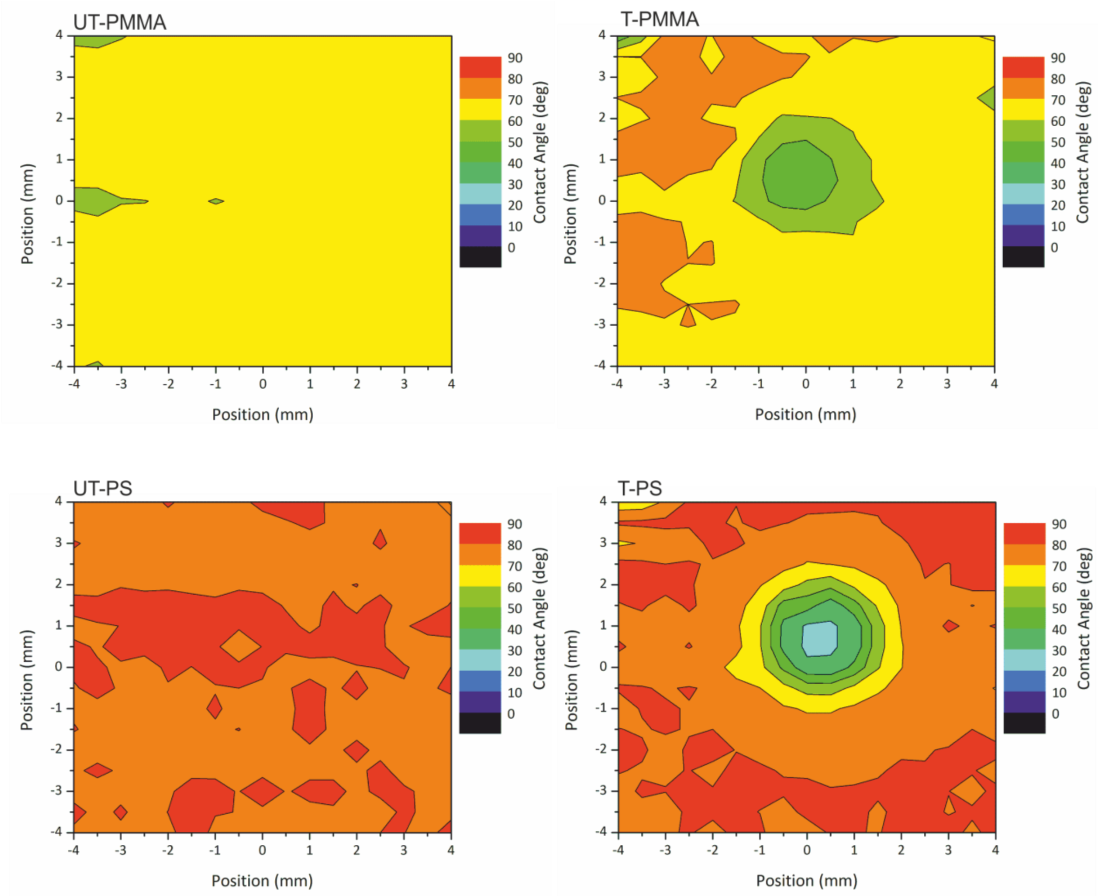

Figure 3.46 2D contact angle plots of untreated poly(methyl methacrylate)(UT-PMMA), treated poly(methyl methacrylate)(T-PMMA), untreated polystyrene (UT-PS) and treated polystyrene (T-PS). Contact angle measurements were made with a spatial resolution of 0.5mm. Plots were from single samples.

3.5.2 X-ray Photoelectron Spectroscopy

Broad scan and high resolution spectra were obtained to determine the chemical modification of the surface resulting from plasma treatment. XPS spectra demonstrated similarities between UT-PMMA and T-PMMA. There were 2 distinct peaks in the broad scans (excluding the auger peaks): O1s and C1s. The ratio of O1s and C1s peaks for UT-PMMA and T-PMMA appeared to be similar. C1s high resolution scans for UT-PMMA and T-PMMA were resolved into 4 components: C-C/C-H at 285eV, C-C-O at 285.8eV, C-O at 286.9eV and O=C-O at 289.2. The C1s peak for UT-PS and T-PS were resolved into 5 components: C-C/C-H at 285eV, C-O at 285.7eV, C=O/O-C-O at 287.3, O=C-O at 289.7 and π-π* shake-up satellite peak at 291.7eV. The O1s high resolution scans for both materials were resolved into 2 components: O=C at 532.1eV and O-C at 533.9eV [5].

The high resolution spectra also demonstrate that the component ratios are similar between the UT-PMMA and T-PMMA. There was no O1s was observed in the broad scan spectra of UT-PS as expected. When the O1s peak region was analysed at high resolution only a slight raise in background noise was detected: this could not be resolved into components. The C1s high resolution spectra of UT-PS demonstrated that the C-C/C-H component contributed the greatest to the peak, although there were small contributions from oxygen containing peaks and the π-π* shake-up satellite peak from the aromatic portion of PS. The presence of oxygen was clearly demonstrated from the broad scan spectra of T-PS. The high resolution spectra indicated that the O1s was composed of O=C and O-C bonds, the latter being the majority. The presence of a large C-O component was observed in the high resolution C1s spectra for T-PS, yet the C-C/C-H component was still the largest. The presence of the C=O/O-C-O, O=C-O and π-π* components were also observed.

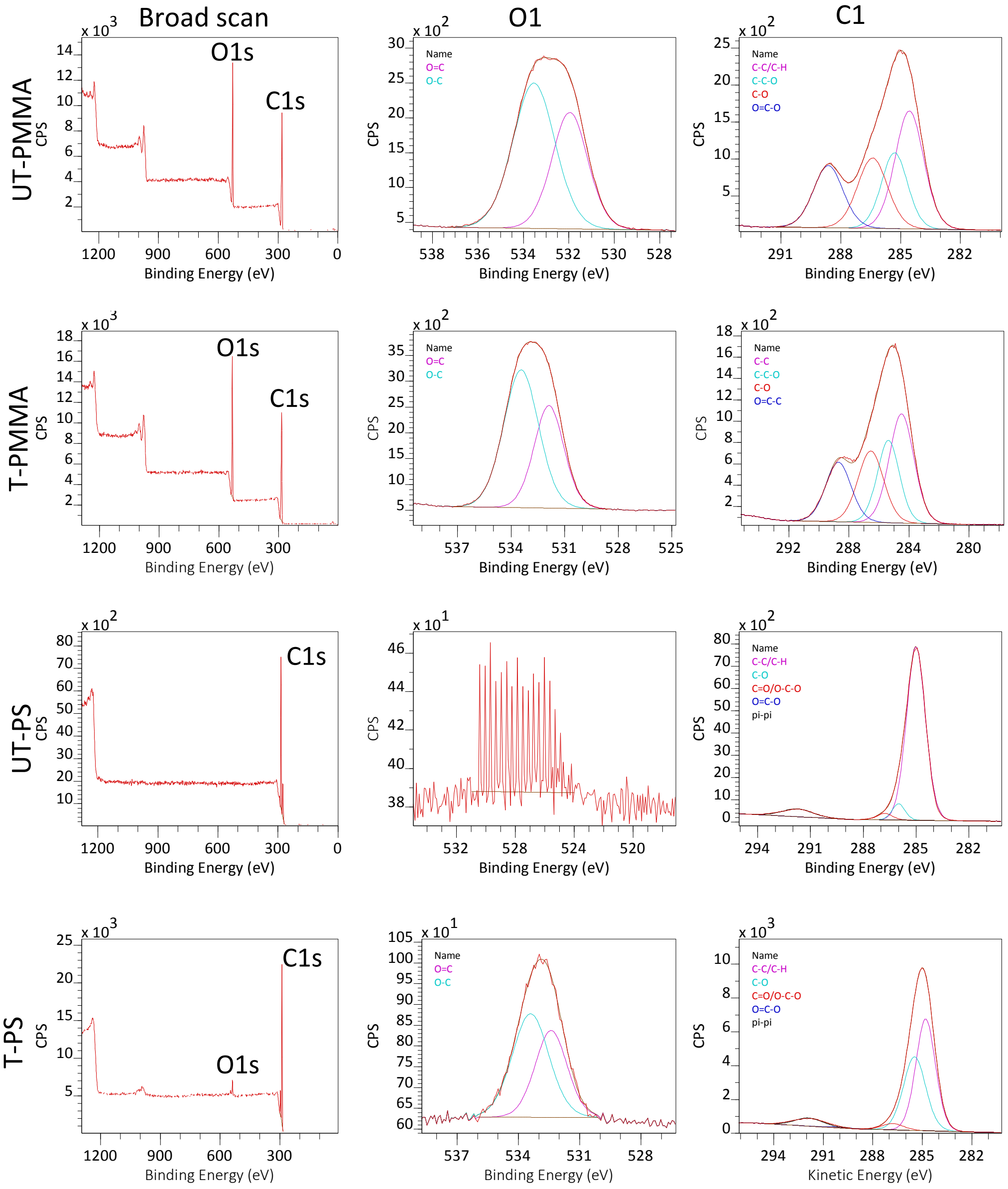

Figure 3.47 Representative x-ray photoelectron spectrographs of untreated poly(methyl methacrylate)(UT-PMMA), treated poly(methyl methacrylate)(T-PMMA), untreated polystyrene (UT-PS) and treated polystyrene (T-PS). Broad scans were taken at a pass energy of 100eV; C1s and O1s high resolution scans were taken at 50eV.

The total surface atomic concentrations were determine from the areas under the peak on broad scan XPS spectra and presented as % ± standard deviations. High resolution spectra were used to determine the contribution of various peak components to the total area. XPS data were obtained on one occasion and therefore have not be subjected to statistical analysis. XPS spectra of UT-PMMA and T-PMMA did not show a large difference in surface oxygen concentration; oxygen accounted for 51.7 ± 0.3% on UT-PMMA, and 52.7 ± 0.5% of the surface atomic concentration on T-PMMA (see Table 3.3). High resolution spectra demonstrated that the component contributions for the O1s of UT-PMMA and T-PMMA differed by only 0.1%. There was also little change between UT-PMMA and T-PMMA in the contribution of C1s components. The only change greater than 1% were for the C-C-O component which increased 3.3% following plasma jet treatment, and the C-O component which decreased 2.4% following plasma jet treatment.

Table 3.3 Atomic concentrations as percentages ± standard deviation of oxygen and carbon for untreated poly(methyl methacrylate)(UT-PMMA) and treated poly(methyl methacrylate)(T-PMMA). Total concentration was derived from the area of peaks in broad scan spectra (100eV pass energy), whereas the peak components were derived from high resolution spectra (50eV pass energy). Atomic concentrations were taken from 3 samples.

		UT-PMMA	T-PMMA
O1s (at.%)	**Total**	51.7 ± 0.3	52.7 ± 0.5
	O=C	40 ± 1.1	39.9 ± 1.4
	O-C	60 ± 1.1	60.1 ± 1.4
C1s (at.%)	**Total**	48.3 ± 0.3	47.3 ± 0.5
	C-C/C-H	38.3 ± 2.1	38.1 ± 3.7
	C-C-O	21 ± 1.3	24.3 ± 1.9
	C-O	20.6 ± 1.5	18.2 ± 5.3
	O=C-O	20.1 ± 0.2	19.5 ± 0.3
	O/C ratio	1.07	1.11

The XPS spectra for UT-PS showed that there was no O1s peak: following plasma treatment (T-PS) an O1s was present and accounted for 11.4 ± 2.7% of the surface atomic concentration (see Table 3.4). In the O1s high resolution spectra for UT-PS only a slight raise in the noise level was detected, therefore it could not be resolved into components. In the O1s high resolution spectra of T-PS the O=C peak accounted for 34.5 ± 5.4%, whereas the single-bound O-C component contributed 65.5 ± 5.8%. In the C1s peak of UT-PS the largest proportion was C-C/C-H component (78.1 ± 15.1%) followed by π-π* component (17.2 ± 10.6%). The remaining oxygen containing peaks contributed approximately 4.6%. In the C1s of T-PS the C-C/C-H component was only 54 ± 1.8% of the area. The π-π* component had also reduced following treatment to 7.5 ± 2.9%. The oxygen containing components contributed 38.5% of the C1s, however most of this can be attributed to the C-O component (37 ± 1.8%).

Table 3.4 Atomic concentrations as percentages ± standard deviation of oxygen and carbon for untreated polystyrene (UT-PS) and treated polystyrene (T-PS). Total concentration was derived from the area of peaks in broad scan spectra (100eV pass energy), whereas the peak components were derived from high resolution spectra (50eV pass energy). Atomic concentrations were taken from 3 samples.

		UT-PS	**T-PS**
O1s (at%)	**Total**	0	11.4 ± 2.7
	O=C	0	34.5 ± 5.4
	O-C	0	65.5 ± 5.8
C1s (at.%)	**Total**	100	88.6 ± 2.7
	C-C/C-H	74.4 ± 11.3	54.0 ± 1.8
	C-O	5.1 ± 0.3	37.0 ± 1.8
	C=O/O-C-O	2.8 ± 0.2	1.3 ± 1.3
	O=C-O	0.6 ± 0.6	0.2 ± 0.2
	π-π*	17 ± 10.9	7.5 ± 2.9
	O/C ratio	0.00	0.13

3.5.3 Atomic Force Microscopy

AFM showed UT-PMMA and T-PMMA to have significantly higher roughness values (Rq and Ra) than UT-PS and T-PS ($p<0.001$). There was no significant difference in the Rq of UT-PMMA and T-PMMA (both 1.7 ± 0.3nm)(Figure 3.48) and Ra values (1.3 ± 0.3nm and 1.2 ± 0.2nm respectively) ($p>0.05$). There was also no significant difference in the Rq or Ra values between UT-PS and T-PS (Rq 0.7 ± 0.5nm, and 0.7 ± 0.3nm respectively, and Ra values of 0.5 ± 0.3nm and 0.5 ± 0.2nm respectively) ($p>0.05$).

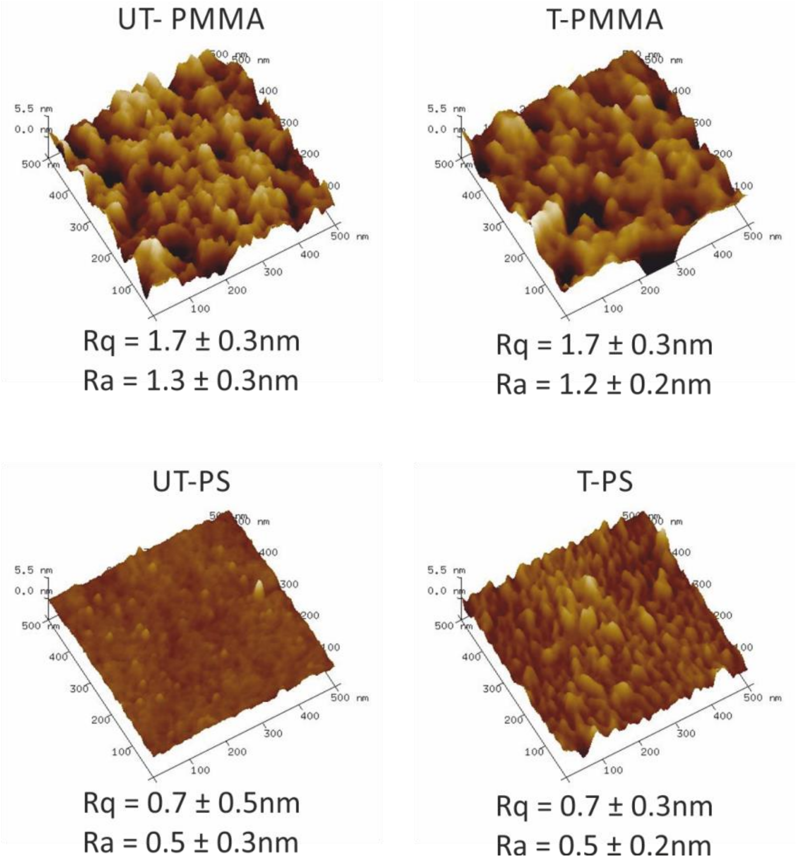

UT- PMMA: Rq = 1.7 ± 0.3nm, Ra = 1.3 ± 0.3nm

T-PMMA: Rq = 1.7 ± 0.3nm, Ra = 1.2 ± 0.2nm

UT-PS: Rq = 0.7 ± 0.5nm, Ra = 0.5 ± 0.3nm

T-PS: Rq = 0.7 ± 0.3nm, Ra = 0.5 ± 0.2nm

Figure 3.48 AFM micrographs including root mean squared roughness (Rq) and average roughness (Ra) values of untreated poly(methyl methacrylate)(UT-PMMA), treated poly(methyl methacrylate) (T-PMMA), untreated polystyrene (UT-PS) and treated polystyrene (T-PS). Ra and Rq were determined from 4 measurements in the centre of 4 samples per parameter. AFM was preformed in tapping mode at a frequency of 1Hz with 512samples/line, using silicon cantilever with a spring constant of 40N/m. The mean AFM was preformed in tapping mode at a frequency of 1Hz with 512samples/line, using silicone cantilever with a spring constant of 40N/m.

3.5.4 Cell Culture

The numbers of attached B3 human LECs were counted in the centre of the sample and also 1.5 mm, 3 mm and 4mm away from the centre point. These results were grouped by substrate, and the number of cells at each position compared. In addition to comparison of position for each substrate, treated parameters (T-PMMA and T-PS) will compared to TCPS and the respective untreated control.

3.5.4.1 Cell Counts - Day 1

At day 1 LEC counts on TCPS were similar (50-64 cells per field of view) at all positions ($p=0.342$) across the sample (Figure 3.49). There were very few LECs on UT-PMMA at any position (8-18 cells per field of view) ($p=0.94$). Very few cells attached to UT-PS regardless of position with an average of <1 cell per field of view on day 1 ($p=0.789$).

T-PMMA had a high density of LECs attached in the central position (0mm) (365 ± 233 cells per field of view) which decreased to 10 ± 12 cells per field of view at the 4mm position. The sequential decrease in cell number became significantly different at the 3mm position onwards ($p\leq0.01$). T-PMMA had significantly more cells than TCPS in the centre and 1.5mm positions ($p<0.05$), and significantly fewer cells than TCPS, as the distance from the centre increased, at the 3mm and 4mm positions ($p<0.05$). T-PMMA had significantly more cells than UT-PMMA at the centre and 1.5mm positions ($p>0.05$), however there was no significant difference between UT-PMMA and T-PMMA at the 3mm and 4mm positions ($p>0.1$), therefore T-PMMA was deemed untreated at these positions.

T-PS had a high density of LECs in the centre (248 ± 184 cells per field of view), similar to T-PMMA, which decreased to an average of 1 cell per field of view at the 3mm and 4mm positions. The centre and 1.5mm positions were not significantly different to each other ($p=0.116$), yet both positions had significantly more cells than the 3mm and 4mm positions ($p<0.05$); with cell counts at 3mm and 4mm not significantly different from each other ($p=0.999$). T-PS was not significantly different to TCPS at the centre and 1.5mm positions ($p>0.1$) but had significantly fewer cells at the 3mm and 4mm positions ($p<0.001$). T-PS had significantly more cells than UT-PS at the centre and 1.5mm positions ($p>0.05$), however there was no significant difference at the 3mm and 4mm positions ($p>0.5$), therefore T-PS was deemed untreated at these positions.

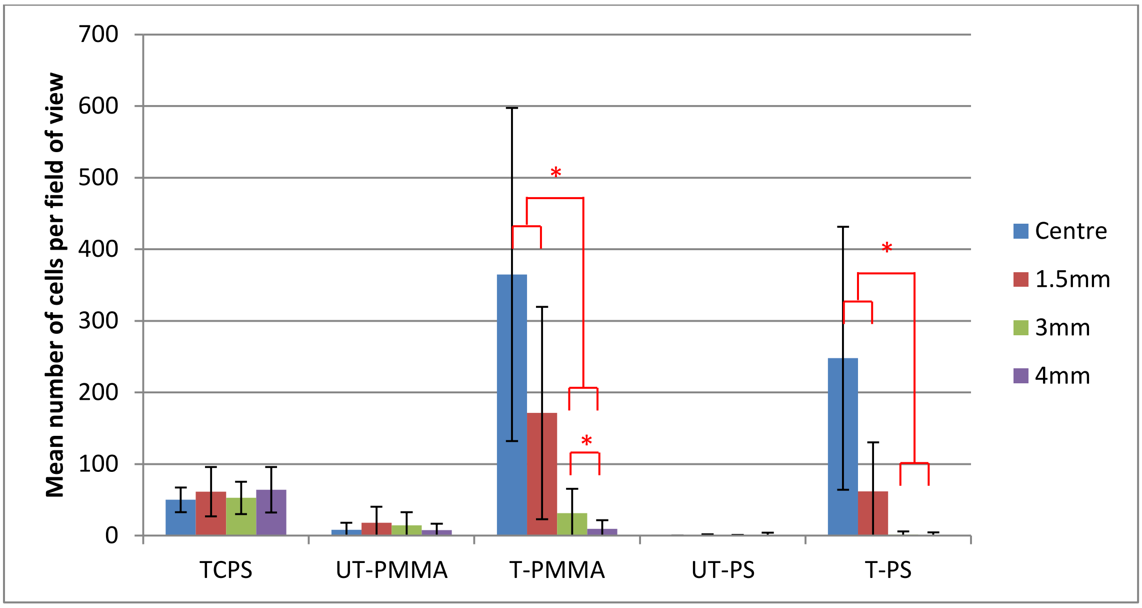

Figure 3.49 Bar chart displaying mean number of B3 lens epithelial cells (LECs) per field of view at the centre of samples and 1.5 mm, 3 mm and 4 mm from the centre of samples at day 1. Cell counts were determined from micrographs of cell nuclei stained with DAPI, seeded onto tissue culture polystyrene (TCPS), untreated poly(methyl methacrylate)(UT-PMMA), treated poly(methyl methacrylate) (T-PMMA), untreated polystyrene (UT-PS) and treated polystyrene (T-PS). Significant differences are only graphically displayed for intra-parameter differences. * indicates significant difference of p<0.05, as determined by one-way ANOVA. Error bars are ± 1 standard deviation.

3.5.4.2 Cell Counts - Day 4

After 4 days the number of LECs across the various positions on TCPS samples ranged from 129-186 cells per field of view, with the number of cells slightly increasing at the 3mm and 4mm positions. This resulted in the 1.5mm and 4mm positions being significantly different from each other (p=0.02). There was no significant difference in the remaining positions (p>0.1) (Figure 3.50). UT-PMMA ranged from 236 ± 135 cells per field of view in the centre position, to only 70 ± 46 cells per field of view at the 4mm position. The centre position was not significantly different to any other position (p>0.1), however the following positions had sequentially significantly fewer cells (p<0.01). The average number of LECs on any position of UT-PS was 1-2 cells per field of view and there was no significant difference between positions (p=0.518).

The number of LECs on T-PMMA decreased as a function of distance from the centre. In the centre of T-PMMA the number of attached LECs was 758 ± 368 cells per field of view, whereas there were 58 ± 11 cells per field of view at the 4mm position. There was no significant difference between the centre and 1.5mm position ($p=0.391$), however the sequential decrease in cell number became significantly different at the 3mm position onwards ($p<0.05$). T-PMMA had significantly more cells than TCPS in the centre and 1.5mm positions ($p<0.05$), no significant difference at the 3mm position ($p=0.447$) and significantly fewer cells than TCPS at the 4mm position ($p<0.001$). There was no significant difference between the T-PMMA and UT-PMMA at the centre ($p=0.064$) despite the large difference in cell number, however the p value was close the 0.05. There was, however, significant difference between T-PMMA and UT-PMMA at 1.5mm from the centre ($p=0.005$). The average cell numbers at 3mm and 4mm positions of T-PMMA were similar to the number of LECs at 3mm and 4mm positions on UT-PMMA ($p=0.417$ and $p=0.575$ respectively), indicating that these positions were untreated.

The average cell number on T-PS decreased from 897 ± 227 cells per field of view in the centre position to an average of 1-2 cells at 3mm and 4mm from the centre. The decrease in cell number was significant for each step ($p<0.001$) until the 3mm position. T-PS had significantly more cells in the centre and 1.5mm positions than TCPS ($p<0.05$). At both 3mm and 4mm from the centre T-PS had significantly fewer cells than TCPS ($p<0.001$). T-PS had significantly more cells in the centre and 1.5mm positions than UT-PS ($p<0.001$). At 3mm and 4mm from the centre T-PS was no longer significantly different from UT-PS ($p=1$) and therefore could be considered untreated at these positions.

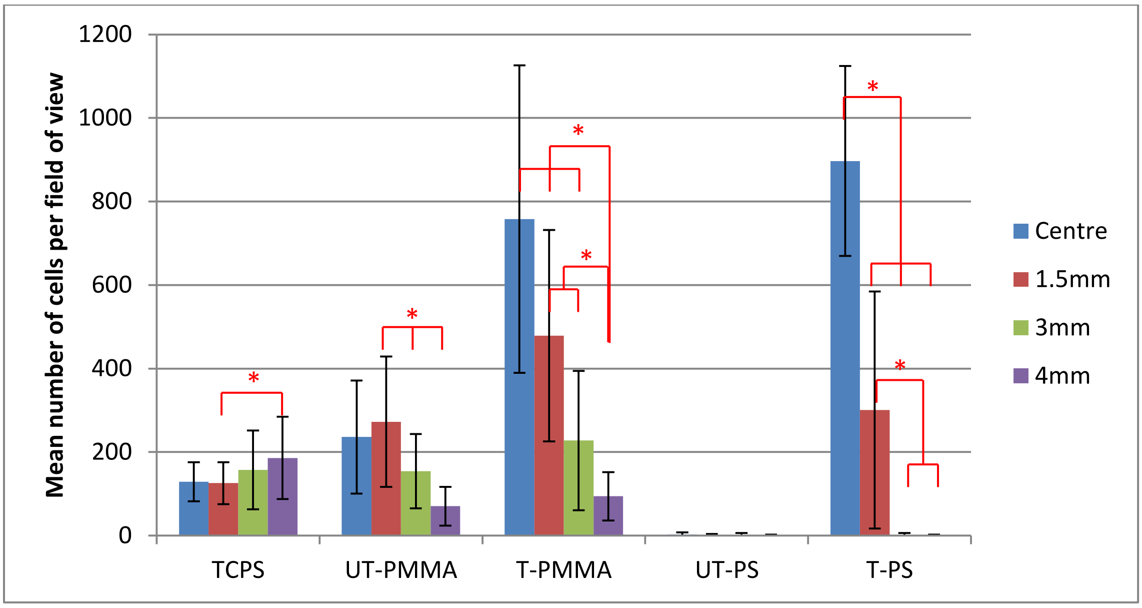

Figure 3.50 Bar chart displaying mean number of B3 lens epithelial cells (LECs) per field of view at the centre of samples and 1.5 mm, 3 mm and 4 mm from the centre of samples at day 4. Cell counts were determined from micrographs of cell nuclei stained with DAPI, tissue culture polystyrene (TCPS), untreated poly(methyl methacrylate)(UT-PMMA), treated poly(methyl methacrylate) (T-PMMA), untreated polystyrene (UT-PS) and treated polystyrene (T-PS). Significant differences are only graphically displayed for intra-parameter differences. * indicates significant difference of p<0.05, as determined by one-way ANOVA. Error bars are ± 1 standard deviation.

3.5.4.3 Cells Counts - Day 7

At day 7 samples were fixed and stained for phalloidin and DAPI, micrographs were taken for cell counts however the density of LECs in the centre of T-PS was too great to accurately count cell number. LECs did not appear to be monolayer and individual nuclei were too difficult to distinguish, therefore cell counts for day 7 have been omitted.

3.5.4.4 Cell Growth Area Montages

The diameter of cell growth on T-PMMA and T-PS was determined from stitched micrographs taken at days 1, 4 and 7 with a 4x objective. At day 1 the diameter of cell growth on T-PMMA was 3.8 ± 0.6mm and this was significantly smaller than the diameter of cell growth observed at days 4 and 7 (p<0.001). After 4 days the diameter of cell growth on T-PMMA had increased to 6.1 ± 1.6mm. At day 4 more LECs attachment was observed in the centre of T-PMMA samples with scattered cell growth outside this central treated region (Figure 3.52a). The diameter of cell growth on T-PMMA at day 7 had increased further to 7 ± 1.3, however this was not significantly different to diameter of cell growth at day 4 (p=0.259). By day 7 LECs were spread across most of the surface of T-PMMA, with the highest LEC density in the centre of the samples (Figure 3.52c).

The diameter of cell growth on T-PS was 2.5 ± 0.6mm on day 1, by day 4 this diameter had increased to 3 ± 0.4mm. The diameter of cell growth at day 4 was significantly larger than both day 1 (p=0.013) and day 7 (p=0.013). A high density of LECs was observed in the centre of T-PS at day 4, with scattered cell growth outside this region (Figure 3.52b). The diameter of cell growth observed on T-PS decreased by 0.6mm to 2.4 ± 0.7mm on day 7. LECs were mainly present in very high density in the central treated area of T-PS samples by day 7, this growth area displayed a very defined boundary region (Figure 3.52d). At all time points T-PMMA had a significantly larger diameter of cell growth compared to T-PS (p<0.001)(Figure 3.51).

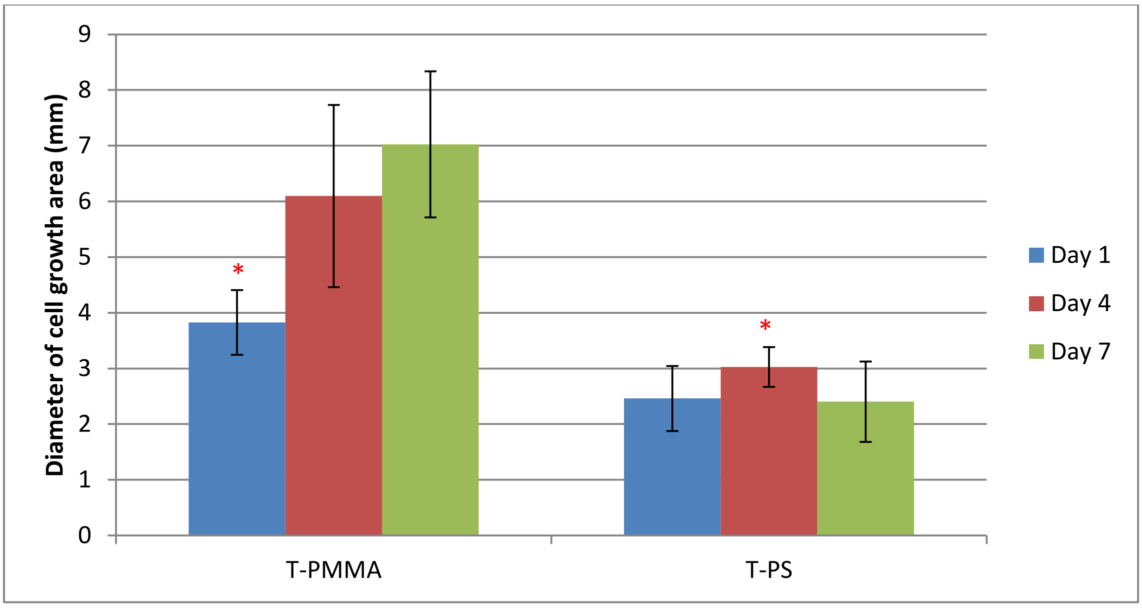

Figure 3.51 Bar chart displaying the diameters of cell growth areas measured from stitched micrographs of B3 lens epithelial cells (LECs) fluorescently stained with DAPI at days 1, 4 and day 7 on treated poly(methyl methacrylate)(T-PMMA) and treated polystyrene (T-PS) samples. Significant differences are only graphical displayed for intra-material differences. * indicates significant difference of p<0.05, as determined by one-way ANOVA. Error bars are ± 1 standard deviation.

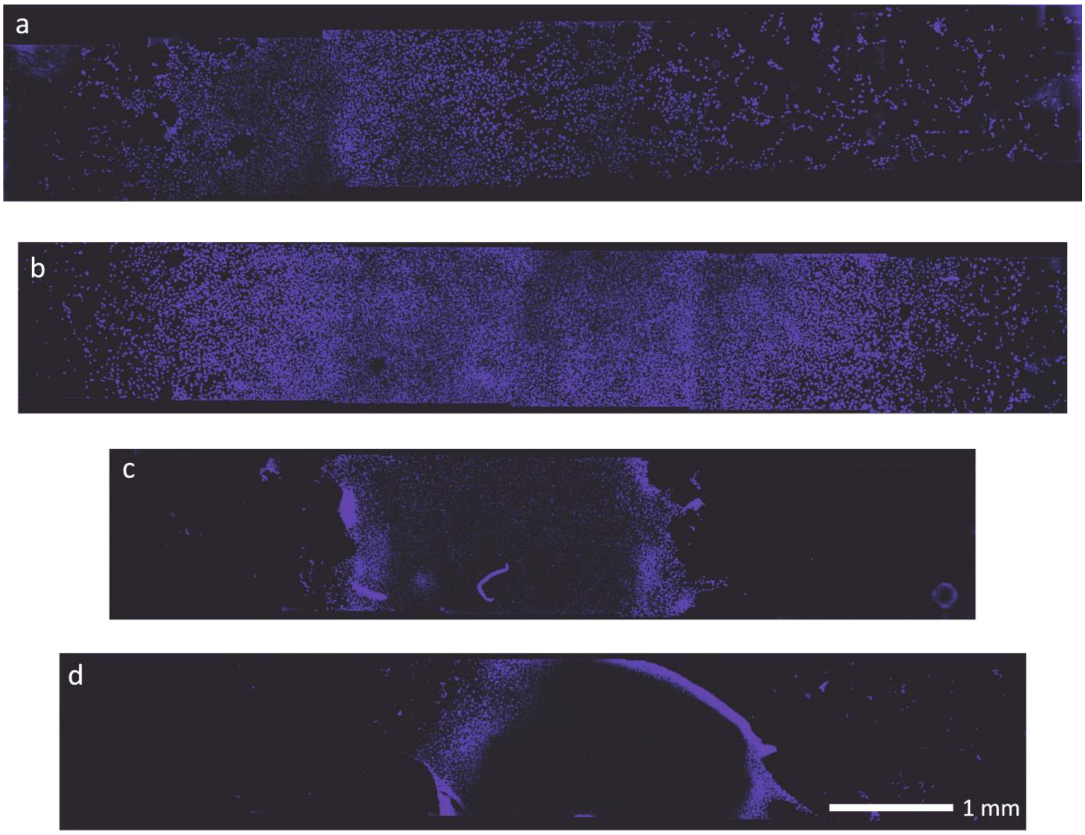

Figure 3.52 Representative stitched images of B3 human lens epithelial cells (LECs) from micrographs taken with an x4 objective, across the centre of treated poly(methyl methacrylate) (T-PMMA) at days 4(a) and 7(b), and treated polystyrene (T-PS) at days 4 (a) and 7 (b). Nuclei were stained with DAPI (blue).

3.5.4.5 High Magnification Cell Morphology

High magnification micrographs of phalloidin and DAPI staining were taken within the centre of the samples to examine the cellular morphology. At day 4 actin staining of human B3 LECs on TCPS indicated that cells had a well spread morphology but had not yet formed a monolayer, and thus did not display typical epithelial cobblestone morphology (Figure 3.53). UT-PMMA had a greater density of LECs attachment on day 4 compared to TCPS. Despite the higher density of LECs cells did not display a cobblestone morphology; directional actin stress fibres were present. T-PMMA had a higher density of LECs on day 4, compared to UT-PMMA. Similar to UT-PMMA a large amount of actin stress fibres were present in cells on T-PMMA and LECs did not display actin localisation at the cell boundaries typical of epithelial cells. Very few cells were present on UT PS and those present were not well spread with either a rounded or spindle morphology. LECs on T-PS on day 4 appeared similar to cells on T-PMMA.

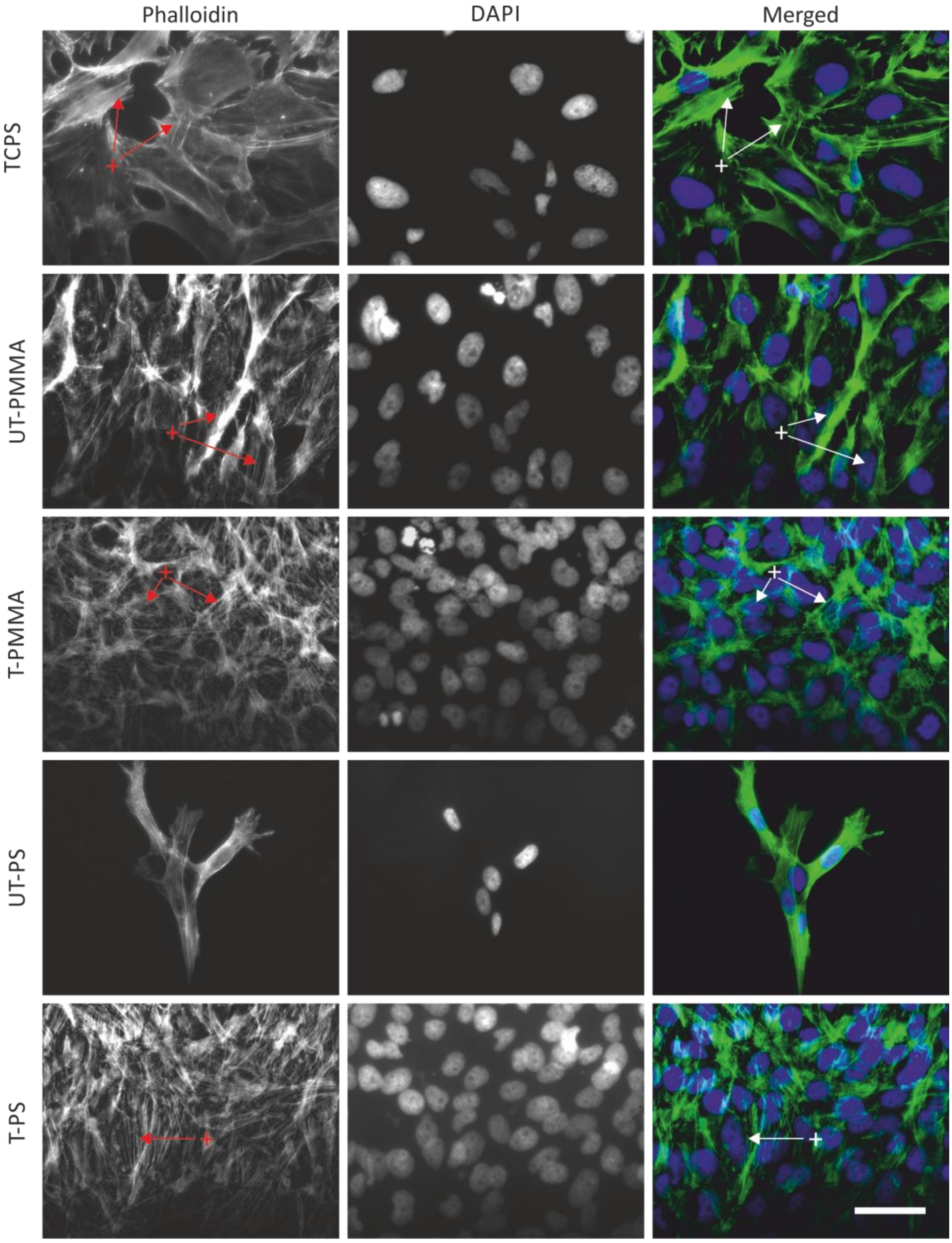

Figure 3.53 Representative high magnification micrographs of human B3 lens epithelial cells (LECs) with phalloidin 488 f-actin staining (green), DAPI nuclear staining (blue) and merged images taken on tissue culture polystyrene (TCPS), untreated poly(methyl methacrylate)(UT-PMMA), treated poly(methyl methacrylate)(T-PMMA), untreated polystyrene (UT-PS) and treated polystyrene (T-PS) at day 4. * = actin localisation at cell periphery, + = actin stress fibres. Scale bar = 50µm.

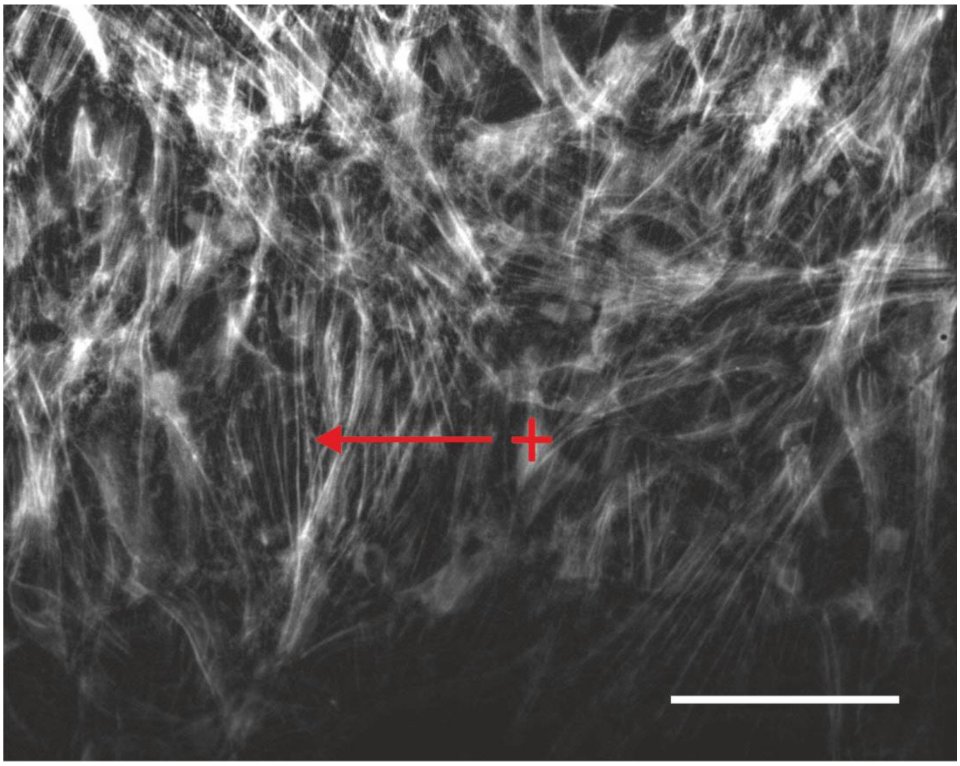

Figure 3.54 High magnification micrograph of phalloidin f-actin staining of lens epithelial cells grown on treated polystyrene on day 7. + = actin stress fibres. Scale bar = 50µm.

By day 7 a monolayer of cell growth had formed on TCPS, however actin localisation at cell boundaries and cobblestone morphology were not observed. Although some cells appeared to have a cuboidal morphology directional stress fibres were present in other cells on TCPS (Figure 3.55). Similar to day 4 there were a greater number of cells present in the centre of UT-PMMA compared to TCPS; overlapping stress fibres were present. A greater number of LECs were observed on T-PMMA compared to UT-PMMA. T-PMMA also had a very high density of overlapping directional actin stress fibres in addition to circular actin configurations, however these latter configurations were less frequent. Few cells were present on UT-PS at day 7 and those that were observed had either a poorly attached rounded morphology or spindle appearance. Cell density on T-PS was so great that individual nuclei could not be distinguished, demonstrating the difficulty posed in cell counting. Despite the presence of strong actin staining identifying individual cells was difficult, although there appeared to be rounded cells and the presence of directional stress fibres.

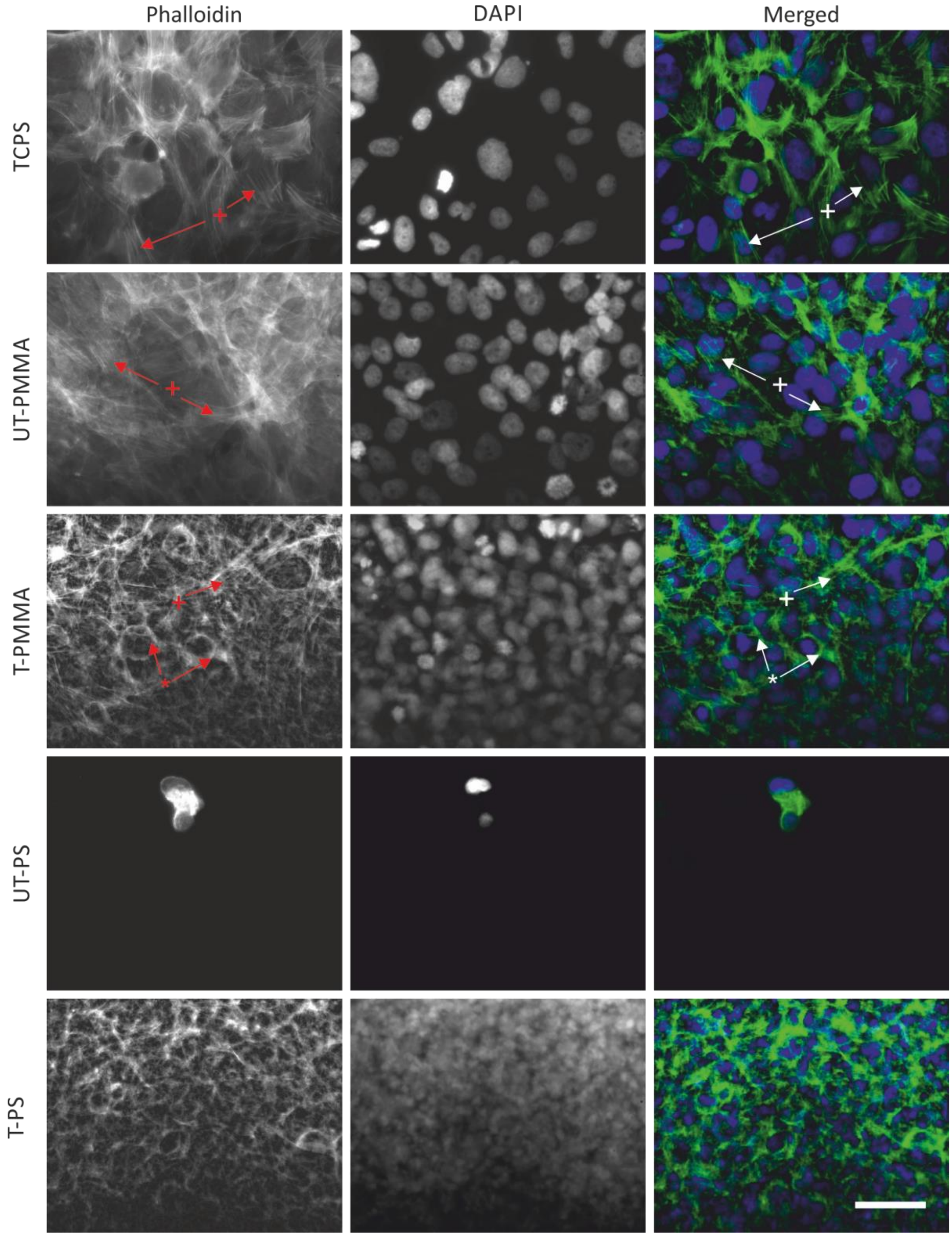

Figure 3.55 Representative high magnification micrographs of human B3 lens epithelial cells (LECs) with phalloidin f-actin 488 staining (green), DAPI nuclear staining (blue) and merged images taken on tissue culture polystyrene (TCPS), untreated poly(methyl methacrylate)(UT-PMMA), treated poly(methyl methacrylate)(T-PMMA), untreated polystyrene(UT-PS) and treated polystyrene(T-PS) at day 7. * = actin localisation at cell periphery, + = actin stress fibres. Scale bar = 50μm.

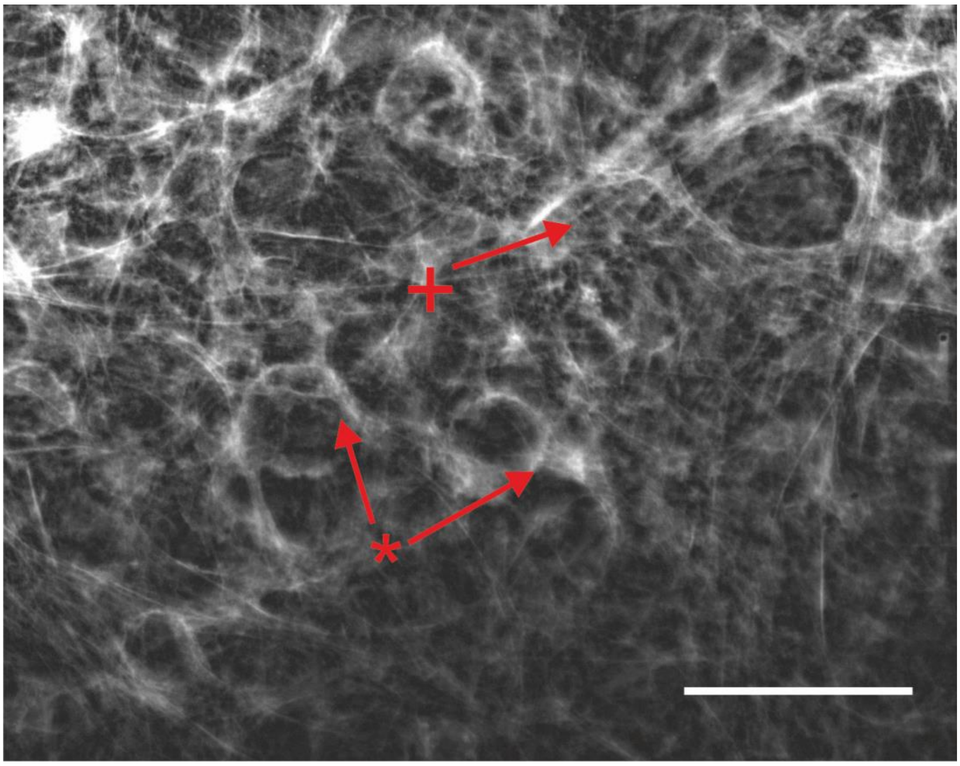

Figure 3.56 High magnification micrograph of phalloidin f-actin staining of lens epithelial cells grown on treated poly(methyl methacrylate) on day 7. * = actin localisation at cell periphery, + = actin stress fibres. Scale bar = 50µm.

3.5.5 Preliminary TGF-β2 ELISA

A preliminary TGFβ2 ELISA showed the level of TGF-β2 to be highest in medium surrounding LECs grown on TCPS wells at all time points. On day 1 the concentration of TGF-β2 in medium from TCPS wells was 252pg/ml (Figure 3.57). The concentration of TGFβ2 in medium wells containing LECs grown on UT-PMMA and T-PMMA was 134pg/ml and 67pg/ml respectively. In addition the medium taken from wells containing LECs grown on UT-PS and T-PS wells had concentrations of 72pg/ml and 229pg/ml respectively.

By day 4 the TGF-β2 concentration in medium taken from TCPS wells had increased to 831pg/ml, which was again much higher than concentrations observed in the other parameters. The concentration of TGF-β2 in medium taken from wells containing LECs grown on UT-PMMA and T-PMMA had become similar at day 4 (190pg/ml and 145pg/ml respectively). Additionally the concentration of TGF-β2 in medium from wells containing

LECs grown on UT-PS and T-PS was 39pg/ml for both parameters: for T-PS this was a considerable lower concentration than that observed on day 1.

The TGF-β2 concentration from in medium from wells containing LECs grown on TCPS increased further by day 7 to 942pg/ml. The concentration observed for medium taken from wells containing LECs grown on UT-PMMA had decreased to 145pg/ml, whereas the concentration of TGF-β2 in medium taken from wells containing LECs grown on T-PMMA had increased to 422pg/ml on day 7. The largest increase was seen in the medium taken from wells containing LECs grown on UT-PS and T-PS where the levels of TGF-β2 had risen ~3-fold to 122pg/ml and 111pg/ml, respectively.

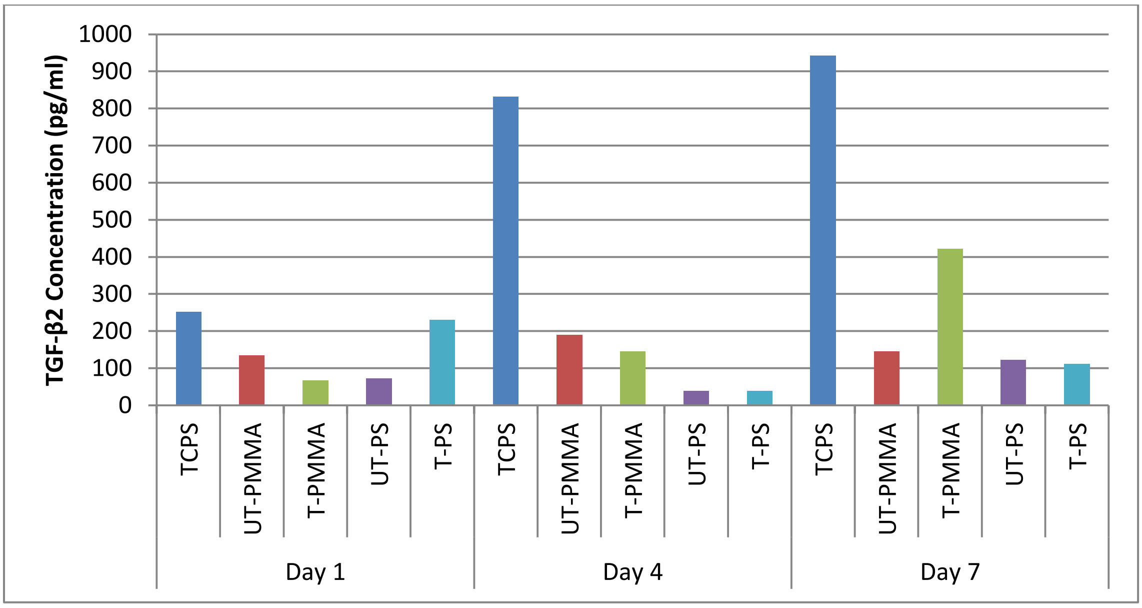

Figure 3.57 Bar Chart showing concentrations of transforming growth factor-β2 (TGF-β2) in medium taken from wells containing LECs grown on tissue culture polystyrene (TCPS), untreated poly(methyl methacrylate)(UT-PMMA), treated poly(methyl methacrylate)(T-PMMA), untreated polystyrene (UT-PS) and treated polystyrene (T-PS) at days 1, 4 and 7. Medium from 4 wells for each parameter were pooled and values are the mean of 2 measurements.

3.5.6 Preliminary Cytokine Multiplex Assay

A magnetic bead based assay was run to examine the concentration of inflammatory cytokines present in the medium surrounding cells grown on PMMA and PS. Pooled medium from each substrate in a single experiment and samples were measured in duplicate, therefore the following data are preliminary.

Cytokine multiplex assay illustrated the concentrations of IL-1α were below the detection limit for all parameters at day 1 and day 4. Values of <1pg/ml were extrapolated from below the standard range for medium from wells containing LECs grown on TCPS and T-PMMA at day 7 (Figure 3.58).

The highest concentrations of cytokines measured by the magnetic bead assay were for IL-6. At day 1 the concentration of IL-6 in medium from wells containing LECs grown on TCPS was 60pg/ml, this was almost twice the concentration observed for medium taken from wells containing LECs grown on any other parameter. Medium taken from wells containing LECs grown on UT-PMMA had a concentration of 17pg/ml, whereas medium taken from wells containing LECs grown on T-PMMA had a concentration of 31pg/ml. Medium taken from wells containing LECs grown on UT-PS had a lower concentration (14pg/ml) compared to the medium taken from wells containing LECs grown on T-PS (21pg/ml) at day 1.

By day 4 the concentration of IL-6 in medium from wells containing LECs grown on TCPS had decreased to 49pg/ml. The concentration of IL-6 in medium from wells containing LECs grown on UT-PMMA had increased to 33pg/ml compared to day 1, however the concentration in medium from wells containing LECs grown on T-PMMA decreased slightly to 29pg/ml. There was an increase in IL-6 concentration in medium from wells containing LECs grown on both UT-PS and T-PS to 21 and 37pg/ml respectively at day 4. At day 7 the concentration of IL-6 in medium removed from wells containing LECs grown on TCPS was similar to that at day 4 (52pg/ml). The concentration of IL-6 in medium from wells containing LECs grown on UT-PMMA remained the same as day 4 (33pg/ml), and the concentration of IL-6 in medium from wells containing LECs grown on T-PMMA increased to 53pg/ml. At day 7 medium from wells containing LECs grown on UT-PS and T-PS both had increased IL-6 concentrations compared to day 4 at 40pg/ml, and 50pg/ml respectively.

The observed basic FGF concentrations in growth medium were very low for all parameters at days 1, 4 and 7. The concentrations of basic FGF in medium taken from wells containing

LECs grown on TCPS were 1, 3 and 5pg/ml for days 1, 4 and 7 respectively. The basic FGF concentration in medium from wells containing LECs grown on all other substrates and all time points ranged from 0-3pg/ml.

TNF-α was not detectable in the medium from wells containing LECs grown on any substrate at any time point excluding T-PMMA at days 4 and 7, which was extrapolated from below the standard range to be <1pg/ml.

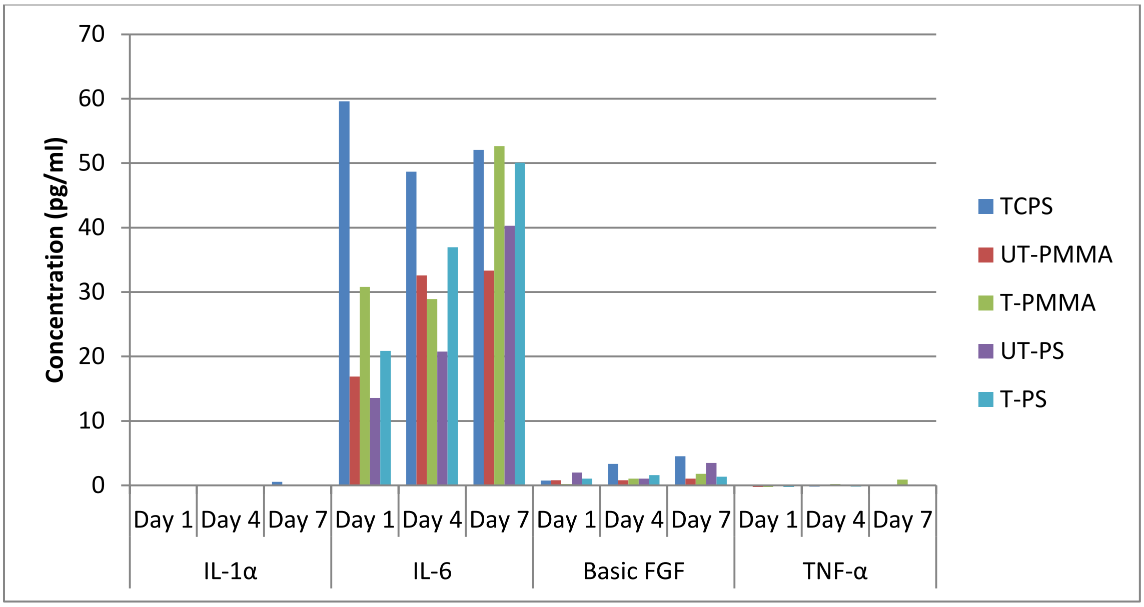

Figure 3.58 Bar Chart showing concentrations of interleukin-1α (IL-1α), interleukin-6 (IL-6), basic fibroblastic growth factor (FGF) and tumour necrosis factor-α (TNF-α) in medium taken from wells containing B3 human lens epithelial cells grown on tissue culture polystyrene (TCPS), untreated poly(methyl methacrylate)(UT-PMMA), treated poly(methyl methacrylate)(T-PMMA), untreated polystyrene (UT-PS) and treated polystyrene (T-PS) at days 1, 4 and 7. Medium from 4 wells for each parameter were pooled and values are the mean of 2 measurements.

3.6 Plasma Polymerisation

The aim of the plasma polymerisation was to prove that helium could but used as a carrier gas for monomers which could be polymerised onto substrates at atmospheric pressure using the plasma jet system. This would enable the greater control of the chemical species incorporated onto polymer substrates. In the following work large bore plasma jet nozzles (≥1mm ID) were used as these did not require tempered tips and could be disposed of if there was contamination from the monomer mixture after use. PS was used in all experiments as a model substrate as the hydrocarbon composition made analysis simpler. Allylamine and heptylamine were used as model monomers as the presence of nitrogen was not previously detected on plasma treated surfaces, which was also of interest from a cellular perspective.

3.6.1 Preliminary Polymerisation – Pre Discharge Mixing

In the following work the allylamine or heptylamine, in helium carrier gas, were mixed with the main helium flow within the capillary before the plasma discharge region. The monomer containing plasma jet was focused on either UT-PS, or PS previously treated for 3min with helium plasma to create a surface with a high wettability. Statistical analysis was excluded as the experiment was performed once.

3.6.1.1 Contact Angle

The average contact angle across the surface of UT-PS was 75.3 ± 3.1° (Figure 3.59). The average contact angle across the surface of helium treated PS was 22.3 ± 1.1°. When UT-PS was treated with allylamine the width of treatment was larger than that observed for heptylamine treated UT-PS. On the left side of the allylamine on UT-PS profile the contact angle had a maximum of 63.4 ± 10.2°, whilst on the right side of the profile contact angles were similar to UT-PS (~75°). In the centre of allylamine treated UT-PS the contact angle was <25°. The section of the profile in which contact angle was <25° spanned 4.5mm. When heptylamine was deposited on UT-PS the contact angle decreased from ≥75° at the edges to <20° in the centre region. The width of the region in which contact angle was <25° was 2.5mm. Treatment of PS, which had been pre-treated with a helium plasma, with either allylamine or heptylamine caused the contact angle to decrease. For both monomer treatments the contact angle decreased to below 20° in the central region. The width of the profile for which contact angle was <20° for allylamine and heptylamine, on treated PS, was 4.5mm for each parameter.

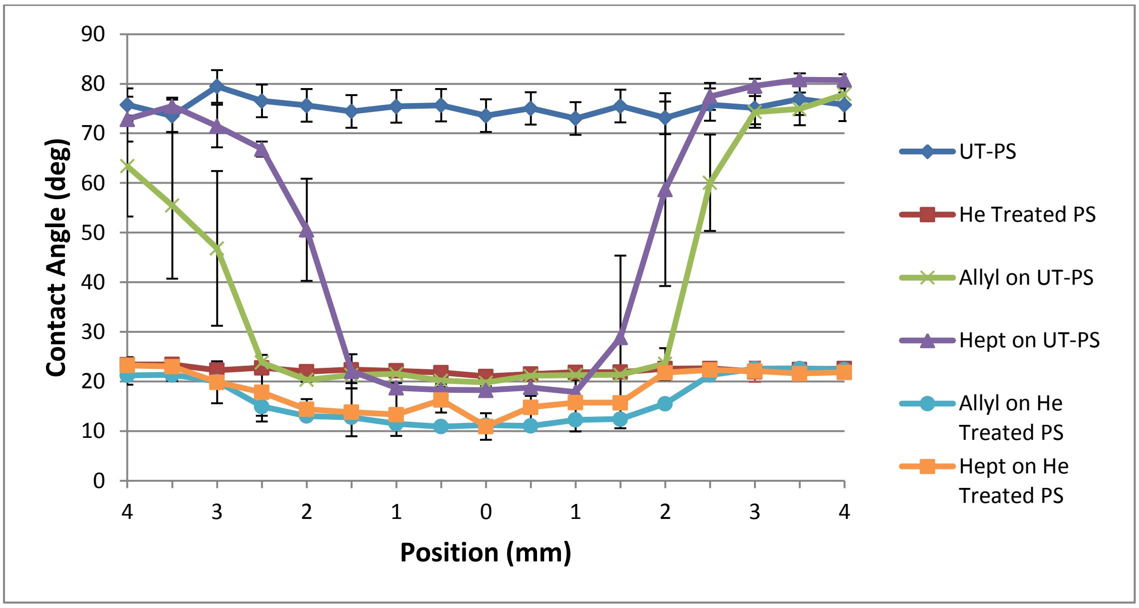

Figure 3.59 Line graph of contact angle profiles taken across untreated polystyrene (UT-PS) and polystyrene (PS) treated with helium (He) plasma for 3min. Either UT-PS or He treated PS samples were also treated with allylamine (Allyl) or heptylamine (Heptyl) polymerisation plasma jet for 5s. Contact angle measurements were taken across central axes of samples at a resolution of 0.5mm. Profiles were taken from 3 samples. Error bars are ± 1 standard deviation.

3.6.1.2 X-ray Photoelectron Spectroscopy

Broad scan XPS spectra were used to obtain approximate atomic concentrations (%) of carbon, nitrogen and oxygen on the surface of samples; concentrations were determined from the area under the the C1s, N1s and O1s peaks. Only the nitrogen and oxygen concentrations are stated as the remainder was carbon. On UT-PS no nitrogen and only 1.5% oxygen were observed (Table 3.5 and Figure 3.60). Following He treatment for 3min there was 2.6% nitrogen and 25.1% oxygen on the surface of samples. When UT-PS was treated with an allylamine plasma the surface contained 4% nitrogen, and the O1s peak contributed 27.9%, which was an increase in comparison to helium treatment alone. Little nitrogen or oxygen, 1.4% and 5.4% respectively, was observed on heptylamine treated UT-PS. When samples previously treated with helium was subjected to monomer containing plasma the concentrations of nitrogen and oxygen increased: again the values were highest on allylamine treated PS. The N1s and O1s peaks on allylamine treated PS contributed 6.2% and 31.5% to the atomic composition respectively, whereas these values were lower on heptylamine treated PS (3.7% and 31.7% for N1s and O1s respectively). However, the presence of a small F1s peak on the allylamine on treated PS sample indicates contamination. The O/C ratios were highest on the allylamine and heptylamine on treated PS samples. The N/C ratio was highest on the allylamine on treated PS sample.

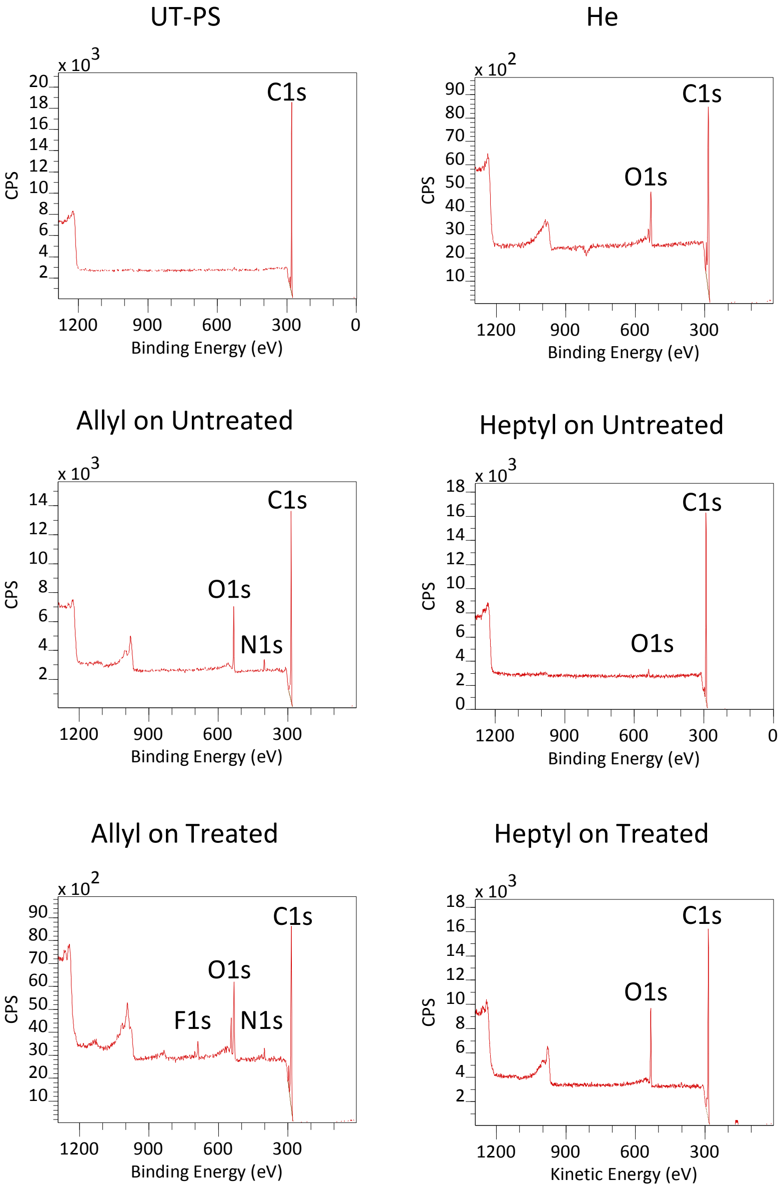

Figure 3.60 X-ray photoelectron spectrographs of untreated polystyrene (UT-PS), helium (He) treated polystyrene (PS), allylamine (Allyl) or heptylamine (Heptyl) deposited on UT-

PS, and Allyl or Heptyl on He pre-treated PS. Broad scans were taken at pass energy of 100eV in the centre of samples.

Table 3.5 Atomic concentrations as percentages ± standard deviation of oxygen and carbon for untreated polystyrene (UT-PS), polystyrene (PS) treated with Helium (He) for 3mins, also on allylamine (Allyl) or heptylamine (Heptyl) deposited on UT-PS or He pre-treated PS. Total concentration was derived from the area of peaks in broad scan spectra (100eV pass energy). Atomic concentrations were taken from single samples.

		UT-PS	He	Allyl on Untreated	Heptyl on Untreated	Allyl on Treated	Heptyl on Treated
Atomic Concentration %	C1s	98.5	72.3	68.1	93.2	55.1	64.4
	N1s	0	2.6	4	1.4	6.2	3.7
	O1s	1.5	25.1	27.9	5.4	31.5	31.7
	F1s	0	0	0	0	7.2	0
	O/C ratio	0.02	0.35	0.41	0.06	0.57	0.49
	N/C ratio	0.00	0.04	0.06	0.02	0.11	0.06

Analysis of high resolution C1s spectra are not present in this preliminary work as it was difficult to distinguish between contributions from C-O and C-N.

3.6.2 Polymerisation Chamber – Pre Discharge Mixing (Chamber)

In the following section the plasma jet was operated in a helium atmosphere. All treatments were performed on UT-PS. The jet system was operated with and without the plasma ignited; i.e. without the application of a voltage to the electrodes. This was to investigate whether there was a deposition of unpolymerised monomer from the gaseous mixture.

3.6.2.1 Contact Angle

The average contact angle of UT-PS was 80.9 ± 1.4° (Figure 3.61). Samples treated with both allylamine and heptylamine, without ignition of the plasma, had contact angle profiles similar to UT-PS. The averages for allylamine and heptylamine without plasma were 80.9 ±

3° and 82.4 ± 1.9° respectively. When surfaces were treated with an allylamine plasma there was a decrease in contact angle across the whole surface, indicating the entire sample surface was treated. The majority of the profile ranged between 30-50°. The contact angle reached two minimum points of ~31° at 1.5-2mm each side of the central position; from these positions the contact angle increased to 44.7 ± 3.7° in the centre. When samples were treated with a heptylamine plasma the entire sample surface was treated (i.e <~80°). The contact angle of heptylamine treated surfaces quickly decreased from 54-59° at the edges to ~20°. The region of the profile in which contact angle was ~20° spanned 5.5mm.

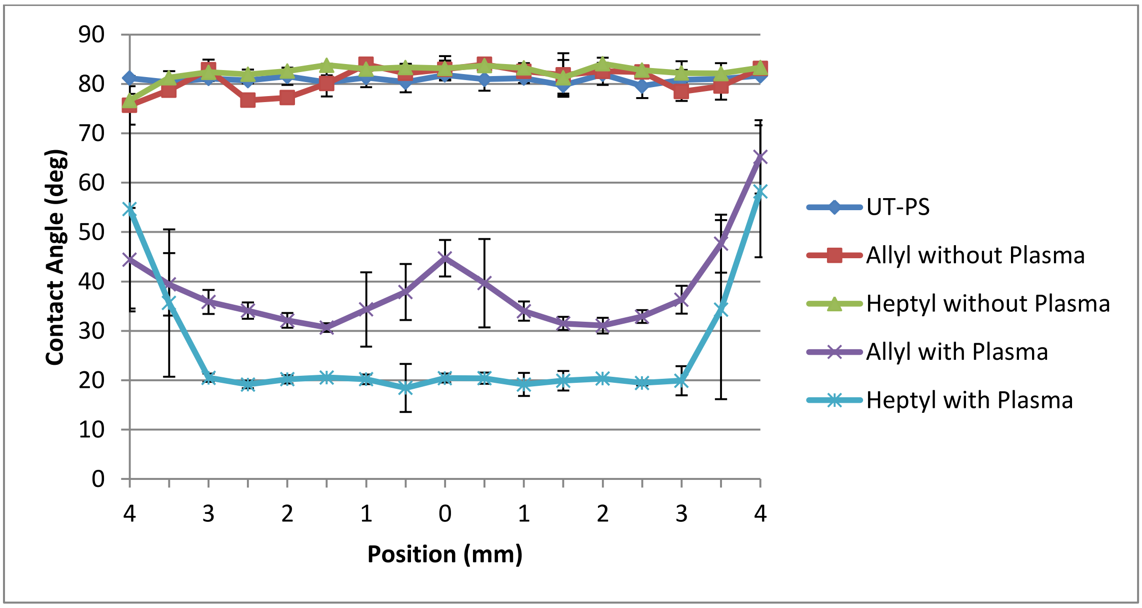

Figure 3.61 Line graph of contact angle profiles taken across untreated polystyrene (UT-PS) and polystyrene samples treated with allylamine (Allyl) or heptylamine (Heptyl) jets, with or without the ignition of a plasma. Contact angle measurements were taken across central axes of samples at a resolution of 0.5mm. Profiles were taken from 3 samples. Error bars are ± 1 standard deviation.

3.6.2.2 X-ray Photoelectron Spectroscopy

The concentration of carbon, nitrogen and oxygen were determined on UT-PS and PS treated with allylamine and heptylamine plasmas from the area under the C1s, N1s and O1s peaks observed in broad scan spectra. The parameters in which the plasma was not ignited were omitted as the contact angle appeared the same as UT-PS. Nitrogen was absent from the surface of UT-PS and there was a 2.2% surface atomic concentration of oxygen (Table 3.6)(Figure 3.62). Following treatment with allylamine plasma there was a 3.7% increase in nitrogen and the concentration of oxygen was 9.2%, indicating that treatment within the chamber reduced the oxygen functionalisation. Despite the lowered concentration of oxygen observed for allylamine treated PS the O1s contributed 25.8% to the heptylamine treated PS, in addition the area of the N1s peak for heptylamine (5.1%) was larger than that observed for allylamine, which was an inversion of the previous observations without the chamber (see section 3.6.1.2). The O/C and N/C ratios were highest for the heptylamine treated PS.

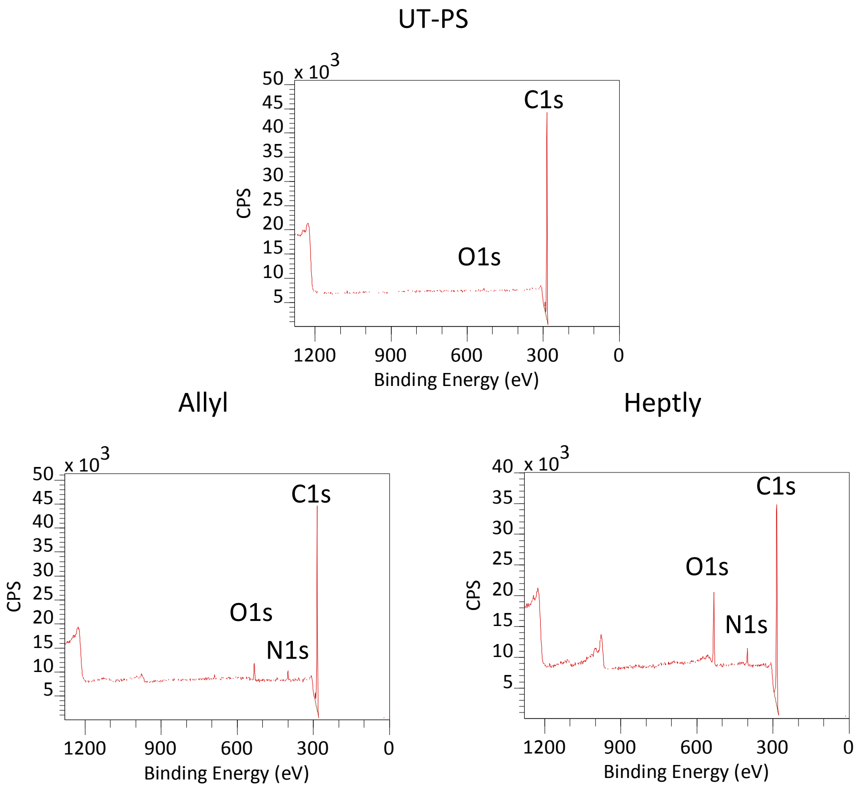

Figure 3.62 X-ray photoelectron spectrographs of untreated polystyrene (UT-PS) and polystyrene treated allylamine (Allyl) or heptylamine (Heptyl) plasma. Broad scans were taken in the centre of samples at pass energy of 100eV.

Table 3.6 Atomic concentrations as percentages ± standard deviation of oxygen and carbon for untreated polystyrene (UT-PS), polystyrene treated with allylamine (Allyl) or heptylamine (Heptyl) plasma jets. Total concentration was derived from the area of peaks in broad scan spectra (100eV pass energy. Atomic concentrations were taken from single samples.

		UT-PS	Allyl	Heptyl
Atomic Concentration %	C1s	97.8	87.1	69.1
	N1s	0.0	3.7	5.1
	O1s	2.2	9.2	25.8
	O/C ratio	0.02	0.11	0.37
	N/C ratio	0.00	0.04	0.07

3.6.2.3 Cell Culture

At day 1 B3 human lens epithelial cells had attached onto TCPS. These LECs displayed a spread morphology. By day 4 the number of cells on TCPS had increased and these cells were beginning to form confluent areas within the wells. At day 7 LECs had formed a confluent monolayer. On UT-PS at all time points very few cells attached to the sample surface. Those LECs which did attached had a very rounded or spindle morphology. There was a tendency for LECs on UT-PS to form clumps. LECs on samples treated with allylamine or heptylamine without plasma ignition were similar to UT-PS at all time points. Samples treated with allylamine plasma were also similar to UT-PS; however, there were more attached cells with a spindle morphology present at day 7. When LECs were seeded onto PS treated with heptylamine with plasma ignition a monolayer formed in the centre of the sample by day 1. At day 1 there was LEC attachment in a distinct central region, with little or no cellular attachment at the edges. At days 4 and 7 the population of LECs in the centre of PS treated with heptylamine, with an active plasma, appeared to increase and the size of individual cells appeared to decrease.

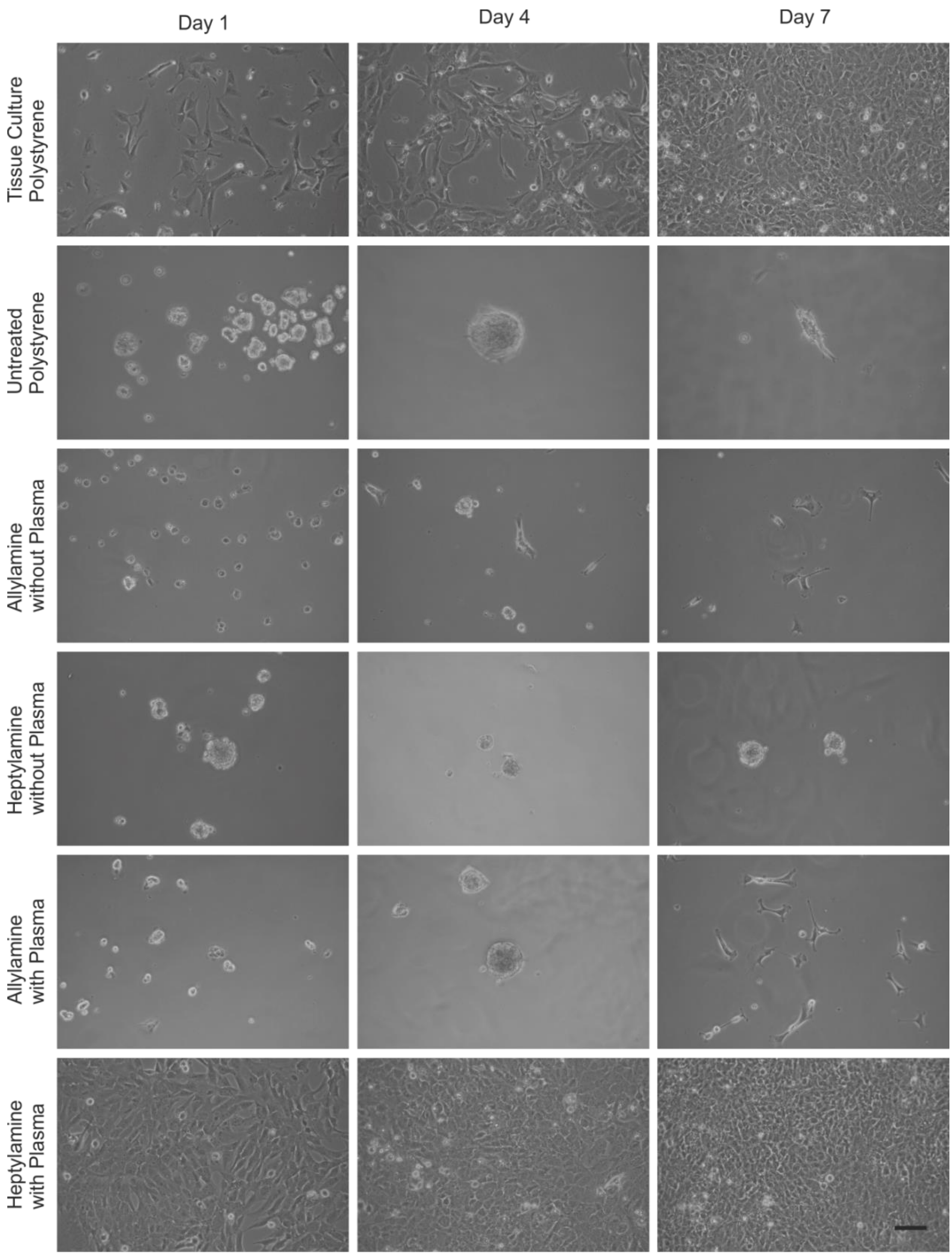

Figure 3.63 Representative phase contrast micrographs of B3 human lens epithelial cell (LEC) line on tissue culture polystyrene (TCPS), untreated polystyrene (UT-PS) and PS samples treated with allylamine or heptylamine jets, with or without the ignition of a plasma. Micrographs were taken in the centre of samples at days 1, 4 and 7. Scale bar = 100µm.

3.6.3 Polymerisation – Post Discharge Mixing

In the following work PS surfaces, positioned 5mm from the nozzle, were treated for 10mins with helium (500sccm) or with a helium:heptylamine mixture of various flow rates (500:20, 50 or 100sccm). The 50sccm and 100sccm flow rates were only examined by XPS to determine which flow rate most efficiently polymerised heptylamine; the efficiency was determined by the quantity of nitrogen observed on the surface. The heptylamine mixture was introduced into the plasma system post-discharge (see methods section), rather than pre-discharge mixing conducted in the previous experiments. Samples were positioned 5mm from the nozzle. This work was not carried out in a chamber as a large oxygen concentration was observed on samples treated with heptylamine within a chamber in the previous work.

3.6.3.1 Contact Angle

The average contact angle of UT-PS was 77.2 ± 3.9° (Figure 3.64). Following treatment with helium for 10mins the entire sample surface was treated. The contact angle ranged from ~31° at the edges to a minimum of 20.3 ± 5° at 0.5mm right of the centre position. The contact angle of helium treated PS was significantly lower (<0.001) than UT-PS at all positions. The contact angle for heptylamine treated surfaces had a larger difference in contact angle from the edge to the centre compared to helium treated PS. At the edges the contact angle was >40° which decreased <20° in the central region. Although heptylamine treatment causes a treatment of the whole sample surface there was a greater effect in the central region. The contact angle of heptylamine treated PS was significantly lower (<0.001) than UT-PS at all positions. The contact angle of heptylamine was significantly higher ($p<0.05$) than helium treated PS at the 4mm-3mm positions at each side, and heptylamine treated PS had a significantly lower ($p<0.05$) contact angle at the 2mm-0.5mm positions (total 1.5mm) right of the centre: this indicates that treatment with heptylamine creates a different surface in comparison to treatment with helium.

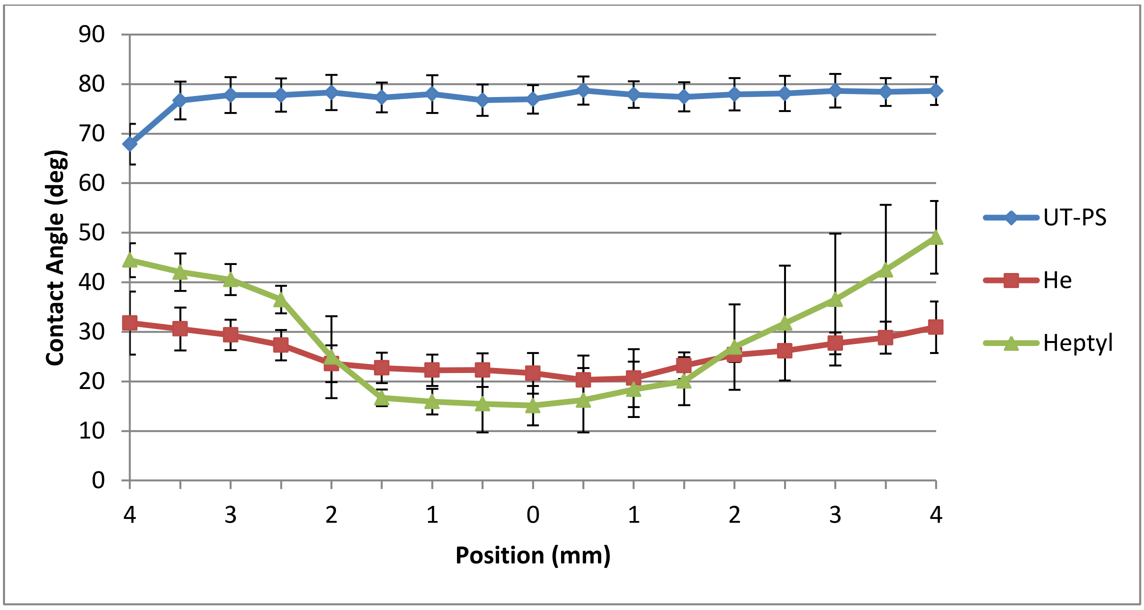

Figure 3.64 Line graph of contact angle profiles taken across untreated polystyrene (PS) and PS samples treated with just helium (He) or a helium:heptylamine (Heptyl) mixture. Contact angle measurements were taken across central axes of samples at a resolution of 0.5mm. Error bars are ± 1 standard deviation.

2D contact angle mapping of helium treated PS demonstrated that the entire sample surface was treated. The average contact angle on helium treated PS was 24.3 ± 1.9°. The contact angle heptylamine treated PS was higher at the edge regions (~45°) compared to helium treated PS, whereas the contact angle in some areas closer to the centre had contact angle of <20°.

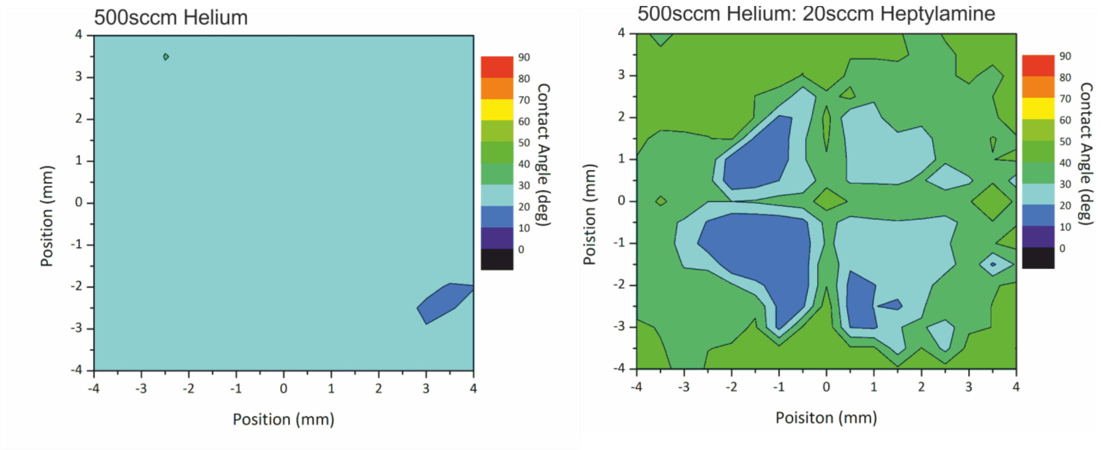

Figure 3.65 2D Contact angle plots of polystyrene (PS) treated with a helium (He) plasma jet with a flow rate of 500sccm, and PS treated with a helium:heptylamine (Heptyl) plasma jet with flow rates of 500sccm:20sccm. Contact angle measurements were made with a spatial resolution of 0.5mm. 2D plots were from single samples.

3.6.3.2 X-ray Photoelectron Spectroscopy

Broad scan spectra were obtained for UT-PS and PS treated with heptylamine plasma jets which had heptylamine mixtures of 20, 50 and 100sccm combined with a fixed helium flow of 500sccm. Broad scan spectra were resolved into 3 peaks: C1s, N1s and O1s. The broad scan spectra of UT-PS only contains a large carbon C1s peak, whereas when PS is treated with a helium plasma a considerable O1s peak was observed in the spectra (Figure 3.66). On the spectra for the 20sccm Heptylamine treated parameter there was clearly a higher oxygen content compared to the helium treated PS (as seen from the O1s/C1s ratio), also a substantial nitrogen peak was observed. The presence of both nitrogen and oxygen were observed on the 50sccm and 100sccm heptylamine treatments, however the relative peak intensities were smaller than those observed on the 20sccm parameter.

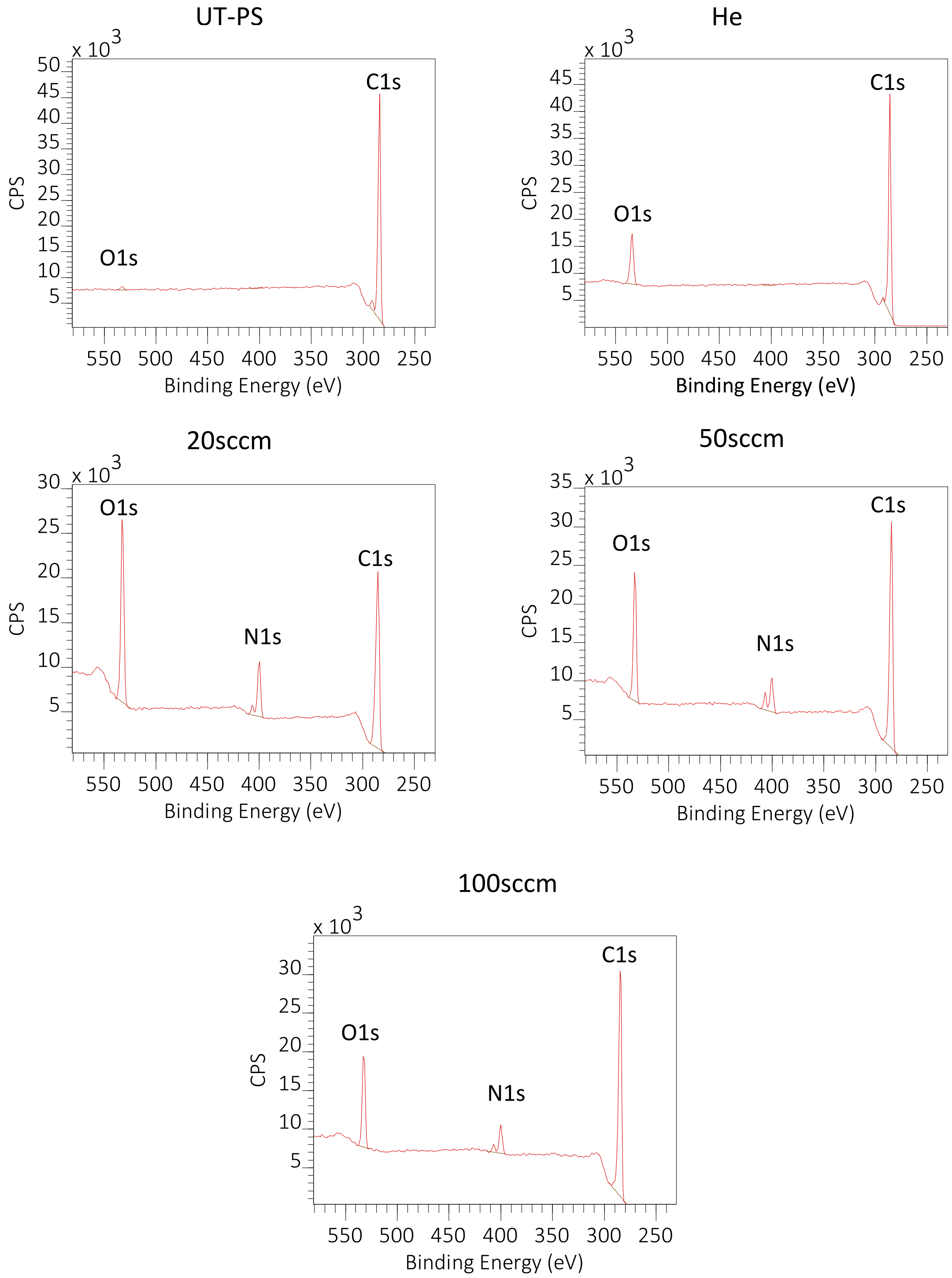

Figure 3.66 X-ray photoelectron spectrographs of untreated polystyrene (UT-PS), helium treated polystyrene (He) and polystyrene (PS) treated with heptylamine plasma of various flow rats: 20sccm, 50sccm and 100scmm. Broad scans were taken in the centre of samples at pass energy of 100eV. Single samples were used.

From the area beneath the C1s, N1s and O1s peaks the total atomic concentration was determined. Only the nitrogen and oxygen concentrations are stated and expressed as percentages. Broad scan XPS spectra taken in the centre of UT-PS demonstrated that there was very little surface nitrogen (0.3%) and oxygen content (1.8%)(Table 3.7). When PS was treated with just helium there was <1% nitrogen (0.8%) but the oxygen concentration had increased to 23.2%. When PS was treated with a gas mixture of helium: 20sccm heptylamine 13.9% surface nitrogen content was observed, as well as 40.8% surface oxygen content: these were the highest concentrations of nitrogen and oxygen observed for all samples. When the flow rate of heptylamine was increased to 50sccm the surface nitrogen and oxygen concentrations were 10.1% and 26.8% respectively. When the heptylamine flow rate was increased further to 100sccm the surface nitrogen and oxygen concentrations were similar to the 50sccm flow rate condition (10.7% and 23.9% for the nitrogen and oxygen concentrations respectively). The O/C and N/C ratios were highest on the 20sccm sample.

Table 3.7 Atomic concentrations as percentages of carbon, nitrogen and oxygen for untreated PS (UT-PS), polystyrene treated for 10mins with helium (He), polystyrene treated with a mixture of helium and 20sccm heptylamine (20sccm), 50sccm heptylamine (50sccm) and 100sccm heptylamine (100sccm). Total concentration was derived from the area of peaks in broad scan spectra taken in the centre of samples (100eV pass energy). Single samples were used.

		UT-PS	20sccm	50sccm	100sccm
Atomic Concentration %	C1s	97.9	45.4	63.1	65.4
	N1s	0.3	13.9	10.1	10.7
	O1s	1.8	40.8	26.8	23.9
	O/C ratio	0.02	0.90	0.42	0.37
	N/C ratio	0.00	0.31	0.16	0.16

XPS broad scans were also obtained across sample surfaces with a spatial resolution of 1mm. Surface atomic concentration was determined from these for each position and results will displayed in 2 charts; one plotting nitrogen concentration and the other plotting oxygen concentration. Almost no nitrogen was observed at any position on UT-PS (Figure

3.67). The surface concentration of nitrogen on the 20sccm parameter was >10% at all positions and reached a maximum of 14.6% at 2mm left of the centre. When treated with a 50sccm heptylamine flow rate the maximum nitrogen concentration, observed in the centre position, was 12.6%: this decreased with distance from the centre to a minimum of 2.3% at the edge. The 100sccm parameter displayed a similar pattern of nitrogen concentration to the 50sccm however; the concentrations on 100sccm parameter were slightly lower. On the 100sccm parameter a maximum nitrogen concentration of 10.7% was observed in the centre of the sample and a minimum nitrogen concentration of <1% was observed at the edge.

Very little oxygen was observed at any position on UT-PS (≤2.3%)(Figure 3.68). The oxygen concentration on all heptylamine treated parameters decreased with distance from the centre. The 20sccm parameter had the highest concentration of oxygen at all positions which ranged from 40.8% in the centre, to 23.9% at the edge. The oxygen concentration on the 50sccm parameter decreased from 32.7% in the centre to a minimum of 12.7% at the edge. The 100sccm parameter had an oxygen concentration of 25.2% in the centre region which decreased to a minimum of 7.6% at the edge. These data demonstrate the entire surface of samples were treated and the extent of treatment, i.e. the concentration of nitrogen and oxygen, decreases with an increase in heptylamine flow rate.

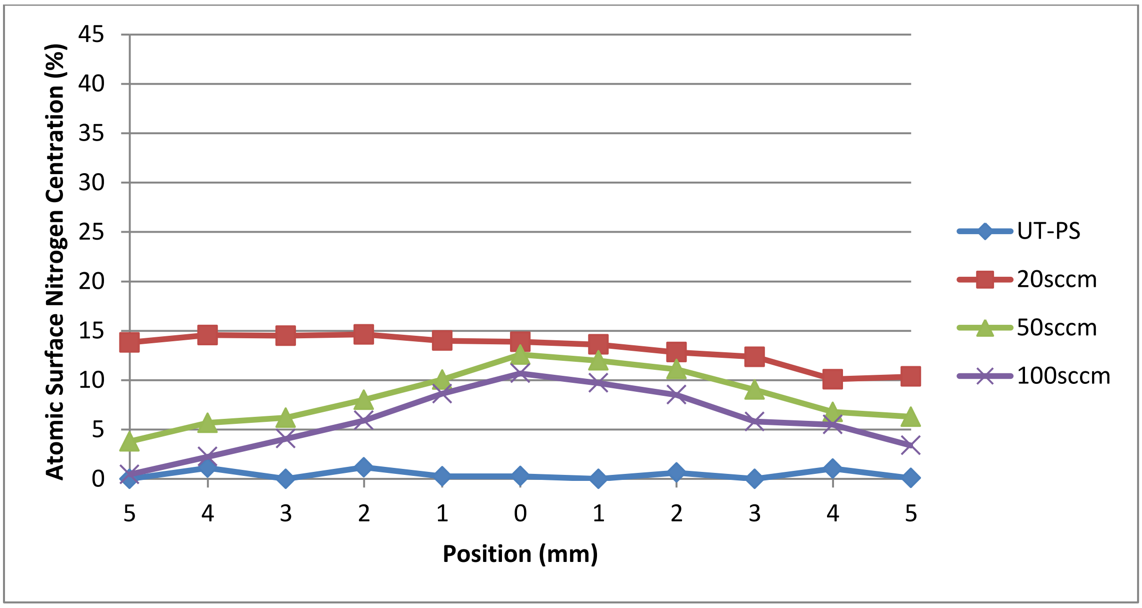

Figure 3.67 Line graph of the atomic nitrogen concentration, as determined from x-ray photoelectron spectroscopy broad scan spectra (100eV pass energy), across the surface of untreated polystyrene (UT-PS) and polystyrene treated with a mixture of 500sccm helium and 20sccm heptylamine (20sccm), 50sccm heptylamine (50sccm) and 100sccm heptylamine (100sccm). Spectra were taken with a spatial resolution of 1mm. Single samples were used.

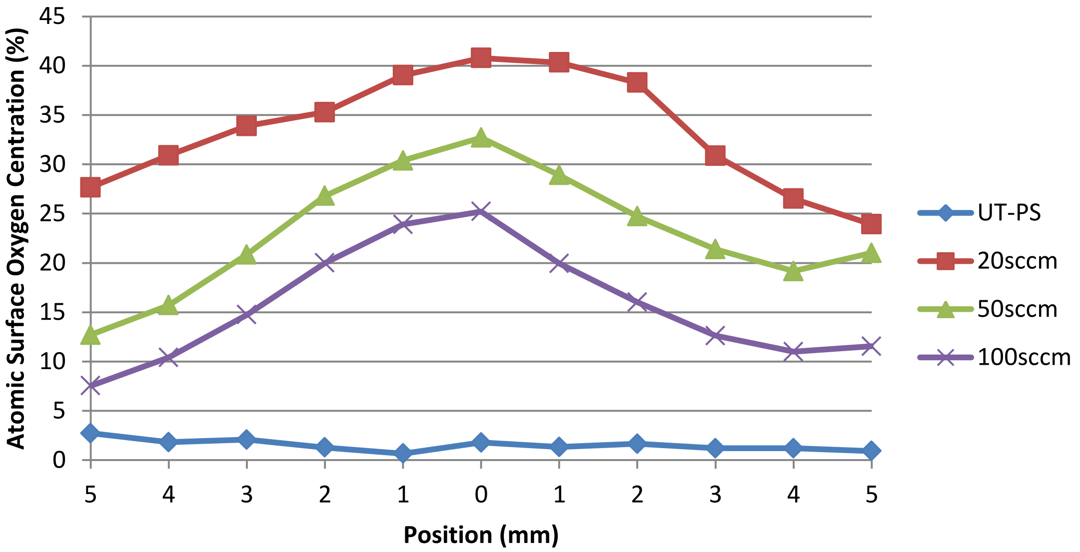

Figure 3.68 Line graph of the atomic oxygen concentration, as determined from XPS broad scan spectra (100eV pass energy), across the surface of untreated polystyrene (UT-PS) and polystyrene treated with a mixture of 500sccm helium and 20sccm heptylamine (20sccm), 50sccm heptylamine (50sccm) and 100sccm heptylamine (100sccm). Spectra were taken with a spatial resolution of 1mm. Single samples were used.

3.6.3.3 Atomic Force Microscopy

The roughness values of UT-PS were Rq = 0.6 ± 0.4nm, and Ra = 0.4 ± 0.2nm (Figure 3.69). The Rq roughness of UT-PS was not significantly different to either helium nor heptylamine treated PS ($p>0.5$), however the Ra value was significantly lower than helium treated PS ($p=0.18$). The Rq and Ra values of helium treated PS were the highest of all 3 parameters (Rq=0.8 ± 0.2nm, Ra=0.6 ± 0.2nm). Helium treated PS had a significantly higher Rq than heptylamine ($p<0.001$). Helium treated PS also had a significantly higher Ra than both UT-PS ($p<0.018$) and heptylamine treated PS ($p<0.001$).

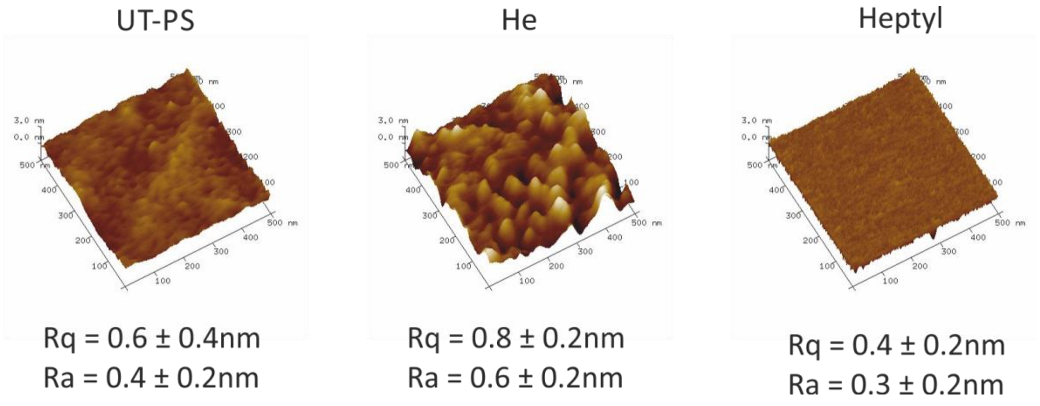

Figure 3.69 AFM micrographs including root mean squared roughness (Rq) and average roughness (Ra) values of untreated polystyrene (UT-PS), helium treated poylstyrene (He) and heptylamine treated polystyrene (Heptyl) (20sccm flow rate). Ra and Rq were determined from 4 measurements in the centre of 4 samples per parameter. AFM was performed in tapping mode at a frequency of 1Hz with 512 samples/line, using silicon cantilever with a spring constant of 40N/m.

3.6.3.4 Cell Culture

3.6.3.4.1 Cell Counts - Day 1

On TCPS the numbers of B3 human LECs ranged from 62-104 cells per field of view across all positions, with the highest number of cells in the centre. There were significantly more cells in the centre position compared to the 3mm position by a small margin ($p=0.45$). There was no significant difference between any other positions ($p>0.05$). On UT-PS there were very few attached cells as expected (2-5 cells per field of view), and there was no significant difference between the positions ($p=0.386$). There were fewer cells on UT-PS than TCPS at all positions ($p<0.01$).

The number of LECs on helium treated PS was highest in the central position and decreased with distance from the centre. At the centre position there were 462 ± 458 cells per field of view, which had decreased to 23 ± 30 cells per field of view by the 4mm position. Due to the large variance the centre position was not significantly different to any other position ($p>0.1$). There was a significant decrease in number of LECs for each subsequent position ($p<0.05$). Again, due to the large variation helium treated PS was not significantly different to neither TCPS nor UT-PS at the centre position; however, it did have significantly more cells than TCPS and UT-PS at the 1.5mm position ($p<0.05$). At the 3mm position helium treated PS was not significantly different to TCPS (p=0.999), yet it had significantly fewer cells than TCPS at the 4mm position (p<0.001). Helium treated PS had significantly more LECs than UT-PS at the 3mm and 4mm positions (p<0.01); therefore helium treated PS could not be considered untreated at any position.

Heptylamine treated PS had the most LECs in the centre position compared to all other parameters (848 ± 361 cells per field of view). The number of cells on heptylamine treated PS decreased significantly at each subsequent position (p<0.05) from the centre, decreasing to 6 ± 10 cells per field of view at the 4mm position. At the centre and 1.5mm positions heptylamine treated PS had significantly more LECs than TCPS (p<0.01), however there were significantly fewer cells on heptylamine treated PS at the 3mm and 4mm positions (p<0.05). Heptylamine had significantly more LECs than UT-PS at the centre, 1.5mm and 3mm positions (p<0.01). At 4mm from the centre heptylamine treated PS was not significantly different to UT-PS (p=0.209) and therefore could be said to be untreated at this position.

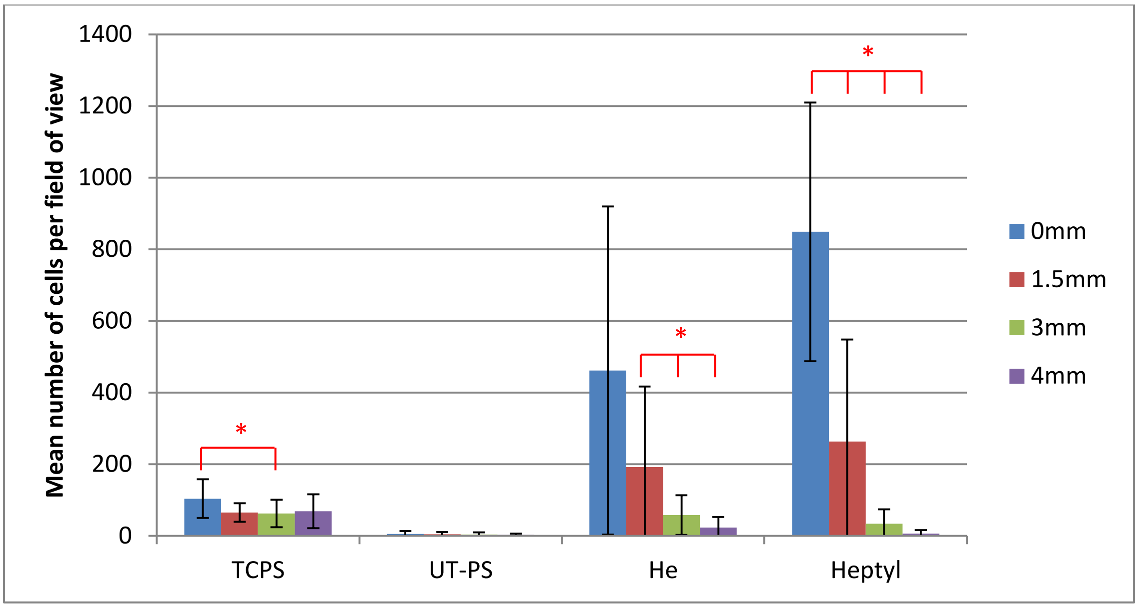

Figure 3.70 Bar chart displaying mean number of DAPI stained B3 human lens epithelial cells (LECs) per field of view at the centre of samples and 1.5mm, 3mm and 4mm from the centre of samples at day 1. Cells were assumed to be mononuclear. Significant differences are only graphically displayed for intra-parameter differences. * indicates significant difference of p<0.05, as determined by one-way ANOVA. Error bars are ± 1 standard deviation.

3.6.3.4.2 Cell Counts - Day 4

Following 4 days of growth the number of LECs on TCPS ranged from 130-314 cells per field of view across all positions. There was no significant difference between these positions ($p>0.1$). The average number of LECs on any position of UT-PS was 1 ($p=0.841$). Due to the large variation of cells in the centre position of TCPS there was no significant difference between TCPs and UT-PS at the centre ($p=0.086$). At all other positions there were significantly fewer cells on UT-PS than TCPS ($p<0.001$).

The number of LECs on helium treated PS decreased with distance from the centre. There were 557 ± 428 cells per field of view in the centre, which decreased to 114± 109 cells per field of view at the 4mm position. Similar to the day 1 time point there was no significantly difference between the centre and 1.5mm position ($p=0.976$); however, there was a significant decrease in number of LECs for each subsequent position ($p<0.05$). Helium treated PS did not have significantly more LECs in the centre position than TCPS ($p=0.703$); however there were significantly more at the 1.5mm and 3mm positions ($p<0.01$). Helium treated PS and TCPS had a similar number of LECs at the 4mm position ($p=0.982$). Helium treated PS had significantly more LECs at each position compared to UT-PS ($p>0.05$) and could therefore not be considered untreated at any position.

Heptylamine treated PS had 483 ± 349 cells per field of view in the centre position on day 4. This decreased at each position to 3 ± 4 cells per field of view at the 4mm position. The decrease from the centre to the 1.5mm position was not significantly different ($p=0.331$), but each subsequent decrease was significant ($p\leq0.1$). There was no significant difference between heptylamine treated PS and TCPS at the centre or 1.5mm positions on day 4, yet there were significantly fewer cells on heptylamine treated PS at the 3mm and 4mm positions ($p<0.001$). There were significantly more cells on heptylamine treated PS than UT-PS at the centre, 1.5mm and 3mm positions ($p<0.05$), yet there was no significant difference between the parameters at the 4mm position ($p<0.001$); therefore heptylamine treated PS could be considered untreated at this position.

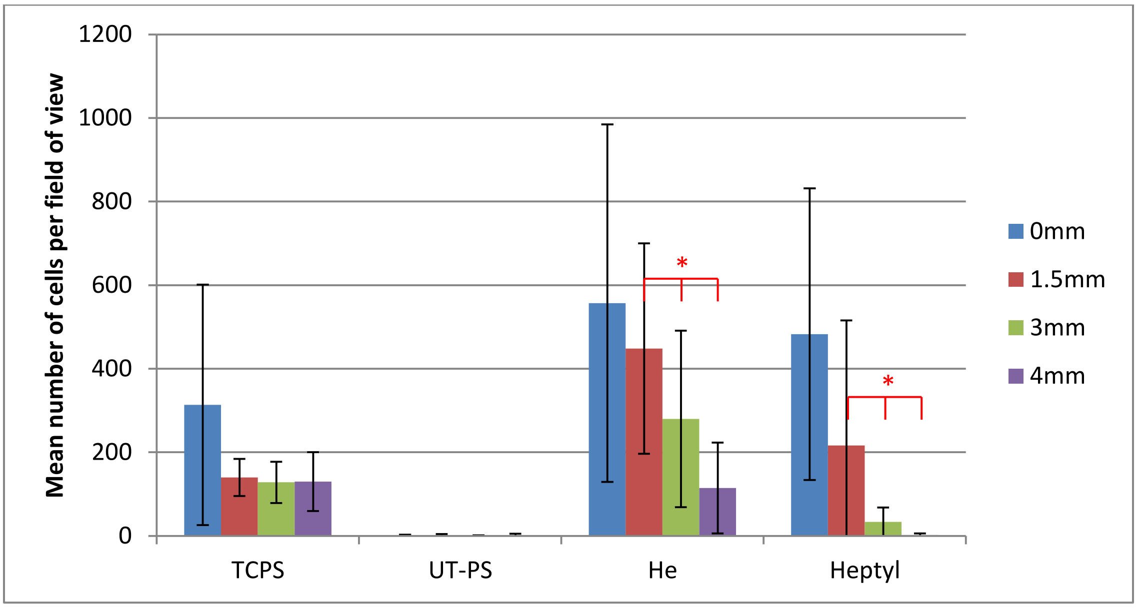

Figure 3.71 Bar chart displaying mean number of DAPI stained B3 human lens epithelial cells (LECs) per field of view at the centre of samples and 1.5mm, 3mm and 4mm from the centre of samples at day 4. Significant differences are only graphically displayed for intra-parameter differences. * indicates significant difference of p<0.05, as determined by one-way ANOVA. Error bars are ± 1 standard deviation.

3.6.3.4.3 Cell Counts - Day 7

At day 7 there were 512-795 cells per field of view across all parameters of TCPS. There were significantly more cells in the centre position compared to the 3mm position (p=0.03) and there was no significant difference between any other position (p>0.1). Similar to the previous time points, there were almost no cells at any position on UT-PS (~1 cell per field of view, p=0.545). There were significantly fewer cells on UT-PS than TCPS at every position on day 7 (p<0.001).

On helium treated PS there were 1065 ± 250 cells per field of view in the centre position, which was more than any other parameter at this position. The pattern of cell growth on helium treated PS was the same as the previous time points: there was no significantly difference between the centre and 1.5mm position (p=0.586); yet there was a significant decrease in number of LECs for each subsequent position (p<0.01). Helium treated PS had significantly more cells than TCPS at the 1.5mm position only (p<0.001). There were significantly fewer cells on UT-PS compared to helium treated PS at every position (p<0.001), therefore the entire sample surface was treated.

There were 472 ± 397 cells per field of view in the centre position of heptylamine treated PS at day 7. This number decreased to 14 ± 19 cells per field of view at the 4mm position. The decrease from the centre to the 1.5mm position was not significant (p=0.845) yet each subsequent decrease was significant (p<0.05). There was no significant difference in the number of LECs between heptylamine treated PS and TCPS in the centre position (p=0.313). There were significantly fewer cells on heptylamine treated PS on the remaining positions (p<0.001). There was no significant difference between the number of cells on heptylamine treated PS and UT-PS at the centre position on day 7 (p=0.59): this was most likely due to the large standard deviation observed in the centre position of heptylamine treated PS. There were significantly more cells on heptylamine treated PS than UT-PS was significantly different at the 1.5mm and 3mm positions (p<0.005). Although there was only a difference of 13 cells per field of view between UT-PS and heptylamine treated PS at the 4mm position, this was significantly different (p=0.004), therefore heptylamine treated PS cannot be considered untreated at any position following 7 days of culture.

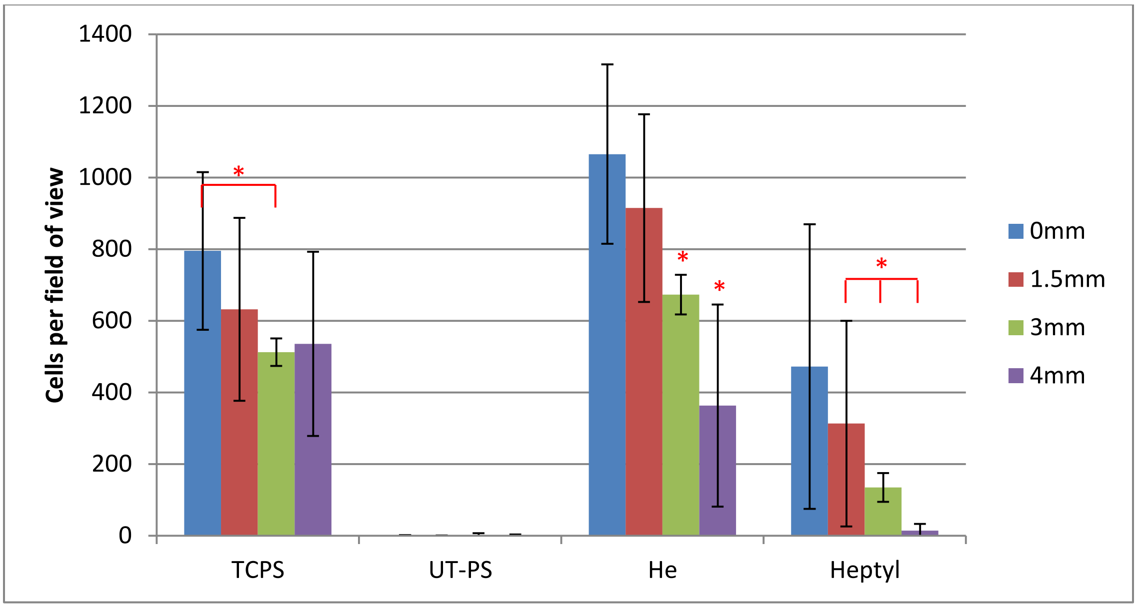

Figure 3.72 Bar chart displaying mean number of DAPI stained B3 human lens epithelial cells (LECs) per field of view at the centre of samples and 1.5mm, 3mm and 4mm from the centre of samples at day 7. Significant differences are only graphically displayed for intra-parameter differences. * indicates significant difference of p<0.05, as determined by one-way ANOVA. Error bars are ± 1 standard deviation.

3.6.3.4.4 Cell Montage

The diameters of cell growth for helium and heptylamine treated PS were similar on day 1 (2.6 ± 0.7mm and 2.5 ± 0.8mm, respectively)(p=0.841)(Figure 3.73). At day 4 the diameter of cell growth on helium treated PS (5.6 ± 1.9mm) was significantly larger than heptylamine treated PS (3.6 ± 1.4mm)(p=0.002). The increase in the diameter of cell growth on helium treated PS from day 1 to day 4 was significant (p<0.001). The diameter of cell growth on heptylamine treated PS was also significant (p=0.043). The diameter of cell growth on helium treated PS (8.3 ± 1.3mm) was significantly larger than heptylamine treated PS (4.3 ± 1mm) on day 7 also (p<0.001)). The diameter of cell growth on helium treated PS increased significantly from day 4 to day 7 (p<0.001), however the increase on heptylamine was not significant (p=0.116).

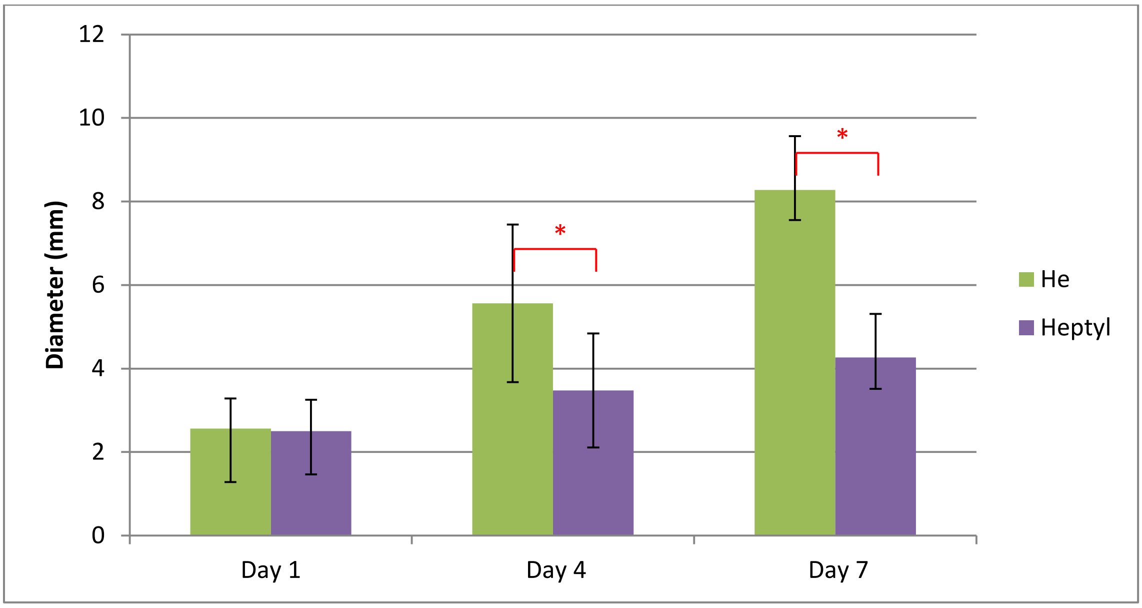

Figure 3.73 Bar chart of diameters of cell growth across samples measured from stitched micrographs of fluorescently stained B3 lens epithelial cells (LECs) at day 1 and day 7 on treated polystyrene (PS) samples. Significant differences are only graphically displayed for differences at each time point. * indicates significant difference of $p<0.05$, as determined by one-way ANOVA. Error bars are ± 1 standard deviation.

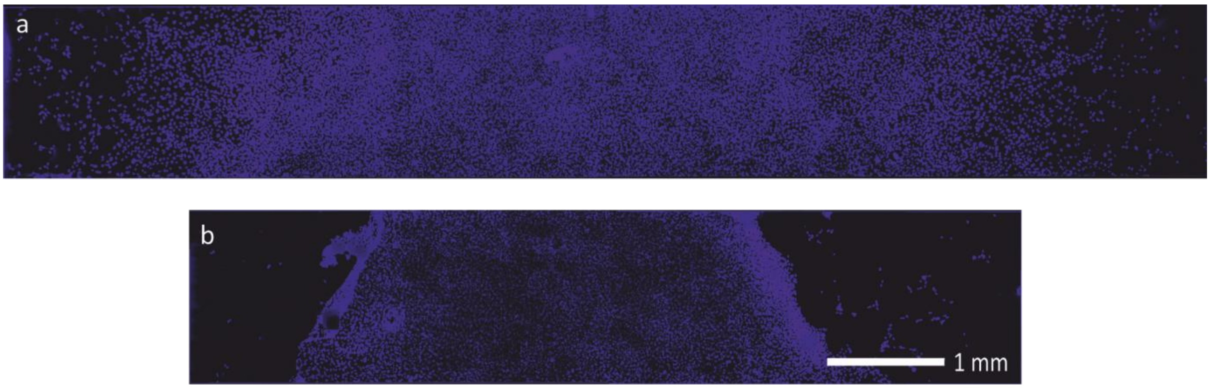

Figure 3.74 Representative stitched micrographs of individual micrographs taken across the centre of treated samples at day 7. B3 lens epithelial cell nuclei were fluorescently stained with DAPI (blue). Cell growth was across a much wider area on helium treated PS (a), compared to heptylamine treated PS (b).

3.6.3.4.5 High Magnification

Cells on TCPS had a well spread morphology and although they appeared cuboidal under phase contrast microscopy did not have strong localisation of actin at the cell boundaries.

Some cells on TCPS did appear cuboid, however actin stress fibres were present in the LECs and some cells did appear to be growing over others (Figure 3.75). Few cells were observed on UT-PS and those present had a rounded morphology suggesting poor attachment. Most cells on helium treated PS were well spread and appeared to have a cobblestone morphology although some actin stress fibres were observed. LECs on heptylamine treated PS were more densely populated and a large presence of actin stress fibre was observed.

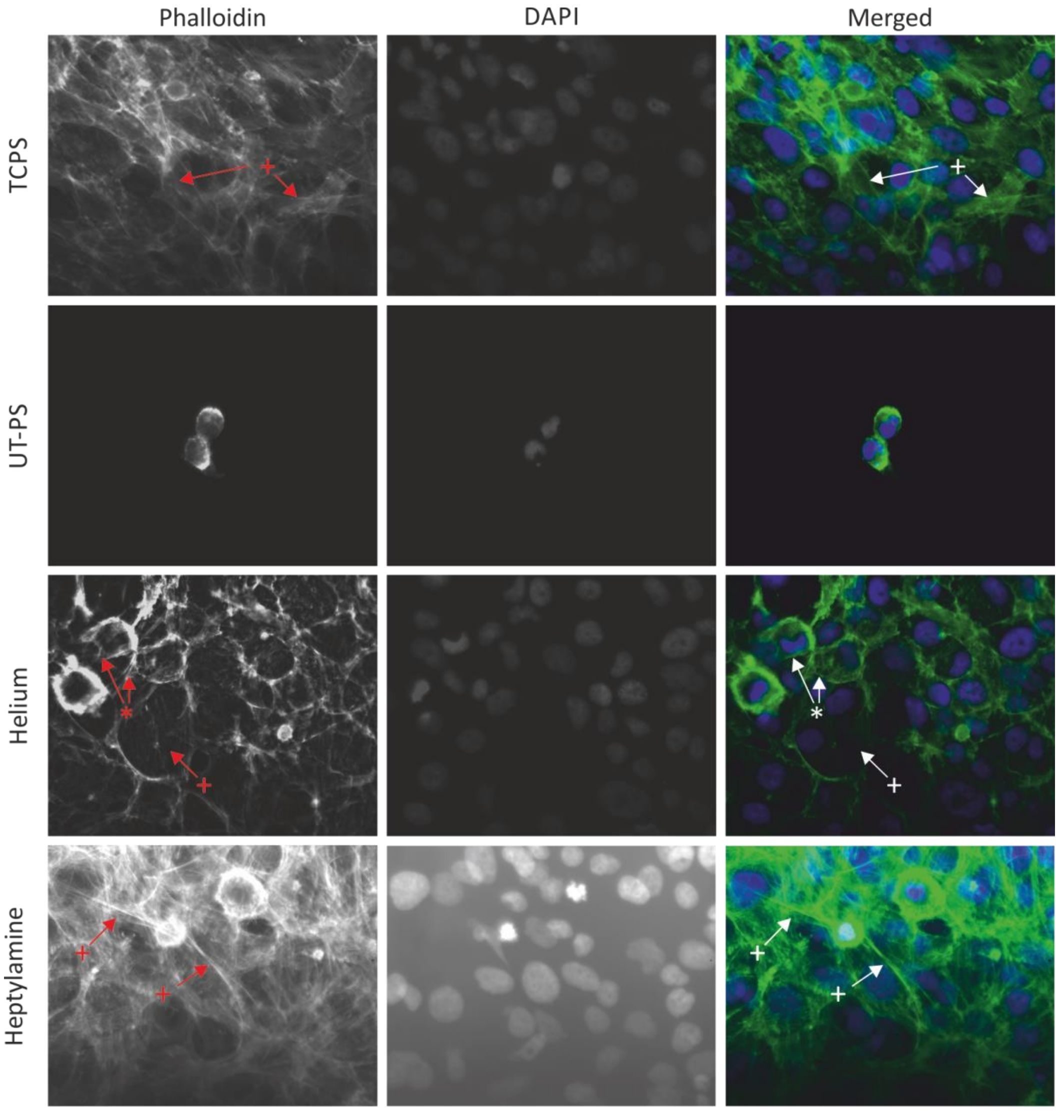

Figure 3.75 Representative high magnification micrographs of human B3 lens epithelial cells (LECs) with phalloidin 488 f-actin staining (green), DAPI nuclear staining (blue) and merged images taken on tissue culture polystyrene (TCPS), untreated polystyrene (UT-PS), helium treated polystyrene (PS), and heptylamine treated PS at day 7. * = actin localisation at cell periphery, + = actin stress fibres. Scale bar = 50µm.

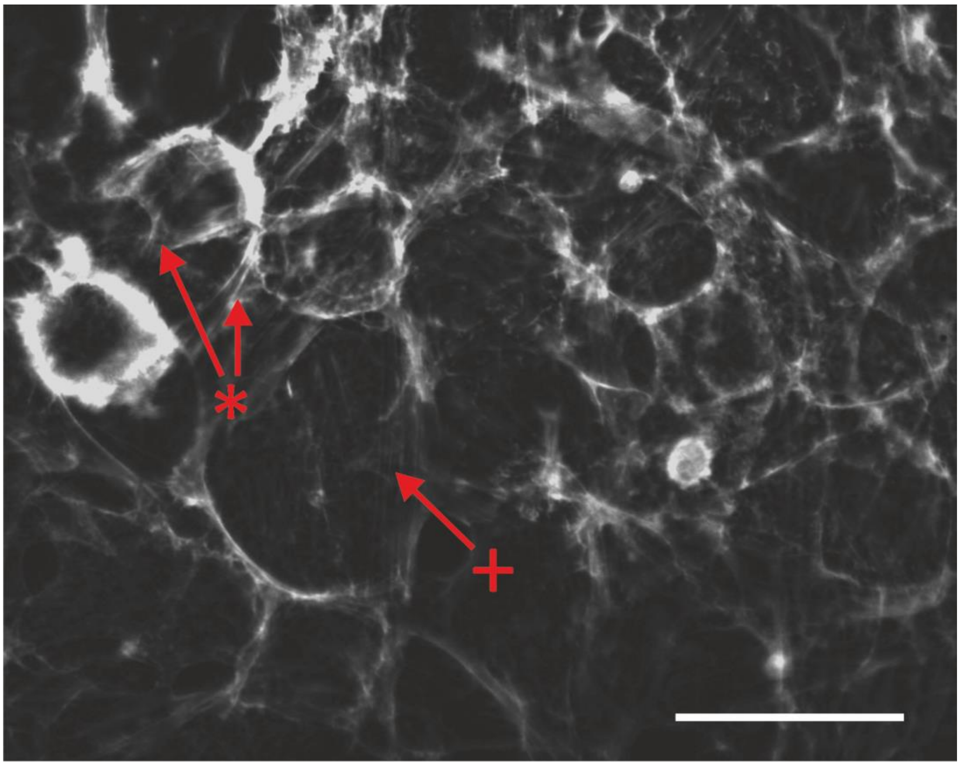

Figure 3.76 High magnification micrograph of phalloidin f-actin staining of lens epithelial cells grown on polystyrene treated with a helium plasma on day 7. + = actin stress fibres. Scale bar = 50µm.

3.6.3.5 Preliminary TGF-β2 ELISA

The level of transforming growth factor-beta 2 (TGF-β2) was examined using ELISA on culture medium surrounding cells grown on helium and heptylamine treated PS, as well as on UT-PS and TCPS controls. The following work was preliminary as it was only conducted once. On day 1 the highest concentration of TGF-β2 was observed in medium from wells containing LECs grown on TCPS wells (52pg/ml). The concentration of TGF-2 in medium from wells containing LECs grown on UT-PS was lower than TCPS at 39pg/ml, yet medium taken from wells containing LECs grown on helium treated PS wells had the lowest concentration of TGF-β2 at 16pg/ml. The concentration of TGF-β2 in medium from wells containing LECs grown on heptylamine treated PS was similar to UT-PS (41pg/ml).

By day 7 the centration of TFG-β2 observed in medium from wells containing LECs grown on heptylamine treated PS (224pg/ml) was much higher than the other parameters. Culture medium from wells containing LECs grown on TCPS, UT-PS and helium treated PS had concentrations of 79, 56 and 87 pg/ml respectively.

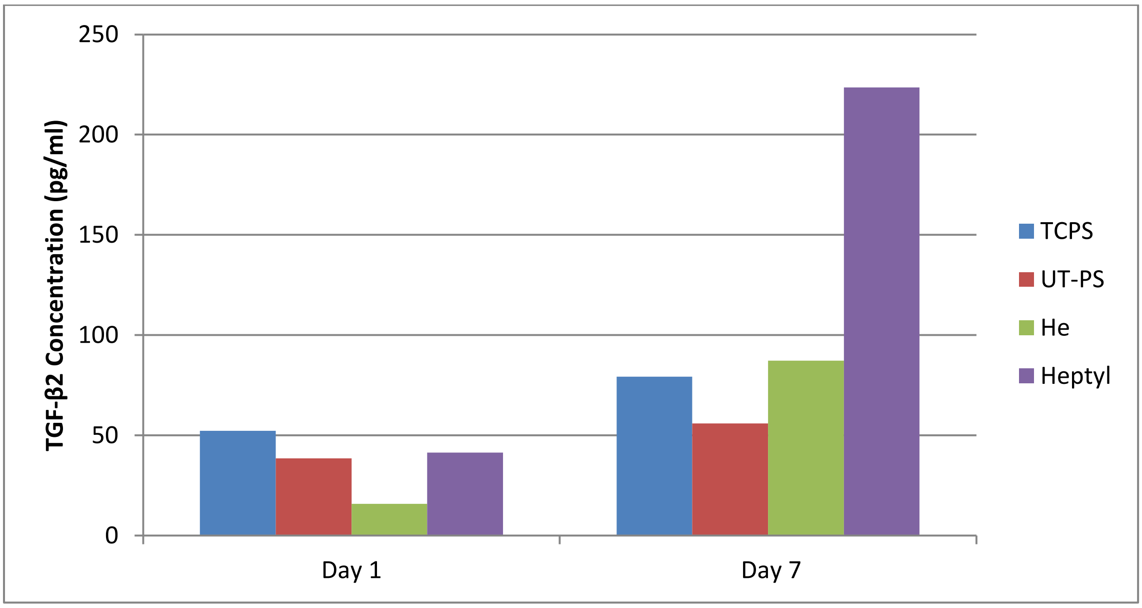

Figure 3.77 Bar chart depicting the concentration of transforming growth factor-β2 (TGF-β2) in culture medium from wells containing B3 human lens epithelial cells grown on tissue culture polystyrene (TCPS), untreated polystyrene (UT-PS) and polystyrene (PS) treated with either helium (He) or heptylamine (Heptyl) plasmas, as determined by enzyme-linked immunosorbant assay (ELISA). B3 lens epithelial cells were grown for up to 7 days. Medium was removed at day 1 or at day 7. Cells had been fed at day 4. Medium from 4 wells for each parameter were pooled and values are the mean of 2 measurements.

3.6.3.6 Cytokine Multiplex Assay

A magnetic bead based assay was run to examine the concentration of inflammatory cytokines present in the medium surrounding cells grown on TCPS, UT-PS, helium and heptylamine treated PS. Pooled medium from wells containing each substrate was from single experiment and samples were measured in duplicate, therefore the following data are preliminary.

The presence of IL-1α was not detected on day 1. By day 7 only small concentrations of IL-1α (3pg/ml) were detected in medium from wells containing LECs grown on TCPS, UT-PS and helium treated PS; whereas, a concentration of 1pg/ml in medium from wells containing LECs grown on heptylamine treated PS was extrapolated from below the standard range.

Medium from wells containing LECs grown on TCPS had the highest concentration of IL-6 (30pg/ml) at day 1 compared to the other parameters. The concentrations of IL-6 in medium from wells containing LECs grown on UT-PS, helium and heptylamine treated PS were 7, 10 and 12pg/ml respectively. By day 7 the concentration of IL-6 in medium from wells containing LECs grown on TCPS had increased almost 4-fold to 118pg/ml. Medium from wells containing LECs grown on UT-PS had the highest concentration of IL-6 on day 7 of 134pg/ml: a 19-fold increase compared to day 1. The concentrations of IL-6 in medium from wells containing LECs grown on treated materials were lower: helium treated PS had ~6-fold increase from day 1 to 62pg/ml and heptylamine treated PS increased ~3-fold to 37pg/ml.

Very little basic FGF was detected in the medium from wells containing LECs grown on any material at either time point. On day 1 the concentrations ranged from 0-2pg/ml, in medium from wells containing LECs grown on each of the controls had a concentration of 1pg/ml, and medium from wells containing LECs grown on helium and heptylamine treated had concentrations of 0pg/ml and 2pg/ml respectively. The concentrations for basic FGF in medium were still low on day 7. The concentrations in medium from wells containing LECs grown on TCPS, UT-PS and helium treated PS each increased by 3pg/ml by day 7; there was a 4pg/ml increase for medium from wells containing LECs grown on heptylamine treated PS.

Little or no TNF-α was detected in medium from wells containing LECs grown on any material at either time point. 0pg/ml was detected in medium from wells containing LECs grown on any surface on day 1. On day 7 concentrations of 0-2pg/ml in medium from wells containing LECs grown on all surfaces were extrapolated from below the standard range.

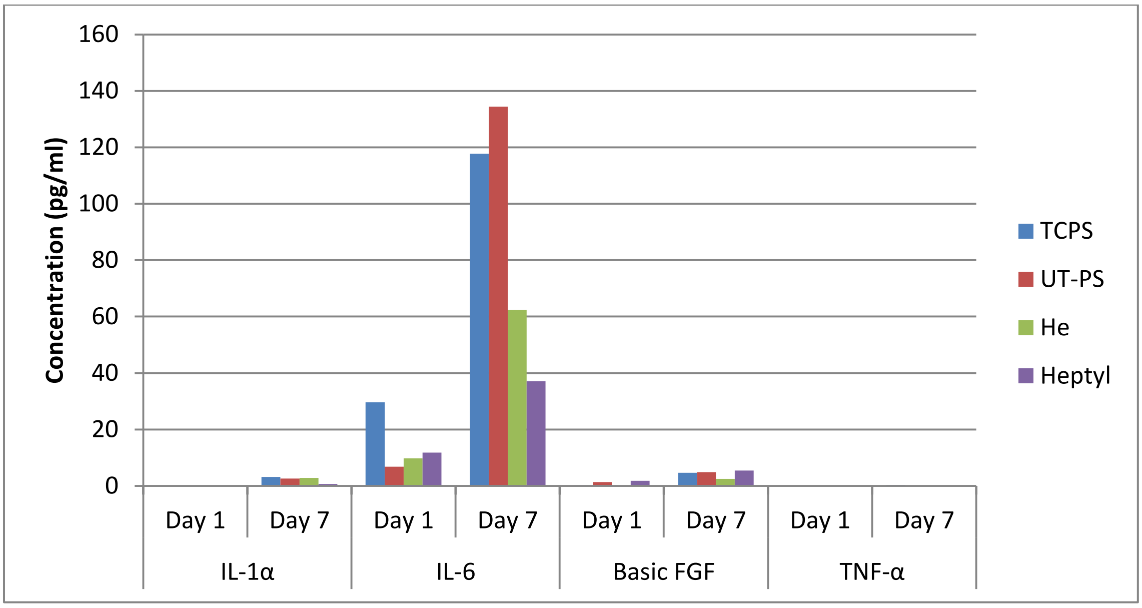

Figure 3.78 Bar Chart demonstrating concentrations of interleukin-1α (IL-1α), interleukin-6 (IL-6) basic fibroblastic growth factor (FGF) and tumour necrosis factor-α (TNF-α), as determined by magnetic bead-based multiplex assay, at day 1 and day 7. Medium was taken from wells in which B3 lens epithelial cells were grown on tissue culture polystyrene (TCPS), untreated polystyrene (UT-PS), helium (He) treated polystyrene (PS) and heptylamine treated PS. Medium from 4 wells for each parameter were pooled and values are the mean of 2 measurements.

3.7 Treatment of Polystyrene with a Pin Plasma System

As a short investigation into the use of an alternative atmospheric pressure plasma system to spatially modify surfaces, PS samples were treated with a “pin plasma” system. This consisted of a powered tungsten wire, encased within a ceramic tube and a ring electrode, at the tip of which a coronal plasma discharge was formed. The tip of this tungsten was placed ~1.3mm from 10x10mm PS samples. Initially, various parameters were investigated by contact angle, following which the numbers of parameters were reduced and further analysis carried out.

3.7.1 Initial Contact Angle Study

In the initial contact angle study variation in 3 parameters were investigated: frequency (20kHz and 15kHz), voltage (17kV and 13kV) and treatment time (20s and 40s). In the following section results will be grouped by frequency into 2 separate figures.

There was very little change in the contact angle of UT-PS between positions. The average contact angle of UT-PS was 81.8° ± 1.6° (Figure 3.79). The entire sample surface for the 20kHz-17kV-20s parameter was treated (<80°); contact angle ranged from ~38 degrees at the edges to ~21° in the centre. The region which was <25° on the 20kHz-17kV-20s parameter spanned 6mm. The profile for the longer treatment time (20kHz-17kV-40s) was similar, however there was a slight decrease in contact angle at the edges (~5-10°) indicating a broadening of the treatment region, compared to the 20s treatment time.

When samples were treated with the 20kHz-13kV-20s parameter the contact angle at the edges was much higher (56.1-68.1°): this decreased to ~22° in the centre region. The section in which contact angle was <25° spanned 5mm, and therefore a smaller central treated than the 17kV parameters. When samples were treated with the 20kHz-13kV-40s parameter the contact angle profile was very similar to the 20kHZ-17kV-20s profile. These results indicated that an increase in treatment time caused a broadening of the treatment region; i.e. the contact angle reduced outward from the centre. It was also evident from comparison of 20kHz-17kV-20s and 20kHz-13kV-20s that a reduction in voltage also decreases the treatment area.

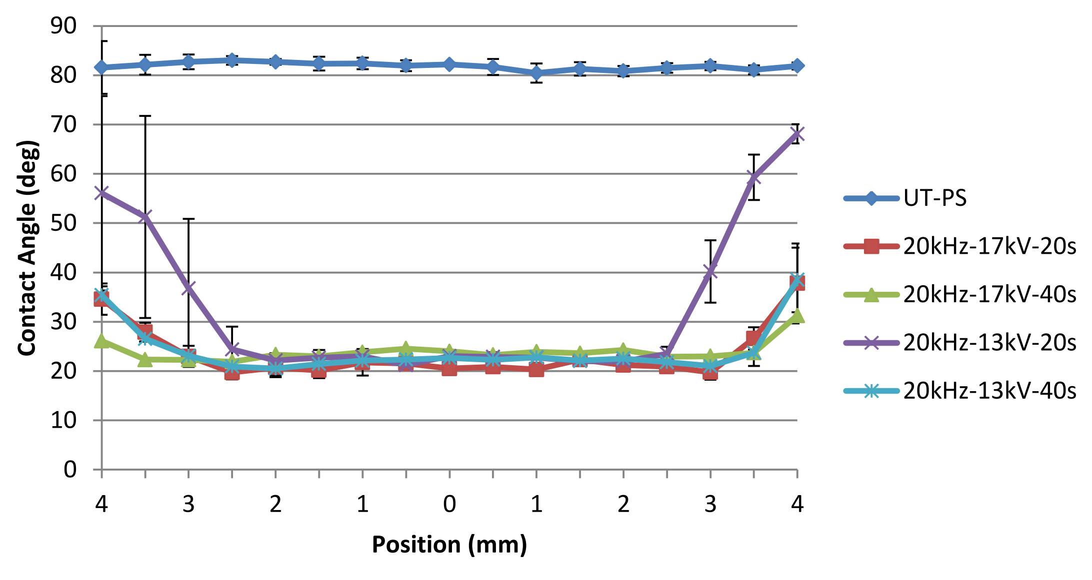

Figure 3.79 Line graph of contact angle profiles taken across untreated polystyrene (UT-PS) and polystyrene (PS) samples treated with a pin plasma system. The frequency of the plasma system was fixed at 20kHz, the voltage was varied between 17kV and 13kV and samples were treated for either 20s or 40s. Contact angle measurements were taken across central axes of samples at a resolution of 0.5mm. Profiles were the mean of 3 samples. Error bars are ± 1 standard deviation.

As stated above the average contact angle for UT-PS was 81.8 ± 1.6°. The contact angles at the edges of the 15kHz-17kV-20s parameter were between 60-80°, which decreased to <25° in the centre region (Figure 3.80). The width of the section of the profile in which contact angle was <25° spanned 4.5mm, which was smaller than that observed for the 20kHz-17kV-20s parameter. With 40s treatment time (15kHz-17kV-40s) the treatment region was slightly broader than the 20s parameter (15kHz-17kV-20s), i.e. the section in which contact angle was <25° was 5mm. When the voltage was reduced to 13kV the central treated region was much more defined. At the edges of the samples the contact angle was ~80° indicating untreated regions, and the section in which contact angle was <25° was 1.5mm for both the 15kHz-13kV-20s and 15kHz-13kV-40s parameters.

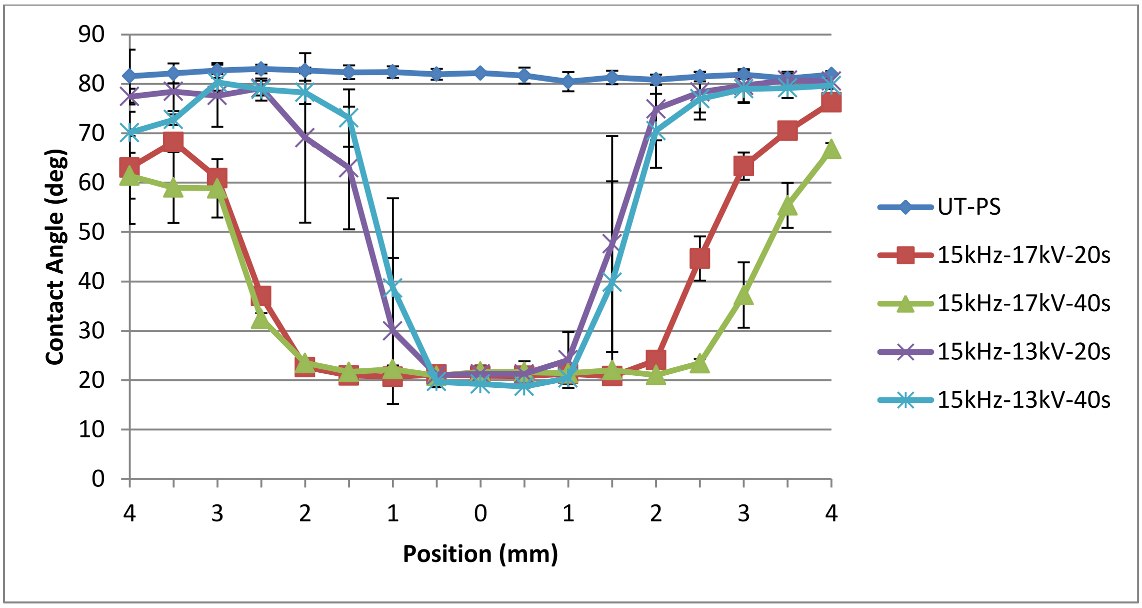

Figure 3.80 Line graph of contact angle profiles taken across untreated polystyrene (UT-PS) and polystyrene (PS) samples treated with a pin plasma system. The frequency of the plasma system was fixed at 15kHz, the voltage was varied between 17kV and 13kV and samples were treated for either 20s or 40s. Contact angle measurements were taken across central axes of samples at a resolution of 0.5mm. Profiles were the mean of 3 samples. Error bars are ± 1 standard deviation.

From the above data it was observed that an increase in frequency, voltage or time caused a broadening of the treatment region in almost all cases. Variation in time had the smallest effect therefore it was decided to fix treatment time at 20s for all subsequent work.

3.7.2 Contact Angle

The contact angle of UT-PS was approximately the same across the surface of the samples and was an average of 82.5 ± 2.3° (Figure 3.81). The maximum contact angle at the edges of the 20kHz-17kV sample was between 56-66° indicating that all of the sample surface was treated. This contact angle reduced to 25-30°, which spanned a distance of 5.5mm. The contact angle in the centre was slightly higher than the previous work (<25°). The contact angle at the edges of the 20kHz-13kV parameter was ~66°, which decreased to ≤25°. The contact angle which was ≤25° spanned 4mm. The reduction of the voltage (with frequency fixed at 20kHz) decreased the contact angle in the centre but also caused the width of treated region to decrease, making a more defined treatment region. The contact angle at the edges of 15kHz-17kV had increased compared to the 20kHz parameters and was >70°. The width of the section in which contact angle was ≤25° for the 15kHz-17kV parameter was 3mm. The 15kHz-13kV parameter followed a similar trend: the contact angle at the edges increased to >75°, however this was still less than the average of UT-PS; the section in the centre of the profile in which contact angle was ≤25° decreased to 2mm.

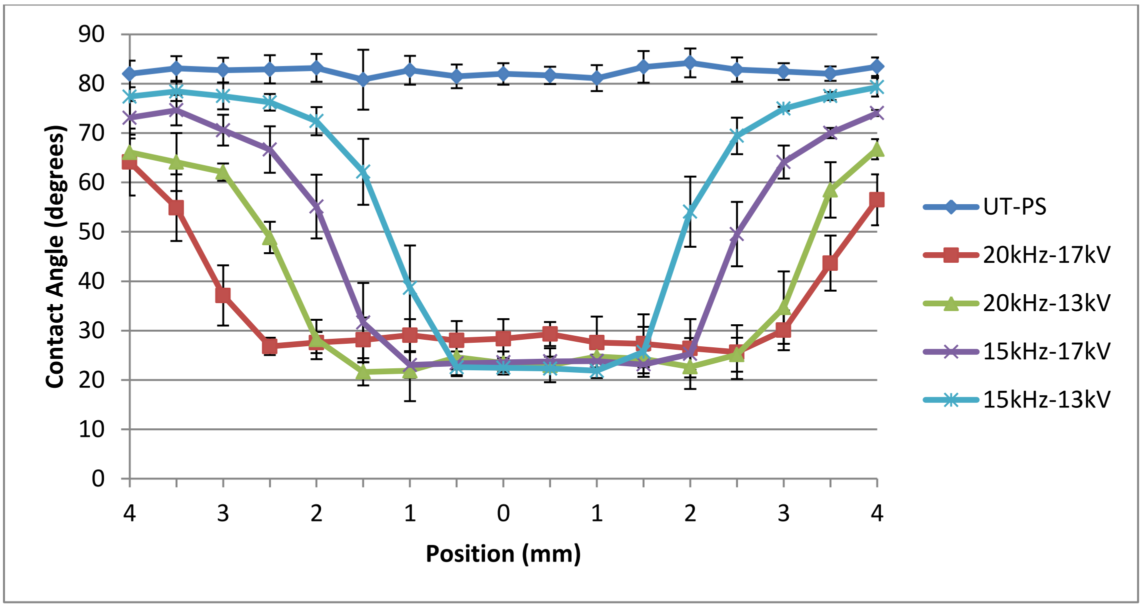

Figure 3.81 Line graph of contact angle profiles taken across untreated polystyrene (UT-PS) and polystyrene (PS) samples treated with a pin plasma system. The frequency of the plasma system was either 20kHz or 15kHz, and the voltage was varied between 17kV and 13kV. Contact angle measurements were taken across central axes of samples at a resolution of 0.5mm. Profiles were the mean of 4 samples. Error bars are ± 1 standard deviation.

These results confirm that a reduction in the frequency or voltage reduces the width of the treatment region. It was observed that the reduction in frequency had the greatest affect.

3.7.3 Atomic Force Microscopy

From AFM analysis the Rq and Ra values for UT-PS were 0.6 ± 0.4nm and 0.3 ± 0.2nm, respectively (Figure 3.82). Following pin plasma treatment the roughness values increased. The Rq values for pin plasma treated substrates ranged from 0.8-1nm, and the Ra values ranged from 0.6-0.8nm. They was very little difference observed in the between all the parameters.

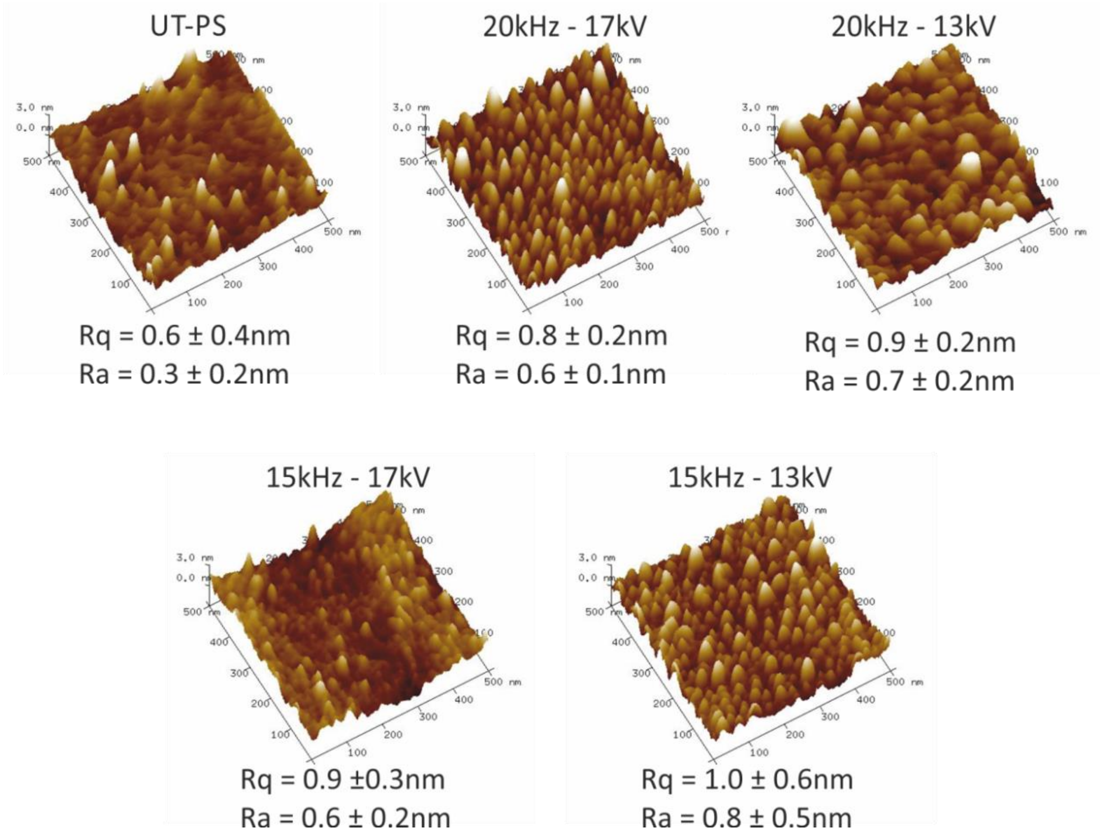

Figure 3.82 AFM was performed in tapping mode at a frequency of 1Hz with 512 samples/line, using silicon cantilever with a spring constant of 40N/m. The root mean square roughness (Rq) and average roughness (Ra) were calculated for untreated polystyrene (UT-PS), and polystyrene treated with a pin plasma operated at either 20kHz or 15kHz frequency and 17kV or 13kV voltage. Ra and Rq were determined from 4 measurements in the centre of 4 samples per parameter. AFM was performed in tapping mode at a frequency of 1Hz with 512 samples/line, using silicon cantilever with a spring constant of 40N/m.

3.7.4 Cell Culture

Human B3 LECs were grown on pin plasma treated substrates to determine if treatment could enable spatially defined cell attachment.

3.7.4.1 Cell Counts - Day 1

The number of LECs observed on TCPS ranged from 69-127 cells per field of view across all positions, with the largest number of cells observed in the centre position (Figure 3.83). UT-PS had an average of 0 cells per field of view at each position.

The samples treated with 20kHz pin plasma had a large number of cells in the centre which decreased as a function of distance in the centre. The 20kHz-17kV parameter had 433 cells per field of view in the centre, this number reduced with an increase in distance from the centre to 16 cells per field of view in the 4mm position.

Samples treated with the 20kHz-13kV parameter had 482 cells per field of view in the centre region. This reduced with distance from the centre; however the centre and 1.5mm positions were similar. The average number of cells at the 4mm position was 24 cells per field of view.

The 15kHz-17kV parameter had a much larger number of cells at the 1.5mm position compared to the centre position (288 and 655 cells per field of view at the centre and 1.5mm positions respectively). By the 4mm position the number of cells had reduced to 5 cells per field of view.

The 15kz-13kV parameter had fewer cells at all positions compared to all other parameters. There were 206 cells per field of view in the centre position. Cells decreased as a function of distance from the centre to 1 cell per field of view at the 4mm position.

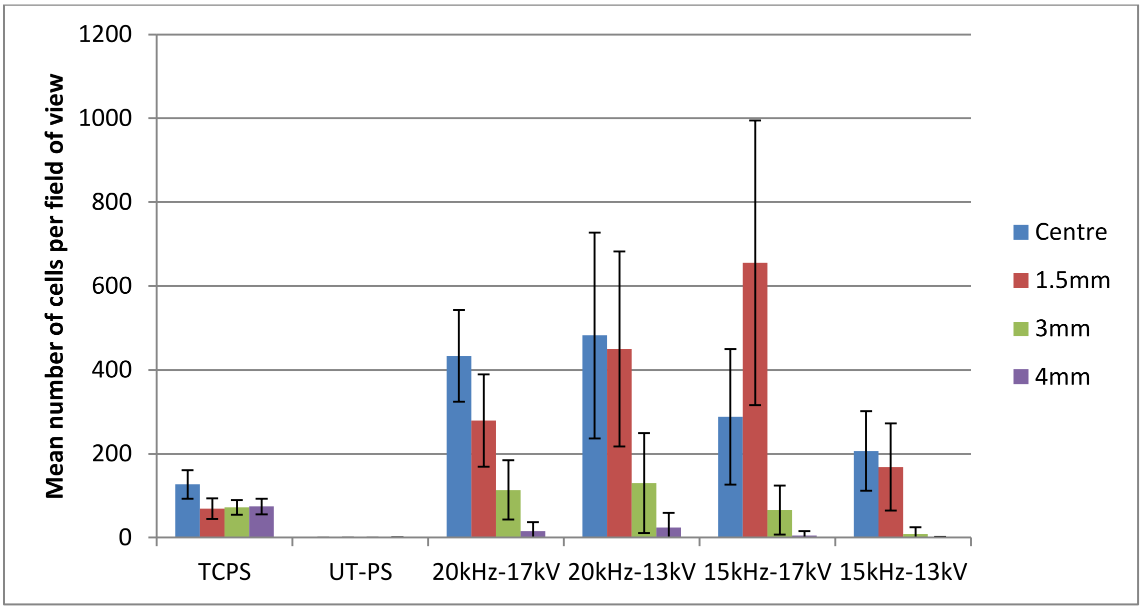

Figure 3.83 Bar chart displaying mean number of B3 human lens epithelial cells (LECs) per field of view at the centre of samples and 1.5mm, 3mm and 4mm from the centre of samples at day 1. The number of cells was determined from micrographs of nuclei stained with DAPI. Cells were assumed to be mononuclear. LECs were seeded onto tissue culture polystyrene (TCPS) untreated polystyrene (UT-PS) or polystyrene treated with a pin plasma operated at 20Khz or 15kHz frequency and 17kV or 15kV voltage. Mean number of cells were from 4 samples. Error bars are ± 1 standard deviation.

3.7.4.2 Cell Counts - Day 4

The number of cells on TCPS had increased compared to day 1 (257-389 cells per field of view across all positions) but there were still more LECs in the central position compared to the other positions (Figure 3.84). There was an average of 0 cells per field of view across all positions on UT-PS at day 4.

There was little change in the centre position of the 20kHz-17kV parameter compared to day 1 (455 ± 289 cells per field of view on day 4); however, there was a more pronounced increase in the number of LECs for the remaining positions. The number of cells still decreased with distance from the centre and there were 75 cells per field of view at the 4mm position.

The 20kHz-13kV parameter was similar to day 1 with a slight increase to number of LECs at each position. The number of LECs decreased with distance from the centre. The number of cells in the centre and 1.5mm positions were 542 and 25 cells per field of view respectively.

There were much more cells in the 1.5mm position than at the centre of the 15kHz-17kV parameter (263 and 799 cells per field of view respectively). From the micrographs in which cells were counted this appeared to be due gaps in the cell growth in the centre position. At the 4m position there were almost no cells (4 ± 12 cells per field of view).

The 15kHz-13kV parameter was similar to day 1 however there was an increase in number of cells in the centre and 1.5mm positions at day 4 (499 and 386 cells per field of view respectively). The number of cells at the 3mm and 4mm positions increased minutely, and there were 2 ± 4 cells per field of view at the 4mm position on day 4.

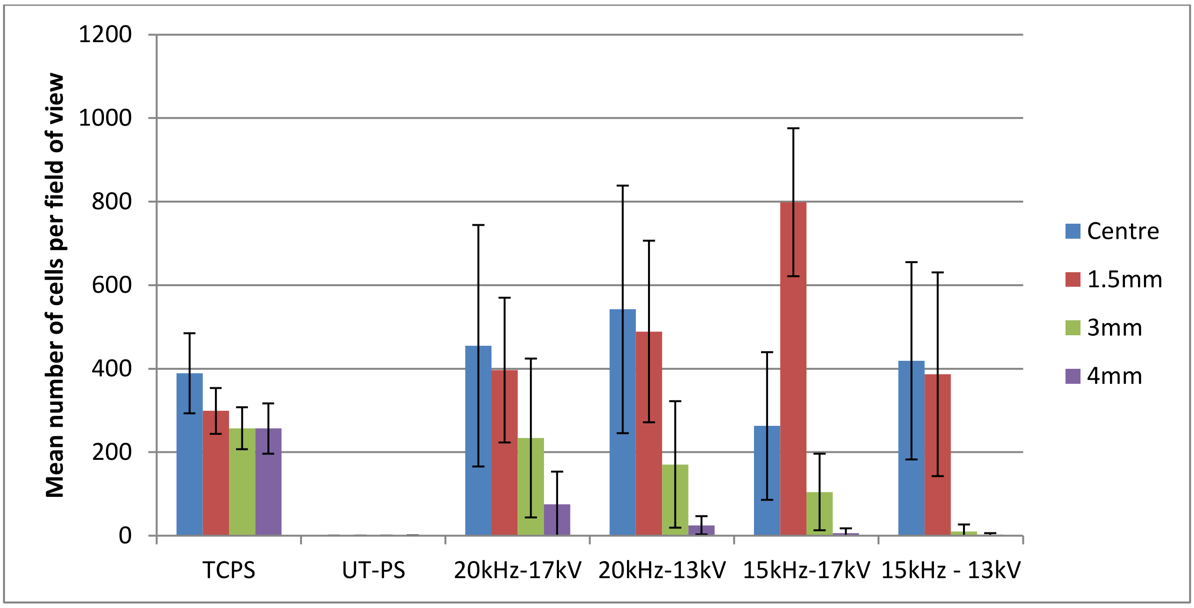

Figure 3.84 Bar chart displaying mean number of B3 human lens epithelial cells (LECs) per field of view at the centre of samples and 1.5mm, 3mm and 4mm from the centre of samples at day 4. LECs were seeded onto tissue culture polystyrene (TCPS) untreated polystyrene (UT-PS) or polystyrene treated with a pin plasma operated at 20Khz or 15kHz frequency and 17kV or 15kV voltage. Mean number of cells were from 4 samples. Error bars are ± 1 standard deviation.

3.7.4.3 Cell Montage

The diameters of cell growth, as measured by stitching of micrographs, demonstrate that each reduction in frequency and/or voltage decreases the diameter of cell growth, observed on pin plasma treated samples at day 4. The diameter of cell growth for the maximum frequency and voltage (20kHz-17kV) was 7.2 ± 1mm; whereas, for the minimum frequency and voltage (15kHz-13kV) the diameter of cell growth was 4 ± 0.6mm.

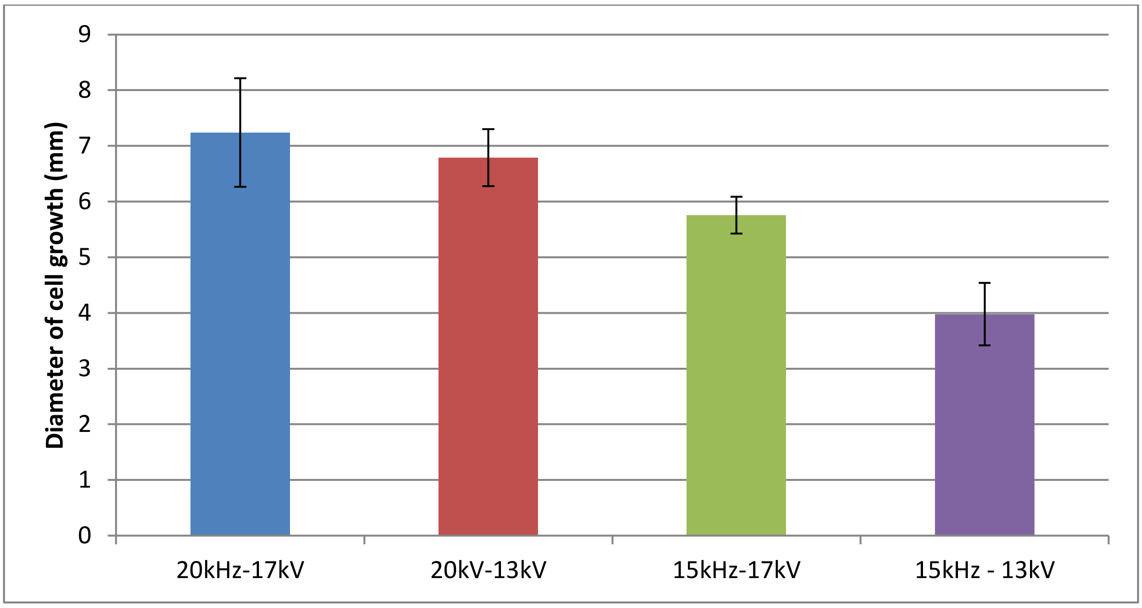

Figure 3.85 Bar chart of diameters of cell growth across samples measured from stitched micrographs of fluorescently stained B3 lens epithelial cells (LECs) at day 4 on pin plasma treated polystyrene (PS) samples. The pin plasma was operated a frequencies of either 20kHz or 15kHz and voltages of 17kV or 13kV. Mean number of cells were from 4 samples. Error bars are ± 1 standard deviation.

From the stitched micrographs it was observed that the density of LECs gradually decreased with distance from the centre of 20kHz parameters, with a greater number of scattered LECs in the edge regions of samples. This was in comparison to the more defined boundary of cell growth observed for LECs grown on PS treated with pin plasmas operating at 15kHz. Beyond this boundary there was very little cell growth. Occasionally either gaps in cell growth or clumps of cell growth were observed within the treated area, indicating that LECs were not forming an epithelial monolayer. Examples of gaps in cell growth can be observed at the intersection of the +x and +y axes on the 20kHz-17kV parameter, Figure 3.86; an example of a clump of cells can be observed directly above the aforementioned gap on the +y axis of 20kHz-17kV, Figure 3.86. The gaps were most often present near the centre of samples, particularly on the 15kHz-17kV parameter, accounting for the lower number of LECs observed in the centre position compared to the 1.5mm position (sections 3.7.4.1 and 3.7.4.2).

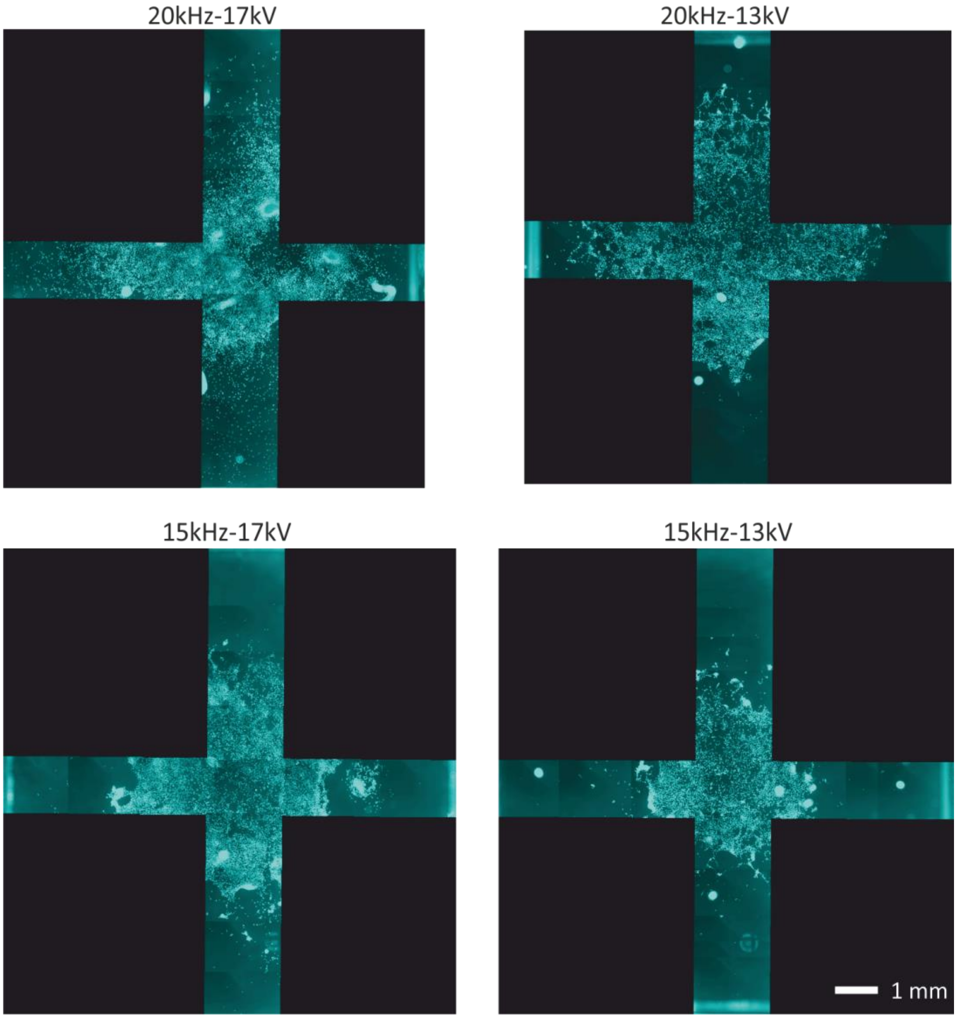

Figure 3.86 Representative stitched micrographs from individual micrographs taken across the centre of treated samples at day 4. B3 human lens epithelial cells (LECs) were fluorescently stained with DAPI. Polystyrene (PS) samples were treated with a pin plasma system operating with frequencies of 20kHz or 15kHZ and voltages of 17kV or 13kV.

4 Discussion

The aim of this study was to modify polymer materials, in a spatially defined manner, to tailor the cellular response of lens epithelial cells (LECs), with the aim of reducing or inhibiting the incidence of posterior capsule opacification (PCO). This work has clearly shown that polystyrene can be modified to encourage cellular attachment and growth in a spatially defined manner [168]. Although polystyrene is not typically used as an implant, it is often used as a model surface to study surface modification due to its hydrocarbon structure [5, 19, 168, 222, 223]. Tissue culture polystyrene (TCPS), which is treated with a proprietary method but most likely to be treated with UV, ozone or plasma methods to incorporate oxygen and/or nitrogen onto the surface, is typically used for cell culture vessels in most laboratories. TCPS provides a good positive control for cell attachment and growth [224, 225]. It was hypothesised that the plasma jet could be used to modify the surface on the same length scale as the cells, to control the response of individual cells; however it has been shown that the area treated by the microplasma jet was much larger than the internal diameter (ID) of the jet nozzle. The area of treatment was controlled by parameters such as flow rate and by varying the distance from the microplasma jet nozzle to the sample surface, yet treatment areas were still on the millimetre scale, even for a nozzle ID of 100µm. Surface functionalisation was characterised by a decrease in contact angle and an increase in the surface oxygen content, as observed by XPS. Treatment with the helium plasma jet caused little change in the surface roughness, suggesting that the method does not affect the polymers’ roughness. Further work on the modification of poly(methyl methacrylate)(PMMA) demonstrated that the principles of microplasma jet treatment could be applied to other materials. Experiments were conducted to investigate the use of the plasma jet design for atmospheric pressure plasma polymerisation. It was hypothesised that this technique could be used to incorporate a wide variety of surface functional groups, depending on the monomer (or molecule) incorporated, onto polymer surfaces.

4.1 Possible Mechanisms of Surface Modification and Optimisation of the Microplasma Jet

Treatment areas of various sizes, created by altering the flow rate and sample-nozzle distance, were observed by spatially resolved contact angle and cell culture studies. The effect of flow rate and sample distance on the size of the treatment areas is related to the basic principles of microplasma jet surface modification. In the plasma jet system helium flows down a quartz capillary toward an electrode powered by ≥6kV and 10-20kHz sinusoidal signal, with or without the presence of a grounded electrode. The powered electrode provides energy to the helium atoms which cause them to vibrate and collide. These collisions cascade and cause the helium atoms to dissociate, losing their electrons [158]. Excited helium atoms and ions are created within the main discharge region of the plasma [160]. The gas flow carries these excited species (atoms and molecules) from the discharge region into ambient air, then these primary species: He^+, He_2^+ and excited He^* (the 2^3S state metastable helium), or electrons collide with molecules and atoms in air (oxygen, nitrogen, H2O etc.) to create secondary ions and radicals [160, 183, 187]. Photons are also created, in the discharge region and in the plasma plume beyond the electrodes, by the photoelectric effect. The photoelectric effect is the emission of the remaining energy from dissociating collisions as a photon, or an electron dropping to a lower energy orbital from an excited state [226, 227]. Charged and excited species, as well as photons in the UV range, can be used to modify material surfaces. These reactive species break the chemical bonds on the surface of materials following which other atoms and molecules can be incorporated onto the surface.

Photons of various wavelengths are emitted from plasmas, for example the visible glow of the plasma plume, however it is the invisible high energy photons which can break surface bonds. So called Vacuum UV photons (VUV), of wavelengths of <200nm, are often attributed to surface modification [156]. Although these photons are referred to as vacuum UV they can propagate through nitrogen atmospheres, however there are quickly absorbed by oxygen molecules. This is one reason why UV photons are unlikely to have played a large part in the surface modification using the atmospheric pressure plasma jet outlined in this work. Most of the high energy UV photons would have been absorbed by oxygen molecules in the air before reaching the surface [227, 228]. In some “shadowing” experiments samples were treated at distances of up to 20/25mm from the nozzle, (Figure 3.7) twice the distance of the longest visible plasma plume: therefore high energy UV photons would have been absorbed by oxygen molecules before reaching this distance, which suggests that changes measured on sample surfaces must be due to other processes. Reuter et al. demonstrated that photons are created in the discharge region of the plasma jet (between and near the electrodes which surround the quartz tubing) and propagate along the flow of helium and excited oxygen [227]. As photons are electromagnetic radiation they can be assumed to travel in a straight line within a single medium, in this case a gaseous mixture of helium and air. As the photons travel in a straight line from their point of creation within the capillary, the beam of photons can only be as wide as the ID of the plasma capillary. Even if a small expansion angle were allowed, all treatment areas were still much larger than the ID of the plasma capillary meaning that UV photons could not be the only mechanism of functionalisation (Figure 3.4). Further evidence that photons were unlikely to have been the main cause of surface functionalisation was the barriers used within the “shadowing” experiments. The “shadowing” experiments (Section 3.3) demonstrated that samples surfaces were treated by the plasma jet even when a barrier was placed in the plasma path. This barrier, when larger than the internal diameter of the jet nozzle, would have blocked all photons from reaching the sample surface. These points therefore suggest that the effect of high energy UV photons functionalising the surface can be discounted. These photons may have contributed, however, to the creation of secondary ions and excited species responsible for surface modification. Various studies have reported little or no optical emission in the 200-300nm UV range [166, 183, 229]. In these studies it is unclear in the methodology whether the spectrometric readings were taken of the discharge region (where Reuter et al. state that UV photons are created [227]), or whether measurements were taken of the plasma plume, for example at angles perpendicular to the plasma flow which would not be observed the discharge region.

Ionic species were also unlikely to have directly caused surface modification. Oh et al. demonstrated ionic species could not survive outside the visible plasma plume [187]. When PS was treated with a 100µm ID microjet (Section 2.2.1.3), which had a plasma plume length of ~1.2mm from the nozzle opening, when the surface was at distance of 10mm from the nozzle ions would not be able to reach the sample. It is therefore assumed that it was radical or metastable species, which could survive in the extended regions of the gas flow, for example metastable He, OH, O_n^* and N_n^*, that may provide enough energy to break surface bonds and enable surface modification [166, 168, 183, 229, 230]. A radical is "a molecular entity containing an unpaired electron"[231] and they are typically highly reactive. Metastable atoms or molecules are those that have not received sufficient energy to be ionised yet have received enough that electrons are promoted to higher energy orbitals, thus having a greater potential energy than their ground state counterparts[160]. These species typically have longer half-lives than ions because although they are excited they are typically neutrally charged. Metastable species will, however, return to their ground state upon collision with lower energy atoms and molecules in the air. As these species are not charged they cannot be observed by mass spectrometry. Optical emission spectroscopy, capable of observing the UV spectrum, could possibly be used to observe the photons emitted from these species as they return to their ground state at distances down-stream from the plasma plume.

If the assumption that the radicals and metastables are responsible for the surface modification, and that they can be carried by the gaseous flow of the plasma, then the various treatment patterns observed for different flow rates and sample-nozzle distances can be explained (Figure 3.30). Other assumptions must first be made: it is assumed that the gas propagates from the jet nozzle in a circular pattern, due to the circular shape of capillary tip, and that the gas has a small expansion angle [232]. Bradley et al. demonstrated using schlieren photography, an imaging technique with which gas density and thus flow can be observed, that the helium gas flows much further from the jet nozzle than the visible plasma plume. This gas initially has a laminar flow but becomes turbulent as it travels further from the jet [232](Figure 4.1). It is assumed that this turbulences results in entrainment of slow-moving, low energy species into the jet of fast-moving, high energy species which were generated by the plasma jet, and subsequent reactions. It is also assumed that an increase in turbulence will result in an increase of this entrainment. These assumptions could perhaps be demonstrated by computer modelling of the fluid dynamics.

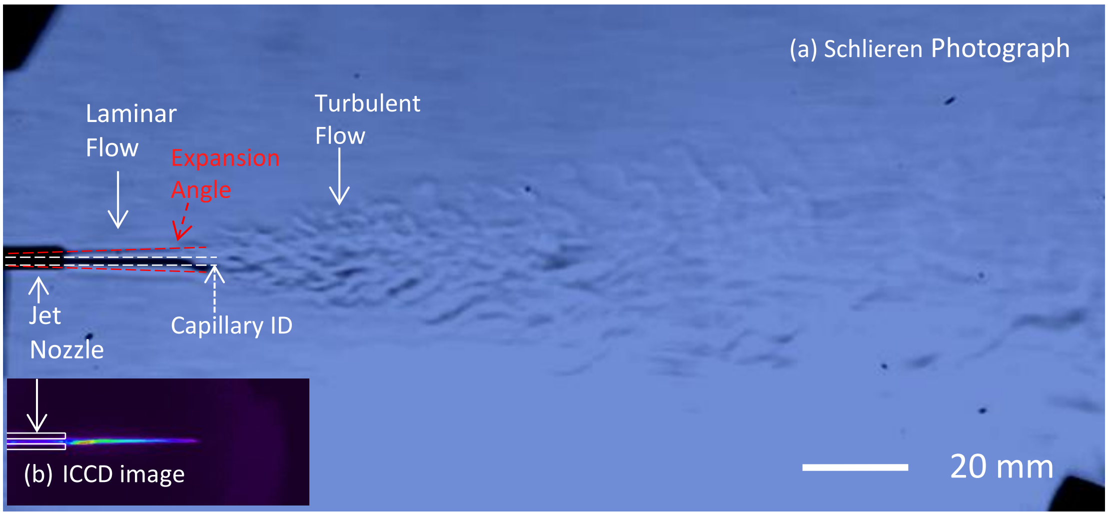

Figure 4.1 (a) Schlieren photograph demonstrating the laminar and subsequent turbulent flow of a helium plasma jet as the exits the plasma jet nozzle. The laminar flow was approximately the size of the nozzle capillary internal diameter (ID) with a slight expansion angle. (b) An intensified charge-coupled device (ICCD) is inset demonstrating the optical emission of the plasma plume. Image altered and reproduced with permission[232].

The gas flows until it meets a flat barrier (a sample) positioned perpendicular to the direction of flow. When the gas, carrying excited species, strikes the sample it spreads across the sample surface (Figure 4.2). It is assumed that the gas expands radially from the point of impact or focus of the jet. This can carry the excited species a few millimetres from the focus of the plasma creating the larger treatment areas. Spatially resolved contact angle measurements were taken across the centre of treated samples, and therefore display a cross section of the treatment pattern. Spatially resolved 2-dimensional contact angle mapping supports the assumption that the gas expands radial and creates a circular treatment pattern (Figure 3.30 and Figure 3.46). The reactive species, e.g. metastables and/or radicals, were likely to revert to their lower energy states by interactions with atoms or molecules in the air surrounding the plasma gas flow. If a high energy species collides with a lower energy atom or molecule it is likely that the high energy species will lose some of its energy, by the transfer of kinetic energy to the other atom, and thus revert to its low energy ground state. As the gas flow from the jet becomes more turbulent, more atmospheric species will be mixed with the excited species causing them to revert to their ground state. This will be referred to as “quenching” of the energetic species. As the plasma gas flow strikes a sample and spreads across the surface it is possible that the flow experiences turbulences as it spreads across the surface (Figure 4.2).

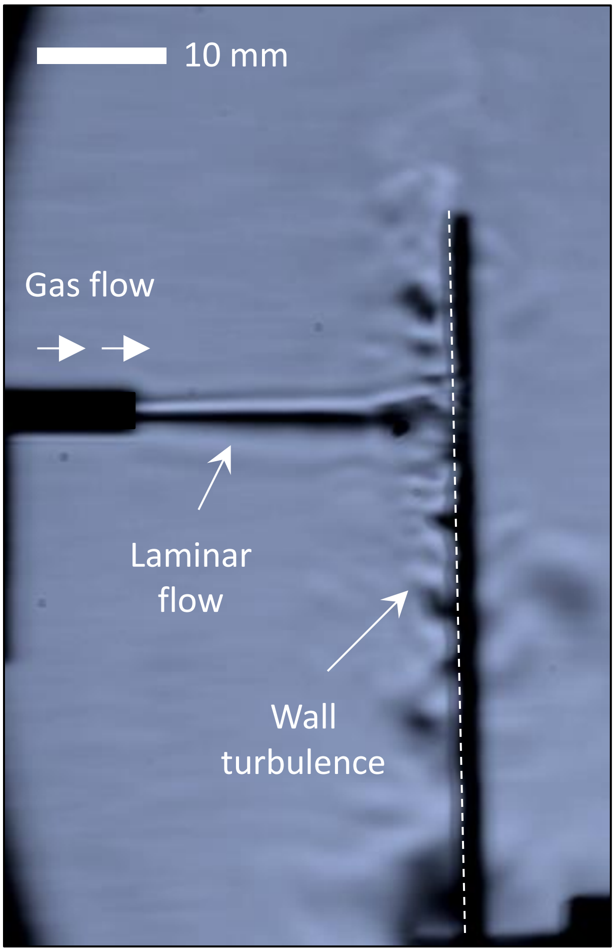

Figure 4.2 Schlieren photograph demonstrating a gaseous jet flow spreading across a flat surface. Wall turbulences are created as the gas spreads across the surface. Image courtesy of Jun-Seok Oh.

It is hypothesised that the momentum of the plasma gas, determined by the flow rate, was a large determinant in the size of the treatment area. If the flow of gas carries the reactive species and turbulence results in a quenching of the reactive species, it is possible that a higher flow rate would carry reactive species further from the nozzle than a lower flow rate. It may be the case that a higher flow rate could result in increased pressure within the 100µm ID plasma jet capillary as the flow of gas would be restricted by the diameter of the nozzle opening. If this were the case the velocity of the gas exiting the nozzle at higher flow rates may be faster than the gas exiting at lower flow rates. When the digital flow meter was used an audible hiss was present at flow rates above 150sccm (“high flow rate”), this indicates that the pressure did in fact increase with higher flow rates; however this was not measured. In future work it may be of interest to measure the flow of helium from the nozzle for each flow rate, prior to experimentation. It is possible that a higher, faster flow rate could maintain a laminar concentrated stream of reactive species for a greater distance than a lower flow rate. It is also assumed that the higher flow rate carried the reactive species further across the sample surface when the gas flow met the perpendicular samples, compared to the lower flow rate. It is possible that the momentum of gas flow would decrease with distance from the nozzle (Figure 4.3).

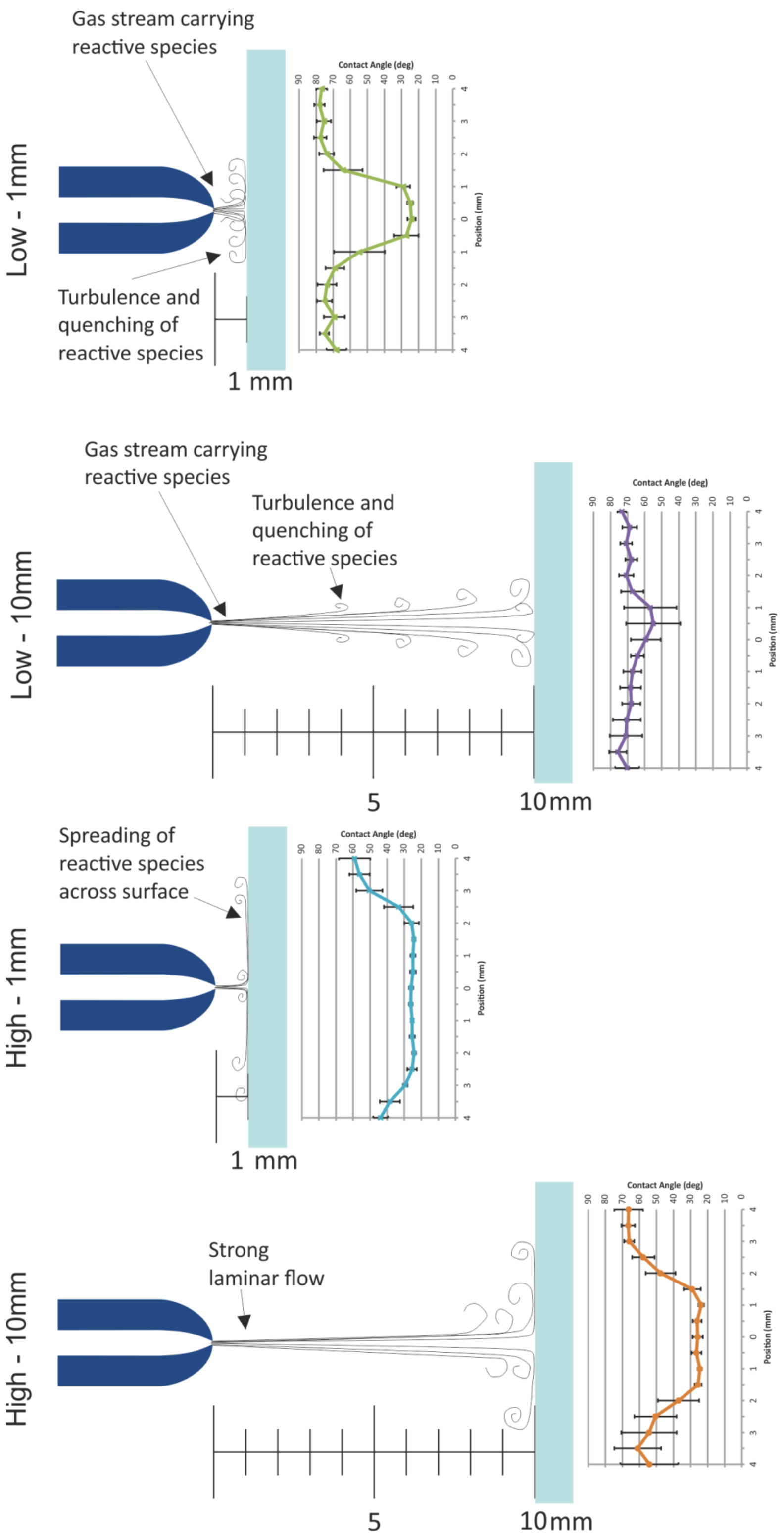

Figure 4.3 Cartoons of gas flow (low and high flow rates) exiting 100µm nozzle and travelling to sample surfaces a 1mm and 10mm from the nozzle. Contact angle profiles for each treatment condition are inset. Nozzle exit, sample size and contact angle profile size are approximately in the same scale.

Contact angle results demonstrated a very distinct treatment region in the centre of samples treated with a plasma microjet (100µm ID nozzle) with a low flow rate - 1mm sample nozzle-distance (L1) parameter (Figure 3.29). The contact angle decreased from ~80° to ~25° in the centre of the samples. A contact angle of ~20-25° seems to suggest a saturation for PS treated with a helium plasma, as the contact angle does not decrease further even with a treatment time of up to 10mins (Figure 3.64). The results suggest that the low flow rate was capable of carrying the reactive species several hundreds of microns radial from the focus of the microplasma jet. It is hypothesised that at distances further than this the gas spreading from the centre was slowed by turbulence and that mixing with atmospheric air increased: this may have caused the reactive species to be quenched by atoms and molecules in the air.

When the sample was positioned 10mm from the nozzle and treated with a low flow rate (L10) the lowest contact angle was 55°. There were also large variations in the contact angles in the centre of samples treated with the L10 parameter. It is possible that the plasma jet with a low flow rate experienced a large amount of turbulence prior to reaching samples positioned 10mm from the nozzle, and many reactive species may have reverted to a ground state due to interaction with the air. The preliminary contact angle analysis of flow rate and distance support this (Figure 3.26). When a sample was positioned at 5mm from the nozzle and treated with low flow rate only one position in the centre of the sample had a contact angle about ~20°. It is possible that the edges of the gaseous stream exiting the nozzle are affected by turbulence first, reducing the treatment at the edges, thus creating the appearance of “smoothing” of the treatment profile of the low flow - 5mm sample (Figure 3.26).

When samples were positioned 1mm from the nozzle and treated with a high flow rate (H1) the treatment region was much wider than observed for the L1 parameter. A *“treated region (or area)”* refers to the section of a contact angle profile in which contact angle was less than ~75-80° (the contact angle of UT-PS). This could be because the high flow rate had a greater momentum to carry the excited species further from the focus of the microplasma jet when the gas stream strikes the sample. When samples were positioned at 10mm from the nozzle (H10) the flow rate was strong enough to carry reactive species to the sample and reduce the contact angle to ~25° (Figure 3.29). The section of maximum treatment (~25°) was smaller on the H10 parameter compared to the H1 parameter. Perhaps the excited species were not spread as far from the focus of the jet by the high flow rate when samples were positioned 10mm from the nozzle compared to 1mm. This may be because momentum of the gaseous stream of excited species decreased due to resistance with air when travelling 10mm from the nozzle. Perhaps this reduction in momentum meant that the reactive species could not be pushed as far across the samples surface, prior to being quenched by turbulence with atmospheric air.

Tan et al. have also demonstrated that an increased flow rate creates a wider treatment area [170]. In their work a plasma jet was passed over a poly(dimethylsiloxane) surface in a line at various speeds and O_2 flow rates. They reported that a reduction in scan speeds resulted in an increase in treated line widths. This was observed by spatially resolved contact angle. In a similarly designed experiment Yonson et al. reported that lower sweep velocities increased treated track widths, however the results were not shown [19]. Yonson et al. hypothesised that at lower sweep velocities gas convection pushed reactive species further from the focus of the jet, and a similar conclusion could be reached from the work of Tan et al. [19, 170]. These results are in agreement with those reported in this thesis and in Doherty et al. (2013)[168].

When x-ray photoelectron spectroscopy (XPS) was performed it clearly demonstrated that there was an increase in surface oxygen content (Figure 3.32, Figure 3.60, Figure 3.62, Figure 3.66), and an increase in the O:C ratio (Table 3.3, Table 3.4, Table 3.5, Table 3.6, and Table 3.7). This increase in oxygen, and the fact that most oxygen observed was single-bonded (C-O), was expected for a plasma operating in air [5, 18]. When spectra were taken across the surface, at a spatial resolution of 1mm, it was demonstrated that oxygen content was lowest at the edges and increased toward the centre position; which suggests that the contact angle was related to the surface oxygen content. As oxygen has a high electronegativity, meaning it has a greater attraction on the electrons within its bonds, it creates a semi-polarity on the surface of the PS. This induced polarity made the surface more hydrophilic via polar interactions, and these polar interactions most likely also caused proteins to adsorb in a confirmation which induced greater cell attachment and growth, compared to non-polar UT-PS. The spatially resolved XPS in this thesis was determined from broad scan spectra only; this is due to the acquisition and analysis times required for obtaining multiple high resolution spectra. Another factor was that on occasion it was observed that oxygen concentration decreased following long beam exposure times/prolonged exposure to high vacuums. It may be noted that nitrogen was typically not observed on surfaces, despite the high percentage of nitrogen present in atmospheric air. This was probably due to the fact that molecule nitrogen, N_2, requires large amounts of energy to modify it into an available form, due to its strong triple bond. In nature nitrogen fixation generally only occurs during lightning storms and by very specialised bacteria and fungi found on the roots of plants. The Haber-Bosch process for converting molecular nitrogen and hydrogen into ammonium was one of the most important inventions of the 20th century, but is performed at high pressures and temperatures. Fitz Haber received the Noble prize in chemistry 1918 for his work on the fixation process [233] and Carl Bosch received it in 1931 for scaling up the process [234]. Work by a Oh et al. shows that only very small concentrations of ionic atomic nitrogen or ions containing single nitrogen species are present in the plasma jet effluent [187] unless the nitrogen is within a heptylamine monomer unit during polymerisation experiments [189].

Atomic force microscopy (AFM) demonstrated treatment with the microplasma jet created very little change in the surface roughness, i.e. <1nm. This also suggests that treatment is not the result of ions striking the surface as these typically create etching on a surface, increasing its roughness [235].

From these results it is assumed that cellular adhesion and subsequent attachment and growth was, indirectly, due to the addition of oxygen onto the surface. It is well documented that creating a more hydrophilic polystyrene surface, by the addition of oxygen, will cause the adsorption of proteins in a conformation expressing specific amino acid sequences to increase cellular attachment [4, 5, 9, 18, 224, 225]. For example, work by Underwood et al. clearly demonstrated that although more fibronectin was observed on untreated PS (which contains no oxygen), the arginine-glycine-aspartic acid (RGD) peptide responsible for cell attachment was only detected via antibody staining on tissue culture polystyrene (TCPS)[225]. The increase in cell attachment due to plasma jet modification was clearly observed in preliminary work using the retinal pigmented epithelial cell line (aRPE-19) (Figure 3.2). The difference in cell attachment is clearly represented when aRPE-19 cells were present on the treated side of a half-treated sample, whereas no cells were present on the untreated half. The aRPE-19 cell line is well-established [213] and was used as a model for ophthalmic epithelial cell attachment, prior to the receipt of lens epithelial cells (LECs). When LECs lines were received they were characterised by antibody staining for αB-crystallin.

Staining for αB-crystallin was positive for both the rabbit N/N1003A lens epithelial cell (LEC) line and the human B3 LEC line (Figure 3.1). Dr. John Reddan kindly donated the N/N1003A and in the paper originally published by Reddan et al. (1986) the cell line was characterised by the presence of both αA and αB-crystallin subunits[214]: this was supported by Sax et al. (1995)[236]. Meakin et al. (1988) did not detect αA- or αB- transcripts in the N/N1003A line [237]. Later work by Krausz et al. (1996), in which the authors examined the expression of crystallins and other markers in lens-derived cell lines, noted that αA-crystallin gene expression was not observed in the N/N1003A line by PCR, but that the αB-crystallin gene was observed [218]. αB-crystallin was the only protein observed in both human and rabbit lens and all lens-derived cell lines which the authors investigated.

The B3 cell line was originally created by Andley et al. (1994) and characterised by the expression of βH- and γ-crystallins [215]. In future work Fleming et al. (1998) reported the absence of γC- and γD-crystallins, the only γ-crystallins of appreciable quantity in humans, but the presence of αA- and αB- transcripts; however a large decrease in the presence of αA- was observed following 10 passages [217]. Wang-su et al. (2003) reported the presence of αB-crystallin as well as the absence of αA (passages 11-14 and 20-25) in the B3 LEC line [216]. Other commonly used LEC lines have been characterised with crystallin proteins, such as the NKR-11 mouse LEC line (γ-crystallin)[238] and αTN-4 mouse LEC line (αA-, αB-)[239]. The work by Krausz et al. (1996) did not show the presence of γ-crystallin in the NKR-11 line but did note the presence of αB- crystallin [218].

It is acknowledged that αB-crystallin is an imperfect lens cells marker due its presence in other tissues; such as heart, lung and kidney [240, 241]; however, the literature is not in agreement on a lens epithelial cell specific marker. αB-crystallin is also present in the retina [32], hence the use of aRPE-19 retinal pigmented epithelial cell line as a positive control. The characterisation of LECs could perhaps have been supported by the detection of other markers such as Pax6, occasionally referred to as a master eye gene or master control gene for eye development, which is present in the lens but also other tissues within the eye [216, 218, 242, 243].

Both the N/N1003A and B3 LECs were tested for cytokeratin as a marker for epithelial cell lines; however no expression was observed. It is suggested that LECs express cytokeratins 7, 8, 18 and possibly 19 but only during development [244-247]. Cytokeratin is expressed in the human lens epithelium until 8-9 weeks post conception[244, 245], or about 16 days post conception in rabbits [245] and may disappear during the invagination of the lens placode. Cytokeratin was not detected by proteome analysis of B3 LEC line or in the lenses of donors aged 60-70 years old [216]. Cytokeratins 8 and 18 have been shown to be expressed in human retinal pigmented epithelial cells [248] therefore the aRPE-19 cell line was used as a positive control. The expression of cytokeratin is often supressed in cells undergoing epithelial-mesenchymal transition (EMT), whereas vimentin (an intermediate filament found in cells of mesenchymal origin) expression is increased [82, 84]. The presence of vimentin (and lack of cytokeratin) has been reported by several authors in lens epithelium and/or cultured lens cells [216, 246, 249, 250].

Cells undergo a series of steps during attachment to synthetic substrates, Grinnell (1976) outlined these as: “adsorption of serum components onto the substratum, contact between the cells and substratum, initial attachment, and progressive attachments leading to cell spreading and an increased strength of cell attachment” [251]. The first of these is the adsorption of proteins onto material surfaces which occurs almost immediately (Figure 1.1) [4]. Secondly cells settle onto the surface from the cell suspension. Thirdly cells initially bind to the adsorbed proteins, if protein conformation is such that the necessary amino acid sequences are available to the cells. This initial attachment will be referred to as adherence throughout this discussion and cells at this stage typically have a rounded morphology. Following this, cells may “spread” across a surface, becoming flatter and extending across a larger area of the surface. These cells will also form a more apical-basal polarity compared to the loosely bound, more rounded adhered cells. Once cells spread they will bind to the surface (or the adsorbed protein layer) more strongly via interactions such as focal adhesion points [4]. Cells at this stage will be referred to as attached cells. Each of these processes are dependent upon the surface properties of the material such as surface roughness, stiffness and chemistry. Some of these stages are also interdependent. Other terms which may be used in the following paragraphs are cell migration and motility, meaning the movement of cells across surfaces.

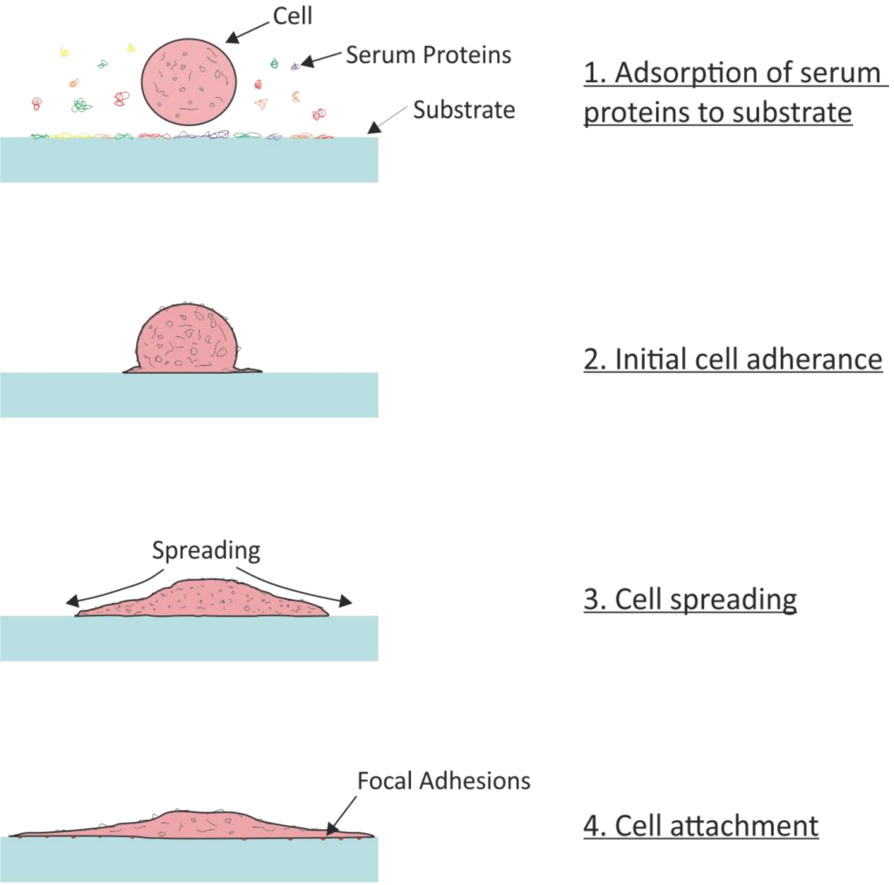

Figure 4.4 Cartoon of cell adhesion, spreading and subsequent attachment. Cell adherence is preceded by the adsorption of proteins onto the substrate.

Following characterisation LECs were seeded onto materials treated with microplasma jets operated with low and high flow rates and positioned either 1mm or 10mm from the nozzle. As these materials had treatment regions of various sizes the presence of LECs was analysed spatially by cell counting at discrete positions (the centre and 1.5mm, 3mm and 4mm from the centre) and by stitching low magnification images to give an overview of the diameter of the area of cell growth. It was observed by phase contrast microscopy that cells attached to the centre of treated PS surfaces in a much higher density than TCPS in less than 2 hours (results not shown).

It was clearly observed when cells are counted at day 1 (Figure 3.34, Figure 3.49 and Figure 3.70) that there were >3 times the number of LECs in the centre of treated samples compared to TCPS wells. There were typically many more LECs at the 1.5mm position of treated materials compared to TCPS also, depending on treatment conditions. This was also supported by the slightly higher number of cells on treated PS compared to TCPS at 1 and 4 hours post-seeding, observed in the sample storage experiments (Figure 3.21 and Figure 3.23); however this work was only conducted once. The number of LECs decreased from the centre region toward the edge at all time points, irrespective of plasma treatment condition (Figure 3.34 and Figure 3.35). The altering of flow rate and sample-nozzle distance did, however, change the extent of the decrease in cell number from the centre to the edge, and the minimum number of LECs observed furthest from the centre, at the 4mm position. For example: the number of cells on samples treated with the low flow rate – 1mm distance (L1) parameter decreased to almost 0 cells per field of view after the 1.5mm position, and the low flow rate – 10mm (L10) parameter resulted in samples with similar yet with slightly more cells at the 3mm and 4mm positions, whereas samples treated with the high flow rate parameters (H1 and H10) had many more cells on the 3mm and 4mm positions compared to samples treated with low flow rates.

An untreated position is defined by significantly fewer LECs compared to TCPS, and no significant difference in the number of cells compared to untreated polystyrene (UT-PS). The positions meeting these criteria for samples treated with the L1 parameter would be 3mm and 4mm from the centre at both day 1 and day 7 (Figure 3.34 and Figure 3.35); therefore there is only treatment with a radius of <3mm from the centre, implying a cell growth area and treatment diameter of <6mm. Results were similar for samples treated with the L10 parameter however the 3mm position did not have significantly fewer cells than TCPS on day 1. This is most likely due to the low number of cells on TCPS by day 1 and the relatively large standard deviations at the 3mm position on the L10 parameter. The samples treated with the high flow rate parameters (at 1mm and 10mm positions, H1 and

H10 respectively) did not have significantly fewer cells than TCPS in any position, at either time point. This implies under the conditions outlined above that the entire sample surface was treated, or at least the diameter of the cell growth/treatment area was >8mm (4mm from the centre being the furthest position at which cells were counted).

These constrictions of cell growth area, as defined by cell counts, were in agreement with montage data for day 7 (Figure 3.36 and Figure 3.51). From the image montages the diameter of cell growth area was defined as the distance between the boundaries of a confluent or densely populated LEC growth situated in the centre of treated samples. The montage results demonstrate that there were untreated regions on the surface of high flow rate treated samples, as diameters of cell growth for the H1 and H10 treated samples were only 8.8mm and 8.1mm respectively (sample size was 10x10mm). The agreement in results was not present on the data collected on day 1. At the 3mm position on samples treated with the L10 parameter the number of LECs was not significantly lower than TCPS: under the conditions defined this meant the treatment area was >6mm, however it was only 4mm ± 0.5mm as defined by stitched micrographs. This may indeed be due to the low number of LECs on TCPS and the high variability observed on day 1, as stated in the previous paragraph. Similarly, on day 1 the cell counts suggest the diameter of treatment on high flow rate treated samples to be >8mm, yet the samples treated with the H1 and H10 parameters had diameters of cell growth of <7mm determined from stitched images. The cell growth montages were defined by the areas of confluent cells growth, and as the cell growth did not have perfectly smooth or flat boundaries there was inherent subjectivity in this measurement. This was more apparent at day 1 as there was less homogeneity between samples at this time point compared to day 7, reflected in the size of the standard deviations in reference to the total diameter on days 1 and 7 (Figure 3.36). It is also of note that some scattered cell growth was observed outside the “cell growth area”, however UT-PS was not completely free of cell growth and patches were observed. The morphology of the cells outside the cell growth areas was typically similar to LECs on UT-PS. This morphology was typically rounded, but occasionally LECs on UT-PS and at the edges of treated samples had spindle morphologies. The rounded morphology suggests that cells did not receive the correct cues from the adsorbed protein layer on these materials to spread and fully attach, and hence remained in the adherence stage (Figure 4.4). Perhaps an algorithm for automated determination of the diameter of cell growth could have been created to provide more objectivity. It is accepted that neither cell counts nor cell montages were a perfect measure of the diameter of the cell growth area on treated samples, and on occasion conflicted with each other; however these methods did provide quantitative and qualitative results. It is perhaps difficult to conclude the size of the treatment area at the day 1 time point as the number of LECs on TCPS is very low, making it difficult to distinguish from low cells numbers and an “untreated” region.

It could be argued that the patches of cells observed outside the cell growth area, particularly on the high flow rate treated samples, (Figure 3.37) were due to some random modification within the tail-end of the turbulence, created after the laminar flow of the jet interacted with the perpendicular sample surface [232]. Spatially resolved XPS analysis, however, demonstrated that the concentration of oxygen near the edges of the samples was ~4% or less (Figure 3.33), which was similar to the concentration of oxygen observed on UT-PS (Table 3.2), however no oxygen was observed by XPS on UT-PS in the PMMA experiment (Table 3.4). The concentration of oxygen on UT-PS, from contamination, typically observed in the literature is ~0.5% [5]. This suggests possible contamination or the presence of adsorbed oxygen and demonstrates the requirement of repeat XPS experiments.

From contact angle analysis the samples treated with high flow rate parameters had significantly lower contact angles than UT-PS at all positions excluding the left-4mm position (Figure 3.29), however the contact angle at the left-4mm position on UT-PS was significantly lower than all other positions on UT-PS (p=0.041-0.012, paired samples t-test). As the contact angle was significantly lower on samples treated with high flow rate parameters than UT-PS (Figure 3.29), yet the oxygen content was approximately the same (Figure 3.33 and Table 3.2) it cannot be ruled out that some random treatment on the outer regions of samples may cause scattered cell growth. Repetition of XPS analysis, particularly with a reduced beam size, could help to answer this question.

In this experiment, and others, it can be noted that the contact angle at the left-4mm, and sometimes left-3.5mm positions, were noticeably lower than the corresponding right position. It is believed this was due to either contamination or damage which occurred when samples were cut by hand. The phenomenon was not observed on PMMA as these were machine cut by Advent Plastics Ltd. In future work it would preferable to obtain machine cut PS.

When the contact angle results are compared to the cell growth area it is evident that a large decrease in contact angle was not required to elicit cellular attachment. This is most evident from samples treated with the L10 parameter (Figure 3.29 and Figure 3.37) which had a minimum contact angle of 55° ± 15.9°. This treatment had a large degree of variability in the centre, most likely due to break-up of the laminar flow and quenching of the energetic species, capable of breaking surface bonds, in the turbulence. Similar cell adherence and attachment (Figure 3.34) was observed in the centre of samples treated with the L10 parameter compared to samples treated with the other parameters which had minimum contact angles of ~25°. The samples treated with L10 parameter also had contact angles considerably higher than TCPS which had an average of 35° ± 2.3°. The L10 parameter had contact angles significantly lower ($p<0.01$) than the UT-PS on the entire right side of the samples/profiles however this was not reflected by either cell counts (statistical comparison of cells counted on left or right has not be conducted but no discernible pattern was observed in the data) or cell growth areas. On the high flow rate samples the contact angles at almost all positions were significantly reduced compared to UT-PS; however cells did not attach and grow on the entire surface at day 1. For these high flow rate parameters the diameter of cell growth area expanded significantly from day 1 to day 7, covering more than the 8mm diameter observed by contact angle, yet not the entire sample. This suggests that the protein interactions within the central treated area provided the necessary binding sites for cellular adherence in the central region very quickly. Following adherence cells may have laid endogenous extracellular matrix (ECM) molecules or remodelled the existing protein adsorbed layer at the boundary region of initial cell adherence, which enabled cell spreading, attachment and growth further from the centre [224, 225].

When the cytoskeletal structure of the LECs was investigated by phalloidin staining and high magnification microscopy, differences in morphology between LECs on TCPS and microplasma treated surfaces were observed (Figure 3.38). On day 7 LECs on TCPS displayed actin localisation (phalloidin staining) around the cell boundaries and LECs displayed a cobblestone-like morphology. This is indicative of epithelial cells. On microplasma treated surfaces some cobblestone-like structures were present however there was a large number of actin stress fibres and cells appeared to grow on top of one another in certain places: depth profiling by confocal microscopy could have clarified this latter point. The cause of the morphological differences is unknown. Some possible causes and the methods to test for them will be discussed in the following paragraphs.

The presence of these stress fibres may be due to phenotypic changes within the LECs. Perhaps the fibres suggest that LECs may have been beginning to differentiate towards a lens-fibre lineage, however the cells do not display a fibrotic morphology. LEC differentiation toward a lens fibre lineage display directional stress fibres, this was demonstrated by Chen et al. (2006) at the edge of lens explants, and could be induced in LECs deeper within the explant by the addition of basic FGF [254]. The stress fibres in this study did not appear to have a uniform direction (Figure 3.38). Differentiation toward lens fibres could be investigated by the presence of Aquaporin 0, or the expression of its gene MIP26 [217]. The increased expression of β- and γ- crystallins could also be used [216, 249]. The actin stress fibres could be involved in cell contraction, characteristic of myofibroblast-like cells, resulting from EMT, which causes contraction of the lens capsule and thus PCO [75]. Staining for α-smooth muscle actin (αSMA) or α5β1 integrin could have supported this theory and could be conducted in future work [75, 82, 84, 85, 119].

Another possibility is that LECs may react differently as they have adhered at a higher density in the central areas on microplasma jet treated samples compared to TCPS (Figure 3.34). Although cells were seeded onto TCPS wells and treated samples at the same density ($1x10^4$cells/cm^2), the area in which cells attached on treated samples was much smaller, as mentioned previously. Perhaps this was due to the size of the initial functional growth area. For example, if the functional growth area for samples treated with the L1 parameter was determined by calculating the area of a circle ($a=\pi r^2$) from diameters of cell growth on days 1 and 7 (Figure 3.36) it would be 0.85-0.91 cm^2, whereas there area of an entire sample was $1cm^2$. The effect of functional growth area could perhaps be investigated by treating a material with a large ID jet; treating the entire sample surface and thus providing a $1cm^2$

functional growth area. This was in effect done during the post-discharge polymerisation experiments (Section 2.2.1.7.1), in which the helium gas control samples had a contact angle across the entire surface of 20-30° (Figure 3.64). XPS analysis demonstrated that surface oxygen concentrations were similar (20.5-23.2%), however these preliminary XPS results need repeating. Human B3 LECs were seeded onto the polymerisation helium control substrates and demonstrated a cobblestone morphology by day 7, although some stress fibres were present (Figure 3.75). As this was a different cell line (B3) it cannot be directly related to the results observed for the N/N1003A rabbit LEC line used during the investigation of flow rate and distance. When the B3 line was seeded onto PS samples treated with the L1 parameter, as a control to the PMMA experiments (Table 2.4), the density of LECs by day 7 was so great that nuclei could not be counted from the micrographs (Figure 3.55). There was also the presence of actin stress fibres and cells appeared to be multi-layered (Figure 3.55). On day 4 B3 cells were confluent yet cells did not appear epithelial (Figure 3.53). These cells appeared to have a smaller area and a "less-epithelial" morphology (particularly on day 7) compared to cells seeded onto treated PMMA(T-PMMA)((Figure 3.55)) or onto PS with a large treatment area (Figure 3.75). The latter two surfaces presented less spatial confinement (defined by contact angle results) to B3 cells compared to those seeded onto PS samples treated with the L1 parameter. If the functional growth area of PS treated with the L1 parameter (from the PMMA experiment) were determined from diameter of cell growth at day 7 (Figure 3.51) it would be 4.52mm^2, whereas the functional growth determined for helium treated PS in the post-discharge polymerisation experiment was 54.1mm^2 (determined from diameter of cell growth at day 7)(actual sample area was 100mm^2 in both cases). There is a clear difference between the morphology of B3 LECs on these substrates at day 7, however as these were treated with different parameters it cannot be concluded that differences observed are due to functional growth area (Figure 4.5). Comparisons between these treatments seem to suggest that over population or cell crowding may contribute to the morphological differences between cells attached to TCPS and microplasma treated substrates; however more work is required to determine this.

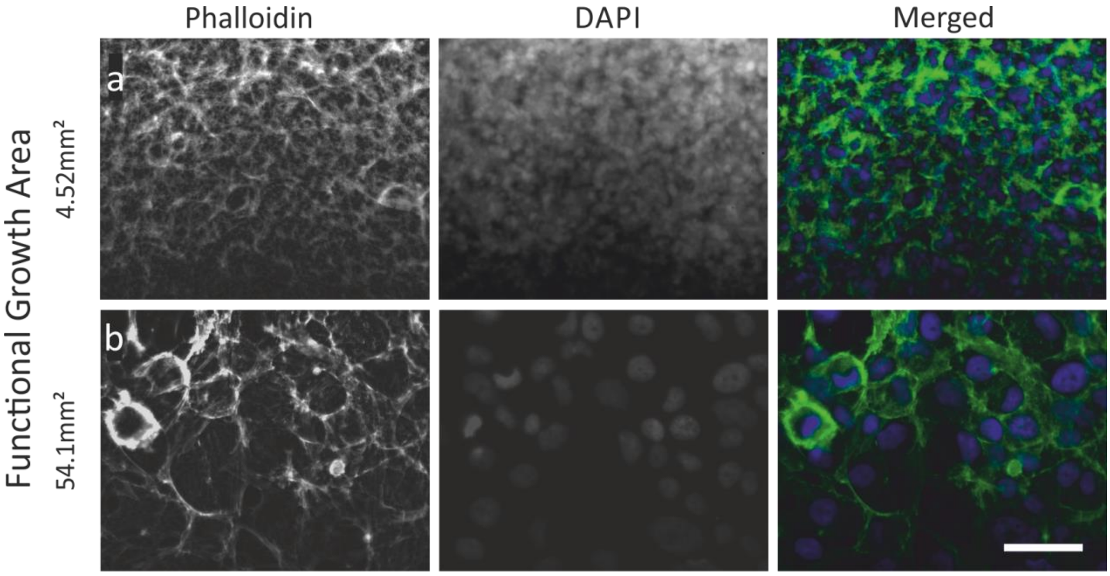

Figure 4.5 High magnification micrographs human B3 lens epithelial cells (LECs) seeded onto polystyrene treated with helium jets. LECs were fixed at day 7 and stained for f-actin (phalloidin, green) and nuclei (DAPI, blue). Samples were treated with a 30sccm - 1mm sample nozzle distance, 100µm internal diameter (ID) jet for 20s (a), or a 500sccm - 5mm sample nozzle distance, 2.3 ID jet for 10mins (b). The functional growth areas were determined by calculating the area of a circle ($a=\pi r^2$) and using half the diameter of cell growth for *r*. Scale bar = 500nm.

The higher density of LECs in the centre could also be due to the seeding method: 90µL of cell suspension was retained on the surface of the sample by surface tension created at the sample edges (Section 2.4.1.4). Using this method a dome-like drop of cell suspension was created on the sample surface (Figure 4.6), the dome height was highest in the centre therefore there was a larger volume of cell suspension in the centre. This may have resulted in a higher population of cells settling and adhering in the centre of samples. This second possibility may have accounted for the larger number of LECs observed in the centre of untreated samples on the early time points of the ageing experiments (Figure 3.20 and Figure 3.22), as cell number should be homogenous across UT-PS.

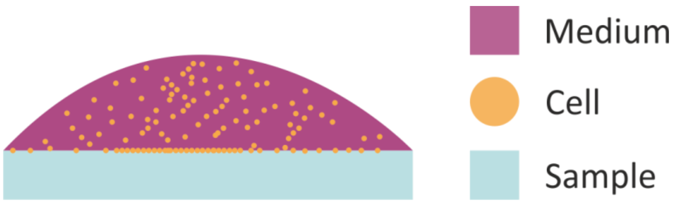

Figure 4.6 Cartoon representing the seeding method used within this PhD. A suspension of cells in culture medium was placed onto sample surfaces such that the liquid was retained on the surface by surface tensions created at the edge of the samples. Using this method the cell suspension covers the entire surface of the sample for cells to settle prior to culture wells being filled with medium. This reduces the number of LECs growing beneath samples. In this method the volume of cell suspension was greatest in the centre of samples which may have caused a higher density of cell attachment in this region.

There is a higher density of cells in the equatorial region of the natural lens, where differentiation into lens fibres occurs, compared to the central lens epithelium. It was proposed that this cell crowding in the lens equator encourages the differentiation of LECs into fibres [33, 249]. It is possible that a similar mechanism occurred on microplasma treated PS. Another possibility is that although LECs on treated materials appeared spread, perhaps there was insufficient room for them to fully spread prior to contacting neighbouring cells, which may hinder the ability of some cells to achieve proper contact inhibition and thus correct monolayer formation [168]. The presence of the stress fibres may suggest cell motility and thus lack of contact inhibition [255].

The seeding density of 1x10^{4}cells/cm^{2} had been optimised for TCPS [44], yet due to the results observed lower seeding densities on microplasma jet treated surfaces were investigated, and the morphology of LECs at day 7 were observed. The hypothesis was that the greater amount of space afforded the LECs would allow them to spread fully before coming into contact with neighbouring cells. This did not result in a more epithelial phenotype in LECs seeded onto treated samples. By day 7 both the 5x10^{3}cells/cm^{2} and 1x10^{4}cells/cm^{2} conditions had confluent monolayers yet the presence of actin stress fibres was still observed (Figure 3.44). The LECs seeded at 1x103cells/cm2 were not confluent at day 7; however observation until they reached confluence may have presented interesting results. Cells seeded on TCPS were only confluent by day 7 when seeded at 1x10^{4}cells/cm^{2} and appeared cuboidal however the presence of some stress fibres were detected. Some small gaps were also visible in the monolayer on TCPS wells and with slightly longer growth these may have closed, reducing the presence of stress fibres due to full contact inhibition or lack of motility. It is of note that observation, by phase contrast microscopy, at 2 hours post-seeding demonstrated that cells on treated materials ($5x10^3$cells/cm^2 or $1x10^4$cells/cm^2 only) were often in contact, whereas cells were well spaced and had a wider area on TCPS. Observations at day 1 were similar (results not shown). This experiment was only conducted once, however, and could benefit from repetition. In future work a single treatment parameter (possibly L10) could be used, to reduce sample requirements, and cells could be examined at various time points, e.g. day 1 and day 4. Time lapse microscopy could also be beneficial [5, 18].

The preliminary results stated above seem to suggest that morphological differences between LECs on TCPS and treated samples were not due to inadequate space provided to LECs (although much further investigation is required to draw a conclusion). It was discussed in Doherty et al. (2013) that the differences in morphology may be related to changes in the surface chemistry and thus contact angle [168]. The contact angle of TCPS was 35° ± 2.3° whereas the contact angle in the centre of samples treated with the L1, H1 and H10 parameters was ~25° (Figure 3.29). This lower contact angle may have created a less stable protein adlayer, due to an increase in weaker hydrophilic-hydrophilic interactions, compared to TCPS. Highly wettable surfaces are often used to prevent protein adsorption, in this case it may result in a protein layer with a greater degree of reversibility. The higher contact angle on samples treated with the L10 parameter is in conflict with this rationale, as LECs on this were morphologically similar to those on L1, H1 and H10; quantification with markers for EMT/fibre differentiation may have shown LECs on PS treated with the L10 parameter to be more similar to those on TCPS than the other treatment parameters. It is assumed that the reduction in contact angle on TCPS is due to an increase in oxygen, however this is unknown. It is possible that nitrogen is present on the surface and the chemical difference between TCPS and treated materials may account for the difference in morphology. All culture vessels used in this work are Griener Bio-One CellStar® which are treated with a proprietary "physical" method to make the surfaces "hydrophilic". Contact angle was performed on discs cut from 12-well plates; this process may produce some damage on the surface and may result in contamination, which could pose problems for highly sensitive XPS analysis. Seven TCPS samples from two different plates were used for contact angle analysis (average contact angle differed between plates by 2.2°), if more time and samples were available contact angle measurements could be repeated and XPS analysis could be attempted. If future work were permitted a more detailed analysis of XPS, including the difference in oxygen concentration between samples treated with L10 and the other parameters, could be investigated. It is possible that the effect of overcrowding and the nature of the modification contribute to the difference in morphology observed on treated samples compared to TCPS and the above paragraphs have outlined possible routes in which these questions could be investigated further.

Whatever the cause of the observed morphological differences it was possible that they coincide with the release of cytokines, involved in inflammation or EMT such as: TGF-β2, interleukin-1α (IL-1α), IL-6, basic fibroblastic growth factor (FGF) or Tumour Necrosis Factor-α (TNFα). Due to the nature of the localised cell growth on microplasma jet treated surfaces it is difficult determine the number of cells on each parameter to compare the preliminary cytokine results, particularly to TCPS. TGF-β2 is perhaps the most important and well-studied cytokine relating to PCO [37, 70, 75, 76, 85]. If cell number is not considered, the TGF-β2 data (Figure 3.40) demonstrates that there was less expression in wells containing LECs grown on microplasma jet treated samples, or UT-PS than in TCPS wells on both time points. At day 1 there was little or no detection of TGF-β2 in medium from wells containing LECs grown on plasma treated samples following subtraction of the values for basal medium, suggesting that there was no endogenous secretion from cells on these samples at this time point (Figure 3.40). On day 7 the values observed for wells containing LECs grown on treated samples ranged from 184-544pg/ml and the change in concentrations approximately matched the change in diameters of cell growth (Figure 3.43). These concentrations were still much lower than that observed in medium taken from TCPS wells (1372pg/ml). If the concentration is determined for every 10,000 cells present in the wells/on materials (number of cells on treated samples determined from the mean across all positions) the concentration of TGF-β2 excreted by cells on treated materials (≤21pg/10^4cells) would be half the concentration excrete from cells on TCPS (45pg/10^4cells). Using this method of calculation, however, results in very high concentrations of TGF-β2 for UT-PS yet this is inaccurate as it was unlikely that 10,000 cells were present on UT-PS. The values observed are also much lower than the values present in the aqueous humour either pre- or post-cataract surgery (1-4ng/ml)[79, 256, 257](Section 1.4). These preliminary results suggest that autocrine production of TGF-β2 was not responsible for the observed change in morphology. These results also suggest that microplasma jet treated samples inhibit the secretion of TGF-β2 in comparison to TCPS, however much more work is required to prove these results and there are some limitations which could be addressed in future work. For example, the ELISA did not differentiate between latent and active TGF-β2, so it is possible that the TGF-β2 in TCPS wells was latent whereas the TGF-β2 in wells containing treated materials, although in lesser concentration, may have been in the active form. TGF-β2 is present in its latent form within the aqueous humour and the lens capsule, yet does not cause differentiation until activated [29]. During cell culture the growth of LECs on the TCPS plates underneath treated and UT-PS samples was occasionally observed. There were few LECs beneath treated samples if any, however patches of LECs were observed beneath UT-PS, these were most likely washed from the surface when medium was added to the well following the 2 hour attachment period (Section 2.4.1.4). In future agar could be used to prevent this [5, 18].

The presence of IL-1α and IL-6 were below the detection limits of the assay in medium from wells containing all materials. Nishi et al. reported in 2 studies that no IL-1α secretion was detected in human anterior capsule explants, taken during cataract surgery, after 1 week of culture. The authors did report ~100-200pg of IL-1α was detected for every 10^6 LECs in some cases, but not all, following 2, 3 and 4 weeks of growth[90, 91]. Other work by Nishi showed that concentrations of 1 and 10pg/ml of IL-1α did not have a significant effect on LEC mitosis [88].

The concentrations of basic FGF detected in medium containing LECs grown on all materials on day 1 were very low (≤1.2pg/ml). The minimum levels of basic FGF in the aqueous and used experimentally are >100pg/ml [89, 258] however basic FGF is typically used in the ng range[86, 88]. By day 7 the concentration of basic FGF detected in culture medium had increased to a maximum of 11.4ng/ml (L1 parameter, Figure 3.41). It is unlikely that these concentrations of basic FGF would affect LEC growth, differentiation or morphology, however further experimentation of a dose dependant response would be required.

The concentrations of TNFα in medium surrounding LECs was <2pg/ml for all materials at both time points, and were extrapolated beyond the standard range of the assay (Figure 3.41). These concentrations are in agreement with the concentration observed in the aqueous humour extracted during cataract surgery [98] yet Nishi et al. report that no TNFα was secreted by LECs cultured from explants [91]. Although the presence of TNFα has been reported in lens cells as well as Sommering's rings and Elsching's pearls following cataract surgery it was not quantified in these reports [93, 100]. As the concentrations of TNFα were similar to those observed in aqueous humour during, rather than after, cataract surgery, it is unlikely that these low concentrations contributed to the morphological changes observed in N/N1003A cells grown on microplasma treated surfaces. As stated previously these results are preliminary and require repetition to confirm the validity, also the nature of the heterogeneous cell growth on treated materials creates difficulties when comparing observed concentrations to TCPS controls.

4.2 PMMA

PMMA was the main material used for intraocular lenses until the development of foldable acrylic hydrogels and it is still often used in developing countries [75, 128, 140, 142, 259]. It provides an affordable and stable (due to its stiff structure compared to acrylic hydrogels) model acrylic based material, and is often used in biomaterials/IOL research [5, 18, 146, 203, 260, 261]. PMMA was treated with the L1 parameter outlined previously (Section 0) as this created the most defined treatment area as demonstrated by contact angle (Figure 3.45 and Figure 3.46) and cell growth studies (Section 3.4.3.4)[168]. PS was used as a control to ensure that the treatment conditions were the same. When the contact angle profiles for the L1 parameters were compared from the optimisation experiment and the PMMA experiment some significant differences were observed in the "untreated" regions between 3mm-4mm from the centre. The reason for this is unclear but may be the result of damage introduced when cutting by hand. As the material was scored to create a trough then snapped to separate pieces of PS, some strain forces may have created heterogeneities on the surface of polystyrene near the edges. On each of the positions which displayed statistical differences, the mean contact angles from the optimisation experiment were lower. Interestingly the mean contact angle of UT-PS (77° ± 6°)(Section 3.4.3.1) from the optimisation was lower than the UT-PS from the PMMA experiments (81.1° ± 3.6°)(Section 3.5.1), although the former mean was reduced by the low contact angle observed on the left-4mm position of the profile (Figure 3.29).

Within the "treated" regions of the PS from each experiment only the right-1.5mm positions were significantly different (p=0.002). This position was near the boundary of the treatment and thus had large standard deviations in each experiment, however the mean difference was 26.6° and the treatment from the PMMA experiment was lower. This suggests the diameter of treatment area during the PMMA experiment was slightly larger. Possible causes of this observed difference could be miniscule differences in the alignment or positioning of the samples/sample holder respective to the nozzle, changes in temperature or moisture content in the atmosphere depending on the time of year experiments and repeats were conducted. Further repetition under a more controlled environment may remove this observed difference. Contact angle analysis with a smaller spatial resolution could maybe give an indication if the observed difference was due to error in sample placement or the atmospheric conditions of the microplasma jet. It is also possible that this difference observed at the boundary was inherent to the microplasma jet system itself; no statistical analysis was performed between repeats within an experiment, although the mean contact angle profiles between repeats appeared qualitatively similar from graphical comparison.

The contact angle in the centre of the PMMA decreased following treatment. The XPS data suggest that the surface oxygen content of T-PMMA and UT-PMMA were similar (52.7 ± 0.5 and 51.7 ± 0.3%, respectively)(Table 3.3). The oxygen concentration observed on UT-PMMA and T-PMMA differed by only 1%. D’Sa et al. reported an increase in oxygen content in the range of 5.7-8.4%, following treatment with a dielectric barrier discharge (DBD) plasma reactor operating in air[5]. The reduction in contact angle on PMMA observed in this work must be due to an increase in oxygen functionalisation as there was no change in root mean square roughness (Rq), and only a difference of 0.1nm in average roughness (Ra) determined from AFM analysis, also no other elements were observed on broad scan spectra. UT-PMMA and T-PMMA also looked topographically similar (Figure 3.48). One possible reason for the small observed change in oxygen concentration may have been the size of the x-ray beam used to excite electrons from the surface. This beam spot was 7mm x 1.5mm and information gathered from electrons emitted from this region was averaged to obtain the XPS spectra. This gathered information from areas outside the treated region (Figure 4.7). From the contact angle results it can be assumed that the diameter of the treated area was 2.5mm on T-PMMA, where treatment is assumed to cause a significant decrease in contact angle compared to UT-PMMA (Section 3.5.1). If a circle of diameter=2.5mm and rectangle of dimension 7mm x 1.5mm were centred, the overlapping area (as determined by ImageJ) would be 3.5mm^2. This area of intersection is approximately 0.333% of the total beam area (10.5mm^2). The observed oxygen concentration is an average of the treated and untreated regions. Even in the treated region the oxygen content would not consistent as the contact angle varied from 60-35° (Figure 3.46); therefore XPS could not measure a difference in the oxygen content. This may be the cause of the similarities in oxygen content observed between UT-PMMA and T-PMMA.

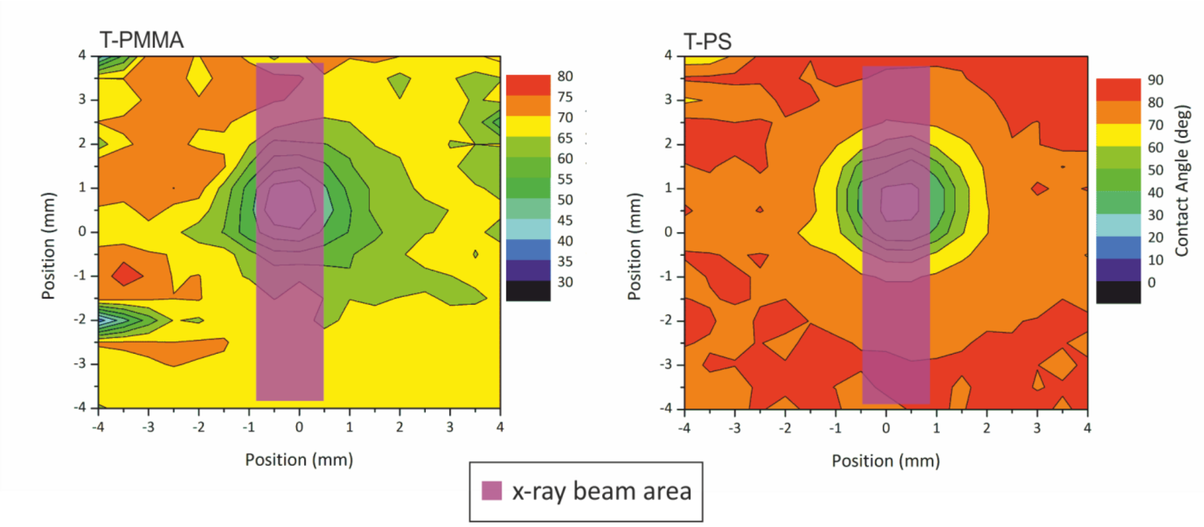

Figure 4.7 Two-dimensional contact angle maps of treated poly(methyl methacrylate) (T-PMMA) and treated polystyrene (T-PS) with an overlaid representation of the x-ray beam size from x-ray photoelectron spectroscopy (XPS). The colour scale of the T-PMMA contact angle map ranges between 30-80° to provide greater detail. The average contact angle of untreated PMMA was 58.9°.The colour scale of the T-PS contact angle map ranges from 0-90°. The average contact angle of untreated PS was 81.1°. Data from the entire x-ray beam area are used to create XPS spectra, the figure demonstrates that only a small portion of the x-ray beam area overlaps the treated regions. This results in lower observed oxygen concentrations than those which might physically be present in the centre of the treated area.

For the reason outlined above the oxygen content observed on T-PS in this instance (Table 3.4) was ~9% smaller compared to the previous XPS results (Table 3.2) obtained from samples treated with a high flow rate. These XPS results require repetition, preferably with a smaller x-ray beam size and, if equipment with a smaller beam size were obtainable, spatially resolved analysis[262]. Despite the restrictions of analysing small treatment areas with the equipment used within this thesis it was demonstrable that functionalisation on PS was due to an increase in oxygen and that nitrogen was absent (Figure 3.47). It is likely that a similar process occurs on PMMA. In future work PMMA samples could be treated with either a large ID jet, or with a high flow rate parameter, to provide a larger treatment area for XPS analysis.

When surfaces were analysed by AFM there was little or no change in roughness following treatment (Figure 3.48). Following plasma treatment the roughness of PMMA typically increases [5, 263-266] however these was not observed. The reported roughness values of pristine PMMA vary but the values are typically less than 10nm. These values will depend upon the source of the material, sensitivity and methodology of the AFM analysis. The roughness values of both UT-PS and T-PS were also the same. The roughness of UT-PS and T-PS (which was treated with the L1 parameter) were lower than those in the previous experiment (Figure 3.31), however the difference was only 0.2nm which was within the standard deviations. In the previous experiment the Rq and Ra of UT-PS and PS treated with the L1 parameter were the same or similar also: this supports the case the L1 parameter does not appear to cause damage to the polymer surfaces.

When B3 human LECs were seeded onto the materials, on day 1, there was a large number of cells in the centre of treated materials which decreased with distance from the centre, whereas TCPS and untreated materials had few cells and similar number of LECs across all positions (Figure 3.49). The increased number of LECs at day 1 on plasma treated PMMA and PS compared to untreated is most likely due to an increase in surface oxygen [5, 18]. On day 4 there were more LECs in the centre and 1.5mm position of UT-PMMA than the 3mm and 4mm positions. There were significantly more in the 1.5mm position. It is possible that the higher number of cells was due to biased cell settling due to the seeding method as discussed previously (Figure 4.6). On day 7 the decrease in the number of cells with distance from the centre on UT-PMMA was also observed and was more pronounced (results not shown). On both day 1 and 4 T-PMMA had more LECs in the centre and 1.5mm positions than UT-PMMA, and a similar number of LECs at the 3mm and 4mm positions, which indicates spatially confined treatment on T-PMMA. The diameter of cell growth on T-PMMA increased with time. This is possibly because UT-PMMA can support LEC growth, however plasma jet treatment encourages an increase in cell adhesion and subsequent attachment in the centre region, as demonstrated by the cell counts on day 1 (Figure 3.49).

By day 7 the concentration of LECs in the centre of T-PS was so dense that nuclei could not be distinguished and counted (Figure 3.55). As stated previously this may be due to the functional growth area - the area of the PS surface which was functionalised to allow LEC attachment and growth (Figure 4.5). This area was smaller on T-PS compared to T-PMMA as LECs will attach on pristine PMMA [5, 18, 64], which may be a reason this was not observed on T-PMMA. The diameters of cell growth, as determined by stitched image montages, on T-PS at all time points ranged from 2.4-3mm and was largest at day 4. The cell counts indicate that the diameter of cell growth should be larger than 3mm, as the 1.5mm positions were not considered untreated by the definitions outlined previously. This discrepancy was possibly due to slight variation in sample size and/or positioning, or small error in alignment of the graticule (Figure 2.21). As the boundary of cell growth on T-PS was very defined, and these boundaries would have been close to the 1.5mm position (due to cell growth diameters of 2.4-3mm) small errors may have resulted in either very high numbers of cells, or very low numbers of cells. This is reflected in the cell counts and the large standard deviations observed at the 1.5mm position of T-PS (Figure 3.49).

It appeared from the high magnification micrographs that the LEC density on T-PMMA was greater than UT-PMMA suggesting that plasma jet had increased growth, although this may be due to the increase in initial cell adhesion and subsequent attachment on T-PMMA. LECs on TCPS secreted higher or similar concentrations of TGF-β2, IL-6 and basic FGF compared to those on UT-PMMA and T-PMMA (Figure 3.57 and Figure 3.58). LECs on both UT-PMMA and T-PMMA had actin stress fibres; however they were present in cells on TCPS also. Cells on TCPS had a larger area than cells on any other material. From phase contrast microscopy (not shown) cells on TCPS appeared closely packed and did not appear to be multi-layered. Cells on UT-PMMA, T-PMMA and T-PS were more closely packed and some cells did appear to be growing on top of others.

Following 7 days of growth there was a significant difference in the cell growth area, as determined by the stitched image montages, of B3 LECs grown on T-PS (2.4mm, Figure 3.51) compared to N/N1003A LECs grown on T-PS (3.2mm, Figure 3.51): in both cases the PS was treated with the L1 parameter. The contact angle results suggest that the treatment area may have been slightly larger on the samples upon which B3 LECs were seeded. It is possible then, that the observed difference in the cell growth diameter was due to the difference in the LEC lines. During the fixation process there was occasionally an error where the edge of the cell monolayer would begin to lift. This most frequently occurred on very defined boundaries of cell growth, i.e. samples treated with the L1 parameter. Perhaps this occurred more frequently on B3 seeded samples due to the very high density of B3 cells at day 7. This dense, well-defined monolayer (Figure 3.52) may have lifted more easily than N/N1003A cells biasing the results. To avoid this in future, different methods of fixation could be investigated. For example: the submersion of samples into wash buffers and fixative, rather than the filling of wells containing samples with reagents. The different species of cell lines may have differed slightly in terms of their mechanisms for binding to surfaces, or rather the adsorbed protein layer. This could be investigated by antibody staining for protein adhesion and conformation on treated surfaces. Integrin expression of the LEC lines could also be investigated. The N/N1003A cell line has been shown to express α5 integrin (of α2, α3, α5 and β2 investigated), suggesting adhesion to fibronectin [267]. The B3 line has been shown to express α2, α3, α5 and β1 (all investigated), suggesting adhesion to laminin, fibronectin, and some collagens; however the level of expression is not mentioned [268]. Human primary LECs have been shown to express α3 and β1 (of α2, α3, α5, α6 and β1 investigated) [16, 111]. However, α5 and β1 integrins (including investigation as α5β1 dimer) have been linked to EMT induced by TGF-β2 [36, 83]. A more detailed study would be required to elucidate whether the growth areas observed were due to the protein adsorption and conformation in specific areas. Further investigation of the integrins involved in the adhesion and attachment of both cells lines would also be required. The difference in cell growth area observed for each of the cell lines may have been due to error in the treatment of the materials at different times. These errors could include temperature of the laboratory and moisture content in the air, as mentioned previously.

The B3 LECs secreted IL-6 (tens of pg/ml) whereas no IL-6 was detected in medium surrounding N/N1003A LECs. Although IL-6 is implicated in increased proliferation there were a greater number of N/N1003A LECs on TCPS at day 7 than B3 LECs (Figure 3.35 and Figure 3.72) [92], and a similar number of adhered cells were observed on day 1. Conversely, there were more N/N1003A cells in the centre of T-PS on day 1 than B3 cells (Figure 3.35 and Figure 3.49), yet there were many more B3 cells by day 7. The secretion of TGFβ-2 was higher from N/N1003A LECs grown on TCPS compared to B3 cells (Figure 3.40 and Figure 3.57), however the N/N1003A LECs appeared more epithelial, with more distinct cobblestone morphologies compared to B3 cells. This indicates that perhaps the levels of

TGF-β2 were not a major contributing factor to the observed morphologies on treated materials. The concentrations of basic FGF secreted from N/N1003A cells were also slightly higher on day 7 than the B3 LECs(Figure 3.41 and Figure 3.58). Basic FGF has been reported to mediate the apoptotic effect of TGF-β2 [86].

In summary, plasma jet treatment increased the adhesion and attachment of B3 LECs in the centre of PMMA. This is possibly due to an increase in oxygen yet little change in the O1s area was observed from the XPS spectra, which may be due to the large beam size compared to the small treatment area. The cell growth area and density of B3 cells in the centre of T-PS was much higher than for N/N1003A LECs. Much further work is required to elucidate the cause of this. Such work could include: measurement of proliferation and metabolic activity, spatially resolved investigation of the adsorption and conformation of proteins on the treated surfaces, analysis of the cell-surface binding mechanisms of each cell line such as expression of integrins, also adhesion and attachment to specific ECM proteins.

4.3 Plasma Polymerisation

The aim of the plasma polymerisation was to incorporate atoms or molecules, other than or in addition to oxygen, onto sample surfaces using an atmospheric pressure jet to polymerise monomers onto surfaces. Amine (-NH_2) containing monomers, allylamine (Allyl), $CH_2=CHCH_2NH_2$ and heptylamine (Heptyl), $CH_3(CH_2)_6NH_2$, (Figure 4.8) were used as model monomers and were deposited onto PS. XPS detection of nitrogen was used to confirm the presence of amine on sample surfaces. Capillaries with large IDs (≥1mm) were used to determine the efficacy of an atmospheric pressure plasma jet for polymerisation. Future work could examine the spatial confinement of treatment.

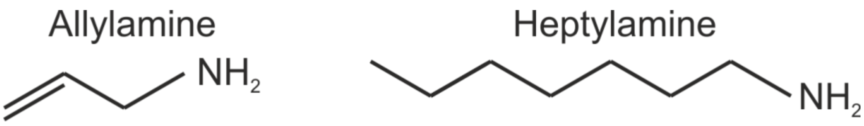

Figure 4.8 Skeletal formulae of allylamine and heptylamine.

In preliminary tests helium gas was passed through flasks containing monomers, at relatively low flow rates, after which the helium containing suspended monomers joined with a main helium flow. The main helium flow rate was typically an order of magnitude higher than the monomer containing flow rate. The combined gas flows then travelled into the quartz capillary and the plasma discharge region, this is referred to as pre-discharge mixing. In the following paragraphs the flow rate of the monomer will be denoted as *X*sccm Heptyl, where *X* is the flow rate, however this does not mean a *X*sccm flow of pure heptylamine but rather a *X*sccm flow of helium containing suspended heptylamine monomers. Oh et al. (2013) calculated the flow of monomers to be ≈10sccm at the highest flow rate [189].

In the initial preliminary polymerisation experiment Allyl or Heptyl were polymerised onto UT-PS or helium pre-treated PS. The pre-treated PS was treated for 3mins at a high flow rate so that the entire surface was treated and had a contact angle of ~20° (Figure 3.59). It was hypothesised that pre-treatment, which would lead to an oxygenated surface, may increase adhesion due to increased polar interactions. The treatment of UT-PS with Allyl and Heptyl containing plasmas created defined treated regions in the centre of samples. The width of the treatment (the trough in the contact angle profile) was wider on samples treated with the Allyl containing plasma compared to the Heptyl containing plasma. This may be due to the fact that the Allyl monomer has a lower molecular weight (57.09Da) than the Heptyl monomer (115.22Da). The helium gas stream may have carried the Allyl molecules further from the focus of the jet, than the Heptyl molecules due to their lower molecular weight.

Treatment of UT-PS with Allyl also resulted in a much higher increase in the area of N1s and O1s peaks observed by XPS, compared to Heptyl treatment (Table 3.5 and Figure 3.60). The concentration of oxygen and nitrogen on Heptyl treated UT-PS was very low yet the decrease in contact angle (in the centre of samples) due to treatment was similar to Allyl. It is unlikely that the dissociation or polymerisation of Heptyl would require greater energy. The absence of a large oxygen peak, which should occur due to the interactions with helium and air as stated previously (Section 4.1), seem anomalous. When Heptyl was deposited on helium pre-treated PS there was also little change in the N1s and O1s. The lower oxygen and nitrogen concentrations also cannot be attributed to the x-ray beam size as the contact angle results indicate similar treatment areas. As the XPS data is from single samples it is possible that there was error and these would require repetition. When Allyl was deposited onto pre-treated PS there was a slight increase in the N1s and O1s peaks. As single samples were used it is difficult to determine if the small changes in nitrogen observed were due to polymerisation and repetition with larger sample numbers would be required for statistical analysis. It is also unclear if pre-treatment did increase adhesion of polymerised amines, large sample sizes and statistical analysis could elucidate this. For the true study of the adhesive interactions of the surfaces and mono/polymers techniques such as AFM, perhaps with modified tips could possibly be used. As this work was preliminary high resolution spectra were not analysed. The spectra would also be difficult to analyse because the differences in binding energy, between carbon-oxygen and carbon-nitrogen can be difficult to determine within high resolution of C1s peaks, as the components have similar binding energies (e.g. 0.2-0.3eV difference for C-O and C-N [155, 269]).

Large amounts of oxygen were present when allylamine was deposited onto UT-PS in the preliminary pre-discharge mixing experiments (Figure 2.14). With the aim of reducing the oxygen functionalisation, polymerisation (using pre-discharge mixing) was conducted in a helium atmosphere (Figure 2.15). In this experiment Allyl and Heptyl jets were also operated without ignition of the plasma. This was to investigate if unpolymerised monomer units were adhering to the surface. When the jet was operated without plasma ignition it caused no change in the contact angle compared to UT-PS, therefore it appeared that unpolymerised monomers were not adhering to the surface (Figure 3.61). As no change in contact angle was observed these samples were not investigated using XPS. Following ignition of the jet a large decrease in contact angle was observed in the centre of the treated samples. The decrease in contact angle was most likely due to an increase in oxygen and nitrogen concentration observed from XPS analysis (Figure 3.62 and Table 3.6). The increase in oxygen and nitrogen was greater when samples were treated with the Heptyl plasma, compared to the Allyl plasma, which is the inverse of the observation in the experiment conducted in air (Table 3.5). Large oxygen functionalisation (25.8%) was observed on Heptyl treated surfaces despite being treated within a helium atmosphere. The lower oxygen and nitrogen concentrations on Allyl, compared to Heptyl, may have contributed to the higher contact angle. Although the chamber was not tested for helium purity or leaks it is possible that the oxygen observed on surfaces was due to a post-treatment oxidation when the sample was returned to air. This is possibly due to radicals, trapped within the plasma polymer film interacting with air [270].

When B3 LECs were seeded onto materials treated with Allyl and Heptyl, with and without plasma ignition, they only adhered and grew on samples treated with Heptyl and plasma ignition. The lack of LECs on samples treated without plasma ignition supports the assumption that monomer units were not adhering to the surfaces. The reduction of contact angle on Allyl treated surfaces indicated that cells would likely adhere however no cell growth was observed on these surfaces. It is possible that the reason for this was a cytotoxic effect of unpolymerised or aggregated Allyl on the samples surfaces, which may have dissolved in the culture medium. During contact angle analysis droplets of liquid were observed in the centre of samples treated with Allyl with plasma ignition (Figure 4.9). Cytotoxicity could be measured using assays outlined in ISO10993 part 5, including the extraction method; this could be quantified by a measure of metabolic activity, for example by resazurin or MTT assays. Due to this observed cellular response allylamine was not studied further. The use of the chamber was also not used in further work as large concentrations of oxygen were observed on Heptyl treated surfaces.

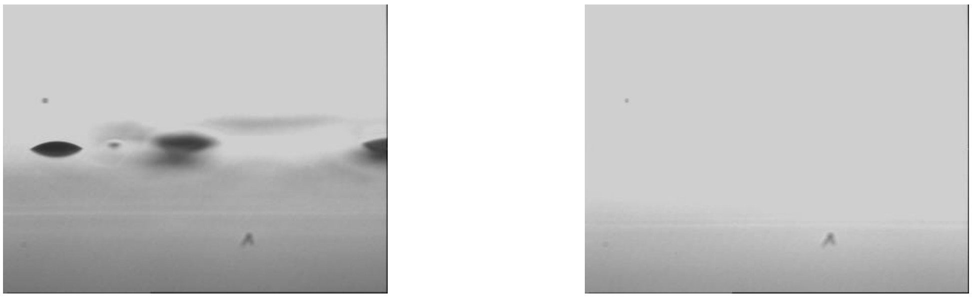
Allylamine w/ ignition

Allylamine w/o ignition

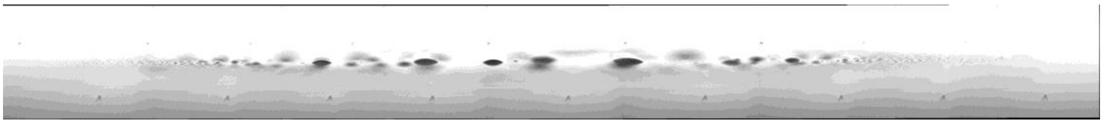
Allylamine w/ plasma montage


Heptylamine w/ ignition

Heptylamine w/o ignition

Figure 4.9 Single frame images taken from DSA100m contact angle system showing surfaces treated with allylamine and heptylamine with (w/) and without (w/o) plasma ignition. Images were taken prior to deposition of water droplets for contact angle measurement. Liquid allylamine droplets can be observed on surfaces treated allylamine with ignition of the plasma.

Following elimination of Allyl and the chamber apparatus the plasma jet was modified. The monomer gas stream was introduced post-discharge. That is, the helium gas was passed through the electrode region and was dissociated by the energy supplied, following this the helium flow containing monomers was added to the dissociated main stream (Figure 2.16). Several authors report an increase in jet stability when introducing larger species (typically oxygen) downstream from the discharge region [206, 209, 212, 229]. It was also observed that plasma discharge was more difficult to maintain when monomers were introduced pre-discharge and difficulty increased with flow rate, but this was not studied. Even when the monomer mixture was introduced post-discharge it was difficult to maintain discharge when the Heptyl mixture flow rate approached 100sccm (main helium flow was fixed at 500sccm).

Various Heptyl mixture flow rates were studied by preliminary spatially resolved XPS. The lowest flow rate (20sccm) appeared to be the most efficient, with the highest concentrations of nitrogen and oxygen at all positions. If the jet becomes less stable at higher flow rates perhaps the transfer of energy and degree of polymerisation is decreased at higher flow rates. This may be a possible reason why the lowest flow rate was the most efficient at adding nitrogen functionalisation. Contradictorily, Oh et al. (2013) reported maximal ionic oligomer concentrations in the jet effluent, where the oligomers were polymerised monomer units, at medium flow rates (40-60sccm) [189]. In the work by Oh et al. only the positive ionic oligomers were studied but perhaps negatively charged ionic oligomers, or even neutral species, play a role in surface polymerisation. Oh et al. (2011) previously reported that many negatively charged species are present in the effluent of a helium plasma jet [187]. Preliminary mass spectroscopy conducted by Oh and time-of-flight secondary ion mass spectroscopy, conducted in collaboration with the University of Nottingham (both unpublished), demonstrated that negative species were present in Heptyl containing plasma jets. Repetition of the XPS data and mass spectroscopy of the negative ionic species in the plasma effluent may elucidate the cause of the higher nitrogen and oxygen concentrations on the low flow rate surfaces. Analysis of the mass spectra at different distances from the nozzle may also provide interesting results. In the work published by Oh et al. (2013) the mass spectrometer sampling orifice was positioned 2mm from the plasma nozzle [189], whereas samples analysed by XPS in this thesis were positioned 5mm from the nozzle. The mass spectrometry orifice also acted as an electrode, thus there was a difference in the operation of the jet. The work by Oh et al. does not report the concentration of oligomer units of different sizes for each flow rate. Perhaps the lower flow rate, and thus lower concentration of monomer units, results in a greater number of smaller oligomer units compared to higher flow rates. Smaller and lighter units may travel further from the jet nozzle, or may travel further before collisions reduce their energy making them less likely to bind to surfaces. Much further work is required to understand the processes of atmospheric pressure polymerisation using a plasma jet.

Further work was conducted using the 20sccm Heptyl flow rate. A 2.7mm ID nozzle was used in this work as it was easier to create the y-shaped configuration jet with larger capillaries (Figure 2.16). When surfaces were treated for 10mins with either a helium jet or a jet containing Heptyl the entire surface was treated. The contact angle across the surface of samples treated with helium was 20-30°, however the contact angle at the edges of samples treated with Heptyl was 40-50° (Figure 3.64). The difference in surface treatment between helium and Heptyl plasmas was clearly demonstrated by the 2D contact angle maps (Figure 3.65). A cross shaped region in which the contact angle was higher (by 10-20°) than surrounding positions was observed on the map of the sample treated with Heptyl. The cause of this is unknown, yet as the maps were of single samples repetition would be required to determine if the observed effect was erroneous or reproducible. The higher contact angles at the edges of Heptyl treated surfaces, compared to helium treated surfaces, may be because the polymerised Heptyl species decreased the overall velocity of the gas flow and may not have spread as far across the surface. Measurements of the gas velocity as it exits the nozzle at various monomer flow rates could be investigated in future work. Perhaps fluid dynamics computer modelling could also assist. The contact angle in the centre of Heptyl treated surfaces was also significantly lower than helium treated surfaces (by ~5°). A possible cause for this observed difference is that plasma polymerised surfaces are known to have a degree of mobility about their bonds [270]. Perhaps the Heptyl surface was thickest in the centre and had a greater degree of mobility, which altered to minimise the surface energy when in contact with water. XPS depth profiling and determination of surface energy, by examining the contact angle of Heptyl surfaces with liquids other than water, could be conducted in future work to investigate this difference. The contact angle results suggest that a Heptyl jet may create a smaller treated area compared to a helium jet if the 100µm nozzle were used.

LECs preferentially adhered to the centre of both helium and Heptyl treated surfaces, despite the entire surface being treated (Figure 3.70 and Figure 3.73): this again suggests that the seeding method possibly encouraged cell adhesion in the centre of samples. The boundaries of cell growth area were much more defined on Heptyl treated surfaces (Figure 3.74), and the cell counts indicated that no position could not be considered untreated on helium treated surfaces. The Heptyl treated samples surprisingly displayed confinement of cell growth despite considerable concentrations of oxygen, nitrogen and reduced contact angles near the edges (Figure 3.67, Figure 3.68 and Figure 3.64).

There was no significant difference in the cell adhesion or growth of LECs in the centre of samples treated with helium or Heptyl plasmas until day 7, at which point there were significantly fewer LECs on Heptyl treated surfaces. Perhaps the presence of nitrogen inhibits LECs from over-proliferation. As there was a larger “functional growth area” on helium treated surfaces this was not due to greater room to spread. It is possible that the presence of nitrogen results in protein adsorption which inhibits this, or once LECs have attached they may deposit ECM which provides cues to halt proliferation. To study if in fact the rate of proliferation is different on these materials a BrdU assay could be performed. The time lapse microscopy and analysis of ECM protein and/or cell-surface binding outlined previously could also yield interesting results for these materials.

LECs grown on surfaces treated with helium within the polymerisation experiment appeared to have a greater degree of actin localisation at the cell periphery and less actin stress fibres compared LECs to TCPS (Figure 3.75), although this was not quantified. Perhaps the chemistry induced on the surface resulted in more favourable protein adsorption compared to TCPS. The large treatment area may also have contributed as stated previously (Figure 4.5). The B3 LECs on TCPS at day 7 appeared similar to the B3 LECs on TCPS at day 7 in the PMMA experiment (Figure 3.55). Both displayed the strong presence of actin stress fibres. Concentration of TGF-β2 secreted by B3 LECs at day 7 in the polymerisation experiment (Figure 3.77) was 4-fold smaller than the concentration secreted by B3 LECs during the PMMA experiments (Figure 3.57). As the TGF-β2 ELISAs were preliminary and conducted at different times this indicates the need for repetition, yet this may suggest that the actin stress fibres were not a result of the presence of TGF-β2. The concentrations of TGF-β2 secreted from cells grown on helium treated surfaces was similar to the concentration observed secreted from cells grown on TCPS, which supports the conclusion that TGF-β2 at these concentrations were not the cause of, nor were the concentrations a result of the observed differences in morphology. The concentration of TGF-β2 in medium surrounding LECs grown on Heptyl treated surfaces was >2-fold larger than other parameters. TGF-β2 has been stated to have an apoptotic effect and perhaps this higher concentration was related to the lower cell number observed in the centre of Heptyl treated surface compared to Helium treated surfaces, as mentioned previously. Much further work would be required to investigate this such as: repetition of the ELISA, TUNEL assay to investigate apoptosis, aforementioned BrdU assay, dose response to TGF-β2 and longer growth periods to check if LECs become quiescent.

The secretion of IL-6 by B3 LECs on TCPS was also different between the PMMA and polymerisation studies at both day 1 and day 7. The concentration was highest in the PMMA experiment on day 1, whereas on day 7 the observed concentration was highest for the polymerisation experiment. The polymerisation experiment was not analysed on day 4. These differences in results demonstrate the need for repetition.

In summary, this work demonstrates that the atmospheric pressure plasma jet can be used for polymerisation. Due to the nature of the jet the surface was also functionalised with oxygen. Further work is required to determine if lower monomer flow rates are more efficient, and to determine if LECs interact with nitrogen containing surfaces differently to surface with only oxygen incorporation.

4.4 Pin Plasma

A preliminary investigation was conducted to examine the possible use of a pin plasma, or plasma needle, system to spatially modify the surface of polymers. The pin plasma system was originally designed for plasma-assisted desorption/ionisation (PADI) applications. The pin plasma system in this application was to be used as an ionisation source to desorb molecules from a material for analysis by mass spectroscopy; therefore its original purpose was surface analysis rather than surface modification. When in operation a coronal discharge is formed at the tip of a tungsten wire. The desorption and ionisation of the surface occurs due to the bombardment of ions, photons, electrons, molecules or atoms from the plasma source. It was hypothesised that the species created in this discharge could be used to alter the surface chemistry of polymers. Bowfield et al. demonstrated that the pin plasma could desorb and ionise PTFE molecules and units, a process which most likely occurs via chain scission [192]. It is possible that ionised species in air around the coronal discharge, and other energetic species likely to be present, could be incorporated into these surfaces during this process. One of the benefits of this system is that it is operated in ambient conditions with no additional gas flow; therefore the spreading of reactive species by the artificial flow of a gaseous plasma medium, as outlined previously in this discussion, would not occur [192].

The main concern presented by treatment with a pin plasma system was damage to the surface, as it was initially designed for desorption. AFM analysis of the centre of the samples indicated that the roughness following treatment only increased by 0.5nm at the most (Figure 3.82). Although no statistical analysis was conducted as this work was preliminary, the roughness values between UT-PS and pin plasma treated PS were very similar. The surface topographies also appeared similar, although the treated samples may have had a greater density of features. It is possible, however, that damage only occurred in a very small area directly under the pin plasma, which could be missed by the AFM scan areas (500nm^2) as the sample was positioned beneath the tip by hand, although 4 areas in the approximate centre of each sample were analysed. This would in effect be a 2µm^2 area. In future single line scans could be taken across the centre of samples on a single axis at the maximum distance on the piezoelectric positioning unit (125µm for the equipment used in this thesis), similar to contact angle profiles. These data could help to demonstrate if surface roughness altered in a spatially defined manner. The nozzle of the polymerisation experiments had an ID of 2.7mm and therefore had a large jet area, which probably enabled enough room within which to position the AFM tip accurately by hand. The results from this experiment (Figure 3.69) were similar to those observed with the microplasma jet (Figure 3.31 and Figure 3.48) and with the pin plasma (Figure 3.82), therefore it is likely that previously reported AFM results were indicative of the treatment in the centre of samples.

Various operating parameters of the pin plasma were optimised. These were: treatment time, voltage and frequency. The voltage and frequency were limited by the equipment and the minimum values required to initiate a plasma, therefore only these maximum and minimum values were investigated. From the initial contact angle tests it was demonstrated that all of these factors altered the width of the treatment in the contact angle profile (Section 3.7.1). Time had the smallest effect, whereas frequency had the greatest effect. As the values of these parameters were increased the width of the treatment profile increased also. As the frequency and voltage applied to the tungsten wire were increased, this may have increased the kinetic energy of the plasma species created around it. These high kinetic energies may have allowed excited species to travel further from the source thus increasing the treatment area. Perhaps the greater energy supplied to the species near the wire enabled the plasma cascade process to propagate across more atoms and molecules, and thus a larger area surrounding the tungsten wire. The minimum frequency (15kHz) and the minimum voltage (13kV) created the smallest treatment area and therefore the system is limited by these factors. The length of the contact angle profile which had a contact angle of ~20° was 2mm (Figure 3.81) which is similar to treatment with the microplasma jet operated with the L1 parameter (Figure 3.29). Optical emission spectroscopy of the pin plasma under various operating parameters could be conducted in future and may prove if a larger discharge is created with higher operating frequency and voltage. Spatially resolved ambient mass spectroscopy may also demonstrate if ionic species or ionisation processes occur further from the source at higher voltages or frequency. Various other parameters which could be altered were not investigated, and these could be studied in future work with the aim of reducing treatment size further. These include wire diameter, sample-wire distance and the angle between the sample and wire; in this work the length of wire was normal to the sample surface.

Similar to the work conducted with plasma jets the minimum contact angle observed on pin plasma treated samples was ~20°. This supports the previous hypothesis that saturation was reached. This may also suggest that the mechanisms of treatment are similar between the plasma jets and the pin plasma operating in atmospheric air. If this reasoning is correct then pin plasma treatment is most likely due to incorporation of oxygen species. Although molecular nitrogen is difficult to incorporate onto surfaces from atmospheric processes, without the addition on ammonia or amine monomers, coronal discharges tend to have higher power densities than glow discharges (such as those in the plasma jets); therefore there may be small concentrations of nitrogen. Ambient mass spectroscopy of the pin plasma and XPS analysis of the treated surfaces could demonstrate the species created and incorporated onto surfaces.

When B3 LECs were seeded onto pin plasma treated PS, and counted at discrete positions, the results were similar to microplasma jet treated surfaces. There were a large number of cells in the centre which decreased with distance. On samples treated with the 15kHz parameters there were little or no LECs at the 3mm and 4mm positions. This was expected as this was observed on PS treated with the L1 parameter, and the contact angle profiles of samples treated with the 15kHz pin plasma parameters and the L1 parameter were similar. The contact angle profiles of the high flow rate microplasma jet treated samples and the 20kHz pin plasma treated samples were also similar (Figure 3.29 and Figure 3.81). Despite this very few LECs were observed at the 4mm position of the 20kHz pin plasma treated parameters, however as day 4 counts are not available for the high flow rate treated PS samples, and as different cell lines were used, it is difficult to compare these treatments. The number of LECs at the 3mm and 4mm position on pin plasma treated surfaces may also increase with longer growth times. It was observed that there was less variability in the regions where the contact angles were ~30-60°, i.e. the regions at the boundary of the central treatment, on samples treated with the pin plasma compared to the microplasma jet. This may indicate that treatment area caused by the pin plasma is more reproducible, which may be a result of the unpredictability of turbulence involved in plasma jet treatment. The number of LECs at the 3mm and 4mm positions of pin plasma treated PS reduced with both frequency and voltage, as did the cell growth diameters observed from stitched montage images. These results are similar to those observed by contact angle. In future work LECs could be grown on substrates for at least 7 days to investigate whether the cell growth area expanded with time, as observed on previous substrates (Figure 3.37 and Figure 3.52).

One interesting observation from the cell counts is that the number of LEC in the centre of PS treated with the 15kHZ-17kV pin plasma, was much less than the number of LECs at the 1.5mm position. Although statistical analysis was not conducted the difference in cell number between positions was considerable. Gaps in cell growth were observed by microscopy in the centre of these samples. This can be observed in the stitched images (Figure 3.86). Perhaps the cause of this was due to damage of the sample, however AFM and contact angle results for samples treated with this parameter were similar to the other treatments. XPS and ToF-SIMS could elucidate whether differences in the surface chemistry caused this and could be performed in future work.

No examination of cell morphology was conducted in this work however it was observed that the LECs within the treated areas had not formed monolayers by day 4 (Figure 3.86), whereas confluence was observed on PS treated with the L1 parameter at day 4 (Figure 3.52). Gaps in cell growth, such as those present on the 15kHz-17kV treated samples, as well as clumping of LECs was observed with the treated regions. These patterns of cell growth were typically not observed in LECs on PS treated with the plasma jets. Much further work, including repetition, is required to determine conclusions from these observations. Further work could include 2D contact angle maps, XPS (spatially defined), ToF-SIMS, longer cell growth periods, high magnification microscopy, time-lapse microscopy and antibody staining for ECM/cell markers as outlined previously in this discussion.

In summary, this preliminary work has demonstrated that a pin plasma system is capable of modifying PS surfaces in a spatially defined manner, which can be tailored by various operational parameters. This treatment also appears to be non-destructive to the polymer surface. LEC adhesion and growth area also seems to be tailored by the operationally parameters, however repetition and much further work is required to develop this instrumentation for polymer surface modification for biomaterial applications.

5 Conclusions

In this body of work the surfaces of various materials were treated with an atmospheric pressure plasma jet. The surface modifications were analysed and the attachment and growth of lens epithelial cells (LECs) on modified surfaces were investigated. The main aim of the project was "…to determine if an atmospheric pressure microplasma jet could be used to create a spatially defined treatment on polymeric surfaces to control cell-surface interactions…". This work clearly demonstrated that this was achieved, specifically that plasma treatment, including polymerisation, increased cell attachment and growth in a spatially defined manner.

The following conclusions were drawn from this work:

1. Atmospheric Pressure Microplasma Jet Treatment
    - The atmospheric pressure microplasma jet system was optimised and could be used to modify the surface of polystyrene (PS) in a spatially defined manner, which could be tailored by changing the flow rate and sample-nozzle distance. Contact angle analysis and measurement of cell growth areas indicate that the minimum size of the treatment was limited to ~1.5-3mm diameter when the 100µm internal diameter capillary was used.
    - XPS analysis indicated that the surface modification was due to the incorporation of oxygen, and this was likely due to reactive species carried within the gas flow of the plasma jet. Spatially resolved XPS analysis indicated that an increase in oxygen corresponded to a decrease in contact angle. Higher spatial resolution XPS could provide a better correlation between the XPS and contact angle results.
    - The plasma jet was not destructive to the polymer surface as evidenced by AFM analysis which demonstrated no significant change in surface roughness following treatment.
    - LEC grown on plasma treated surfaces did not display typical epithelial cobblestone morphology. LECs appeared confined to treated areas however they displayed actin stress fibres not present in LECs grown on TCPS.

2. Microplasma Jet Modification of Poly(Methyl Methacrylate)(PMMA)
    - Similarly to PS, the microplasma jet could be used to create spatially defined modification of PMMA in a non-destructive manner. This indicates that the surface treatment could be used on acrylic-based IOLs.
    - Surface modification was likely due to incorporation of oxygen but this was not demonstrated for PMMA. Due to the presence of oxygen in pristine PMMA and the large x-ray spot size, in comparison to the treatment size, it was difficult to determine differences in oxygen concentration between untreated and treated PMMA.
    - Surface treatment increased the initial attachment of LECs onto PMMA surfaces compared to untreated PMMA. This result and the insignificant change in surface roughness following treatment indicates that the cellular response was due to a change in surface chemistry. There was a greater presence of actin stress fibres on both treated and untreated PMMA compared to TCPS.
    - Spatially-defined microplasma jet treatment of the periphery of an intraocular lens (IOL) optic may increase the rate of adhesion of the IOL to the lens capsule, thus preventing LEC migration to the central portion of the IOL optic.

3. Atmospheric Pressure Plasma Jet for Plasma Polymerisation
    - An atmospheric pressure plasma jet system, operating in air, can be used to polymerisation heptylamine films onto surface, however the method incorporates oxygen also. The incorporation of oxygen, either during or following treatment, may be a limiting factor in this treatment process.
    - Plasma polymerised films increased the attachment and growth of LECs compared to untreated PS, however further work is required to elucidate a difference in cellular response on plasma polymerised surfaces (containing nitrogen and oxygen functionalisation) and plasma treated surfaces (containing oxygen functionalisation).

4. Surface Modification using a Pin Plasma Device

- Non-destructive spatially defined surface modification of PS can be achieved using a pin plasma device.
- Treatment size can be tailored by altering the voltage and frequency supplied to the pin plasma.
- The surface treatment increases the LEC adhesion and growth in a spatially defined manner. Further examination is required.

6 Future Work

In the following section the key areas of future work which would greatly complement this thesis will be outlined.

One of the key areas of future work would be repetition and further investigation of XPS. Some of the XPS contained within this thesis was based on single samples. It would be valuable to repeat these experiments. Spatially resolved XPS analysis of samples treated with the various flow rates and sample nozzle distances may provide clues to the cause of the difference in cell growth on samples treated with the various parameters. Analysis of high resolution spectra of C1, O1s and N1s peaks of the plasma polymerised samples would demonstrate the various functional groups present. One of the limiting factors of the XPS equipment was the size of the x-ray beam, which was 1.5mm wide and 7mm in height. The size of the spot meant that there was overlap between the positions taken and spectra were in fact an average of the electrons emitted from a 10.5mm^2 area. Ideally an x-ray photoelectron spectrophotometer with small beam size could be used to obtain data with a higher spatial resolution.

Other spectroscopic techniques could help in the understanding of the process by which the plasmas modify the surfaces and thus influence cellular response in a spatially defined manner. ToF-SIMS could be used to map chemical changes on a surface. Mass spectroscopy and optical emission spectroscopy could further demonstrate which species are present within the plasma plume and further down-stream.

Another limitation in the methodology in this thesis is the determination of the cell growth area from stitched images. This was a subjective measure and would benefit from an algorithm/macro within a software package which could determine this more objectively. An increased number of positions taken during cell counts, i.e. greater spatial resolution, could also provide a more accurate measure. A form of qualitative analysis such as staining for phenotypic markers at each position may also yield interesting results. These methods could benefit greatly from computer automation of the microscopy.

Time lapse microscope could be conducted in future work. From this time lapse microscopy the spreading, migration and growth of cells could be observed. This may elucidate whether cells initially adhered to a central region then migrated further out, or whether cells adhered outside this central region in a lower density and proliferated more slowly there, due to the lower density. This may indicate whether initial protein adsorption only permits adhesion and attachment in specific areas, and if so, does it take the LECs longer to grow on regions which did not allow initial cell adhesion? If it were observed that cells initially adhered in the centre, then after some time migrated towards the edges, this information could indicate time points at which ECM remodelling could be investigated. The quantification of the density, orientation and position of ECM proteins on the substrates prior to cell seeding, could also elucidate the reason for the initial cell attachment in the centre [225, 252, 253]. The study of initial protein adsorption may also provide interesting results in comparison to TCPS, due to the much higher cell density observed on microplasma treated surfaces. Time lapse microscopy could also provide information on whether LECs are migrating on top of one another and how LECs settle and spread on the surface.

Staining with an antibody for alpha smooth muscle actin (αSMA), along with phalloidin, would also be very useful in future work. αSMA is a marker for epithelial-mesenchymal transition (EMT) and may explain the presence of stress fibres in LECs on plasma treated surfaces.

It is suggested that the seeding method may have caused a greater number of cells to settle in the centre of the PS and PMMA coupons contributing to the high cell counts in the centre of samples. The cell suspension was placed on the samples such that surface tension at the edge of the samples held the drop on the surface in a dome, or bubble, shape. As the bubble effect may have cause more cells to settle in the centre (Figure 4.6), in future work it may be beneficial to mount samples within a well with soft agar such that the sample surface and agar surfaces are approximately level (Figure 6.1). Then the cell suspension could be seeded into the entire well, rather than just on the sample surface as done previously. Cells which settle on the agar should not grow.

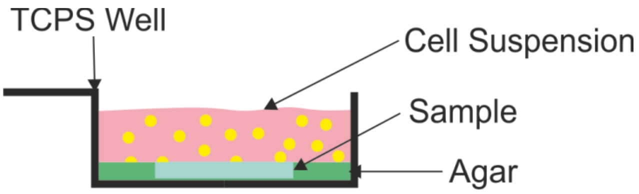

Figure 6.1 Example of seeding with agar. Agar and sample surfaces are approximately level. Cell suspension seeded into entire well.

Much further work is required in the investigation of the secretion and effect of cytokines. One of the difficulties was comparing concentrations between samples, which had different numbers of cells. In future additional samples could be seeded from which cells could be trypsinised and counted to help correlate excretion with cell number. It may also be of interest to examine the expression of the genes of these cytokines and their receptors by quantitative polymerase chain reaction (qPCR). Immunocytochemical staining of the receptors may then suggest whether LECs in the centre or periphery of the cell growth area on treated samples are influenced by these cytokines.

Finally, work could be undertaken to use the plasma polymerisation process, following further optimisation, to create surface functional groups which inhibit the attachment of LECs. This is one of the smaller aims stated in section 1.7 and a possible route to overcome PCO outlined in the literature.

7 References

1. Williams, D., F., ed. Definitions in Biomaterials. first ed. Progress in Biomedical Engineering. Vol. 4. 1987, Elsevier Science Publishers.
2. Williams, R.L. and Wong, D., Ophthalmic biomaterials, in Biomedical Materials, R. Narayan, Editor. 2009, Springer. p. 327-348.
3. Ratner, B.D., The biocompatibility manifesto: Biocompatibility for the twenty-first century. Journal of Cardiovascular Translational Research, 2011. 4(5): 523-527.
4. Eskin, S.G., et al., Some background concepts, in Biomaterials Science: An Introduction to Materials in Medicine, B.D. Ratner, et al., Editors. 2004, Elsevier Academic Press. p. 237-292.
5. D'Sa, R.A., et al., Protein adhesion and cell response on atmospheric pressure dielectric barrier discharge-modified polymer surfaces. Acta Biomaterialia, 2010. 6(7): 2609-2620.
6. Vroman, L., Effect of adsorbed proteins on the wettability of hydrophilic and hydrophobic solids. Nature, 1962. 196(4853): 476-477.
7. McKenzie, J.L. and Webster, T., Protein interactions at materials surfaces, in Biomedical Materials, R. Narayan, Editor. 2009, Springer. p. 215-238.
8. Anfinsen, C.B., Principles that govern the folding of protein chains. Science, 1973. 181(4096): 223-230.
9. Sethuraman, A., et al., Effect of surface wettability on the adhesion of proteins. Langmuir, 2004. 20(18): 7779-7788.
10. Mittal, K.L., Contact Angle, Wettability and Adhesion. First ed. 1993, VSP BV.
11. Ranter, B.D., et al., Biomaterials Science: An Introduciton to Materials in Medicine. 1st ed. 1996, Academic Press.
12. Gray, J.J., The interaction of proteins with solid surfaces. Current Opinion in Structural Biology, 2004. 14(1): 110-115.
13. Aplin, A.E., et al., Signal transduction and signal modulation by cell adhesion receptors: The role of integrins, cadherins, immunoglobulin-cell adhesion molecules, and selectins. Pharmacological Reviews, 1998. 50(2): 197-264.
14. Ruoslahti, E. and Pierschbacher, M.D., New perspectives in cell adhesion: RGD and integrins. Science, 1987. 238(4826): 491-497.
15. Hynes, R.O., Integrins: Versatility, modulation, and signaling in cell adhesion. Cell, 1992. 69(1): 11-25.
16. Nishi, O., et al., Detection of cell adhesion molecules in lens epithelial cells of human cataracts. Investigative Ophthalmology & Visual Science, 1997. 38(3): 579-85.
17. Schakenraad, J.M. and Busscher, H.J., Cell-polymer interactions: The influence of protein adsorption. Colloids and Surfaces, 1989. 42(3-4): 331-343.
18. D'Sa, R.A., et al., Lens epithelial cell response to atmospheric pressure plasma modified poly(methylmethacrylate) surfaces. Journal of Materials Science: Materials in Medicine, 2010. 21(5): 1703-1712.
19. Yonson, S., et al., Cell treatment and surface functionalization using a miniature atmospheric pressure glow discharge plasma torch. Journal of Physics D: Applied Physics, 2006. 39(16): 3508-3513.

20. Webb, K., et al., Relative importance of surface wettability and charged functional groups on NIH 3T3 fibroblast attachment, spreading, and cytoskeletal organization. Journal of Biomedical Materials Research, 1998. 41(3): 422-430.
21. Khatua, D., et al., Influence of charge densities of randomly sulfonated polystyrene surfaces on cell attachment and proliferation. Journal of Nanoscience and Nanotechnology, 2011. 11(5): 4227-4230.
22. Wong, J.Y., et al., Balance of chemistry, topography, and mechanics at the cell–biomaterial interface: Issues and challenges for assessing the role of substrate mechanics on cell response. Surface Science, 2004. 570(1–2): 119-133.
23. Filová, E., et al., Regionally-selective cell colonization of micropatterned surfaces prepared by plasma polymerization of acrylic acid and 1,7-octadiene. Physiological Research, 2009. 58(5): 669-684.
24. Kearns, V., et al., Biomaterials surface topography to cellular response: Technologies, cell techniques and biomedical applications, in Surface Modifications of Biomaterials, R.L. Willaims, Editor. 2011, Woodhead Publishing Limited. p. 169-204.
25. Williams, R.L., Lecture Notes, K.G. Doherty, Editor. 2010.
26. Ruskell, G., et al., The eye, in Gray's Anatomy: The Anatomical Basis of Clinical Practice, S. Standring, Editor. 2008, Churchill Livingstone Elesvier.
27. National Eye Institute, N.I.o.H., NEI Catalog Number: NEA09. Accessed 2012.
28. Davson, H., Physiology of the Eye. Fourth ed. 1980, Churchill Livingstone.
29. Danysh, B.P. and Duncan, M.K., The lens capsule. Experimental Eye Research, 2009. 88(2): 151-164.
30. Maidment, J.M., et al., Regional differences in tyrosine kinase receptor signaling components determine differential growth patterns in the human lens. Investigative Ophthalmology & Visual Science, 2004. 45(5): 1427-1435.
31. Dickson, D.H. and Crock, G.W., Interlocking patterns on primate lens fibers. Investigative Ophthalmology & Visual Science, 1972. 11(10): 809-815.
32. Andley, U.P., Crystallins in the eye: Function and pathology. Progress in Retinal and Eye Research, 2007. 26(1): 78-98.
33. Zwaan, J. and Hendrix, R.W., Changes in cell and organ shape during early development of the ocular lens. Integrative and Comparative Biology, 1973. 13(4): 1039-1049.
34. Martini, F.H., Fundamentals of Anatomy and Physiology fifth ed. 2001, Pentice Hall.
35. Grierson, I., The Eye Book: Eyes and Eye Problems Explained. 2000, Liverpool University Press.
36. De Iongh, R.U., et al., Transforming growth factor-β-induced epithelial-mesenchymal transition in the lens: A model for cataract formation. Cells Tissues Organs, 2005. 179(1-2): 43-55.
37. Apple, D.J., et al., Posterior capsule opacification. Survey of Ophthalmology, 1992. 37(2): 73-116.
38. Mann, I., The lens, in Development of The Human Eye. 1969, Grunge and Stratton Inc.,. p. 46-67.
39. McAvoy, J.W., et al., Lens development. Eye, 1999. 13(3B): 425-437.
40. Bron, A.J., et al., The lens and zonules, in Wolff's Anatomy of the Eye and Orbit, A.J. Bron, R.C. Tripathi, and B.J. Tripathi, Editors. 1997, Chapman & Hall. p. 411-442.
41. Davson, H., Accomodation, in Physiology of The Eye, H. Davson, Editor. 1980, Churchill Livingstone. p. 767-782.

42. Kauffman, P.L., Accomdation and presbyopia: Neuromuscular and biophysical aspects, in Adler's Physiology of the Eye, W.H. Hart, Editor. 1992, Mosby-Year Book Inc. p. 391-411.
43. Refojo, M.F., Ophthalmic applications, in Biomaterials Science: An Introduction to Materials in Medicine, B.D. Ratner, et al., Editors. 2004, Elsevier Academic Press. p. 583-591.
44. Lace, R., Intraocular lenses and their potential to prohibit posterior capsule opacification, University of Liverpool, UK. 2013, PhD.
45. Brian, G. and Taylor, H., Cataract blindness - Challenges for the 21st century. Bulletin of the World Health Organization, 2001. 79(3): 249-256.
46. West, S.K. and Valmadrid, C.T., Epidemiology of risk factors for age-related cataract. Survey of Ophthalmology, 1995. 39(4): 323-334.
47. Organisation, W.H. Prevention of avoidable blindness and visual impairment. in Sixity-Second World Health Assembly. 2009.
48. Pascolini, D. and Mariotti, S.P., Global estimates of visual impairment: 2010. British Journal of Ophthalmology, 2012. 96(5): 614-618.
49. Francis, P.J., et al., Lens biology: Development and human cataractogenesis. Trends in Genetics, 1999. 15(5): 191-196.
50. Zigman, S., The role of sunlight in human cataract formation. Survey of Ophthalmology, 1983. 27(5): 317-326.
51. Wu, R., et al., Smoking, socioeconomic factors, and age-related cataract: The Singapore Malay eye study. Archives of Ophthalmology, 2010. 128(8): 1029-1035.
52. Kanthan, G.L., et al., Alcohol consumption and the long-term incidence of cataract and cataract surgery: The blue mountains eye study. American Journal of Ophthalmology, 2010. 150(3): 434-440.
53. Costello, M.J., et al., Ultrastructural analysis of damage to nuclear fiber cell membranes in advanced age-related cataracts from India. Experimental Eye Research, 2008. 87(2): 147-158.
54. Jedziniak, J.A., et al., The concentration and localization of heavy molecular weight aggregates in aging normal and cataractous human lenses. Experimental Eye Research, 1975. 20(4): 367-369.
55. Shinohara, T., et al., Cataracts: Role of the unfolded protein response. Medical Hypotheses, 2006. 66(2): 365-370.
56. Davson, H., The lens, in Physiology of The Eye, H. Davson, Editor. 1980, Churchill Livingstone. p. 139-202.
57. Patterson, C.A. and Delamere, N.A., The lens, in Adler's Physiology of The Eye, W.H. Hart, Editor. 1992, Mosby-Year Book Inc.,. p. 348-390.
58. Costello, M.J., et al., Multilamellar spherical particles as potential sources of excessive light scattering in human age-related nuclear cataracts. Experimental Eye Research, 2010. 91(6): 881-889.
59. Costello, M.J., et al., Ultrastructure of fiber cells and multilamellar inclusions in experimental diabetes. Investigative Ophthalmology & Visual Science, 1993. 34(7): 2174-2185.
60. Costello, M.J., et al., Cellular architecture in age-related human nuclear cataracts. Investigative Ophthalmology & Visual Science, 1992. 33(11): 3209-3227.
61. National Eye Institute, N.I.o.H., NEI Catalog Number: NEA12. Accessed 2012.
62. National Eye Institute, N.I.o.H., NEI Catalog Number: NEA13. Accessed 2012.

63. Minassian, D.C., et al., The deficit in cataract surgery in England and Wales and the escalating problem of visual impairment: Epidemiological modelling of the population dynamics of cataract. British Journal of Ophthalmology, 2000. 84: 4-8.
64. Yuen, C.H.W., et al., Modification of the surface properties of a lens material to influence posterior capsular opacification. Clinical and Experimental Ophthalmology, 2006. 34(6): 568-574.
65. Resnikoff, S., et al., Global data on visual imparment in the year 2002. Bulletin of the World Health Organization, 2004. 82(11): 844-851.
66. The Royal College of Ophthalmologists. Cataract surgery guidelines. 2005 [cited 2010 [Acessed: 14/04/10]; Available from: http://www.rcophth.ac.uk/docs/publications/CataractSurgeryGuidelinesMarch2005Updated.pdf.
67. Coombles, A. and Garty, D., Cataract surgery. Fundamentals of Clinical Ophthalmolgy, ed. S. Lightman. 2003, BMJ Books.
68. Williams, R.L. and Kearns, V.R., Drug-device combination products for ocular applications, in Drug-Device Combination Products: Delivery Technologies and Applications, A. Lewis, Editor. 2010, Woodhead Publishing Limited. p. 311-340.
69. Healthwise Inc. Phacoemulification for cataract surgery. 2011 [Acessed: 30/04/2012]; Available from: http://www.emedicinehealth.com/script/main/art.asp?articlekey=138867&ref=129647.
70. Wormstone, I.M., et al., Posterior capsule opacification. Experimental Eye Research, 2009. 88(2): 257-269.
71. Matsushima, H., et al., Preventing secondary cataract and anterior capsule contraction by modification of intraocular lenses. Expert Review of Medical Devices, 2008. 5(2): 197-207.
72. Kappelhof, J.P., et al., The ring of Soemmerring in man: An ultrastructural study. Graefe's Archive for Clinical and Experimental Ophthalmology, 1986. 225(1): 77-83.
73. Linnola, R.J., et al., Adhesion of fibronectin, vitronectin, laminin, and collagen type IV to intraocular lens materials in pseudophakic human autopsy eyes : Part 1: Histological sections. Journal of Cataract & Refractive Surgery, 2000. 26(12): 1792-1806.
74. Wormstone, I.M., et al., Human lens epithelial cell proliferation in a protein-free medium. Investigative Ophthalmology & Visual Science, 1997. 38(2): 396-404.
75. Saika, S., Relationship between posterior capsule opacification and intraocular lens biocompatibility. Progress in Retinal and Eye Research, 2004. 23(3): 283-305.
76. Wormstone, I.M., Posterior capsule opacification: A cell biological perspective. Experimental Eye Research, 2002. 74(3): 337-347.
77. Wormstone, I.M., Posterior capsule opacification, in Encyclopedia of the Eye, A.D. Darlene, Editor. 2010, Academic Press. p. 469-475.
78. Allen, J.B., et al., The lens influences aqueous humor levels of transforming growth factor-β2. Graefe's Archive for Clinical and Experimental Ophthalmology, 1998. 236(4): 305-311.
79. Wallentin, N., et al., Effect of cataract surgery on aqueous TGF-β and lens epithelial cell proliferation. Investigative Ophthalmology & Visual Science, 1998. 39(8): 1410-8.
80. Marcantonio, J.M. and Vrensen, G.F.J.M., Cell biology of posterior capsular opacification. Eye, 1999. 13(3 B): 484-488.

81. Saika, S., et al., Response of lens epithelial cells to injury: Role of lumican in epithelial-mesenchymal transition. Investigative Ophthalmology & Visual Science, 2003. 44(5): 2094-2102.

82. Zeisberg, M. and Neilson, E.G., Biomarkers for epithelial-mesenchymal transitions. The Journal of Clinical Investigation, 2009. 119(6): 1429-1437.

83. Hay, E.D., An overview of epithelio-mesenchymal transformation. Acta Anatomica, 1995. 154(1): 8-20.

84. Hay, E.D. and Zuk, A., Transformations between epithelium and mesenchyme: Normal, pathological, and experimentally induced. American Journal of Kidney Diseases: The Official Journal of the National Kidney Foundation, 1995. 26(4): 678-690.

85. Wormstone, I.M., et al., TGF-β2-induced matrix modification and cell transdifferentiation in the human lens capsular bag. Investigative Ophthalmology & Visual Science, 2002. 43(7): 2301-2308.

86. Mansfield, K.J., et al., FGF-2 counteracts loss of TGFβ affected cells from rat lens explants: Implications for PCO (after cataract). Molecular Vision, 2004. 10: 521-532.

87. Wormstone, I.M., et al., FGF: An autocrine regulator of human lens cell growth independent of added stimuli. Investigative Ophthalmology & Visual Science, 2001. 42(6): 1305-1311.

88. Nishi, O., et al., Effects of the cytokines on the proliferation of and collagen synthesis by human cataract lens epithelial cells. British Journal of Ophthalmology, 1996. 80(1): 63-68.

89. McAvoy, J.W. and Chamberlain, C.G., Fibroblast growth factor (FGF) induces different responses in lens epithelial cells depending on its concentration. Development, 1989. 107(2): 221-228.

90. Nishi, O., et al., Synthesis of interleukin-1 and prostaglandin E2 by lens epithelial cells of human cataracts. British Journal of Ophthalmology, 1992. 76(6): 338-341.

91. Nishi, O., et al., Synthesis of interleukin-1, interleukin-6, and basic fibroblast growth factor by human cataract lens epithelial cells. Journal of Cataract & Refractive Surgery, 1996. 22: 852-858.

92. Meacock, W.R., et al., Role of cytokines in the pathogenesis of posterior capsule opacification. British Journal of Ophthalmology, 2000. 84(3): 332-336.

93. Prada, J., et al., Detection of tumor necrosis factor alpha and interleukin 1 alpha gene expression in human lens epithelial cells. Journal of Cataract & Refractive Surgery, 2000. 26(1): 114-117.

94. Van Gelderen, B.E., et al., Cytokines in aqueous humour and serum before and after corneal transplantation and during rejection. Ophthalmic Research, 2000. 32(4): 157-164.

95. Dick, A.D. and Carter, D.A., Cytokines and immunopathogenesis of intraocular posterior segment inflammation. Ocular Immunology and Inflammation, 2003. 11(1): 17-28.

96. Malecaze, F., et al., Role of interleukin 6 in the inflammatory response after cataract surgery: An experimental and clinical study. Archives of Ophthalmology, 1991. 109(12): 1681-1683.

97. Zhou, Z.H. and He, S.Z., An experimental study of the interleukin 1 levels in aqueous humor after intraocular lens implantation. Ophthalmologica, 1998. 212(3): 157-159.

98. Takai, Y., et al., Multiplex cytokine analysis of aqueous humor in eyes with primary open-angle glaucoma, exfoliation glaucoma, and cataract. Investigative Ophthalmology & Visual Science, 2012. 53(1): 241-247.

99. Lewis, A.C., Interleukin-6 in the pathogenesis of posterior capsule opacification and the potential role for interleukin-6 inhibition in the future of cataract surgery. Medical Hypotheses, 2013. 80(4): 466-474.

100. Shigemitsu, T., et al., Immunocytochemical features of lens after cataract tissue - Signalling molecules (growth factors, cytokines, other signalling molecules), cytoskeleton proteins, cellular and extracellular matrix proteins. International Ophthalmology, 2001. 23(3): 137-144.

101. Saika, S., et al., Immunolocalization of TGF-β1, -β2 and -β3, and TGF-β receptors in human lens capsules with lens implants. Graefe's Archive for Clinical and Experimental Ophthalmology, 2000. 238(3): 283-293.

102. Esparza, J., et al., Fibronectin upregulates gelatinase B (MMP-9) and induces coordinated expression of gelatinase A (MMP-2) and Its activator MT1-MMP (MMP-14) by human T lymphocyte cell lines. A process repressed through RAS/MAP kinase signaling pathways. Blood, 1999. 94(8): 2754-2766.

103. Eldred, J.A., et al., MMP2 activity is critical for TGFβ2-induced matrix contraction—Implications for fibrosis. Investigative Ophthalmology & Visual Science, 2012. 53(7): 4085-4098.

104. Ohadi, C., et al., Posterior capsule opacification. Current Opinion in Ophthalmology, 1991. 2(1): 46-52.

105. Schaumberg, D.A., et al., A systematic overview of the incidence of posterior capsule opacification. Ophthalmology, 1998. 105(7): 1213-1221.

106. Boureau, C., et al., Cost of cataract surgery after implantation of three intraocular lenses. Clinical Ophthalmology, 2009. 3(1): 277-285.

107. Bozukova, D., et al., Polymers in modern ophthalmic implants-Historical background and recent advances. Materials Science and Engineering: R: Reports, 2010. 69(6): 63-83.

108. Peng, Q., et al., Surgical prevention of posterior capsule opacification: Part 2: Enhancement of cortical cleanup by focusing on hydrodissection. Journal of Cataract & Refractive Surgery, 2000. 26(2): 188-197.

109. Trivedi, R.H., et al., Post cataract-intraocular lens (IOL) surgery opacification. Nature, 2002. 16(1): 217 - 241.

110. Tetz, M.R. and Nimsgern, C., Posterior capsule opacification: Part 2: Clinical findings. Journal of Cataract & Refractive Surgery, 1999. 25(12): 1662-1674.

111. Beck, R., et al., Inhibition of lens epithelial cell adhesion by the calcium antagonist Mibefradil correlates with impaired integrin distribution and organization of the cytoskeleton. Graefe's Archive for Clinical and Experimental Ophthalmology, 2001. 239(6): 452-458.

112. Fernandez, V., et al., Efficacy of various drugs in the prevention of posterior capsule opacification: Experimental study of rabbit eyes. Journal of Cataract & Refractive Surgery, 2004. 30(12): 2598-2605.

113. Walker, T.D., Pharmacological attempts to reduce posterior capsule opacification after cataract surgery - a review. Clinical and Experimental Ophthalmology, 2008. 36(9): 883-890.

114. Kearns, V.R. and Williams, R.L., Drug delivery systems for the eye. Expert Review of Medical Devices, 2009. 6(3): 277-290.

115. Duncan, G., et al., Thapsigargin-coated intraocular lenses inhibit human lens cell growth. Nature Medicine, 1997. 3(9): 1026-1028.
116. Duncan, G., et al., Lens cell survival after exposure to stress in the closed capsular bag. Investigative Ophthalmology & Visual Science, 2007. 48(6): 2701-2707.
117. Pandey, S.K., et al., Intracapsular ring sustained 5-fluorouracil delivery system for the prevention of posterior capsule opacification in rabbits: A histological study. Journal of Cataract & Refractive Surgery, 2002. 28(1): 139-148.
118. Awasthi, N. and Wagner, B.J., Suppression of human lens epithelial cell proliferation by proteasome inhibition, a potential defense against posterior capsular opacification. Investigative Ophthalmology & Visual Science, 2006. 47(10): 4482-4489.
119. Wormstone, I.M., et al., Characterisation of TGF-β2 signalling and function in a human lens cell line. Experimental Eye Research, 2004. 78(3): 705-714.
120. Wormstone, M.I., et al., Short-term exposure to transforming growth factor-β induces long-term fibrotic responses. Experimental Eye Research, 2006. 83(5): 1238-1245.
121. Liu, C.S.C., et al., A study of human lens cell growth in vitro: A model for posterior capsule opacification. Investigative Ophthalmology & Visual Science, 1996. 37(5): 906-914.
122. Tan, D.T.H., et al., Randomized clinical trial of a new dexamethasone delivery system (surodex) for treatment of post-cataract surgery inflammation. Ophthalmology, 1999. 106(2): 223-231.
123. Tan, D.T.H., et al., Randomized clinical trial of surodex steroid drug delivery system for cataract surgery: Anterior versus posterior placement of two surodex in the eye. Ophthalmology, 2001. 108(12): 2172-2181.
124. Wadood, A.C., et al., Safety and efficacy of a dexamethasone anterior segment drug delivery system in patients after phacoemulsification. Journal of Cataract & Refractive Surgery, 2004. 30(4): 761-768.
125. Morrison, D., et al., Applications in the anterior segment, in Biomaterials and Regenerative Medicine in Ophthalmology, T. Chirila, Editor. 2010, Woodhead Publishing Limited. p. 17-64.
126. Ratner, B.D., Surface properties and surface characterisation of materials, in Biomaterials Science: An Introduction to Materials in Medicine, B.D. Ratner, et al., Editors. 2004, Elsevier Academic Press. p. 40-58.
127. Bozukova, D., et al., Plasma surface fluorination of hydrogel materials coating stability and in vitro biocompatibility testing. Soft Materials, 2010. 8(2): 164-182.
128. Hollick, E.J., et al., Posterior capsular opacification with hydrogel, polymethylmethacrylate, and silicone intraocular lenses: two-year results of a randomized prospective trial. American Journal of Ophthalmology, 2000. 129(5): 577-584.
129. Tognetto, D., et al., Biocompatibility of hydrophilic intraocular lenses. Journal of Cataract & Refractive Surgery, 2002. 28(4): 644-651.
130. Nishi, O., Preventing posterior capsule opacification by creating a discontinuous sharp bend in the capsule. Journal of Cataract & Refractive Surgery, 1999. 25(4): 521-526.
131. Nishi, O., et al., Effect of intraocular lenses on preventing posterior capsule opacification: Design versus material. Journal of Cataract & Refractive Surgery, 2004. 30(10): 2170-2176.

132. Sacu, S., et al., Effect of intraocular lens optic edge design and material on fibrotic capsule opacification and capsulorhexis contraction. Journal of Cataract & Refractive Surgery, 2004. 30(9): 1875-1882.
133. Nishi, O., et al., Speed of capsular bend formation at the optic edge of acrylic, silicone, and poly(methyl methacrylate) lenses. Journal of Cataract & Refractive Surgery, 2002. 28(3): 431-437.
134. Linnola, R.J., Sandwich theory: Bioactivity-based explanation for posterior capsule opacification. Journal of Cataract & Refractive Surgery, 1997. 23(10): 1539 - 1542.
135. Linnola, R.J., et al., Intraocular lens bioactivity tested using rabbit corneal tissue cultures. Journal of Cataract & Refractive Surgery, 1999. 25(11): 1480-1485.
136. Linnola, R.J., et al., Adhesion of fibronectin, vitronectin, laminin, and collagen type IV to intraocular lens materials in pseudophakic human autopsy eyes: Part 2: Explanted intraocular lenses. Journal of Cataract & Refractive Surgery, 2000. 26(12): 1807-1818.
137. Linnola, R.J., The Sandwich Theory: A bioactivity based explaination of posterior capsule opacication after cataract surgery with intraocular lense implantation, University of Oulu, Finland. 2001, PhD.
138. Linnola, R.J., et al., Adhesion of soluble fibronectin, vitronectin, and collagen type IV to intraocular lens materials. Journal of Cataract & Refractive Surgery, 2003. 29(1): 146-152.
139. Johnston, R.L., et al., In vitro protein adsorption to 2 intraocular lens materials. Journal of Cataract & Refractive Surgery, 1999. 25(8): 1109-1115.
140. Li, N., et al., Effect of AcrySof versus silicone or polymethyl methacrylate intraocular lens on posterior capsule opacification. Ophthalmology, 2008. 115(5): 830-838.
141. Prosdocimo, G., et al., Posterior capsule opacification after phacoemulsification: silicone CeeOn Edge versus acrylate AcrySof intraocular lens. Journal of Cataract & Refractive Surgery, 2003. 29(8): 1551-5.
142. Apple, D.J., Influence of intraocular lens material and design on postoperative intracapsular cellular reactivity. Transactions of the American Ophthalmological Society, 2000. 98: 257-283.
143. Apple, D.J., et al., Silicone oil adhesion to intraocular lenses: An experimental study comparing various biomaterials. Journal of Cataract & Refractive Surgery, 1997. 23(4): 536-544.
144. Awasthi, N., et al., Posterior capsular opacification: A problem reduced but not yet eradicated. Archives of Ophthalmology, 2009. 127(4): 555-562.
145. Fagerholm, P., et al., Heparin surface modified intraocular lenses implanted in the monkey eye. Journal of Cataract & Refractive Surgery, 1989. 15(5): 485-490.
146. Larsson, R., et al., Intraocular PMMA lenses modified with surface-immobilized heparin: evaluation of biocompatibility in vitro and in vivo. Biomaterials, 1989. 10(8): 511-516.
147. Rønbeck, M. and Kugelberg, M., Posterior capsule opacification with 3 intraocular lenses: 12-year prospective study. Journal of Cataract & Refractive Surgery, 2014. 40(1): 70-76.
148. Rønbeck, M., et al., Comparison of glistenings in intraocular lenses with three different materials: 12-year follow-up. Acta Ophthalmologica, 2013. 91(1): 66-70.
149. Yao, K., et al., Improvement of the surface biocompatibility of silicone intraocular lens by the plasma-induced tethering of phospholipid moieties. Journal of Biomedical Materials Research - Part A, 2006. 78(4): 684-692.

150. Huang, X.D., et al., Surface modification of silicone intraocular lens by 2-methacryloyloxyethyl phosphoryl-choline binding to reduce Staphylococcus epidermidis adherence. Clinical and Experimental Ophthalmology, 2007. 35(5): 462-467.

151. Huang, X.D., et al., Reduced silicone oil adherence to silicone intraocular lens by surface modification with 2-methacryloyloxyethyl phosphoryl-choline. Current Eye Research, 2013. 38(1): 91-96.

152. Pot, S.A., et al., Selenium functionalized intraocular lenses inhibit posterior capsule opacification in an ex vivo canine lens capsular bag assay. Experimental Eye Research, 2009. 89(5): 728-734.

153. Wang, Y., et al., Surface modification of acrylate intraocular lenses with dielectric barrier discharge plasma at atmospheric pressure. Science in China, Series B: Chemistry, 2009. 52(8): 1235-1243.

154. Zhang, L., et al., Surface modification of polymethyl methacrylate intraocular lenses by plasma for improvement of antithrombogenicity and transmittance. Applied Surface Science, 2009. 255(15): 6840-6845.

155. D'Sa, R.A., et al., Inhibition of lens epithelial cell growth via immobilisation of hyaluronic acid on atmospheric pressure plasma modified polystyrene. Soft Matter, 2011. 7(2): 608-617.

156. Szili, E.J., et al., Surface modification of biomaterials by plasma polymerisation (In Press), in Surface Modification of Biomaterials: Methods, analysis and appliciations, R.L. Williams, Editor. 2011, Woodhead Publishing Limited. p. 3-38.

157. Suh, T.S., et al., Surface modification of polymethyl methacrylate intraocular lenses with the mixture of acrylic acid and acrylamide via plasma-induced graft copolymerization. Journal of Applied Polymer Science, 2002. 85(11): 2361-2366.

158. Foest, R., et al., Microplasmas, an emerging field of low-temperature plasma science and technology. International Journal of Mass Spectrometry, 2006. 248(3): 87-102.

159. Tonks, L. and Langmuir, I., A general theory of the plasma of an arc. Physical Review, 1929. 34(6): 876-922.

160. Chan, C.M., Plasma modification, in Polymer Surface Modification and Characterization. 1994, Carl Hanser Verlag. p. 225-264.

161. Piel, A., Definition of a plasma state, in Plasma Physics: An Introduction to Laboratory, Space, and Fusion Plasmas. 2010, Springer Berlin Heidelberg. p. 29-43.

162. Chan, C.M., et al., Polymer surface modification by plasmas and photons. Surface Science Reports, 1996. 24(1-2): 1-54.

163. Nasser, E., Fundamentals of gaseous ionization and plasma electronics. Wiley Series in Plasma Physics. 1971, Wiley-Interscience.

164. Kong, M.G., et al., Plasma medicine: An introductory review. New Journal of Physics, 2009. 11(115012): 1-35.

165. Laroussi, M. and Akan, T., Arc-free atmospheric pressure cold plasma jets: A review. Plasma Processes and Polymers, 2007. 4(9): 777-788.

166. Laroussi, M. and Lu, X., Room-temperature atmospheric pressure plasma plume for biomedical applications. Applied Physics Letters, 2005. 87(11): 113902.

167. Stoffels, E., et al., Plasma needle: A non-destructive atmospheric plasma source for fine surface treatment of (bio)materials. Plasma Sources Science and Technology, 2002. 11(4): 383-388.

168. Doherty, K.G., et al., Polystyrene surface modification for localized cell culture using a capillary dielectric barrier discharge atmospheric-pressure microplasma jet. Plasma Processes and Polymers, 2013. 10(11): 978-989.
169. Desmet, T., et al., Nonthermal plasma technology as a versatile strategy for polymeric biomaterials surface modification: A review. Biomacromolecules, 2009. 10(9): 2351-2378.
170. Tan, H.M.L., et al., Surface modification of poly(dimethylsiloxane) for controlling biological cells' adhesion using a scanning radical microjet. Thin Solid Films, 2007. 515(12): 5172-5178.
171. Laroussi, M. Mechanisms of interaction of cold plasma with bacteria. 2008. Ponta Delgada, Azores.
172. Lee, K., et al., Sterilization of bacteria, yeast, and bacterial endospores by atmospheric-pressure cold plasma using helium and oxygen. Journal of Microbiology, 2006. 44(3): 269-275.
173. Isbary, G., et al., Non-thermal plasma-More than five years of clinical experience. Clinical Plasma Medicine, 2013. 1(1): 19-23.
174. Leduc, M., et al., Cell permeabilization using a non-thermal plasma. New Journal of Physics, 2009. 11(115021): 1-12.
175. Laroussi, M., Low-temperature plasmas for medicine? IEEE Transactions on Plasma Science, 2009. 37(6 PART 1): 714-725.
176. Laroussi, M., The biomedical applications of plasma: A brief history of the development of a new field of research. IEEE Transactions on Plasma Science, 2008. 36(4 PART 3): 1612-1614.
177. Bárdos, L. and Baránková, H., Plasma processes at atmospheric and low pressures. Vacuum, 2008. 83(3): 522-527.
178. Becker, K.H., et al., Microplasmas and applications. Journal of Physics D: Applied Physics, 2006. 39(3): R55-R70.
179. Walsh, J.L., et al., Three distinct modes in a cold atmospheric pressure plasma jet. Journal of Physics D: Applied Physics, 2010. 43(7): 075201.
180. Oshima, N., et al., Development of atmospheric pressure plasma jet with slit nozzle. Japanese Journal of Applied Physics, 2011. 50(1 PART 2): 01AH06.
181. Kakei, R., et al., Production of ultrafine atmospheric pressure plasma jet with nano-capillary. Thin Solid Films, 2010. 518(13): 3457-3460.
182. Park, H.S., et al., Optical and electrical characterization of an atmospheric pressure microplasma jet with a capillary electrode. Physics of Plasmas, 2010. 17(3): 033502.
183. Walsh, J.L., et al., Contrasting characteristics of pulsed and sinusoidal cold atmospheric plasma jets. Applied Physics Letters, 2006. 88(17): 171501.
184. Walsh, J.L., et al., The manipulation of atmospheric pressure dielectric barrier plasma jets. Plasma Sources Science and Technology, 2012. 21(3): 034007.
185. McKay, K., et al., Mass spectrometric diagnosis of an atmospheric pressure helium microplasma jet. Journal of Physics D: Applied Physics, 2013. 46(46): 464018.
186. Oh, J.S., et al., Discharge and plasma bullet formation in a capillary DBD atmospheric-pressure microplasma jet. IEEE Transactions on Plasma Science, 2011. 39(11 PART 1): 2352-2353.
187. Oh, J.-S., et al., Time-resolved mass spectroscopic studies of an atmospheric-pressure helium microplasma jet Journal of Physics D: Applied Physics, 2011. 44(36): 365202-365211.

188. Oh, J.-S., et al., Imaging gas and plasma interaction in the surface chemical modification of polymers by micro-plasma jet Journal of Physics D: Applied Physics, 2011. 44(15): 155206-155211.
189. Oh, J.-S. and Bradley, J.W., Heavy ion formation in plasma jet polymerization of heptylamine at atmospheric pressure. Plasma Processes and Polymers, 2013. 10(10): 839-852.
190. Topala, I., et al., Experimental and theoretical investigations of dielectric-barrier plasma jet in Helium. IEEE Transactions on Plasma Science, 2012. 40(11 PART1): 2811-2816.
191. Mericam-Bourdet, N., et al., Experimental investigations of plasma bullets. Journal of Physics D: Applied Physics, 2009. 42(5): 055207.
192. Bowfield, A., et al., Surface analysis using a new plasma assisted desorptionionisation source for mass spectrometry in ambient air. Review of Scientific Instruments, 2012. 83(6): 063503-1 - 063503-7.
193. Kieft, I.E., et al., Electrical and optical characterization of the plasma needle. New Journal of Physics, 2004. 6(149): 1-14.
194. Stoffels, E., et al., Superficial treatment of mammalian cells using plasma needle. Journal of Physics D: Applied Physics, 2003. 36(23): 2908-2913.
195. Salter, T.L., et al., Ambient surface mass spectrometry using plasma-assisted desorption ionization: Effects and optimization of analytical parameters for signal intensities of molecules and polymers. Analytical Chemistry, 2013. 85(3): 1675-1682.
196. Ratner, B.D. and Hoffman, A.S., Physicochemical surface modification of materials used in medicine, in Biomaterials Science: An Introduction to Materials in Medicine, B.D. Ratner, et al., Editors. 2004, Elsevier Academic Press. p. 201-219.
197. France, R.M. and Short, R.D., Plasma treatment of polymers effects of energy transfer from an argon plasma on the surface chemistry of poly(styrene), low density poly(ethylene), poly(propylene) and poly(ethylene terephthalate). Journal of the Chemical Society - Faraday Transactions, 1997. 93(17): 3173-3178.
198. Vasilets, V.N., et al., Regulation of the biological properties of medical polymer materials with the use of a gas-discharge plasma and vacuum ultraviolet radiation. High Energy Chemistry, 2006. 40(2): 79-85.
199. Idage, S.B. and Badrinarayanan, S., Surface modification of polystyrene using nitrogen plasma. An X-ray photoelectron spectroscopy study. Langmuir, 1998. 14(10): 2780-2785.
200. Martin, Y., et al., Study of the effect of process parameters for n-heptylamine plasma polymerization on final layer properties. Thin Solid Films, 2007. 515(17): 6844-6852.
201. Wilson, D.J., et al., Plasma modification of PTFE surfaces - Part I: Surfaces immediately following plasma treatment. Surface and Interface Analysis, 2001. 31(5): 385-396.
202. Matsushima, H., et al., Active oxygen processing for acrylic intraocular lenses to prevent posterior capsule opacification. Journal of Cataract & Refractive Surgery, 2006. 32(6): 1035-1040.
203. D'Sa, R.A. and Meenan, B.J., Chemical grafting of poly(ethylene glycol) methyl ether methacrylate onto polymer surfaces by atmospheric pressure plasma processing. Langmuir, 2010. 26(3): 1894-1903.

204. Noma, Y., et al., Local surface modification of polymer material using low-temperature microplasma. Journal of Photopolymer Science and Technology, 2007. 20(6): 785-792.
205. Motrescu, I., et al., Micro-patterning of functional groups onto polymer surface using capillary atmospheric pressure plasma jet. Journal of Photopolymer Science and Technology, 2012. 25(4): 529-534.
206. Vogelsang, A., et al., Fluorocarbon plasma polymer deposition by an atmospheric pressure microplasma jet using different precursor molecules – A comparative study. Plasma Processes and Polymers, 2013. 10(4): 364-371.
207. Kearns, V., et al., Plasma polymer coatings to aid retinal pigment epithelial growth for transplantation in the treatment of age related macular degeneration. Journal of Materials Science: Materials in Medicine, 2012. 23(8): 2013-2021.
208. Carton, O., et al., Plasma polymerization of acrylic acid by atmospheric pressure nitrogen plasma jet for biomedical applications. Plasma Processes and Polymers, 2012. 9(10): 984-993.
209. Benedikt, J., et al., Thin film deposition by means of atmospheric pressure microplasma jet. Plasma Physics and Controlled Fusion, 2007. 49(12b): B419.
210. Whittle, J.D., et al., Reconciling the physical and chemical environments of plasma: A commentary on "mechanisms of plasma polymerisation - Reviewed from a chemical point of view". Plasma Processes and Polymers, 2012. 9(9): 840-843.
211. Vogelsang, A., et al., Locally resolved analysis of polymer surface functionalization by an atmospheric pressure argon microplasma jet with air entrainment. Plasma Processes and Polymers, 2010. 7(1): 16-24.
212. Benedikt, J., et al., Atmospheric pressure microplasma jet as a depositing tool. Applied Physics Letters, 2006. 89(25): 251504.
213. Dunn, K.C., et al., ARPE-19, a human retinal pigment epithelial cell line with differentiated properties. Experimental Eye Research, 1996. 62(2): 155-169.
214. Reddan, J.R., et al., Retention of lens specificity in long-term cultures of diploid rabbit lens epithelial cells. Differentiation, 1986. 33(2): 168-174.
215. Andley, U.P., et al., Propagation and immortalization of human lens epithelial cells in culture. Investigative Ophthalmology & Visual Science, 1994. 35(7): 3094-3102.
216. Wang-Su, S.T., et al., Proteome analysis of lens epithelia, fibers, and the HLE B-3 cell line. Investigative Ophthalmology & Visual Science, 2003. 44(11): 4829-4836.
217. Fleming, T.P., et al., Expression of growth control and differentiation genes in human lens epithelial cells with extended life span. Investigative Ophthalmology & Visual Science, 1998. 39(8): 1387-1398.
218. Krausz, E., et al., Expression of crystallins, Pax6, Filensin, CP49, MIP, and MP20 in lens- derived cell lines. Investigative Ophthalmology & Visual Science, 1996. 37(10): 2120-2128.
219. Thévenaz, P. and Unser, M., User-friendly semiautomated assembly of accurate image mosaics in microscopy. Microscopy Research and Technique, 2007. 70(2): 135-146.
220. Taylor, M., et al., Picoliter water contact angle measurement on polymers. Langmuir, 2007. 23(13): 6875-6878.
221. Weightman, P., A new high sensitivity Auger spectrometer. Physica Scripta, 1992. T41: 277-281.

222. Häidopoulos, M., et al., Angle-resolved XPS study of plasma-deposited polystyrene films after oxygen plasma treatment. Plasma Processes and Polymers, 2008. 5(1): 67-75.
223. Paynter, R.W., XPS studies of the modification of polystyrene and polyethyleneterephthalate surfaces by oxygen and nitrogen plasmas. Surface and Interface Analysis, 1998. 26(9): 674-681.
224. Grinnell, F. and Feld, M.K., Fibronectin adsorption on hydrophilic and hydrophobic surfaces detected by antibody binding and analyzed during cell adhesion in serum-containing medium. Journal of Biological Chemistry, 1982. 257(9): 4888-4893.
225. Underwood, P.A., et al., Effects of polystyrene surface chemistry on the biological activity of solid phase fibronectin and vitronectin, analysed with monoclonal antibodies. Journal of Cell Science, 1993. 104(3): 793-803.
226. Bahre, H., et al., Vacuum ultraviolet (VUV) emssion of an atmospheric pressure plasma jet operated in helium-oxygen mixtures in ambient air. Acta Technica, 2011 56: T199.
227. Reuter, S., et al., Generation of atomic oxygen in the effluent of an atmospheric pressure plasma jet. Plasma Sources Science and Technology, 2009. 18(1).
228. France, R.M. and Short, R.D., Plasma treatment of polymers Effects of energy transfer from an argon plasma on the surface chemistry of poly(styrene), low density poly(ethylene), poly(propylene)and poly(ethylene terephthalate). Journal of the Chemical Society, Faraday Transactions, 1997. 93(17): 3173-3178.
229. Léveillé, V. and Coulombe, S., Design and preliminary characterization of a miniature pulsed RF APGD torch with downstream injection of the source of reactive species. Plasma Sources Science and Technology, 2005. 14(3): 467-476.
230. Xinpei, L., et al., A single electrode room-temperature plasma jet device for biomedical applications. Applied Physics Letters, 2008. 92(15): 151504-151504-3.
231. Perkins, M.J., Radical Chemisty: The Fundamentals. Oxford Chemistry Primers, ed. R.G. Compton, et al. 2005, Oxford University Press.
232. Bradley, J.W., et al., Schlieren photography of the outflow from a plasma jet. IEEE Transactions on Plasma Science, 2011. 39(11 PART 1): 2312-2313.
233. Nobelprize.org. "The Nobel Prize in Chemistry 1918". 2013 [cited 2013 [Acessed: 18/10/2013]; Available from: <http://www.nobelprize.org/nobel_prizes/chemistry/laureates/1918/>.
234. Nobelprize.org. "The Nobel Prize in Chemistry 1931". 2013 [cited 2013 [Acessed: 18/10/2013]; Available from: <http://www.nobelprize.org/nobel_prizes/chemistry/laureates/1931/>.
235. Ting, Y.-H., et al., Surface roughening of polystyrene and poly(methyl methacrylate) in Ar/O2 plasma etching. Polymers, 2010. 2(4): 649-663.
236. Sax, C.M., et al., Analysis of α-crystallin expression in cultured mouse and rabbit lens cells. Experimental Eye Research, 1995. 61(1): 125-127.
237. Meakin, S.O., et al., A rabbit lens epithelial cell line supports expression of an exogenous crystallin gene characteristic of lens fiber cell differentiation. Experimental Eye Research, 1989. 48(1): 131-137.
238. Russell, P., et al., Tissue culture of lens epithelial cells from normal and Nakano mice. Investigative Ophthalmology & Visual Science, 1977. 16(3): 243-246.
239. Yamada, T., et al., Synthesis of α-crystallin by a cell line derived from the lens of a transgenic animal. Current Eye Research, 1990. 9(1): 31-37.

240. Bhat, S.P. and Nagineni, C.N., αB subunit of lens-speciific protein α-crystallin is present in other ocular and non-ocular tissues. Biochemical and Biophysical Research Communications, 1989. 158(1): 319-325.
241. Dubin, R.A., et al., Expression of the murine αB-crystallin gene is not restricted to the lens. Molecular and Cellular Biology, 1989. 9(3): 1083-1091.
242. Wormstone, I.M., et al., A focus on the human lens in vitro. Environmental Toxicology and Pharmacology, 2006. 21(2 SPEC. ISS.): 215-221.
243. Ashery-Padan, R. and Gruss, P., Pax6 lights-up the way for eye development. Current Opinion in Cell Biology, 2001. 13(6): 706-714.
244. Božanić, D., et al., Involvement of cytoskelatal proteins and growth factor receptors during development of the human eye. Anatomy and Embryology, 2006. 211(5): 367-377.
245. Kasper, M. and Viebahn, C., Cytokeratin expression and early lens development. Anatomy and Embryology, 1992. 186(3): 285-290.
246. Kivelä, T. and Uusitalo, M., Structure, development and function of cytoskeletal elements in non-neuronal cells of the human eye. Progress in Retinal and Eye Research, 1998. 17(3): 385-428.
247. Pitz, S. and Moll, R., Intermediate-filament expression in ocular tissue. Progress in Retinal and Eye Research, 2002. 21(2): 241-262.
248. Robey, H.L., et al., Cytokeratins and retinal epithelial cell behaviour. Journal of Cell Science, 1992. 102(2): 329-340.
249. Piatigorsky, J., Lens differentiation in vertebrates. Differentiation, 1981. 19(1-3): 134-153.
250. Power, W., et al., Morphological appearances of human lens epithelial cells in culture. Documenta Ophthalmologica, 1993. 84(4): 351-363.
251. Grinnell, F., Cell spreading factor: Occurrence and specificity of action. Experimental Cell Research, 1976. 102(1): 51-62.
252. Kalaskar, D.M., et al., Characterization of the interface between adsorbed fibronectin and human embryonic stem cells. Journal of the Royal Society Interface, 2013. 10(83): 20130139.
253. Lhoest, J.B., et al., Fibronectin adsorption, conformation, and orientation on polystyrene substrates studied by radiolabeling, XPS, and ToF SIMS. Journal of Biomedical Materials Research, 1998. 41(1): 95-103.
254. Chen, Y., et al., A role for Wnt/planar cell polarity signaling during lens fiber cell differentiation? Seminars in Cell & Developmental Biology, 2006. 17(6): 712-725.
255. Naumanen, P., et al., Mechanisms of actin stress fibre assembly. Journal of Microscopy, 2008. 231(3): 446-454.
256. Jampel, H.D., et al., Transforming growth factor-β in human aqueous humor. Current Eye Research, 1990. 9(10): 963-969.
257. Tripathi, R.C., et al., Protein composition of human aqueous humor: SDS-PAGE analysis of surgical and post-mortem samples. Experimental Eye Research, 1989. 48(1): 117-130.
258. Tripathi, R.C., et al., Detection, quantification, and significance of basic fibroblast growth factor in the aqueous humor of man, cat, dog and pig. Experimental Eye Research, 1992. 54(3): 447-454.
259. Hollick, E.J., et al., Lens epithelial cell regression on the posterior capsule with different intraocular lens materials. British Journal of Ophthalmology, 1998. 82(10): 1182-1188.

260. Schroeder, A.C., et al., Impact of fibronectin on surface properties of intraocular lenses. Graefe's Archive for Clinical and Experimental Ophthalmology, 2009. 247(9): 1277-1283.
261. Liu, D.S. and Weng, J.N., Preparation of TiO2/PMMA IOL and its safety evaluation by animal experiments. International Journal of Ophthalmology, 2008. 8(8): 1533-1535.
262. West, J., et al., Microplasma writing for surface-directed millifluidics. Lab on a Chip, 2007. 7(8): 981-983.
263. Fricke, K., et al., Modification of the physicochemical surface properties of polymers during the plasma-based decontamination, in International Plasma Chemistry Society 20. 2011, International Plasma Chemistry Society: Philldelphia, USA.
264. Cui, L., et al., Improved adhesion of dense silica coatings on polymers by atmospheric plasma pretreatment. ACS Applied Materials and Interfaces, 2013. 5(17): 8495-8504.
265. Gonzalez Ii, E. and Hicks, R.F., Surface analysis of polymers treated by remote atmospheric pressure plasma. Langmuir, 2010. 26(5): 3710-3719.
266. Ii, E.G., et al., Surface activation of poly(methyl methacrylate) via remote atmospheric pressure plasma. Plasma Processes and Polymers, 2010. 7(6): 482-493.
267. McLean, S.M., et al., Detection of integrins in human cataract lens epithelial cells and two mammalian lens epithelial cell lines. British Journal of Ophthalmology, 2005. 89(11): 1506-9.
268. Nebe, B., et al., Induction of apoptosis by the calcium antagonist mibefradil correlates with depolarization of the membrane potential and decreased integrin expression in human lens epithelial cells. Graefe's Archive for Clinical and Experimental Ophthalmology, 2004. 242(7): 597-604.
269. Gerenser, L.J., XPS studies of in situ plasma-modified polymer surfaces. Journal of Adhesion Science and Technology, 1993. 7(10): 1019-1040.
270. Gengenbach, T.R., et al., Contributions of restructuring and oxidation to the aging of the surface of plasma polymers containing heteroatoms. Plasmas and Polymers, 1997. 2(2): 91-114.

Publications from this Thesis

"Polystyrene Surface Modification for Localized Cell Culture Using a Capillary Dielectric Barrier Discharge Atmospheric-Pressure" Doherty, K.G., Oh, J.-S., Unsworth, P., Bowfield, A., Sheridan, C.M., Weightman, P., Bradley, J.W., Williams, R.L., Microplasma Jet. Plasma Processes and Polymers, 2013. 10(11): p. 978-989.